UNIVERSITY OF CALIFORNIA

Santa Barbara

# Correlated Structure-Property Relationships in Cementitious Solids via Unconventional Spin Polarization Transfer

A dissertation submitted in partial satisfaction of the

requirements for the degree Doctor of Philosophy

in Chemical Engineering

by

Nathan Andrew Prisco

Committee in charge:

Professor Bradley F. Chmelka, Chair

Professor Michael F. Doherty

Professor Songi Han

Professor Mahdi M. Abu-Omar

September 2020

The dissertation of Nathan Andrew Prisco is approved.

_____
Mahdi M. Abu-Omar

_____
Songi Han

_____
Michael F. Doherty

_____
Bradley F. Chmelka, Chair

September 2020

**Correlated Structure-Property Relationships in Cementitious Solids via Unconventional Spin Polarization Transfer**



by

Nathan Andrew Prisco

*For my father, Leonard Thomas Prisco*

# ACKNOWLEDGEMENTS

The past five years have been an incredible opportunity, the diversity and depth of work presented in this dissertation would not have been possible without the dedication and support of several people and institutions. Foremost, I should like to extend my sincerest gratitude to my advisor Professor Bradley F. Chmelka who encouraged me to apply dimensional property analyses to generalize aspects of non-equilibrium spin polarization transfer and to develop pragmatic insights into important industrial materials.

Brad, without your unrelenting enthusiasm and personal support I would not have had the motivation nor opportunity to carry out this engaging endeavor. The workload was heavy and the expectations very high, but these diverse projects have expanded my scientific interests and afforded me a profound depth of understanding into fundamental chemical physics, material science, and applied engineering. I am particularly grateful for the sense of salesmanship that you cultivated in me which has opened the door to new and exciting opportunities. Undoubtedly, the reason that I was selected by the University of Alaska Fairbanks and the Department of Energy Advanced Manufacturing Office to be the inaugural and sole “Arctic Innovator” was due in a large part to your professional guidance.

My gratitude to my other committee members Professors Michael Doherty, Songi Han, and Mahdi Omar for their diverse knowledge bases and unique perspectives which was of great benefit to my graduate studies.

Over the course of my graduate career I have greatly benefited from the collaborative environment at UCSB which has guided my work. I am especially grateful to Dr. Rahul Sangodkar and Dr. Zachariah Berkson for their time and generous assistance in facilitating

my *induction* into the field of magnetic resonance. After which, I remain indebted to the MRL facilities staff, especially Dr. Jerry Hu and Jaya Nolt, for their time and efforts in repairing and salvaging several instrument threatening rotor crashes. Also, I thank Dr. Thomas Farmer whose ingenious and simple approach to the description of non-equilibrium crystallization processes motivated my own pursuit of dimensional property analyses. I extend my appreciation to Professor Eric McFarland whose passion for energy innovation encouraged me to engage with the campus community and pursue new professional opportunities. Lastly, I thank all the members of the Chmelka group and greater UCSB community who participated in stimulating scientific and personal discussions these past five years including George Degen, Patrick Corona, Warren Jin, Tsatsral Battsengel, Shona Becwar, Maxwell Berkow, Dr. Niels Zussblatt, Julia Fisher, Dr. Mathew Idso, Dr. Philipp Selter, and Michael "*New Guy*" Schmithorst.

During my graduate studies I had the unique opportunity to collaborate with several industrial, governmental, and academic partnerships. The month I spent visiting École polytechnique fédérale de Lausanne was among the most productive exchanges of my graduate career. Foremost, I extend my gratitude to Dr. Arthur Pinon and Professor Lyndon Emsley for stimulating discussion regarding the Dynamic Nuclear Polarization and the spin-diffusion barrier. Also, to Dr. Brennan Walder, Dr. Frederic Parazo, and Dr. Jayasubba Reddy Yarava for developing new methodologies to measure spin-diffusion coefficients in inorganic oxides. At the U.S. Army Core of Engineer's Engineering Research and Development Center (ERDC) to Dr. Jedadiah Burroughs, Dr. Chuck Weiss, and Dr. Edward Perkins for their knowledge of structural solids and for accommodating my visit. And to Halliburton, the U.S.

Federal Highway Administration, the U.S. Army Research Office, and the NSF supported IRG-3 for supporting my graduate studies.

Finally my greatest thanks to my father, Leonard Prisco, who taught me the value of hard work, consistency, and pursuing my goals with a singular vision. If it wasn't for you, I would have never grown an appreciation for the great outdoors. Here is to the next great adventure.

Nathan Prisco

Santa Barbara, California 2020

VITA OF NATHAN ANDREW PRISCO
August 2020

EDUCATION

Doctor of Philosophy in Chemical Engineering, University of California, Santa Barbara, September 2020 (expected)

Bachelor of Science in Chemical Engineering, University of Texas, Austin, December 2014 (with honors)

PROFESSIONAL EMPLOYMENT

**University of California Santa Barbara**, Santa Barbara, California
Teaching assistant
Transport Processes: Heat Transfer — Winter 2019
Chemical Engineering Thermodynamics — Spring 2018
Separation Processes — Fall 2016

**LP Amina Energy and Environmental**, Beijing, China
R&D engineer — January – September 2015

**Colorado Center for Biorefining and Biofuels**, Boulder, Colorado
REU Researcher — Summer 2014

**College Houses Student Housing Cooperative**, Austin, Texas
Director of Taos Cooperative — August 2013 – May 2014

**Center for Enabling New Technologies through Catalysis**, Madison, Wisconsin
REU Researcher — Summer 2013

VISITING RESEARCHER

École Polytechnique Fédérale de Lausanne, Switzerland — March 2017

PUBLICATIONS

**N. Prisco**; A. Pinon; L. Emsley; B. Chmelka. "Scaling Analyses for Hyperpolarization Transfer across a Spin-Diffusion Barrier and into Bulk Solid Media." Submitted to *Phys. Chem. Chem. Phys.*

K. Manjesh; Z. Berkson; R. Clark; Y. Shen; **N. Prisco**; Z. Zeng; H. Zheng; L. McCusker; J. Palmer; B. Chmelka; J. Rimer. "Crystallization of Mordenite Platelets using Cooperative Organic Structure-directing Agents." *J. Am. Chem. Soc.*, **2019**, 141, pp 20155.

B. Walder; **N. Prisco**; F. Paruzzo; J. Reddy; B. Chmelka; L. Emsley; "Measurement of Proton Spin Diffusivity in Hydrated Cementitious Solids." *J. Phys. Chem. Lett.,* **2019**, 1017, pp 5064.

K. Gottschling; L. Stegbauer; G. Savasci; **N. Prisco**; Z. Berkson; C. Ochsenfeld; B. Chmelka; B. Lotsch; "Molecular insights into carbon dioxide sorption in hydrazone-based covalent organic frameworks with tertiary amine moieties." *Chem. Mater.,* **2019**, 6, pp 1946.
D.W. Janes; T. Inoue; **N. Prisco**; M.J. Maher; P.F. Nealey; C.J. Ellison. "Spatially-controllable and uniform photochemical transfer printing of block copolymer nanopatterns." *Mol. Syst. Des. Eng.,* **2017**, 2, pp 597

T.A. Arshad; C.B. Kim; **N. Prisco**; J.M. Katzenstein; D.W. Janes; R.T. Bonnecaze; C.J. Ellison. "Precision Marangoni Driven Patterning." *Soft Matter.,* **2014**, 10, pp 8043

J.M. Katzenstein; C.B. Kim; **N. Prisco**; R. Katsumata; Z. Li; D.W. Janes; G. Blachut; C.J. Ellison. "A Photochemical Approach to Directing Flow and Stabilizing Topography in Polymer Films." *Macromolecules*, **2014**, 47, pp 6804

J.M. Katzenstein; D.W. Janes; J.D. Cushen; N.B. Hira; D.L. McGuffin; **N. Prisco**; C.J. Ellison. "Patterning by Photochemically Directing the Marangoni Effect." *ACS Macro Lett.,* **2012**, 1, pp 1150.

MANUSCRIPTS TO BE SUBMITTED

**N. Prisco**; W. Pearl; S. Lewis; P. Corona; Z. Berkson; K. Weigandt; M. Helgeson; B. Chmelka. "Atomic- and Meso-scale Compositions of Hydrating Volcanic Glasses in Roman-Inspired Structural Solids." To be submitted to *J. Am. Chem. Soc.*

**N. Prisco**; R. Sangodkar; T. Farmer; B. Walder; L. Emsley; M. Doherty; T. Ley; G. Scherer; B. Chmelka. "Compositions and Thicknesses of Surface Hydration Layers on Tricalcium Silicate Particles." To be submitted to *Langmuir*.

PRESENTATIONS

1) "*Quantitative Scaling Analyses for non-Boltzmann Spin Polarization Transfer*." Experimental NMR Conference, Baltimore, MD. 11 March 2020. Presentation.
2) "*Quantitative Scaling Analyses for Estimating Domain Sizes and Compositions at Particle Surfaces By Surface-Enhanced NMR.*" AiChE Annual Meeting, Orlando, Fl, 8 November 2019. Presentation.
3) "*Influence of local structures and surface interactions on the crystallization, dissolution, and hydration of aluminosilicate-based structural materials*." Army Core

of Engineers Engineering Research and Development Center (ERDC), Vicksburg, MS. 1 March 2019. Presentation.

4) "*Understanding $^{1}H$-$^{1}H$ polarization transfer at solvent-particle interfaces under low-temperature DNP conditions*." Experimental NMR Conference, Orlando, Fl. 28 April 2018. Poster.
5) "*Determining thicknesses of thin hydrated layers on low-surface-area tricalcium silicate particles via DNP-enhanced NMR spin diffusion*." Experimental NMR Conference, Asilomar, CA. 25 March 2017. Poster.
6) "*Influence of additive species on dissolution, hydration, and crystallization*." First-year Graduate Student Symposium, UCSB, Santa Barbara, CA. 25 September 2016. Presentation.
7) "*Enhancing rate of selective hydrogenation catalysts by modulation of Pd crystallite diameter*." AiChE Annual Meeting, Atlanta, GA, 16 November 2014. Poster.
8) "*Heterogeneous acid catalyzed conversion of furfuryl alcohol to valuable chemicals*." 247$^{th}$ ACS Conference, Dallas, CA. 16 March 2014. Poster.

AWARDS

1$^{st}$ place, UT Austin ChE Senior Design Project, 2014
Sally Seal and A.E. Chionsini Endowed Scholarship in Chemical Engineering, 2013
Boy Scouts of America Eagle Scout, 2010

ABSTRACT

**Correlated Structure-Property Relationships in Cementitious Solids via Unconventional Spin Polarization Transfer**

by

Nathan Andrew Prisco

Mechanical properties of composite materials are often hierarchical emerging from atomic-level structures, chemical and physical interactions, dimensions and distributions of ordered or disordered domains, and dynamics over time scales relevant to the process or system. Identifying correlated structure-property relationships is central to the rational design of advanced structural composites, but is challenging for systems with heterogeneous compositions, poor long-range order, and low particle surface areas. Advanced solid-state nuclear magnetic resonance (NMR) techniques are sensitive to ordered and disordered environments and enable the preferential detection of surface species or interactions, the resolution of distinct local atomic structures in bulk materials, and the measurement of domain sizes ranging from <1nm to micrometer length scales. In contrast to conventional NMR, Dynamic Nuclear Polarization (DNP) involves the manipulation of coupled electron-nuclear spin ensembles to generate a large nuclear magnetization gradient that dramatically enhances NMR signal sensitivity. An advantage of DNP-NMR is that hyperpolarization emanates from paramagnetic centers, enabling surface-enhanced NMR spectroscopy of porous or nonporous

solids. Despite the widespread application of this technique, quantitative models of DNP polarization transfer are difficult to implement and rely on coupled spin polarization generation, propagation, and dissipation processes that bridge quantum mechanical and classical phenomena. In Chapter two and three of this manuscript, a constitutive model is derived to quantitatively describe aspects of mesoscopic spin polarization transfer. From dimensional property analysis, spin polarization analogs of the dimensionless Biot number (Bi), Hatta number (Ha), Damköhler number (Da), and Thiele modulus ($\phi$) are discovered and their general relevance to spin polarization transport processes demonstrated. Importantly, by analogy to heat and mass transfer film theory, a DNP transfer coefficient, $k_{DNP}$, with units of m/s is empirically measured and reveals new insights into the transfer of spin hyperpolarization across the electron-nuclear spin interface (*i.e.*, spin-diffusion barrier). In Chapter four and five of this manuscript, combined DNP-enhanced $^{1}$H-$^{1}$H spin diffusion experiments and modelling analyses are used to measure the compositions and dimensions of silicate hydrates which form on tricalcium silicate particles in contact with water. The dimensions and compositions of these surface hydrates are believed to crucially influence the early hydration kinetics of industrially relevant cement-water mixtures, thus by understanding these processes at the atomic-level, new criteria is provided to inform chemical admixture design and to aid in the prediction of hydration rates. Lastly, in Chapter six of this manuscript, advanced two-dimensional $^{27}$Al{$^{29}$Si} heteronuclear correlation experiments are used to monitor hydration processes involving volcanic glasses in cementitious mixtures. These analyses provide new geochemical insights regarding the structure of vitreous pyroclastic minerals and informs the design of modern Roman-inspired pozzolanic concretes with improved longevity and a lower carbon footprint in comparison to traditional cements.

TABLE OF CONTENTS

LIST OF FIGURES

## Chapter I.

# Synopsis

By analogy to heat and mass transfer film theory, in Chapter two and three of this manuscript, a general approach is introduced for determining hyperpolarization transfer rates between dilute electron spins and a surrounding nuclear ensemble. These analyses provide new quantitative relationships for understanding, predicting, and optimizing the effectiveness of hyperpolarization protocols, such as Dynamic Nuclear Polarization (DNP) under magic-angle spinning conditions. An empirical DNP polarization-transfer coefficient is measured as a function of the bulk matrix $^{1}$H spin density and indicates the presence of two distinct kinetic regimes associated with different rate-limiting polarization transfer phenomena. Dimensional property relationships are derived and used to evaluate the competitive rates of spin polarization generation, propagation, and dissipation that govern hyperpolarization transfer between large coupled spin ensembles. The quantitative analyses agree closely with experimental measurements for the accumulation, propagation, and dissipation of hyperpolarization in solids and provide evidence for kinetically-limited transfer associated with a spin-diffusion barrier. The results and classical approach yield general design criteria for analyzing and optimizing polarization transfer processes involving complex interfaces and composite media for applications in materials science, physical chemistry and nuclear spintronics.

In Chapter four and five of this manuscript, dynamic nuclear polarization (DNP) surface-enhanced NMR analyses enable the simultaneous measurement of the molecular-level compositions and meso-scale dimensions of hydrated surface domains and offer new insights

into the early hydration of industrially relevant cementitious mixtures. Hydration of cementitious silicate particles is initiated at surfaces in contact with water and proceeds over different timescales which are commonly described as distinct kinetic stages (*e.g.*, induction, acceleration, deceleration). Despite several decades of detailed investigation, the transformations occurring at the liquid-solid interface during early times (*ca.* hours) have remained elusive. Characterization of these hydrated near-surface silicates is challenging due to the poor long-range order of cement hydrates and the exceedingly dilute quantities of hydration products formed at early times. Such transformations occurring at the silicate particle surface are important to understand as they are thought to influence silicate dissolution, hydration, and subsequent strength development. The results demonstrate the use of non-equilibrium NMR spin polarization transfer to assess the compositions of complicated multicomponent materials over challenging *ca*. <1 nm to 100 nm length scales which may be inaccessible by other means. These analyses suggest that silicate particle surfaces initially form a thin layer of disordered hydrates (<10 nm) upon contact with water that continue to evolve over the course of the induction period until relatively ordered calcium silicate hydrates are detected that are associated with surface nucleation products.

In Chapter six of this manuscript, advanced two-dimensional solid-state NMR techniques are used to monitor the hydration of Roman-inspired concrete. Hydrothermal conversion of multicomponent aluminosilicate glasses into value-added products including zeolites and cementitious solids depend on complex heterogeneous hydration, dissolution, and precipitation processes that are difficult to monitor by conventional characterization methods. Despite similarities in bulk compositions, local structural differences between vitreous precursors may result in significant variations in the quantities, distributions, and types of

hydrothermal products formed. This has important consequences for Roman-inspired pozzolanic concretes which are of high modern interest due to their improved durability and reduced carbon footprint. Importantly, in such cementitious mixtures, similar volcanic ashes (*i.e.*, rhyolite) procured from different geographic formations may, nonetheless, exhibit vastly different propensities for mechanical strength development. Advanced 1D and 2D solid-state nuclear magnetic resonance (NMR) techniques, small-angle neutron scattering (SANS), and complementary bulk analyses suggest that certain volcanic glass specimen are compositionally heterogeneous and are comprised of locally ordered subunits similar to crystalline tectosilicate minerals, zeolites, or $SiO_2$ polymorphs over <1 nm to 25 nm length scales. Specifically, 2D $^{27}Al\{^{29}Si\}$ heteronuclear correlation experiments allow for the measurement of Al-O-Si distributions in unhydrated volcanic glasses and, upon hydration, enable $^{27}Al$ isotopic tracking of the conversion of volcanic glass-Al into into cementitious binder phases. These analyses indicate that hydration activity is negatively correlated to the extent of $Al/SiO_2$ intermixing and that Al-rich tectosilicate regions of volcanic glass are preferentially converted into cementitious hydrates. Additionally, mechanical strength is correlated to the formation of binder phases including calcium aluminosilicate hydrate, a complex layered mineral with varying extents of condensation, distributions of several distinct $Al^{IV}$ sites, and local structural order. New structure-property relationships are obtained which inform the molecular optimization of modern concrete systems, reveal fundamental insights into the geological formation of vitreous pyroclastic minerals, and provide new understanding of structural mortars similar to those used in the construction of important cultural heritage sites.

## Chapter II.

# Thermodynamics and Scaling Analyses of Polarization Transport in Heterogeneous Solids

## 2.1. Introduction

In coupled energy transfer and dissipation processes, dimensional property analyses provide bases for understanding complex phenomena in large systems ranging from industrial-scale process equipment[1] to complex micromechanical systems[2]. Extending such analyses to the propagation of spin polarization is important for emerging applications of hyperpolarized magnetic resonance[3–7] and processes based on spin transport over multiple length scales[8,9]. In quantum computing, the coupling of electron qubits with highly polarized nuclear spin packets (*e.g.*, nuclear spintronics) is a promising strategy for extending coherence lifetimes and for facilitating short-term data storage functions[10,11]. Another example is dynamic nuclear polarization (DNP), which exploits the coupling of electron-nuclear spin ensembles to enhance dramatically NMR signal sensitivity in solids[12]. Quantitative models of DNP polarization transfer[13,14], are often challenging to implement as the generation, propagation, and dissipation of hyperpolarization can span time scales ranging from $10^{-9}$ to $10^{5}$ s, length scales from <1 nm to μm, and involve considerations of both quantum mechanical and classical phenomena. Materials systems on which these examples are based share key features, specifically complex and poorly defined interfaces between the electron spin(s) and surrounding nuclear ensemble[15]. In Chapter two, an introduction to spin thermodynamics is presented for describing the transfer of net nuclear magnetization (*i.e.*,

spin polarization) from dilute paramagnetic centers to a surrounding nuclear spin ensemble. By application of a material energy balance, a general model is derived for meso-scale (1–100 nm) spin transport phenomena that enables rate-limiting processes to be identified and quantitative prediction of hyperpolarization performance. In large systems, the generation, dissipation, and propagation and spin polarization exhibit fundamental similarities to thermal energy transfer, molecular diffusion, and to charge transport but importantly combines distinct aspects of these phenomenon and emerges from different physical origins.

## 2.2. Discovery of Spin Angular Momentum

The discovery of spin angular momentum, its modern applications in advanced medical imaging, molecular-level spectroscopy, and quantum computing may be best understood from a series of theoretical and hardware advancements over the past century. At the end of the 19$^{th}$ century, there was widespread interest in the line spectra of elements. Line spectra are produced when an atomic gas is excited by electrical discharge in a vacuum tube and the produced electromagnetic radiation is passed through a prism to separate frequencies of radiation into a series of discrete spectral lines unique to each element. Zeeman first observed spectral line-splitting in the presence of a magnetic field, which seemed to suggest the magnetic field influenced the motion of electrically charged ions.[16] An early classical electrodynamical theory arose shortly thereafter from the important contributions of Larmor who demonstrated that Zeeman splitting could be accounted for by the orbital oscillations of a single-type of charged particle.[17] Through the work of Thomson and Rutherford a general picture of the atom and its interactions with electromagnetic radiation emerged[18,19], yet the theory of line spectra at that time was not consistent with Planck's quantized theory of black body radiation.

In classical electrodynamical theory, an electron may orbit the nucleus, yet as energy is released from the atom in the form of radiation the electron's orbit must decay continuously with no restriction until it is eventually touching the nucleus. Within this framework, the frequency of revolution is a continuous function of the energy; therefore, it is not possible to obtain a result where a finite amount of homogeneous radiation is produced. Many of these issues were reconciled by the introduction of quantum electrodynamical theory in 1913 by Niels Bohr.[20,21] Bohr postulates that, W, the energy required to remove an electron to an infinite distance from the nuclei (*e.g.*, flame ionization) is directly related to Planck's quantized theory of black body radiation, see equation (2.1). The frequency of revolution (ω) for a single electron in a circular orbit around the nucleus is given by equation (2.2).

$$W = nh\frac{\omega}{2} \tag{2.1}$$

$$\omega = \frac{4\pi^2 me^2 E^2}{n^3 h^3} \tag{2.2}$$

Further analysis shows that as an electron transitions from one allowed state to another allowed state it transmits a frequency of radiation which corresponds with the half the frequency of revolution of the electron in the final allowed state. From application of equations (2.1) and (2.2) it is demonstrated that the ordinary hydrogen line spectrum from electrical discharge in a vacuum tube, or the *Balmer series,* is generated in the scenario where the atom transitions from a state of n = 1 to a state of n = 2. Bohr's method of analysis supplanted the classic electrodynamical atomic theories of the time and provides a physical intuition for atomic equilibrium based on the notion of stable mechanical states which are preserved through the universal constancy of angular momentum.

Although Bohr's early quantum electrodynamical theory provides for a general description of spectral emission lines, it does not immediately explain the phenomenon of

Zeeman splitting in the presence of a magnetic field. Experimental evidence for the quantized nature of the electron's magnetic dipole moment, or spin, was first provided by the Stern-Gerlach experiment which measured the deflection of silver (Ag) atoms through an inhomogeneous magnetic field.[22] In this experiment, a beam of silver atoms is passed through an inhomogeneous magnetic field which exerts a torque on the particles resulting in a deflection in their trajectory. Full interpretation of these experimental results took many years, but several important realizations were made. For particles with randomly oriented magnetic dipoles, classical theories would predict that the deflected atoms would strike the detector in a broad continuous pattern. Instead, the beam is split into two, roughly equal components which indicates that the orientation of the magnetic dipole of a silver atom is spatially quantized exhibiting a spin quantum number of ½. Furthermore, although $^{107}$Ag has a total of 47 electrons, 47 protons, and 60 neutrons its measured magnetic dipole moment roughly corresponds to that of only a *single* electron. Importantly, the magnetic moments of the other 46 electrons cancel each other out to a very good approximation. As will be discussed in following sections, the electron magnetic dipole moment is vastly larger in comparison with nuclear magnetic dipole moments which do not contribute much to the observed deflection of the silver atom. More generally, measurement of magnetic dipole moments of the elements led to the identification of electron *p* and *s* orbitals and improved understandings of atoms and their chemical interactions. After these pioneering advancements, Rabi developed similar experimental apparatuses, but with higher levels of precision, and was able to measure nuclear magnetic dipole moments which are typically several orders of magnitude weaker than that of the electron.[23] This has important consequences for nuclear magnetic resonance (NMR)

spectroscopy which exploits the resonant phenomena of nuclear spin ensembles to probe local atomic structures and bonding environments.

## 2.3. General Principles of Magnetic Resonance

In the presence of a magnetic field ($B_0$), nuclei that have a net magnetic moment align either parallel (spin-up) or anti-parallel (spin-down) with respect to the $B_0$ field which is defined as the z-axis. These nuclear spins precess about the magnetic field at the Larmor frequency ($\omega$) which depends on the intrinsic gyromagnetic ratio of the nuclei ($\gamma$) and the strength of the applied $B_0$ field,

$$\omega = -\gamma B_0 \, . \tag{2.3}$$

The differences in the Larmor frequency between dissimilar nuclei such as $^{1}H$, $^{13}C$, and $^{29}Si$ are quite large such that at a conventional field strength of 11.74 T their resonant frequencies are 499.85 MHz, 125.72 MHz, and 99.38 MHz, respectively. This large degree of separation enables manipulations and detection of nuclear spin ensembles by isotope selective excitation of their nucleus specific Larmor frequency by use of narrow < 1.5 MHz broadband radiofrequency pulses. After r.f. saturation, the recovery of nuclear magnetization produces a weak oscillating voltage response, or resonance, which is recorded by the detector coil. Importantly, as a spectroscopic tool, the effective magnetic field, $B = B_0 + B_{loc}$, experienced by a nuclear spin is influenced to a relatively small degree by its local bonding environment or by interactions with neighboring spins. Thus, there are small differences in the precession frequencies of chemically inequivalent nuclei that allow for the resolution of distinct chemical environments in ordered and disordered systems. The magnitude of the measured NMR signal intensity is proportional to the total spin polarization per unit volume, or the specific magnetization.

At a specific temperature and magnetic field strength, a Boltzmann distribution of spin states is established at thermal equilibrium yielding net spin polarization, the origin of NMR signal intensity. Spin polarization, *P*, refers to the expectation value of the bulk nuclear spin orientation in the z-axis and is given:

$$P = \frac{N_+ - N_-}{N_+ + N_-} \tag{2.4}$$

where $N_+$ and $N_-$ correspond to the total number of nuclear spins oriented parallel or anti-parallel with the $B_0$ field, respectively. At thermal equilibrium, the spin polarization is given as follows,

$$P = \tanh\left(\frac{\gamma \hbar B_0}{2k_B T}\right) \tag{2.5}$$

where is the gyromagnetic ratio (MHz/T), ħ is the reduced Planck's constant (J·s), $k_B$ is the Boltzmann constant ($J \cdot K^{-1}$), $B_0$ is the static magnetic field strength (T), and $T$ is temperature (K). To simplify the following analyses which are concerned with nonthermal polarization levels, or spin hyperpolarization, a normalized spin polarization, $\tilde{P}$, is defined,

$$\tilde{P} = \frac{P}{\tanh\left(\frac{\gamma \hbar B_0}{2k_B T}\right)} \tag{2.6}$$

such that $\tilde{P}$ is equal to unity at thermal equilibrium under isothermal conditions which are most commonly employed in magnetic resonance. Of course, it is possible to imagine circumstances where isothermal conditions may not be applicable including in in-situ gas-phase analyses of heterogeneous reactions or in the delivery of a hyperpolarized substance for in vivo medical imaging[3]. For these examples, transient effects associated with the recovery of nuclear magnetization by thermally driven spin-lattice relaxation must be considered.

Early investigation of magnetic resonance phenomena led to the identification of two types of relaxation processes termed spin-lattice relaxation and spin-spin relaxation with characteristic relaxation times corresponding to $T_1$ and $T_2$ respectively[24]. These quantities correspond to the response of a nuclear spin ensemble to a series of r.f. pulse manipulations and its eventual recovery to thermal equilibrium. In Figure 2.1a, the net nuclear magnetization vector is depicted for both types of relaxation processes. The $T_1$ relaxation time corresponds to the return to z-axis after a train of excitation pulses is used to randomize the orientation of the nuclear spin ensemble by varying the experimental delay, see Figure 2.1b. The $T_2$ relaxation time corresponds to the irreversible dephasing of net magnetization that occurs in the x,y-axis due to spin-spin interactions and can be approximately measured by increasing, $n$ = 1, 2, 3…, the total number of 90°-180° spin echoes, see Figure 2.1b. For large spin systems, these processes are most conveniently described using continuum Bloch equations which describe the net magnetization of a nuclear spin ensemble,

$$\frac{dM_z(t)}{dt} = \gamma(\mathrm{M(t)} \times \mathrm{B(t)})_z - \frac{M_z(t) - M_0}{T_1} \tag{2.7a}$$

$$\frac{dM_x(t)}{dt} = \gamma(\mathrm{M(t)} \times \mathrm{B(t)})_x - \frac{M_x(t)}{T_2} \tag{2.7b}$$

$$\frac{dM_y(t)}{dt} = \gamma(\mathrm{M(t)} \times \mathrm{B(t)})_y - \frac{M_y(t)}{T_2} \tag{2.7c}$$

where $M$ is the net magnetization vector, $B = B_0 + B_{\mathrm{loc}}$ is the effective field experienced by the spin ensemble, and $M_0$ is the equilibrium magnetization vector. The previously defined spin polarization is proportional to the z-component of the net magnetization vector per unit volume (specific magnetization[25,26]) such that,

$$P(t) \sim \frac{M_z(t)}{\rho_n V} \tag{2.8a}$$

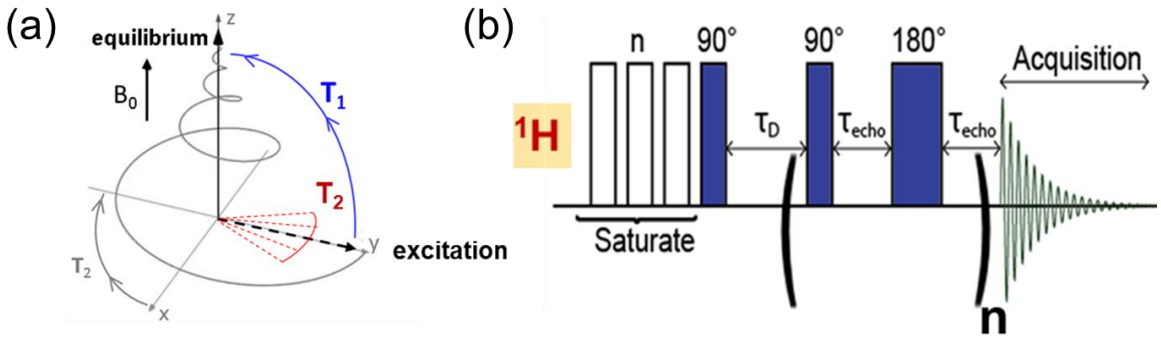


**FIGURE 2.1)** Schematic diagram for (a) the net magnetic dipole moment in response to r.f. manipulations, and (b) an r.f. pulse sequence for measuring either the $T_1$ or $T_2$ relaxation time of an $^1$H spin ensemble.

$$P_0 \sim \frac{M_0}{\rho_n V} \tag{2.8b}$$

where $\rho_n$ is the nuclear spin density and $V$ is the total sample volume. The latter description is preferred for complex heterogeneous spin systems where the compositions (*i.e.*, $\rho_n$ values) are not spatially uniform. Because the spin-lattice relaxation time is always longer than the spin-spin lattice relaxation time ($T_1 > T_2$), the rate at which measurements can be repeated depends on the value of $T_1$ which typically range from $10^{-2}$ s to $10^4$ s for nuclear spin ensembles. In addition to the sensitivity limitations arising from the low spin polarization of the nuclear spin ensemble at thermal equilibrium, the time required for an NMR experiment depends importantly on the $T_1$ relaxation time. The relative sensitivity ($s_{nmr}$) of a conventional NMR experiment may be represented as,

$$s_{nmr} = \frac{\rho_n V P_0}{\sqrt{T_1}} \tag{2.9}$$

which provides an index for the total amount of NMR signal intensity that can be measured per time for a given sample. Although the first successful measurement of nuclear magnetic resonance was performed by Purcell (awarded the 1952 Nobel Prize in Physics), an earlier

negative result reported by Gorter occurred due to the misfortune of choosing crystalline samples with excessively long $T_1$ values. As will be developed in the following sections, the process of spin hyperpolarization by cross-effect DNP can be considered to be a type of relaxation phenomenon involving the interactions of electron and nuclear spin ensembles.

## 2.4. Hyperpolarization and Spin Temperature

Applications of NMR spectroscopy typically rely on the manipulation of nuclear magnetic dipole moments by radiofrequency excitation. By exploiting nuclear magnetic resonance phenomena, small differences in the precession frequency of the nuclear magnetic moment may be detected allowing for resolution of chemically distinct environments in solids, liquids, or gases. The energy involved in these spin transitions is exceedingly low in comparison to other physical processes for example: nuclear fission ($10^9$ – $10^{11}$ kJ/mol), chemical reaction ($10^1$ – $10^3$ kJ/mol), and the nuclear Zeeman interaction ($10^{-7}$ – $10^{-4}$ kJ/mol). The sensitivity of NMR is intrinsically limited by the relatively weak nuclear magnetic dipole moment and associated gyromagnetic ratio. Even at the world's largest currently available magnetic field strength of 45 T (National High Magnetic Field Laboratory, Tallahassee, Fl, U.S.A) and at room temperature, $^{13}$C nuclei are polarized to 0.0039 % such that only 39 out of 1,000,000 nuclear spins contribute to the resonant phenomena as determined by Equation 2.5. Under otherwise identical conditions, due to its larger gyromagnetic ratio, the electron spin is polarized to 10.2 % such that 102,000 out of 1,000,000 electron spins contribute to the resonant phenomena. Recent advancements in dynamic nuclear polarization (DNP) NMR spectroscopy partially overcome these sensitivity limitations by transferring the high spin polarization of the electron to surrounding nuclear spins improving sensitivity by two to five orders of magnitude. Specifically, in cross-effect DNP, unpaired electron spins (*e.g.*, on dilute

nitroxide biradicals) are partially saturated by microwave irradiation, resulting in hyperfine transfer to nearby nuclear spins generating large amounts of spin hyperpolarization.[12]

By definition, spin hyperpolarization refers to non-equilibrium polarization levels which are generated and maintained by pumping energy into a nuclear spin ensemble. For DNP mechanisms[12] including the Overhauser effect, solid-effect, cross-effect, or thermal mixing that rely on the transfer of the electron spin polarization to nearby nuclear spins the maximum polarization increase that can be achieved relative to thermal equilibrium is determined by the gyromagnetic ratios, $\gamma_e/\gamma_n$, which corresponds to 658 for $^1$H nuclei or 2,620 for $^{13}$C nuclei. Figure 2.2) is schematic diagram representing cross-effect DNP which involves microwave saturation of electron-electron spin pairs to generate non-equilibrium nuclear spin hyperpolarization,

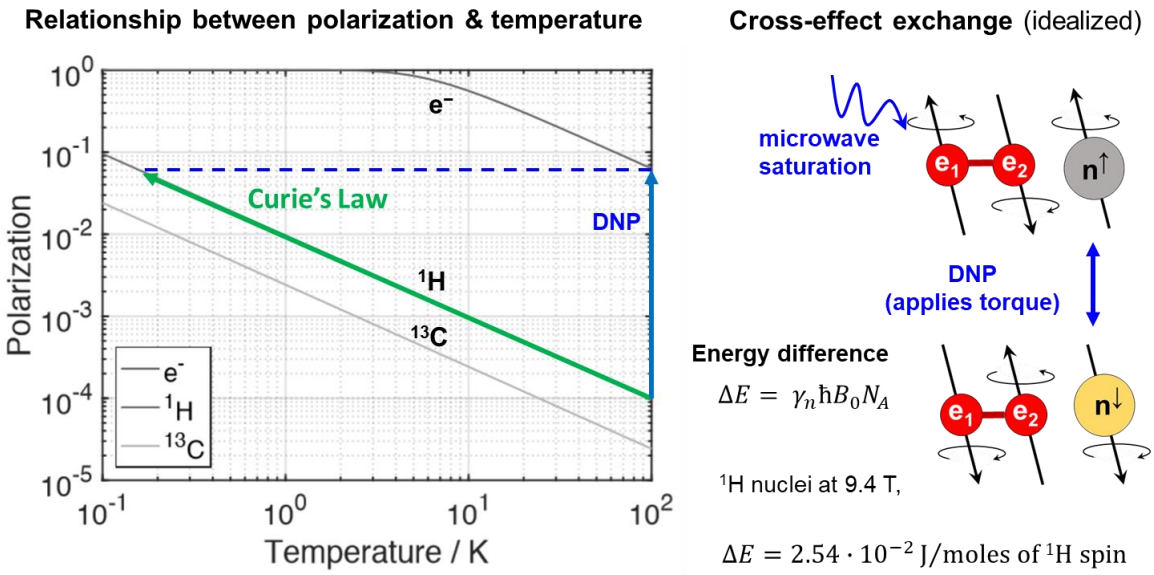


**FIGURE 2.2)** Comparison between DNP polarization of $^1$H nuclei mediated by the cross-effect and conventional $^1$H polarization levels (thermal equilibrium) which are governed by Curie's law under the high-temperature approximation. Temperature dependent plot corresponds to 9.4 T field strength adapted from reference[27]. Further details of the cross-effect mechanism will be discussed in Chapter 3.

where the initial state of the $^{1}$H spin system corresponds to a temperature of 100 K. Cross-effect DNP is driven by partial microwave saturation of an electron spin ensemble to achieve frequency matching condition, $\omega_n = |\omega_{e1} - \omega_{e2}|$, where the frequency difference between two coupled electron spins matches the nuclear precession frequency[28,29]. In this schematic diagram the $^{1}$H polarization level is increased by a factor of $\gamma_e/\gamma_{1H} = 658$ from 96 per 1,000,000 spins to 63,200 per 1,000,000 spins. To reach the same $^{1}$H polarization level without DNP, it would be necessary to cool the system from 100 K to 0.2 K following the relationship given by Curie's law. This leads to the concept of the Zeeman spin temperature introduced by Abragam[25], which is the inverse of Equation 2.5,

$$T_Z = \frac{\gamma\hbar B_0}{2k_B \cdot \operatorname{atanh}(P)} \tag{2.10}$$

such that the Zeeman spin temperature ($T_Z$) of the $^{1}$H ensemble is cooled to 0.2 K by cross-effect DNP at a thermal temperature of 100 K. Partial saturation by microwave irradiation maintains an effective polarization difference between the coupled electron spins driving hyperpolarization transfer when the frequency matching condition is met. However, due to competing electron relaxation processes, quantum conversion efficiencies[12] less than the theoretical maximum, 658, are often encountered[28,30]. DNP is a kinetic process, and as soon as $^{1}$H spin hyperpolarization is generated it will be attenuated back to equilibrium polarization levels by thermally driven spin-lattice relaxation. Thus, depending on the relative rates of hyperpolarization generation and dissipation, steady-state $^{1}$H hyperpolarization levels will be diminished in accordance to classical spin thermodynamics[25]. Finally, because cross-effect DNP relies on short-range (~$1/r^6$) hyperfine couplings, this hyperpolarization must be transferred away from the paramagnetic centers by nuclear spin-diffusion to improve the

sensitivity for applications in nuclear spintronics, medical imaging, or molecular-level spectroscopy.

## 2.5. Comparisons between Heat, Mass, and Spin Polarization Transfer

As discussed in Section 2.3, the process of spin-lattice relaxation is directly analogous to a first-order irreversible chemical reaction that returns polarization levels to thermal equilibrium. Due to this feature of spin polarization, the dissipation and propagation of hyperpolarization through a bulk nuclear ensemble is partially analogous to the reaction and diffusion of a chemical species[31,32]. Whereas molecular diffusion is driven by, $\nabla C$, a concentration gradient; nuclear spin diffusion is driven by, $\nabla P$, a polarization gradient[25,33]. This is an important distinction, because polarization does not depend on volume density, instead it corresponds to a Zeeman spin-temperature associated with the expectation value of the net nuclear spin orientation. For this reason, a polarization gradient is more closely analogous to a temperature gradient, $\nabla T$, than it is to a molecular concentration gradient. Under the spin-temperature hypothesis[25], the relationship between Zeeman energy and spin polarization is analogous to the relationship between thermal energy and temperature. In this manuscript the propagation of hyperpolarization is described as the conduction of Zeeman energy (in units of Watts) from regions of high to low polarization levels. Table 2.1 below, compares the propagation of heat, mass, and Zeeman energy in response to a potential gradient.

**Table 2.1**. Comparing Thermal, Mass, and Zeeman energy (spin polarization) transfer

| | |
|---|---|
| Heat Conduction | $\boldsymbol{q = -k\nabla T}$<br>$q \equiv$ heat flux in units of W $m^{-2}$<br>$k \equiv$ thermal conductivity in units of W $m^{-1}$ $K^{-1}$<br>$\nabla T \equiv$ temperature gradient in units of K $m^{-1}$ |
| Molecular Diffusion (no ionic charge) | $\boldsymbol{j = -\mathcal{D}\nabla C}$<br>$j \equiv$ molecular flux in units of mol $s^{-1}$ $m^{-2}$<br>$\mathcal{D} \equiv$ molecular diffusion coefficient in units of $m^2$ $s^{-1}$<br>$\nabla C \equiv$ concentration gradient in units of mol $m^{-4}$ |
| Spin Polarization Diffusion (homogeneous magnetic field) | $\boldsymbol{q_n = -\rho_n C_z \mathcal{D}_n \nabla P}$<br>$q_n \equiv$ Zeeman energy flux in units of W $m^{-2}$<br>$\mathcal{D}_n \equiv$ spin diffusion coefficient in units of $m^2$ $s^{-1}$<br>$\nabla P \equiv$ spin polarization gradient in units of $P$' $m^{-1}$<br>$\rho_n \equiv$ nuclear spin density in units of mol $m^{-3}$<br>$C_z \equiv$ Zeeman heat capacity in units of W mol $P'^{-1}$ |

$P$' ≡ unitless polarization-level

Although the SI unit of magnetization is the Weber, the spin thermodynamic conduction equation in Table 2.1 allows for a more intuitive description of hyperpolarization processes. Unlike molecular diffusion, nuclear spin diffusion in rigid solids do not involve the physical migration of species, instead it involves dipole-dipole mediated spin flips that propagate spin polarization from regions of high to low polarization. The Zeeman heat capacity is given by $C_z = CB_0{}^2$, where $C$ is Curie's constant, and $B_0$ is the magnetic field strength[34]. For nuclei with spin quantum number, I = 1/2, the energy exchanged per mol spin flips is given,

$$C_z = \gamma_n \hbar B_0 N_A \tag{2.11}$$

where $\gamma_n$ is the gyromagnetic ratio and $N_A$ is Avogadro's number, and $B_0$ is the magnetic field strength. In the presence of a homogeneous magnetic field, spin-diffusion is a non-activated process with a net energy change of $\Delta E = 0$. For spin-diffusion across an inhomogeneous magnetic field gradient, Equation 2.11 implies that there an energy penalty of $\Delta E = \gamma_n \hbar \Delta B_{i,j}$

for spin flips between inequivalent nuclei. For such conditions, simple thermal-like conduction relationships[32] like those proposed in Table 2.1 due not strictly apply, and the process of nuclear spin-diffusion is fundamentally altered.

## 2.6. Nuclear Spin Diffusion and Paramagnetic Relaxation

In principle, in a rigid solid, the spin-diffusion coefficient depends on the strength of nuclear dipole-dipole couplings and the separation distance between neighboring spins. Due to the short range of the dipolar interaction (~$1/r^3$), the spin-diffusion coefficient ($\mathcal{D}_n$) may depend on molecular structure and be highly anisotropic[35]. In this manuscript, tensorial dependences of $\mathcal{D}_n$ are neglected such that the spin-diffusion coefficient is assumed to be a constant that depends on nuclear spin density, magnetic field strength, and the magnitude of the dipole-dipole interaction. The propagation of spin polarization is then a random-walk type of process involving mutual spin flips between dipole-dipole coupled nuclei,

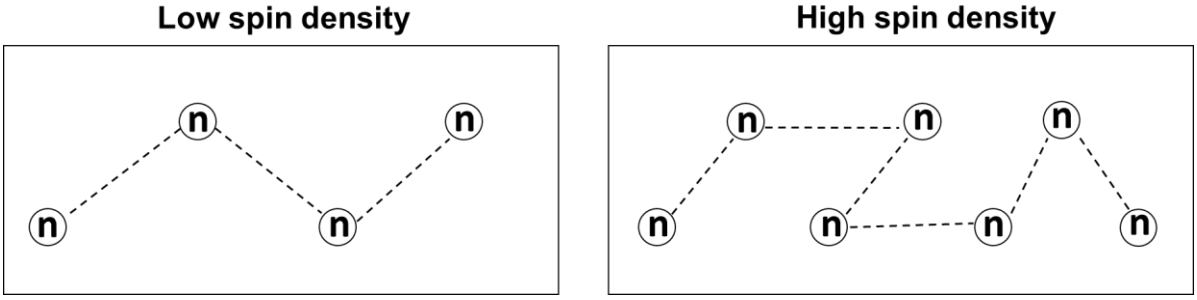


**FIGURE 2.3**) Schematic illustration of spin diffusion as a random-walk process depending on the nuclear spin density.

where certain frequency-matching criteria ($\omega_{n,i} \approx \omega_{n,j}$) must be met to facilitate a spin flip over time scales relevant to DNP NMR[27]. An order of magnitude approximation of the spin-diffusion coefficient in a rigid lattice under static conditions (no sample spinning) was first developed by Bloembergen[32],

$$\mathcal{D}_n = w \cdot a^2 \tag{2.12}$$

as a function of the transition probability (w) and the distance between spins (a). The transition probability is related to the magnitude of the dipolar interaction, which contributes to dipolar broadening of the spectral linewidth and shorter spin-spin relaxation times ($T_2$). Bloembergen[32] obtains the following relationship,

$$w \approx \frac{1}{c \cdot T_2} \tag{2.13}$$

between the transition probability, a numerical constant c = 50, and the $T_2$ relaxation time. Under more realistic assumptions, a similar result, but with c = 12, was obtained by Khutsishvili[31] for polycrystalline solids by averaging up to six-nearest neighbors and accounting for spin-diffusion between non-equivalent nuclei. Khutsishvili[31] reports that under static conditions,

$$T_2 = 0.65 \frac{a^3}{\hbar {\gamma_n}^2} \tag{2.14}$$

neglecting chemical shift anisotropy or other forms of line broadening. As demonstrated by Pinon[27], these results may be combined yielding a scaling relationship,

$$\mathcal{D}_n \sim {\gamma_n}^2 {\rho_n}^{1/3} \tag{2.15}$$

between the gyromagnetic ratio (${\gamma_n}^2$) and nuclear spin density ($\rho_n$) under the assumption that the nuclear spins are randomly distributed and experience a constant $B_0$ field strength. This situation becomes more complex under magic-angle-spinning conditions which reduces the effective strength of the dipole-dipole interactions. Nonetheless, under MAS conditions, a similar ${\rho_n}^{1/3}$ dependence of the diffusion coefficient has been predicted by reduced Liouville space (LCL) calculations[35]. The scaling dependence in Eq. 2.15 is expected to be generally valid in the presence of a homogeneous magnetic field, however the process of nuclear spin

diffusion across an inhomogeneous magnetic field gradient (such as in the vicinity of a paramagnetic center) under MAS conditions is fundamentally altered and remains an active area of research.

Exceedingly dilute concentrations of paramagnetic ions in a solid sample can significantly shorten $T_1$ relaxation times by paramagnetic enhanced relaxation (PRE) effects. These phenomena are often exploited in spectroscopy to improve sensitivity and in magnetic resonance imaging (MRI) where patients are typically injected with a $Gd^{3+}$ paramagnetic "contrast agent" to shorten measurement times. In comparison to nuclear $T_1$ relaxation times of solids which commonly range between ~0.1 *s* to 1,000 *s* at conventional 11.7 T field strengths, the electron $T_{1,e}$ relaxation time is typically on the order of $10^{-7}$ to $10^{-4}$ *s*. The hyperfine interaction broadly refers to electron-nuclear interactions (Fermi contact shift, Knight shift, spin-orbital coupling, *etc*.), however for this section, emphasis is on the paramagnetic electron-nuclear dipole-dipole interaction which is expected to dominate PRE relaxation processes in diamagnetic solids. The paramagnetic dipole interaction is a short-range interaction with a ~$1/r^3$ scaling dependence with a classical energy of,

$$\mathrm{E}_{dipolar} = \frac{\mu_e \cdot \mu_N}{r^3} - \frac{3(\mu_e \cdot \vec{r})(\mu_N \cdot r)}{r^5} \sim \frac{1}{r^3} \tag{2.16}$$

where *r* is the nuclear-electron separation distance, $\mu_e$ is the electron magnetic dipole moment, and $\mu_N$ is the nuclear magnetic dipole moment. Importantly, while direct paramagnetic relaxation is a short-range interactions, PRE effects can propagate through a nuclear spin ensemble by the process of nuclear spin diffusion as first recognized by Bloembergen.

## 2.7. Zeeman Energy Shell Balance

In cross-effect DNP, a dilute suspension of stable nitroxide biradical polarizing agents are suspended in a frozen glassy solvent matrix. Under microwave excitation, spin hyperpolarization emanates radially from the paramagnetic centers, see Figure 2.4a, which are assumed to be homogeneously distributed and spherically symmetric, see Figure 2.4b.

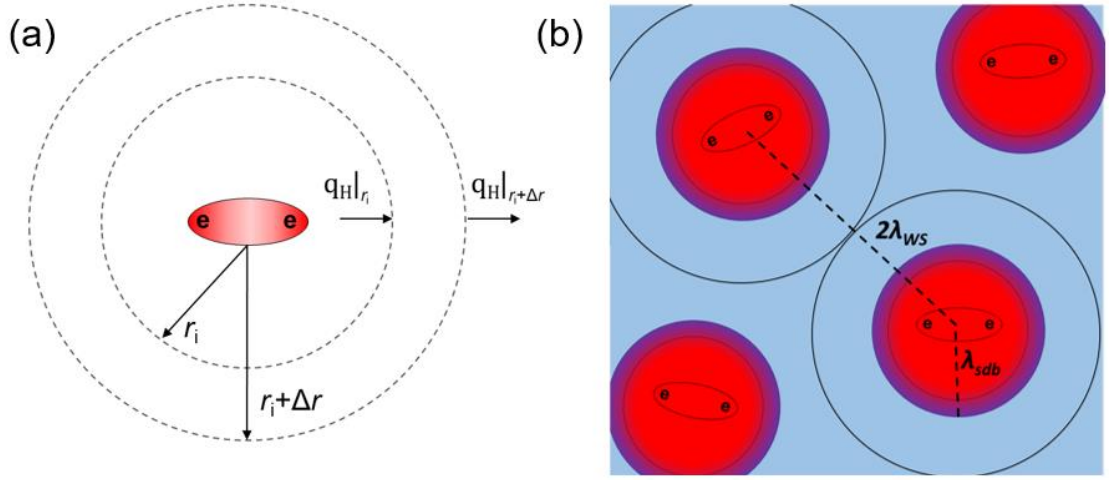


**FIGURE 2.4)** Schematic diagram of (*a*) a differential energy shell balance at an arbitrary radius, $r_i$, away from a paramagnetic center, and (*b*) a homogeneously distributed suspension of paramagnetic centers (here, nitroxide biradicals) in glassy solid matrix.

In real systems, paramagnetic centers may aggregate or physically interact such that multi-electron spin clusters can form significantly altering cross-effect DNP rates.[36] Additionally, quantum mechanical simulations indicate that DNP activities may have strong orientational dependences with respect to the static $B_0$ field. Despite these mechanistic complexities, it can be shown that simple spin thermodynamic relationships can be used to extract hyperpolarization build-up rates and generalize polarization transfer phenomena in large, heterogeneous spin systems. By an energy-shell balance, the total Zeeman energy must be conserved such that,

$$Accumulation = Generation - Consumption + In - Out \tag{2.17}$$

where excess Zeeman energy (*i.e.*, hyperpolarization) is generated by the cross-effect or other DNP mechanisms, is propagated by nuclear spin diffusion, and is dissipated by thermally driven $T_1$ relaxation processes. As discussed above, the Zeeman energy refers to the potential energy experienced by a nuclear spin ensemble in the presence of a magnetic field. The apparent rate of Zeeman energy generation by cross-effect DNP, $Q_{DNP}$, will depend on the efficiency of the quantum excitation and proximity to the paramagnetic center. Within the bulk of the frozen solvent matrix ($r > \lambda_{sdb}$), the $B_{loc}$ field is negligible small such that, $Q_{DNP} = 0$, however, hyperpolarization is propagated throughout the bulk matrix by nuclear spin diffusion and attenuated by thermally driven $T_1$ relaxation. This results in the dissipation of excess Zeeman energy at a total rate of, $Q_{T1}$, by reorientation of the nuclear spins with respect to the static magnetic field. This energy may be dissipated as minute amounts of heat (as Gorter's first experimental set up attempted to detect), or as electrical work as detected by the radiofrequency coil in modern NMR instruments. The Zeeman energy balance through the frozen solvent matrix is thus,

$$Accumulation = \rho_n C_z(\tilde{P}(r,t) - \tilde{P}(r,t+\Delta t)) \cdot 4\pi r^2 \Delta r \tag{2.18a}$$

$$Generation = Q_{DNP} \cdot 4\pi r^2 \Delta r \Delta t \tag{2.18b}$$

$$Consumption = Q_{T1} \cdot 4\pi r^2 \Delta r \Delta t \tag{2.18c}$$

$$In = (q_n \cdot 4\pi r^2)|_r \Delta t \tag{2.18d}$$

$$Out = (q_n \cdot 4\pi r^2)|_{r+r} \Delta t \tag{2.18e}$$

through a differential annular slice of thickness $\Delta r$. The constitutive equation is obtained by dividing by $4\pi\Delta r\Delta t$ and taking the limit of $\Delta r \rightarrow 0$ and $\Delta t \rightarrow 0$, respectively,

$$\lim_{\Delta t\to 0}\left[\rho_n C_z \frac{\tilde{P}(r,t)-\tilde{P}(r,t+\Delta t)}{\Delta t}\cdot r^2\right] = \lim_{\Delta r\to 0}\left[\frac{(q_n\cdot r^2)|_r-(q_n\cdot r^2)|_{r+\Delta r}}{\Delta r} + (Q_{DNP}-Q_{T1})r^2\right] \quad (2.19a)$$

$$\rho_n C_z \frac{\partial \tilde{P}}{\partial t} = -\frac{1}{r^2}\cdot\frac{\partial(q_n\cdot r^2)}{\partial r} + Q_{DNP} - Q_{T1} \quad (2.19b)$$

where $q_n = -\rho_n C_{z,n}\mathcal{D}_n\nabla\tilde{P}$ corresponds to the Zeeman energy flux due to nuclear spin diffusion given in Section 2.5. From the Bloch equation, the total Zeeman energy relaxation rate, $Q_{T1}$, is given,

$$Q_{T1} = \rho_n C_{z,n}\frac{(\tilde{P}_0 - \tilde{P}(r,t))}{T_1} \quad (2.20)$$

noting that the normalized polarization level at thermal equilibrium, $\tilde{P}_0$, is equal to unity. By substitution of $q_n$ and $Q_{T1}$ the constitutive equation obtained for 1D radial symmetry is,

$$\rho_n C_z\frac{\partial\tilde{P}(r,t)}{\partial t} = \frac{1}{r^2}\cdot\frac{\partial}{\partial r}\left(\rho_n C_{z,n}\mathcal{D}_n\frac{\partial\tilde{P}(r,t)}{\partial r}\cdot r^2\right) + Q_{DNP} - \rho_n C_{z,n}\frac{(\tilde{P}(r,t)-1)}{T_1} \quad (2.21)$$

where to a very good approximation $Q_{DNP} = 0$ in the bulk frozen matrix. Under the given assumptions, this energy balance satisfies the first Law of Thermodynamics and is valid for coupled nuclear spin ensembles in homogeneous magnetic fields and for polarization transfer across interfaces. However, special consideration is needed in evaluation of the boundary conditions of this system considering that hyperpolarization emanates from paramagnetic centers which induce a strong inhomogeneous $B_{loc}$ field gradient that impedes spin transport by nuclear spin diffusion.

## 2.8. Thermal-like Conduction Relations Between Spin Ensembles

An advantage of DNP-NMR is that hyperpolarization emanates from paramagnetic centers, enabling surface-enhanced NMR spectroscopy of porous or nonporous solids. This is highly enabling to the characterization of heterogeneous catalysts[37], hydrating cementitious solids[38], organic-inorganic hybrid structural materials, and solid-particle systems involved in additive manufacturing where the desirable material properties depend crucially on the compositions and interactions present at the surface. In a typical DNP sample formulation, small amounts of solid sample are mixed with a DNP solvent matrix containing stable biradical polarizing agent under conditions of incipient wetness impregnation. In the idealized process diagram in Figure 2.5, the DNP solvent matrix perfectly wets the target particle surface such that there is strong dipole-dipole contact between the dissimilar materials. In this diagram hyperpolarization of the DNP solvent matrix can lead to theoretical polarization values as high as 658 times thermal equilibrium. This hyperpolarization is relayed through $^{1}$H nuclei which act as spin carriers delivering excess Zeeman energy to the target particle surface by the process of nuclear spin diffusion. The transient accumulation, propagation, and dissipation of nuclear spin hyperpolarization in this process can be described by a series of coupled partial differential equations that are comparable to those employed in transient heat transfer analyses. The spatial polarization in the frozen DNP solvent matrix, $\tilde{P}_M(z,t)$, and the solid-particle surface, $\tilde{P}_S(z,t)$, are given,

$$\rho_{\mathrm{H},M} C_{\mathrm{z}} \frac{\partial \tilde{P}_M}{\partial t} = \nabla\left(\rho_{\mathrm{H},M} C_{\mathrm{z}} \mathcal{D}_{\mathrm{H},M} \nabla \tilde{P}_M\right) - \rho_{\mathrm{H},M} C_{\mathrm{z}} \frac{\left(\tilde{P}_M - 1\right)}{T_{1,M}} + Q_{DNP} \tag{2.22}$$

$$\rho_{\mathrm{H},S} C_{\mathrm{z}} \frac{\partial \tilde{P}_S}{\partial t} = \nabla\left(\rho_{\mathrm{H},S} C_{\mathrm{z}} \mathcal{D}_{\mathrm{H},S} \nabla \tilde{P}_S\right) - \rho_{\mathrm{H},S} C_{\mathrm{z}} \frac{(\tilde{P}_S - 1)}{T_{1,S}} \tag{2.23}$$

noting that hyperpolarization is only generated within the DNP solvent matrix which contains biradical polarizing agents. Meanwhile, the solid-particle target acts as a hyperpolarization "sink" and dissipates excess Zeeman energy at a rate proportional to $\rho_{\mathrm{H},S} C_{\mathrm{z}} {T_{1,S}}^{-1}$ until thermal polarization is attained, $\tilde{P}_S = 1$. Thermal-like boundary conditions describe the rate of Zeeman energy transfer across the interface, z = $\delta$, such that,

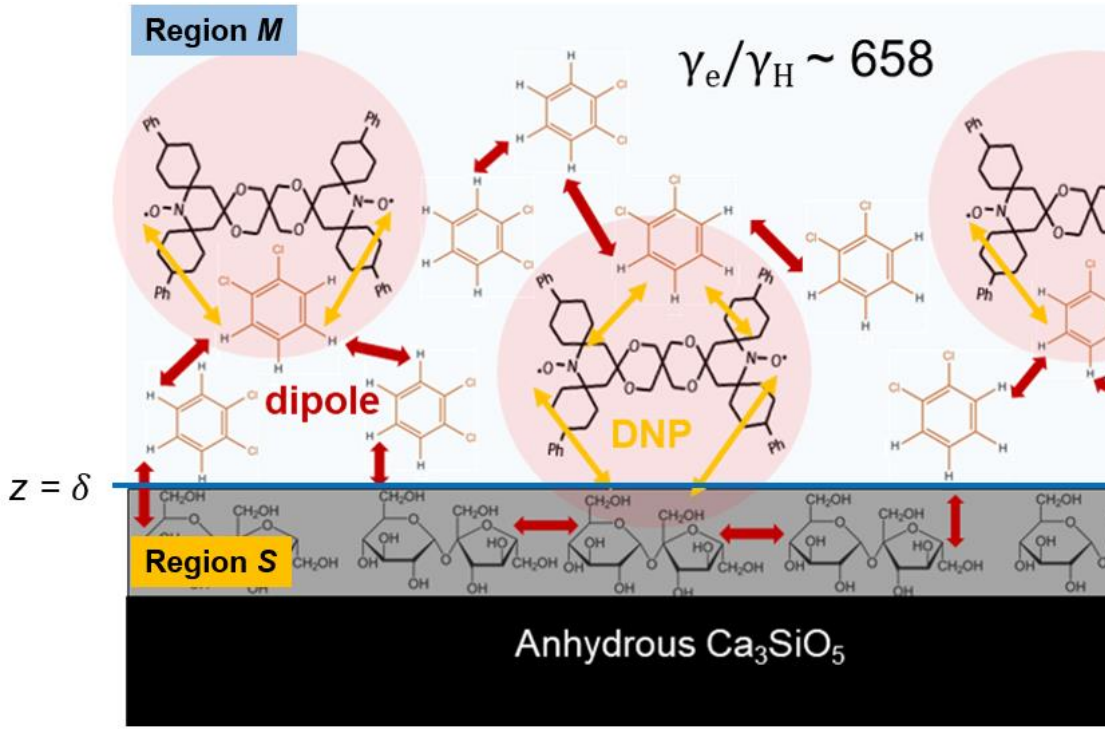


**FIGURE 2.5)** Idealized process diagram for DNP polarization transfer to a solid-particle surface. This system depicts a frozen solution of TEKPol in partially deuterated 1,2-dichlorobenzene in contact with an anhydrous tricalcium silicate, $Ca_3SiO_5$, particle surface coated with a monolayer of sucrose. Region *M* refers to the frozen DNP solvent matrix and Region *S* refers to the adsorbed sucrose monolayer. Yellow arrows depict direct transfer by cross-effect DNP to hyperfine coupled $^1$H nuclei and red arrows depict transfer mediated by $^1$H-$^1$H spin diffusion.

$$\tilde{P}_S(\delta, \mathrm{t}) = \tilde{P}_M(\delta, \mathrm{t}), \tag{2.24}$$

the polarization is a continuous function across the interface. Additionally, the total amount of Zeeman energy flowing across the interface is conserved,

$$\rho_{\mathrm{H},S} C_{\mathrm{z}} \mathcal{D}_{\mathrm{H},S} \frac{\partial \tilde{P}_S(\delta, \mathrm{t})}{\partial z} = \rho_{\mathrm{H},S} C_{\mathrm{z}} \mathcal{D}_{\mathrm{H},S} \frac{\partial \tilde{P}_S(\delta, \mathrm{t})}{\partial z}, \tag{2.25}$$

and is proportional to the grouping, $\rho_{\mathrm{H},i} C_{\mathrm{z}} \mathcal{D}_{\mathrm{H},i}$, which is the Zeeman spin conductivity with units W/m per polarization-level. This is directly analogous to a thermal conductivity which has units of W/m per degree Kelvin. Similar boundary conditions have previously been implemented for conventional NMR spin diffusion analyses by Clauss and coworkers.[39] By Equation 2.25, the total Zeeman energy flowing across an interface is dependent on the relative propensity of each media to accept and conduct spin polarization. Although the process of nuclear spin diffusion has many features that are similar to reaction-diffusion type processes, it is most directly analogous to thermal energy conduction.

In real systems, interfacial polarization transfer processes can be exceedingly complex. This is also true for thermally conducting systems, where poor interfacial contact may necessitate the use of jump-boundary conditions or other physically justified descriptions of heat transfer at disordered interfaces or grain boundaries.[40] In many regards, for spin polarization transfer, interfaces are even more sensitive to interfacial phenomena which can significantly influence polarization transfer in the bulk media. For example, assuming dipolar relaxation dominates, different conformations of molecular species or neighbor interactions at the interface can lead to significantly faster dipolar relaxation. Additionally, as depicted in the schematic diagram in Figure 2.5, the biradical polarization agent can adsorb or interact with particle surfaces.[41] At the very least, this may result in non-negligible DNP generation rates, $Q_{\mathrm{DNP}}$, penetrating into the solid-particle surface that can strongly influence

hyperpolarization build-up rates observed in the bulk media. For strongly favorable adsorption, concentration of the polarizing agent at the surface can lead to enhanced PRE effects that propagate through the system. In Chapter 3, more detailed experimental evidence and discussion will be devoted to understanding complex interfacial phenomena which are important both in hyperpolarized magnetic resonance and quantum computing applications.

## 2.9. Film Approximation Applied to the Electron-Nuclear Interface

In a frozen DNP solvent matrix containing dilute concentrations of paramagnetic centers, as in Figure 2.4, the average separation distance between paramagnetic centers is approximately two times the Wigner-Seitz radius, $d = 2\lambda_{ws}$.[33] More generally in condensed matter physics, the Wigner-Seitz radius represents a fictitious sphere formed around a single dopant representing a volume of bulk material corresponding to the bulk dopant concentration and is given,

$$\lambda_{ws} = \left(\frac{3}{4\pi\rho_{pc}N_A}\right)^{1/3}, \tag{2.26}$$

where $\rho_{pc}$ is the concentration of paramagnetic centers (i.e., nitroxide biradicals) and $N_A$ is Avogadro's number. For example, a 2 mM biradical solution would have a Wigner-Seitz radius corresponding to 5.83 nm and a mean separation distance of 11.6 nm. The mesoscopic spin transport model, Equation 2.21, would only be applicable over the region $\lambda_{sdb} < r < \lambda_{ws}$. Due to periodicity, there will be a local minimum in the spatial polarization profile as r approaches $\lambda_{ws}$ such that,

$$\rho_{\mathrm{H}} C_{\mathrm{z}} \mathcal{D}_{\mathrm{H}} \frac{\partial \tilde{P}}{\partial r}\Big|_{\lambda_{\mathrm{ws}}} = 0\,, \tag{2.27}$$

beyond the Wigner-Seitz radius, $r > \lambda_{ws}$, it is statistically probable that the $^{1}H$ nuclei will be closer to another paramagnetic center and thus will have a higher polarization level. Because Zeeman energy diffuses from regions of high to low polarization, Equation 2.27, corresponds to a zero Zeeman energy flux condition. As discussed in Section 2.6, the process of nuclear spin-diffusion is fundamentally altered near a paramagnetic center. By analogy to heat and mass transfer film theory, it is possible to describe the electron-nuclear interface by use of a DNP polarization transfer coefficient (units m/s) that is directly analogous to a mass transfer coefficient (units m/s). In this section the physical justification for use of a film theory will be introduced, full derivation and experimental validation of this approach is provided in Chapter three.

A significant general challenge encountered in the description of hybrid electron-nuclear spin systems in quantum computing[11] and hyperpolarized magnetic resonance[15] applications is the existence of a complex and poorly defined interface impeding coherence (spin-spin dipolar ordering dominated by $T_2$ relaxation-type processes) or hyperpolarization transfer (z-component of the nuclear magnetization vector dominated by $T_1$ relaxation-type processes) away from paramagnetic centers. Within the context of solid-state NMR, which is primarily concerned with the z-component of the nuclear magnetization vector, this interface is called the spin-diffusion barrier and has been the subject of fundamental interest since the seminal work of Bloembergen. As discussed in Section 2.6, nuclear spin-diffusion in a homogeneous magnetic field involves spin flip transitions between neighboring spins with a similar precession frequency, $\omega_i = \omega_{i+1}$, and is an energy-conserving, $\Delta E_{i(i+1)} = 0$, process that occurs spontaneously. However, in DNP-NMR, hyperpolarization emanates from paramagnetic centers where local fields ($B_{loc}$) are inhomogeneous, see Figure 2.6. For $^{1}H$-$^{1}H$

spin diffusion to occur between frequency-shifted neighbours, $\omega_i \neq \omega_{i+1}$, an energy penalty of $\Delta E_{i(i+1)} = \gamma \Delta B_{i(i+1)}$ is incurred.[42] This energy barrier must be overcome or supplied by some other kinetic or relaxation driven process impeding the transport of hyperpolarization away from paramagnetic centers.[43] The physical significance of this energy barrier is that diffusive flux of Zeeman energy, $q_H$, is a complex function of the $B_{loc}$ field and is no longer suitably described by simple conduction relationships (i.e., Fourier's law, Fick's 1st law).

By measurement of nuclear spin diffusion through a spatially varying magnetic field, Genack and Redfield proposed that this energy penalty can be accommodated by coupling between the Zeeman energy reservoir (a.k.a. Zeeman Hamiltonian) and the dipolar energy reservoir (a.k.a. Dipolar Hamiltonian). The significance of the Genack-Redfield model is that

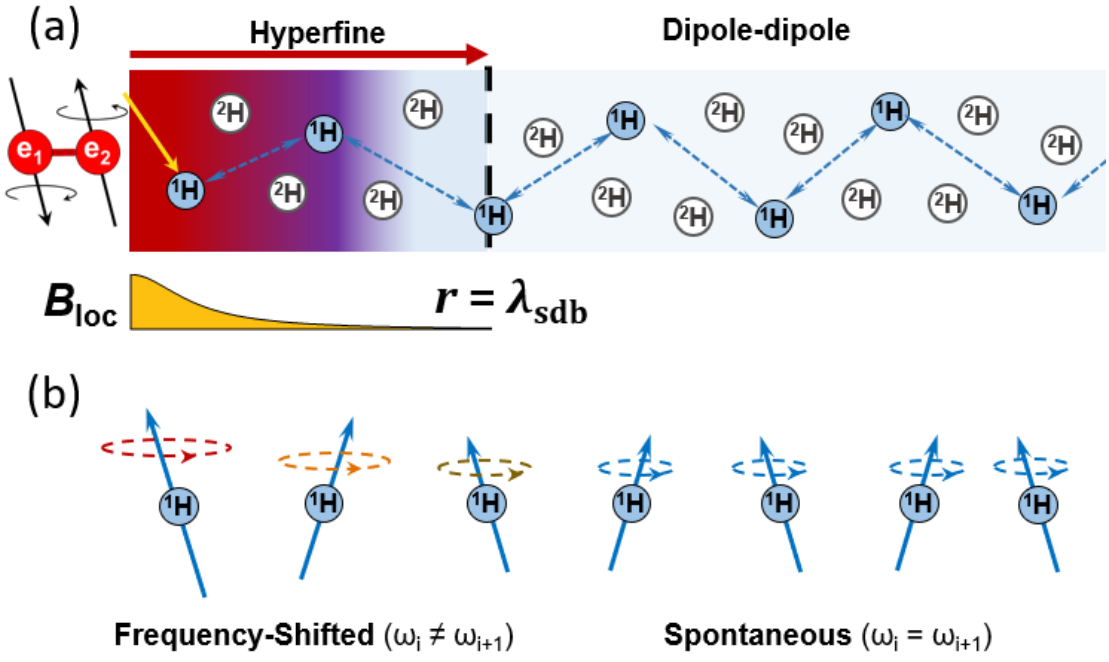


**FIGURE 2.6)** Schematic representation of (a) hyperpolarization transfer away from a paramagnetic center across a spin-diffusion barrier of radius $\lambda_{sdb}$, and (b) representation of frequency-shifted nuclei which is a contributing factor to the existence of the spin-diffusion barrier.

the Zeeman energy flux, $q_H$, through an inhomogeneous magnetic field gradient (*i.e.*, a $B_{loc}$ field) can be described by a set of coupled differential equations which represent a magnetic analogue of the Nernst-Planck equation that may partially account for the physical origin of the spin-diffusion barrier. The Genack-Redfield model, with notation consistent to the previous discussion, is given as,

$$\frac{\partial M_z}{\partial \mathrm{t}} = \mathcal{D}_z \nabla \cdot [\nabla M_z - \chi(T_d) \nabla B_{i(i+1)}] \tag{2.28}$$

$$\frac{\partial \chi(T_d)}{\partial \mathrm{t}} = -q_H \cdot \frac{\nabla B_{i(i+1)}}{{H_d}^2} + \mathcal{D}_d \nabla^2 \chi(T_d) \tag{2.29}$$

where $M_z$ is the z-component of the net magnetization, $\mathcal{D}_z$ is the spin-diffusion coefficient associated with the diffusion of Zeeman energy, $\mathcal{D}_d$ is the spin-diffusion coefficient associated with the diffusion of dipolar order, ${H_d}^2$ is the mean square of the effective dipole-dipole magnetic field (*e.g.*, strength of the dipole interaction), $\chi(T_d)$ is a dipolar magnetic susceptibility which can be regarded as a dipolar heat capacity, and $T_d$ is the spin-temperature of the dipolar reservoir. In Equation 2.28, spin-lattice $T_1$ relaxation is omitted because the Genack-Redfield model was developed to describe situations where the diffusion time scale was much shorter than the $T_1$ relaxation time, $\tau << T_1$. As described in Section 2.4, the notion of a Zeeman spin temperature ($T_z$) can be used interchangeably with either the spin polarization, *P*, or the z-component of the net nuclear magnetization, $M_z$. There is also a thermodynamic temperature associated with spin-spin ordering, or the dipolar energy reservoir which is the Dipolar spin temperature ($T_d$). Dementyev and coworkers measured the rate at which dipolar order diffuses away from paramagnetic centers in DNP-NMR and found that this property is influenced less by the spin-diffusion barrier than is the Zeeman spin temperature.[34,43] Importantly, for in the presence of a homogeneous field, $\Delta B_{i(i+1)} = 0$, then

Equation 2.28 is reduced to a similar form as presented in Section 2.6 which represents the Fourier-like or Fickian-like transport of polarization. The Genack-Redfield model identifies an important contribution to polarization transfer through an inhomogeneous gradient, the influence of the dipole-dipole energy reservoir. This challenges the application of spin thermodynamic models, such as Equation 2.21, which implicitly rely on knowledge of electron-nuclear interactions that are not easily measured directly[15]. A novel contribution of this manuscript is demonstrating how under conditions of both microwave irradiation and MAS, simple analytical solutions consistent with the Genack-Redfield model may be obtained by dimensional scaling analyses. By relatively simple experiments, rate-law parameters can be extracted which provide detailed quantitative insights regarding the nature of quantum interfaces (*e.g.*, the spin-diffusion barrier) and other rate-limiting processes that emerge in complex spin systems.

By analogy to Newton's law of cooling, many challenges associated with the thermodynamic description of the electron-nuclear interface can be circumvented by use of a DNP polarization-transfer coefficient ($k_{\mathrm{DNP}}$, with units of m/s). This approach is best understood by analogy to convective heat transfer at an interface, where a similar energy barrier impedes the flow of heat due to the formation of a viscous boundary layer. Newton's law of cooling states that the rate of heat transfer at a surface is proportional to the temperature gradient and, despite its names, was formulized by French scientists Jean-Baptiste Joseph Fourier (1768 – 1830) and Jean-Baptise Biot (1774 – 1862).[45] Here the Zeeman energy flux, $q_{\mathrm{H}} = -(\rho_{\mathrm{H}} C_{\mathrm{z}} k_{\mathrm{DNP}})\Delta\tilde{P}$, is defined at the spin-diffusion barrier interface $r=\lambda_{\mathrm{sdb}}$. The grouping, $\rho_{\mathrm{H}} C_{\mathrm{z}} k_{\mathrm{DNP}}$, has units of W/m$^2$ per polarization-level and is mathematically analogous to a heat-transfer coefficient (W/m$^2$·K), but here represents polarization transfer across a local magnetic

field gradient. Far from paramagnetic centers ($r \geq \lambda_{sdb}$), the DNP generation rates, $Q_{DNP}$, are negligible. Assuming that polarization propagates radially (via dipolar couplings) from each paramagnetic center, the Zeeman energy flux into the bulk ensemble can be represented by a Neumann boundary condition:

$$\rho_{\mathrm{H}} C_{\mathrm{z}} \mathcal{D}_{\mathrm{H}} \frac{\partial \tilde{P}}{\partial r}|_{\lambda_{\mathrm{sdb}}} = (\rho_{\mathrm{H}} C_{\mathrm{z}} k_{\mathrm{DNP}}) \Delta \tilde{P} \,, \tag{2.30}$$

where $\Delta \tilde{P} \equiv (\bar{P}_{\mathrm{CE}} - \tilde{P}|_{\lambda_{\mathrm{sdb}}})$ is the polarization difference across a "spin diffusion barrier". Equation 2.30 represents a generation boundary condition, with rate-law parameters $k_{\mathrm{DNP}}$ and $\bar{P}_{\mathrm{CE}}$ governing the apparent rate of Zeeman energy into the bulk nuclear spin ensemble. Further discussion and justification for this approach will be provided in Chapter three, Here, it is noted that $\lambda_{sdb}$ has a physical significance that is at least partially analogous to the Debye length in electrolyte solutions[47]. In Figure 2.7, a comparison is made between thermal energy, ion diffusion, and hyperpolarization transfer at an interface where simple conduction-like relationships do not apply. For thermal energy transfer, heat transfer to the bulk fluid is impeded by a viscous boundary layer. For dilute electrolyte solutions, an electric field associated with the surface potential is screened by charges resulting in the accumulation of ion density near the surface. For polarization transfer, the precession frequency of nuclei near the paramagnetic centers are displaced resulting in an energy barrier of $\Delta E_{i(i+1)} = \gamma \Delta B_{i(i+1)}$ as suggested by the Genack-Redfield model. By introducing the DNP film transfer coefficient, a foundational basis is provided for the description of large coupled spin systems by dimensionless property analysis similar to those employed in heat and mass transfer.

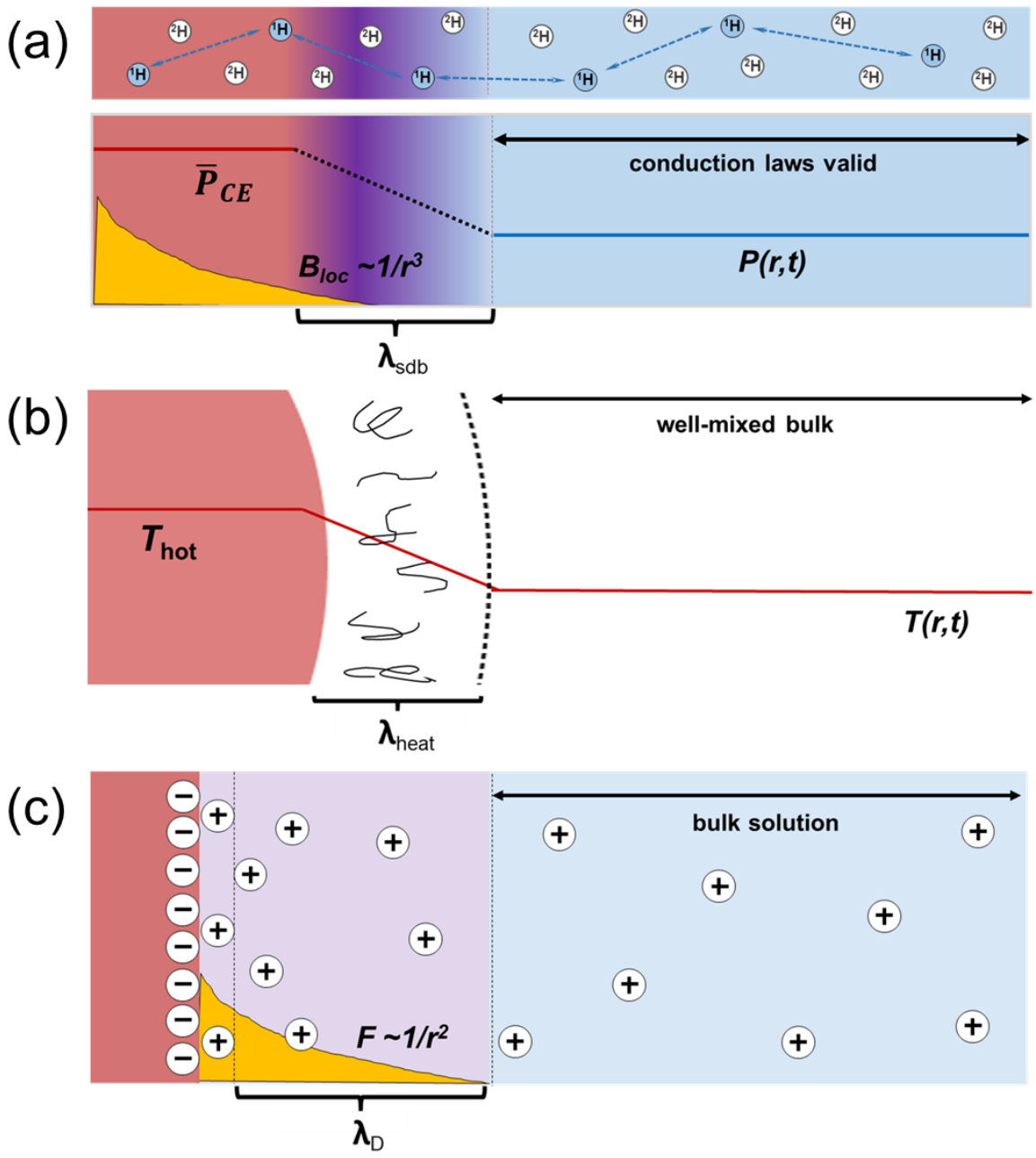


**FIGURE 2.7)** Comparison between (a) polarization transfer across the spin-diffusion barrier ($\lambda_{sdb}$), (b) heat transfer across a stagnant boundary layer ($\lambda_{heat}$), (c) ion density near a charged interface characterized by a Debye length ($\lambda_D$).

## 2.10. Motivating Dimensional Scaling Analyses

To motivate the use of dimensional analysis, which is widely employed in engineering analyses involving heat, momentum, and mass transfer, it is useful to discuss an interesting problem involving bacterial locomotion. Although awarded with the 1952 Nobel Prize in Physics for the discovery of nuclear magnetic resonance and, later, making pioneering contributions to the field of radioastronomy, Purcell is widely known among chemical engineers for a paper titled, "Life at Low Reynold's Number".[2] Given their small size, bacteria swimming in solution do not have the benefit of inertial forces to maintain their momentum and trajectory. In fact, most forms of reciprocal motion employed by human swimmers at such length scales would exactly negate any forward momentum leaving the microscopic swimmer suspended in place. This requires an active forward moving force of magnitude $\sim\eta^2/\rho$ where $\eta$ is viscosity and $\rho$ is density to constantly drive the organism towards nutrient rich zones. Most of their nutrients are collected by diffusion, however, motile microscopic organisms will swim a path length equal to several times the characteristic diffusion length to sample new environments. There was significant interest in the type of motion used by their flagellum, however due to its small size it was not possible to observe flagellar motions by in-situ microscopy. Instead, by tracking the swim path of a bulk E. coli organism through solution, the dynamic modes (*i.e.*, period of motion, waving vs. rotating, etc.) of their flagellar motions could be extracted. Purcell showed that, by means of nondimensional scaling analysis, the mechanical efficiency, dynamic modes, and swim path of E. coli could be fully described by use of a symmetric matrix consisting of three measurable parameters. These types of analyses would have been intractable if it were necessary to solve the complete Navier-Stokes equation for different types of flagellar motions and demonstrates the utility of dimensional scaling in

identifying the most important physics of the problem. In Chapter three, it will be similarly demonstrated that spin thermodynamics of large coupled spin systems can be accurately described by polarization analogues of the Biot number, Thiele modulus, Damköhler number, and Hatt number. These dimensional groups are used to identify conditions under which classical spin thermodynamic treatments (see Figure 2.8) can accurately describe spin polarization transfer in large spin systems.

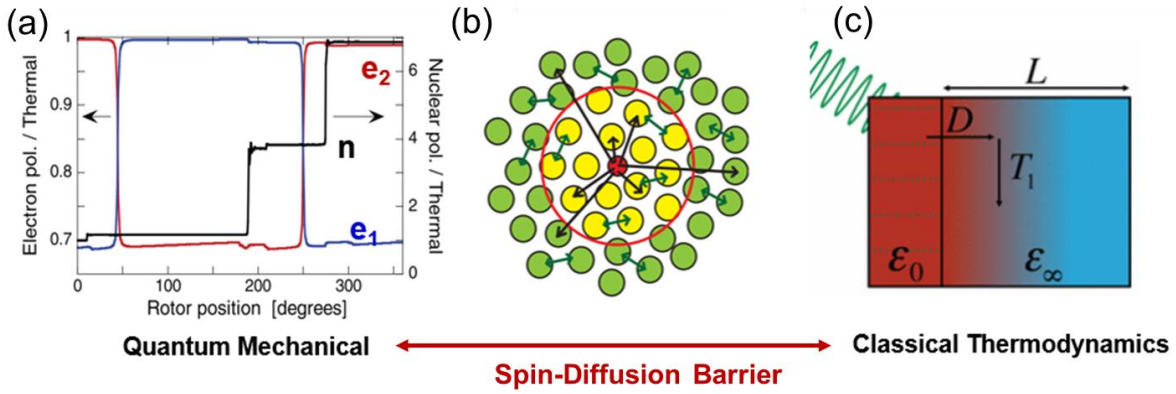


**FIGURE 2.8)** Schematic representation of DNP across multiple length and time scales, including (a) individual electron-nuclear spin reorientation over $10^{-6}$ *s*, diagram reproduced from (Thurber and Tycko, 2012); (b) the range of direct DNP transfer to nuclei within a few nanometers and a slow transfer step across the spin-diffusion barrier over ~$10^{-4}$ to $10^{1}$ *s*, diagram reproduced from (Smith and Griffin *et al.*, 2012); and (c) classical spin thermodynamics between large coupled dissimilar spin reservoirs over <1 nm to 10's μm lengthscales, diagram reproduced from (Pinon and Emsley *et al.*, 2017).

## 2.11. Conclusions

In emerging applications of hyperpolarized magnetic dimensional scaling analyses provide a strong experimental foundation for the measurement of simple rate-late parameters to describe complex hyperpolarization transfer processes. It is demonstrated that continuum analyses can provide important insights near quantum interfaces (*i.e.*, the spin-diffusion

barrier), as the Nernst-Planck equation does for electrolyte systems. Within the context of DNP-NMR, the dimensional analyses enable hyperpolarization transfer rates to be predicted from paramagnetic centers into surrounding composite solid media over relatively large distances, mediated by dipolar couplings and spin-lattice relaxation. In a broader context, these results provide a system-level description of complex composite spin systems. Such approaches may be used to guide the selection of material properties to optimize polarization transfer between dissimilar spin reservoirs which remains crucial to hyperpolarized magnetic resonance and quantum information applications. Similar scaling analyses are expected to yield system-level insights into spin-transfer phenomena in other condensed matter systems where transitions from quantum mechanical to classical properties feature prominently.

## References


1. Whitman, W. G. & Keats, J. L. Rates of Absorption and Heat Transfer between Gases and Liquids. *Ind. Eng. Chem.* **14**, 186–191 (1922).
2. Purcell, E. M. Life at low Reynolds number. *Am. J. Phys.* **45**, 3–11 (1977).
3. Nelson, S. J. *et al.* Metabolic Imaging of Patients with Prostate Cancer Using Hyperpolarized [1-13C]Pyruvate. *Sci. Transl. Med.* **5**, 198ra108 (2013).
4. Lee, Y., Heo, G. S., Zeng, H., Wooley, K. L. & Hilty, C. Detection of living anionic species in polymerization reactions using hyperpolarized NMR. *J. Am. Chem. Soc.* **135**, 4636–4639 (2013).
5. Theis, T. *et al.* Direct and cost-efficient hyperpolarization of long-lived nuclear spin states on universal 15N2-diazirine molecular tags. *Sci. Adv.* **2**, 1–8 (2016).
6. Cavaillès, M. *et al.* Tailored Microstructured Hyperpolarizing Matrices for Optimal Magnetic Resonance Imaging. *Angew. Chemie - Int. Ed.* **57**, 7453–7457 (2018).
7. Zangara, P. R. *et al.* Two-Electron-Spin Ratchets as a Platform for Microwave-Free Dynamic Nuclear Polarization of Arbitrary Material Targets. *Nano Lett.* **19**, 2389–2396 (2019).
8. Shiomi, Y. *et al.* Spin pumping from nuclear spin waves. *Nat. Phys.* **15**, 22–26 (2019).
9. Kurizki, G. *et al.* Quantum technologies with hybrid systems. *Proc. Natl. Acad. Sci. U. S. A.* **112**, 3866–3873 (2015).
10. Ranjan, V. *et al.* Probing Dynamics of an Electron-Spin Ensemble via a Superconducting Resonator. *Phys. Rev. Lett.* **110**, 067004 (2013).

11. Gangloff, D. A. *et al.* Quantum interface of an electron and a nuclear ensemble. *Science (80-. ).* **364**, 62–66 (2019).
12. Lilly Thankamony, A. S., Wittmann, J. J., Kaushik, M. & Corzilius, B. Dynamic nuclear polarization for sensitivity enhancement in modern solid-state NMR. *Prog. Nucl. Magn. Reson. Spectrosc.* **102**–**103**, 120–195 (2017).
13. Karabanov, A., Wiśniewski, D., Lesanovsky, I. & Köckenberger, W. Dynamic Nuclear Polarization as Kinetically Constrained Diffusion. *Phys. Rev. Lett.* **115**, 1–5 (2015).
14. Sharma, G. *et al.* Enhancement of nuclear spin coherence times by driving dynamic nuclear polarization at defect centers in solids. *Phys. Rev. B* **205423**, 1–12 (2019).
15. Tan, K. O., Mardini, M., Yang, C., Ardenkjær-Larsen, J. H. & Griffin, R. G. Three-Spin Solid Effect and the Spin Diffusion Barrier in Amorphous Solids. *Sci. Adv.* **5**, eaax2743 (2019).
16. Zeeman, P. The effect of magnetisation on the nature of light emitted by a substance. *Nature* **43**, 226–239 (1897).
17. Larmor, J. On the theory of the magnetic influence on spectra; and on the radiation from moving ions. *Philos. Mag.* **44**, 503–512 (1897).
18. Rutherford, E. F. R. S. The origin of β and γ rays from radioactive substances. *Philos. Mag.* **24**, 453–462 (1912).
19. Thomson, J. J. F. R. S. On the structure of the atom : an investigation of the stability and periods of oscillation of a number of corpuscles arranged at equal intervals around the circumference of a circle ; with application of the results to the theory of atomic structure. *Philos. Mag.* **7**, 237–265 (1904).
20. Bohr, N. On the constitution of atoms and molecules. **26**, 1–25 (1913).
21. Bohr, N. 1918 on the quantum theory of line–spectra. *Skr. Naturvidensk. og Mathem. Afd.* **9**, 1–3 (1918).
22. Gerlach, W. & Stern, O. Der experimentelle Nuchweis der Richtungsquantelung in Magnetfeld. *Zeitschrift für Phys.* **9**, 349 (1922).
23. Rabi, I. I., Zacharias, J. R., Millman, S. & Kusch, P. A New Method of Measuring Nuclear Magnetic Moment. *Phys. Rev. Lett.* **53**, 318 (1937).
24. Bloembergen, N., Purcell, E. M. & Pound, R. V. Relaxation Effects in Nuclear Magnetic Resonance Adsorption. *Phys. Rev.* **73**, 679–712 (1947).
25. Abragam, A. *The Principles of Nuclear Magnetism*. (Oxford University Press, 1961).
26. Clauss, J., Schmidt-Rohr, K. & Spiess, H. W. Determination of domain sizes in heterogeneous polymers by solid-state NMR1 J. Clauss, K. Schmidt-Rohr and H. W. Spiess, Determination of domain sizes in heterogeneous polymers by solid-state NMR, Acta Polym., 1993, 44, 1–17. *Acta Polym.* **44**, 1–17 (1993).
27. Pinon, A. C. Spin Diffusion in Dynamic Nuclear Polarization Nuclear Magnetic Resonance. (Lausanne, EPFL, 2018). doi:10.5075/epfl-thesis-8519
28. Thurber, K. R. & Tycko, R. Theory for cross effect dynamic nuclear polarization under magic-angle spinning in solid state nuclear magnetic resonance: the importance of level crossings. *J. Chem. Phys.* **137**, 084508 (2012).
29. Mentink-Vigier, F., Vega, S. & De Paëpe, G. Fast and accurate MAS-DNP simulations of large spin ensembles. *Phys. Chem. Chem. Phys.* **19**, 3506–3522 (2017).
30. Mentink-Vigier, F., Akbey, Ü., Oschkinat, H., Vega, S. & Feintuch, A. Theoretical aspects of Magic Angle Spinning - Dynamic Nuclear Polarization. *J. Magn. Reson.*

**258**, 102–120 (2015).
31. Khutsishvilli. Spin diffusion. *Usp. Fiz. Nauk* **87**, 211–254 (1965).
32. Bloembergen, N. On the interaction of nuclear spins in a crystalline lattice. *Physica* **15**, 386–426 (1949).
33. Pinon, A. *et al.* Measuring Nano- to Microstructures from Relayed Dynamic Nuclear Polarization NMR. *J. Phys. Chem. C* **121**, 15993–16005 (2017).
34. Dementyev, A. E., Cory, D. G. & Ramanathan, C. Rapid diffusion of dipolar order enhances dynamic nuclear polarization. *Phys. Rev. B - Condens. Matter Mater. Phys.* **77**, 1–5 (2008).
35. Halse, M. E., Zagdoun, A., Dumez, J. N. & Emsley, L. Macroscopic nuclear spin diffusion constants of rotating polycrystalline solids from first-principles simulation. *J. Magn. Reson.* **254**, 48–55 (2015).
36. Leavesley, A. *et al.* Maximizing NMR signal per unit time by facilitating fast e-e-n cross effect DNP. *Phys. Chem. Chem. Phys.* **20**, 27646 (2018).
37. Berkson, Z. J. *et al.* Preferential Siting of Aluminum Heteroatoms in the Zeolite Catalyst Al-SSZ-70. *Angew. Chemie* **131**, 6321–6325 (2019).
38. Sangodkar, R. P. *et al.* Influences of Dilute Organic Adsorbates on the Hydration of Low-Surface-Area Silicates. *J. Am. Chem. Soc.* **137**, 8096–8112 (2015).
39. Clauss, J., Schmidt-Rohr, K. & Spiess, H. W. Determination of domain sizes in heterogeneous polymers by solid state NMR. *Acta Polym.* **44**, 1–17 (1993).
40. Carslaw, H. S. & Jaeger, J. C. *Conduction of Heat in Solids*. (Oxford Science Publications, 1959).
41. Perras, F. A. *et al.* Optimal sample formulations for DNP SENS: The importance of radical-surface interactions. *Curr. Opin. Colloid Interface Sci.* **33**, 9–18 (2018).
42. Genack, A. Z. & Redfield, A. G. Nuclear spin diffusion and its thermodynamic quenching in the field gradients of a Type-II superconductor. *Phys. Rev. Lett.* **31**, 1204–1207 (1973).
43. Ramanathan, C. Dynamic nuclear polarization and spin diffusion in nonconducting solids. *Appl. Magn. Reson.* **34**, 409–421 (2008).
44. Wittmann, J. J., Eckardt, M., Harneit, W. & Corzilius, B. Electron-driven spin diffusion supports crossing the diffusion barrier in MAS DNP. *Phys. Chem. Chem. Phys.* **20**, 11418–11429 (2018).
45. Fourier, J. *Théorie analytique de la chaleur*. (Paris: Fils, Firmin Didot Père et, 1822).
46. Perras, F. A. *et al.* Full-Scale Ab Initio Simulation of Magic- Angle-Spinning Dynamic Nuclear Polarization Full-Scale Ab Initio Simulation of Magic-Angle-Spinning Dynamic Nuclear Polarization. *J. Phys. Chem. Lett.* **11**, 5655–5660 (2020).
47. Lee, A. A., Perez-Martinez, C. S., Smith, A. M. & Perkin, S. Scaling Analysis of the Screening Length in Concentrated Electrolytes. *Phys. Rev. Lett.* **119**, 1–5 (2017).
48. Kubicki, D. J. *et al.* Rational design of dinitroxide biradicals for efficient cross-effect dynamic nuclear polarization. *Chem. Sci.* **7**, 550–558 (2016).
49. Perras, F. A. & Pruski, M. Large-scale ab initio simulations of MAS DNP enhancements using a Monte Carlo optimization strategy. *J. Chem. Phys.* **149**, (2018).
50. Mentink-Vigier, F. Optimizing nitroxide biradicals for cross-effect MAS-DNP: The role of: G -tensors' distance. *Phys. Chem. Chem. Phys.* **22**, 3643–3652 (2020).
51. Mentink-Vigier, F. *et al.* Computationally Assisted Design of Polarizing Agents for Dynamic Nuclear Polarization Enhanced NMR: The AsymPol Family. *J. Am. Chem.*

*Soc.* **140**, 11013–11019 (2018).
52. Levitt, M. H. *Spin Dynamics: Basics of Nuclear Magnetic Resonance*. (John Wiley & Sons, Ltd, 2008).
53. Smith, A. A., Corzilius, B., Barnes, A. B., Maly, T. & Griffin, R. G. Solid effect dynamic nuclear polarization and polarization pathways. *J. Chem. Phys.* **136**, 015101 (2012).
54. Bird, R. B., Stewart, W. E. & Lightfoot, E. N. *Transport Phenomena*. (John Wiley & Sons, Ltd, 2007).
55. Rossini, A. J. *et al.* One hundred fold overall sensitivity enhancements for Silicon-29 NMR spectroscopy of surfaces by dynamic nuclear polarization with CPMG acquisition. *Chem. Sci.* **3**, 108–115 (2012).
56. Thiele, E. W. Relation between Catalytic Activity and Size of Particle. *Ind. Eng. Chem.* **31**, 916–920 (1939).
57. Damköhler, G. *The Effect of Turbulence on the Flame Velocity in Gas Mixtures*. *National Advisory Committee for Aeronautics* **1112**, (1947).
58. Damköhler, G. Der Einfluss der Turbulenz auf die Flammengeschwindigkeit in Gasgemschen. *Zeitschrift für Elektrochemie und Angew. Phys. Chemie* **46**, 601–652 (1940).

## Chapter III.

# Scaling analyses for hyperpolarization transfer across a spin-diffusion barrier and into bulk solid media

Nathan A. Prisco, Arthur C. Pinon, Lyndon Emsley, and Bradley F. Chmelka. *Phys. Chem. Chem. Phys.*, in review.

## 3.1. Abstract

By analogy to heat and mass transfer film theory, a general approach is introduced for determining hyperpolarization transfer rates between dilute electron spins and a surrounding nuclear ensemble. These analyses provide new quantitative relationships for understanding, predicting, and optimizing the effectiveness of hyperpolarization protocols, such as Dynamic Nuclear Polarization (DNP) under magic-angle spinning conditions. An empirical DNP polarization-transfer coefficient is measured as a function of the bulk matrix $^{1}$H spin density and indicates the presence of two distinct kinetic regimes associated with different rate-limiting polarization transfer phenomena. Dimensional property relationships are derived and used to evaluate the competitive rates of spin polarization generation, propagation, and dissipation that govern hyperpolarization transfer between large coupled spin ensembles. The quantitative analyses agree closely with experimental measurements for the accumulation, propagation, and dissipation of hyperpolarization in solids and provide evidence for kinetically-limited transfer associated with a spin-diffusion barrier. The results and classical approach yield general design criteria for analyzing and optimizing polarization transfer

processes involving complex interfaces and composite media for applications in materials science, physical chemistry and nuclear spintronics.

## 3.2. Introduction

In coupled energy transfer and dissipation processes, dimensional property analyses provide bases for understanding phenomena in systems ranging from industrial-scale process equipment[1] to complex micromechanical systems[2]. Extending such constitutive analyses to the propagation of spin polarization is important for emerging applications of hyperpolarized magnetic resonance[3–7] and processes based on spin transport over multiple length scales[8,9]. In quantum computing, the coupling of electron qubits with highly polarized nuclear spin packets (*e.g.*, nuclear spintronics) is a promising strategy for extending coherence lifetimes and for facilitating short-term data storage functions[10,11]. Another example is dynamic nuclear polarization (DNP), which exploits the coupling of electron-nuclear spin ensembles to enhance dramatically NMR signal sensitivity in solids[12]. Quantitative models of DNP polarization transfer, however, have been challenging to implement[13,14], as the generation, propagation, and dissipation of hyperpolarization can span time scales ranging from $10^{-9}$ to $10^{5}$ s, length scales from <1 nm to μm, and involve considerations of both quantum mechanical and classical phenomena. Materials systems on which these examples are based share key features, specifically complex and poorly defined interfaces between the electron spin(s) and surrounding nuclear ensemble[15]. Here, we show that the transfer of net nuclear magnetization (*i.e.*, spin polarization) from dilute paramagnetic centers to a surrounding nuclear spin ensemble exhibits fundamental similarities to thermal energy transfer and to charge transport, but importantly combines distinct aspects of both. A general model is derived for meso-scale (1–100 nm) spin transport phenomena that enables rate-limiting

processes to be identified and quantitative prediction of hyperpolarization performance. The resulting insights provide criteria to guide the selection of material properties and conditions to exploit the enhanced sensitivity of hyperpolarization for diverse applications in materials science, biology and medicine, and quantum information processing.

Recent advancements in magic-angle spinning (MAS) DNP-NMR spectroscopy enable large polarization gradients to be generated near paramagnetic centers. In DNP, unpaired electron spins (*e.g.*, on dilute nitroxide biradicals) are partially saturated by microwave irradiation, resulting in hyperfine transfer to nearby nuclear spins[12]. A limitation inherent to DNP is that hyperpolarization emanates from paramagnetic centers that also impede $^{1}$H–$^{1}$H spin diffusion, resulting in a spin-diffusion barrier[15–18]. Fundamental insights have typically come from quantum-mechanical treatments that have elucidated the cross-effect mechanism and field dependence[19–21]. While these approaches have been extended to realistically sized spin systems[22,23], it remains challenging to quantitatively predict hyperpolarization transfer rates to distant $^{1}$H nuclei, particularly across the spin-diffusion barrier (Fig. 3.1a) and across interfaces (Fig. 3.1b). Here, a film approximation is used to obtain dimensionless parameters that generalize spin polarization transport phenomena, elucidate rate-limiting processes, and identify conditions for which classical thermodynamic models[24] can accurately reproduce spin polarization transfer kinetics. This approach provides simple quantitative criteria that allows polarization build-up rates and gains to be predicted on the basis of sample composition, deuteration level, and radical concentration.

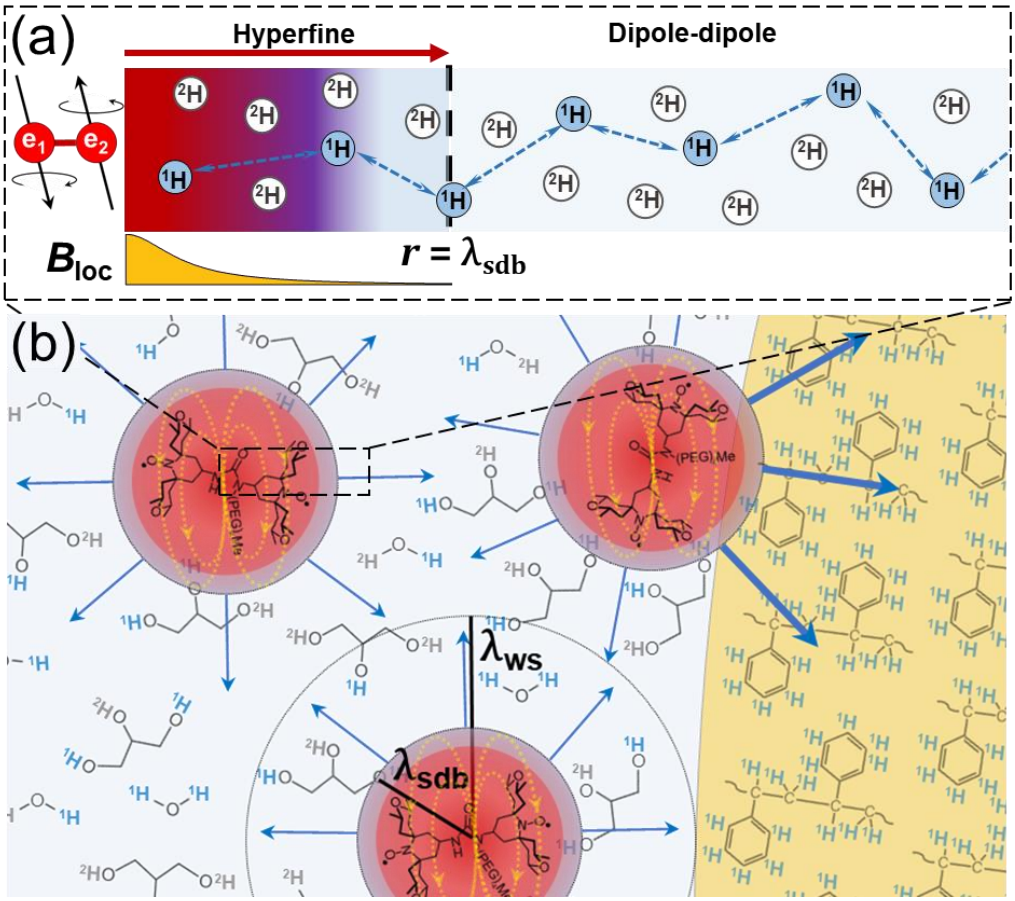


**FIGURE 3.1**. Schematic diagrams of (a) a spin-diffusion barrier and, (b) polarization transfer from paramagnetic centers in a partially deuterated glycerol-water matrix to a polymeric solid. Each biradical molecule is assumed to polarize a spherical region represented by the Wigner-Seitz radius, $\lambda_{\mathrm{ws}} = (3/4\pi\rho_{\mathrm{pc}}N_A)^{1/3}$ where $\rho_{\mathrm{pc}}$ is the biradical concentration[24]. The interface between the spin-diffusion barrier and the bulk diamagnetic matrix occurs at $\lambda_{\mathrm{sdb}}$, and the mean biradical separation is $2\lambda_{\mathrm{ws}}$.

Rate-law descriptions have previously been used to describe solid-effect DNP[25,26] and may be similarly justified for the cross-effect[19,27]. Notably, rate-law approximations are consistent with the Genack-Redfield model[28], which is a magnetic analogue of the Nernst-Planck equation that may partially account for the physical origin of the spin-diffusion barrier. While spin-diffusion in a homogeneous magnetic field is non-activated, the presence of a strong local magnetic field gradient imposes an energy barrier impeding polarization transfer. We show

how under conditions of both microwave irradiation and MAS, simple analytical solutions to the Genack-Redfield model may be obtained by dimensional scaling analyses. By analyzing transient polarization levels of a bulk $^{1}$H spin ensemble and determining apparent rate coefficients, detailed quantitative insights may be obtained regarding the nature of quantum interfaces (*e.g.*, the spin-diffusion barrier) and other rate-limiting processes that emerge in complex spin systems.

### 3.3. Dimensional scaling analyses applied to the spin-diffusion barrier

Classical descriptions have long been used to describe certain spin-relaxation phenomena and energy conduction processes in large coupled spin systems[29]. Under the spin-temperature hypothesis[30], the relationship between Zeeman energy and spin polarization is analogous to the relationship between thermal energy and temperature. The Zeeman energy refers to the potential energy experienced by a spin ensemble in the presence of a magnetic field, which maintains a Boltzmann distribution of spin states yielding net magnetization, the origin of NMR signal intensity. Although transient polarization transfer processes are complicated, it has been shown[31] that the net nuclear magnetization oriented with respect to a static magnetic field ($B_0$) obeys simple relaxation equations that are amenable to thermodynamic descriptions. In hyperpolarization schemes, electron spin excitation processes are used to transfer excess Zeeman energy to a spin system to generate non-Boltzmann (*i.e.*, hyper) polarization that leads to dramatically improved NMR signal sensitivity. Zeeman energy transfer occurs from regions of high to low polarization via dipole-mediated spin flips[29] in a strongly coupled ensemble, which propagates over length scales that are suitable for a continuum description[24]. The Zeeman heat capacity is given by $C_z = CB_0{}^2$, where $C$ is Curie's constant, and $B_0$ is the magnetic field strength[32]. Notably, this implies that the Zeeman heat capacity of an ensemble

of nuclear spins can vary spatially with respect to the inhomogeneous local field $B_{loc}$ that are induced near a paramagnetic center. For $I = ½$ nuclei such as $^1$H under MAS, $C_{z,n} = \gamma_n \hbar B_0 N_A$, where $\gamma_n$ is the gyromagnetic ratio and $N_A$ is Avogadro's number, $C_z = 2.54\text{x}10^{-2}$ J/mol for $^1$H nuclei at 9.4 T far from the paramagnetic center where magnetic fields are homogeneous. With the spin polarization, $\tilde{P}$, normalized with respect to Boltzmann equilibrium, the Zeeman energy flux, can be expressed as $q_n = -\rho_n C_{z,n} \mathcal{D}_n \nabla \tilde{P}$, where $\rho_n$ is the spin density (mol·m$^{-3}$) and $\mathcal{D}_n$ is the spin diffusion coefficient (m$^2$·s$^{-1}$). In the rigid limit,[33] spin diffusivities scale as $\mathcal{D}_n \propto \gamma_n^2 \rho_n^{1/3}$ and can be directly measured.[34–36] A similar $\rho_n^{1/3}$ scaling dependence of $\mathcal{D}_n$ under MAS conditions has been predicted by reduced Liouville space (LCL) calculations.[37] A transient energy balance for the equilibration of polarization, $\tilde{P}(t)$ among $^1$H nuclei in a diamagnetic spin ensemble (*e.g.*, the frozen DNP-solvent) yields:

$$\rho_H C_z \frac{\partial \tilde{P}}{\partial t} - \nabla \cdot \left( \rho_H C_z \mathcal{D}_H \nabla \tilde{P} \right) = \rho_H C_z \frac{\left(1 - \tilde{P}\right)}{T_1} + \dot{Q} \,, \tag{3.1}$$

where $\dot{Q}$ (W/m$^3$) is the DNP source term associated with the microwave excitation and hyperfine processes that generate hyperpolarization. In a bulk solid, such hyperpolarization propagates by spin diffusion and dissipates at a rate of $T_1^{-1}$, the inverse of the $^1$H spin-lattice relaxation time (measured as described in the Supplementary Information, Section S1). A reference $\mathcal{D}_H$ value of $5 \cdot 10^{-16}$ m$^{-2}$s$^{-1}$ has been measured for polystyrene ($\rho_H$ = 70 M) under similar MAS DNP NMR conditions[38]. This constitutive model is valid for coupled nuclear spin ensembles in homogeneous fields and for polarization transfer across interfaces.

However, because hyperpolarization emanates from paramagnetic centers where local fields ($B_{loc}$) are inhomogeneous (Fig. 3.1a), thermodynamic models such as Eq. 3.1 implicitly rely on knowledge of electron-nuclear interactions that are not easily measured directly[15]. By

analogy to Newton's law of cooling, this can be circumvented by use of a DNP polarization-transfer coefficient ($k_{\mathrm{DNP}}$, with units of m/s), where the Zeeman energy flux, $q_{\mathrm{H}} = -(\rho_{\mathrm{H}} C_{\mathrm{z}} k_{\mathrm{DNP}})\Delta\tilde{P}$, is defined at the spin-diffusion barrier interface $r=\lambda_{\mathrm{sdb}}$. The grouping, $\rho_{\mathrm{H}} C_{\mathrm{z}} k_{\mathrm{DNP}}$, has units of W/m$^2$ per polarization-level and is mathematically analogous to a heat-transfer coefficient (W/m$^2$·K), but here represents polarization transfer across a thin local magnetic field gradient. Far from paramagnetic centers ($r \geq \lambda_{\mathrm{sdb}}$), the DNP generation rates, $\dot{Q}$, are negligible. Assuming that polarization propagates radially (via dipolar couplings) from each paramagnetic center, the Zeeman energy flux into the bulk ensemble can be represented by a Neumann boundary condition:

$$\rho_{\mathrm{H}} C_{\mathrm{z}} \mathcal{D}_{\mathrm{H}} \frac{\partial \tilde{P}}{\partial r}\Big|_{\lambda_{\mathrm{sdb}}} = (\rho_{\mathrm{H}} C_{\mathrm{z}} k_{\mathrm{DNP}})\Delta\tilde{P}\,, \tag{3.2}$$

where $\Delta\tilde{P} \equiv (\bar{P}_{\mathrm{CE}} - \tilde{P}|_{\lambda_{\mathrm{sdb}}})$ is the polarization difference between $\bar{P}_{\mathrm{CE}}$, the effective polarization generated among core nuclei by cross-effect exchange or other DNP mechanisms[12], and $\tilde{P}|_{\lambda_{\mathrm{sdb}}}$, the polarization at the thermal contact interface between core and bulk nuclei given by, $\lambda_{\mathrm{sdb}}$, the barrier radius. In the context of the Genack-Redfield model, the barrier radius $\lambda_{\mathrm{sdb}}$ corresponds to a 'vortex radius' over which spin diffusion is partially suppressed due to the influence of the strong local inhomogeneous field $B_{\mathrm{loc}}$. This imposes an energy barrier that can result in a steep reduction in steady-state hyperpolarization levels near the paramagnetic centers as recently corroborated by quantum mechanical simulations[18]. Thus, $\lambda_{\mathrm{sdb}}$ has a physical significance that is at least partially analogous to the Debye length in electrolyte solutions[39], which corresponds to a characteristic length scale over which ion density surrounding a charged interface varies with respect to a decaying local electric field. Whereas the Debye length represents a the distance over which charge neutrality is violated due to electrostatic screening, the spin-diffusion barrier radius may represent a distance over

which hyperfine coupled nuclei undergo frequency-shifted spin precession that can impede or alter spin-diffusion rates.[15,17,18]

Previous experimental and theoretical estimates of the barrier radius $\lambda_{\mathrm{sdb}}$ have ranged from 0.3 to 1.7 nm for a monoradical due to differences in experimental conditions and conflicting definitions of the spin-diffusion barrier.[16] Specifically, the spin-diffusion barrier is either defined as the distance over which spin-diffusion is completely suppressed or, alternatively, partially hindered in comparison to the bulk. Here, the latter definition is preferred, such that $\lambda_{\mathrm{sdb}}$ is regarded as a scaling distance over which local $\mathcal{D}_{\mathrm{H}}$ values rapidly approach bulk values. It is anticipated that $\lambda_{\mathrm{sdb}}$ is related to the pseudopotential radius derived, in the continuum limit, by de Gennes[31] and Khutisivhili[40]. The pseudopotential radius gives a characteristic length scale over which direct paramagnetic relaxation and spin-diffusion are competing. A similar theory was advanced by Goldman[41] and an experimental value of 1.7 nm reported for the steep transition in the local diffusion rate, albeit under static, low field, and low temperature conditions. It is inferred from these past approaches that $\lambda_{\mathrm{sdb}}$ has a complex dependence on sample composition, field strength, and MAS rate. However, determination of the barrier radius under DNP NMR conditions remains an active area of research.[15,18,24]

Although $\lambda_{\mathrm{sdb}}$ values are not explicitly known, it is still possible to measure the apparent rate of polarization transfer across the barrier by means of a film approximation. The definition for the empirical DNP polarization-transfer coefficient is provided in Eq. 3.2. Notably, $k_{\mathrm{DNP}}$ (m/s) accounts for the rate of polarization transfer to the bulk spin ensemble and, $\bar{P}_{\mathrm{CE}}$, accounts for the polarization gain. For these analyses, $\lambda_{\mathrm{sdb}}$ is designated to be 1.8 nm from the biradical center which is larger than the 1.2 nm electron-electron separation distance of the commonly used AMUPol biradical.[42] For the cross-effect mechanism, an upper-bound for $\bar{P}_{\mathrm{CE}}$ is

$\gamma_e/\gamma_H$=658, although lower values are often encountered due to electron spin-relaxation effects[43,44] or due to an inhomogeneous distribution of microwave intensity [45]. Typically, film coefficients are measured empirically (by Eq. 3.2) and used to develop correlations in response to a change in process conditions. Film coefficients can also provide fundamental insights into the system by comparison to a film theory. A film theory often involves a reduction of the physics involved in the process, and may not quantitively match the empirical film coefficient, but provide a general understanding of the scaling dependences[46]. One of the earliest examples is the "two-film theory" developed by Whitman[1] which, by analogy to mass transfer, predicts,

$$k_{\mathrm{DNP}} \sim \frac{\mathcal{D}_{\mathrm{H}}}{\Delta\lambda}, \tag{3.3a}$$

that the transfer coefficient (m/s) scales with respect to a slow diffusion rate over an indeterminate film thickness ($\Delta\lambda$); a similar approach invoking a "heterogeneous reaction velocity" (m/s) was also introduced by Nernst[47]. Another mass transfer model of potential relevance to DNP NMR is the "surface renewal theory" developed by Danckwerts[48] which, by analogy, predicts,

$$k_{\mathrm{DNP}} \sim \sqrt{\mathcal{D}_{\mathrm{H}}\omega}\,, \tag{3.3b}$$

that the transfer coefficient depends on the square root of the product of the diffusion coefficient ($m^2/s$) and a surface renewal frequency ($s^{-1}$). In mass transfer, $\omega$ may correspond to the circulation of eddy currents which periodically replenishes the solute concentration at a gas—liquid interface in contact with a liquid bulk. For DNP NMR, cross-effect transfer events may occur at some frequency $\omega$, replenishing hyperpolarization levels within the barrier which subsequently diffuses into the bulk. Although, Eq. 3.3a-b do not account for $T_1$ relaxation, both mass transfer models have been solved for the mathematically analogous

condition of a first-order irreversible chemical reaction[49]. Given the success of *ab initio* simulations in modelling cross-effect DNP[18,23], it is anticipated that quantum mechanical calculations will afford greater mechanistic insights than can be obtained by a film theory. Nevertheless, the approach remains the same as it is employed in the design and optimization of industrial scale process equipment[1,46]. The empirical transfer coefficient $k_{DNP}$ provides a means to quantify rate-limitations, predict sensitivity improvements, and report scaling dependences in a simple experimental formulism. For example, it is generally known how a heat transfer coefficient scales with fluid velocity, and it would be similarly useful to know how a DNP transfer coefficient scales with $^1$H spin density, field strength, or MAS rate. It will be demonstrated that $k_{DNP}$ and $\bar{P}_{CE}$ provide a foundational basis for the continuum description of large composite spin systems by dimensional property analyses.

The relative rates of generation, propagation, and dissipation of hyperpolarization can be compared by using a scaling analysis, which leads to dimensionless parameters that are analogous to those characteristic of classical energy or mass transfer processes. Specifically, nondimensionalizing Eq. 1 for $\tilde{r} = r/L$ and $\tilde{t} = t/T_1$ yields:

$$\frac{\partial \tilde{P}}{\partial \tilde{t}} - \phi_P^{-2}\left(\frac{2}{\tilde{r}}\frac{\partial \tilde{P}}{\partial \tilde{r}} + \frac{\partial^2 \tilde{P}}{\partial \tilde{r}^2}\right) = (1 - \tilde{P}) , \tag{3.4}$$

where the dimensionless parameter $\phi_P \equiv L/(\mathcal{D}_H T_1)^{0.5}$ arises naturally along with a characteristic dimension $L=(\lambda_{ws}^3-\lambda_{sdb}^3)/3\lambda_{sdb}^2$, which corresponds to a classical spin packet around each paramagnetic center to which energy is transferred. The spin packet is defined by a Wigner-Seitz sphere, see Fig. 3.1b, which is a fictitious spherical volume around a single biradical that accurately represents the bulk volume density of biradical species. Importantly, the Wigner-Seitz radius, $\lambda_{ws}$, is progressively larger at lower biradical concentrations[24] with values of 5.8 nm and 3.2 nm at 2 mM or 12 mM, respectively. At the center of this sphere, there is a

collection of core nuclei within the barrier radius, $\lambda_{sdb}$, that are in poor thermal contact with the bulk. By convention in similar heat transfer analyses, $L$ corresponds to the ratio of the volume and thermal contact area as given above. The parameter $\phi_P$ is analogous to the well-known Thiele modulus associated with mass transfer in heterogeneous catalysts, but, in the present context, $\phi_P$ represents the relative rates of polarization transfer by spin diffusion and energy dissipation by spin-lattice relaxation.

Similarly, nondimensionalization of the boundary condition in Eq. 3.2 yields $\partial\tilde{P}/\partial\tilde{r}=\mathrm{Bi}_P\Delta\tilde{P}$, where $\mathrm{Bi}_P\equiv k_{DNP}L/\mathcal{D}_H$ corresponds to a dimensionless Biot number. In transient heat transfer processes, the Biot number reflects the rate of heat transfer at the surface of an object relative to the rate of internal heat conduction within its body [50]. This has direct analogy to polarization transfer processes, where the Biot number reflects the rate of polarization transfer across the spin-diffusion barrier relative to the rate of spin diffusion within a diamagnetic bulk solid. Low Biot number conditions indicate that a solid medium is "thermally thin" on the basis of its internal transport properties, its dimensions, and the rate at which energy is delivered to or dissipated from it, as shown schematically in Fig. 3.2a. For a thin cooling fin, internal temperature gradients can be neglected to an extraordinarily good approximation enabling simple analytical descriptions of transient heat exchange (*i.e.*, by means of a lumped-element approximation[50]). For spherical geometries with $\mathrm{Bi}_P$ <0.65 (derivation in Appendix A2, A3), spin-diffusion resistances can be considered negligible, and hyperpolarization will be distributed essentially instantaneously and uniformly ($\nabla^2\tilde{P}=0$) into the bulk spin ensemble over a characteristic time scale (*e.g.*, $T_{DNP}$), as depicted in the upper solid trace of Fig. 3.2b. For DNP NMR, the condition "thermally thin" (low Biot number) indicate that polarization transfer across the spin-diffusion barrier is rate-limiting, and that

build-up times in the surrounding matrix do not depend significantly on bulk spin-diffusion properties.

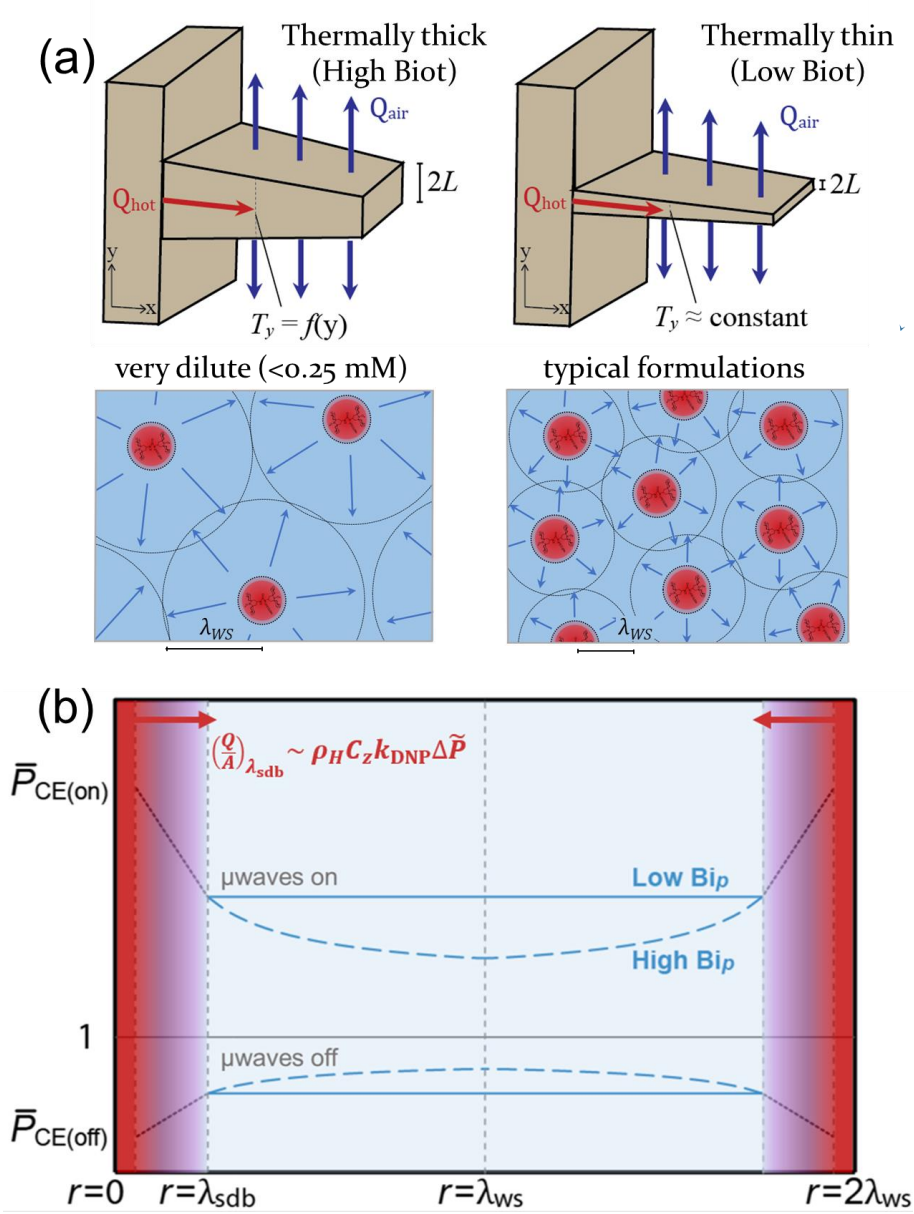


**FIGURE 3.2.** (a) Comparison between a thermally thick and thermally thin cooling fin and their analogy to bulk polarization transfer in dilute biradical suspensions. (b) Schematic steady-state polarization profiles, $\tilde{P}(r)$, between two biradical species in a frozen DNP matrix with ($\bar{P}_{CE(on)}$) or without ($\bar{P}_{CE(off)}$) microwave excitation. For low $Bi_P$ conditions (<0.65), the diamagnetic bulk approaches a nearly uniform polarization level (upper solid line), whereas for high $Bi_P$ conditions (>0.65), a polarization gradient exists (upper dashed line). Thermal equilibrium corresponds to unity. The film-transfer model assumes a linear polarization gradient across the spin-diffusion barrier.

Furthermore, small values of $Bi_P$ justify the use of a lumped-element approximation, similar to those employed in transient heat transfer analyses. For such an approximation, the rate of spin-diffusion in the diamagnetic bulk can be considered infinitely fast relative to the rate of exchange across the spin diffusion barrier, the latter of which is rate-limiting. This allows the boundary condition (Eq. 3.2) to be transformed into a uniform source term, $\dot{Q} = \rho_{\mathrm{H}} C_{\mathrm{z}} k_{\mathrm{DNP}} L^{-1} \Delta\tilde{P}$, as detailed in Appendix 3A2. The consequence of this is that the DNP matrix can be regarded as a homogeneous continuum, rather than as ~$10^{16}$ interacting spin packets. In this description, the continuum element is the spin packet defined by the Wigner-Seitz sphere. For an initial condition $\tilde{P}(r,0) = 0$ corresponding to saturation recovery, an analytical expression is obtained for the characteristic time to build-up polarization, $T_{\mathrm{DNP}}^{\mathrm{o}}$:

$$T_{\mathrm{DNP}}^{\mathrm{o}} = \frac{T_1^{\mathrm{o}}}{(1 + k_{\mathrm{DNP}} L^{-1} T_1^{\mathrm{o}})} \quad , \tag{3.5a}$$

$$k_{\mathrm{DNP}} L^{-1} = \frac{T_1^{\mathrm{o}} - T_{\mathrm{DNP}}^{\mathrm{o}}}{T_1^{\mathrm{o}} T_{\mathrm{DNP}}^{\mathrm{o}}} \quad , \tag{3.5b}$$

from which $k_{\mathrm{DNP}}$ is straightforwardly obtained from experimentally measured values of $T_1^{\mathrm{o}}$ and $T_{\mathrm{DNP}}^{\mathrm{o}}$, and known values of $L$ ; the superscript '$^{\mathrm{o}}$' denotes properties of spin packets isolated from dipolar contact with dissimilar spin reservoirs. Here, the characteristic build-up time, $T_{\mathrm{DNP}}^{\mathrm{o}}$, is associated with cumulative polarization transfer between core and bulk nuclei in a homogeneous frozen solution and the spin-lattice relaxation time, $T_1^{\mathrm{o}}$, is that of the bulk nuclei in the absence of biradical. Eq. 3.5b manifests the direct relationship between $k_{\mathrm{DNP}} L^{-1}$ and experimental values for $T_1^{\mathrm{o}}$ and $T_{\mathrm{DNP}}^{\mathrm{o}}$, which are conveniently measured even if the spin-diffusion barrier radius is not explicitly known. Importantly, under low Biot conditions, the film transfer model accounts for the mono-exponential kinetics for polarization build-up that

are commonly observed for $^1$H spin-diffusion-mediated DNP-NMR experiments in frozen biradical matrices[24,27]. From measured build-up times, values for $k_{DNP}$ are determined using Equation 3.5a and yield quantitative insights into rate-limiting polarization transfer processes. Specifically, $k_{DNP}$ is an apparent rate constant which lumps together the contributions of hyperfine interactions, relaxation processes, and slow diffusion steps that limit apparent polarization transfer rates between core and bulk nuclei.

As demonstrated in Eq. 3.5a, for a similar transfer coefficient, $k_{DNP}$, and a similar biradical concentration, by means of $L$, it is expected that shorter bulk $T_1^o$ values will directly correspond to shorter characteristic build-up times ($T_{DNP}^o$). This phenomenon can be understood by analogy to the mass transfer enhancement factor (E) which for spin polarization is,

$$\mathrm{E} \equiv \frac{\text{polarization transfer rate (with relaxation)}}{\text{polarization transfer rate (no relaxation)}} \quad ,$$

the ratio between the polarization transfer rate in the presence of $T_1^o$ relaxation versus the polarization transfer rate in the absence of $T_1^o$ relaxation. Thus, the depletion of polarization increases the $\nabla\tilde{P}$ driving force resulting in a greater polarization transfer rate within the barrier. Numerical simulations for the E factor have been tabulated by van Krevelen and Hoftijzer[51], and are reported on a nondimensional basis with respect to the Hatta number (Ha). The spin polarization analogue of the Hatta number is Ha = $(\mathcal{D}_H T_1^{-1})^{0.5}/k_{DNP}$, and provides the ratio between the rate of relaxation *within the barrier region* versus the apparent polarization transfer rate *into the barrier region*. For larger Ha number, polarization levels are expected to be depleted across the barrier from that of core nuclei, $\bar{P}_{CE}$, to that of bulk nuclei, $\tilde{P}|_{\lambda_{sdb}}$, consistent with recent *ab initio* simulations[18]. To avoid referring to the quantity, E, as a

polarization transfer rate enhancement, polarization transfer away from paramagnetic centers accelerated by nuclear relaxation will be hereafter described as a "spin Hatta effect". Such effects influence polarization build-up times and absolute polarization gains in DNP NMR experiments.

Although cross-effect DNP is routinely used to enhance NMR signal intensity, determining absolute polarization levels is challenging[52–54], even for low $Bi_P$ conditions for which the polarization level of the diamagnetic bulk is nearly uniform. The effective polarization levels generated by cross-effect transfer can be obtained by lumped-element solution of Eq. 3.1 under conditions with and without microwave irradiation, $\bar{P}_{\mathrm{CE(on)}}$ and $\bar{P}_{\mathrm{CE(off)}}$ respectively, which yield:

$$\varepsilon_{\theta}^{\mathrm{o}} = \frac{1 + k_{\mathrm{DNP}} L^{-1} \bar{P}_{\mathrm{CE(on)}} T_1^{\mathrm{o}}}{1 + k_{\mathrm{DNP}} L^{-1} T_1^{\mathrm{o}}} \quad , \tag{3.6}$$

$$\theta_{\mathrm{depo}}^{\mathrm{o}} = \frac{1 + k_{\mathrm{DNP}} L^{-1} \bar{P}_{\mathrm{CE(off)}} T_1^{\mathrm{o}}}{1 + k_{\mathrm{DNP}} L^{-1} T_1^{\mathrm{o}}} \quad , \tag{3.7}$$

where $\varepsilon_{\theta}^{\mathrm{o}}$ and $\theta_{\mathrm{depo}}^{\mathrm{o}}$ are the mean steady-state polarization levels [55] in the bulk with or without microwave irradiation respectively, normalized with respect to thermal equilibrium. For dilute paramagnetic centers, $\rho_{\mathrm{pc}}$, these quantities are directly related to the commonly reported signal enhancement, $\varepsilon_{\infty}^{\mathrm{o}} \approx \varepsilon_{\theta}^{\mathrm{o}} / \theta_{\mathrm{depo}}^{\mathrm{o}}$, which is the ratio of NMR signal intensity with and without microwave irradiation, as discussed in the Methods section below. Here, $\bar{P}_{\mathrm{CE(on)}}$ provides an upper-bound for polarization levels that are attainable among bulk $^1$H nuclei under microwave irradiation, and $\bar{P}_{\mathrm{CE(off)}}$ quantifies the extent of MAS-induced depolarization,

which in the absence of microwave irradiation, results in partial inversion of the nuclear spin ensemble to polarization levels below thermal equilibrium[54,55], as depicted schematically in the lower traces of Fig. 3.2. For dilute paramagnetic centers, low $Bi_P$ conditions prevail for strongly coupled nuclei (*e.g.*, $^{1}H$, $^{19}F$, $^{31}P$), while high $Bi_P$ conditions are expected for dilute or low-γ nuclei (*e.g.*, $^{13}C$, $^{15}N$, $^{29}Si$) which have weaker dipole interactions. Notably, the relationships developed in Eq. 3.5a, 3.6, and 3.7 provide a means to estimate polarization build-up times and signal gain as a function of sample composition and bulk relaxation properties. These expressions exhibit close agreement with $T_1$ vs. $T_{DNP}$ and $T_1$ vs. $\varepsilon_\theta^o$ scaling dependences predicted by first principle quantum mechanical simulations[23], which provides validation for the present approach (see model fit in Appendix 3A6, Fig. 3A5). Furthermore, these analyses suggest that transient properties (as in Eq. 3.5a) can be inferred from steady-state polarization gains (by Eq. 3.6 and 3.7). Thus, time-saving *ab initio* simulations[18,22] that calculate steady-state polarization profiles may also be able to predict polarization build-up times.

## 3.4. Hyperpolarization transfer rates in frozen dilute radical solutions

Although hyperpolarization transfer by the cross-effect[19] occurs on the order of μs to milliseconds and $^{1}H$ spin diffusion between[24] paramagnetic centers occurs on the order of tens of milliseconds, the characteristic time ($T_{DNP}^o$) is often several seconds indicating the presence of a slow-exchange step[26]. Were this slow-exchange step overcome, many applications which rely on the detection of insensitive spin pairs could be greatly expedited[56]. For DNP-NMR experiments involving water-soluble biomolecules at conventional 9.4 T field strengths, the benchmark DNP matrix consists of frozen glycerol-water 60/30/10 ($d_8$-glycerol/$D_2O$/$H_2O$) solutions containing AMUPol, a stable nitroxide biradical[57]. Although this system has been

empirically optimized, the accumulation of non-Boltzmann polarization levels depends on the competitive rates of spin polarization generation, spin diffusion, and spin relaxation which have not been systematically elucidated. As shown in Fig. 3.3a, measured values of the characteristic times $T_1^o$ and $T_{DNP}^o$ are strongly influenced by the volumetric $^1$H spin density ($\rho_H$) which can be adjusted from 0 to 110 M for glycerol-water systems. The $^1$H spin-lattice relaxation time ($T_1^o$) is strongly dependent on $^1$H-$^1$H dipole-dipole couplings and varies by an order of magnitude from 20 – 200 s over the measured $\rho_H$ range. In the presence of AMUPol, characteristic build-up times ($T_{DNP}^o$) are correspondingly shorter due to electron-nuclear interactions which propagate through the lattice.

Although $T_{DNP}^o$ values are often considered a metric of DNP performance, they inherently depend (Eq. 3.5a) on properties of the matrix and are shorter at higher biradical concentrations[58,59]. The polarization transfer coefficient, $k_{DNP}$, depends on the effective local environment near the paramagnetic centers ($r< \lambda_{sdb}$), as opposed to the extensive properties of the bulk nuclear spin ensemble to which they are coupled. In Fig. 3.3b, $k_{DNP}$ values are plotted versus the cube root of the $^1$H density $\rho_H^{1/3}$ of the frozen DNP matrix, which scales proportionally with the mean $^1$H–$^1$H distance and the $^1$H spin-diffusion coefficient $\mathcal{D}_H$ in a homogeneous magnetic field as discussed above. Importantly, for all conditions measured in Fig. 3.3, $Bi_P$ <0.1 indicating that polarization transfer across the spin-diffusion barrier is rate-limiting, which also validates the use of the lumped-element approximation. Specifically, for $k_{DNP}$ = 1.1 nm/s and a spin diffusivity of $\mathcal{D}_H \approx 330$ nm$^2$/s corresponding to $\rho_H$ = 20 M estimated from the reference value above, the low Biot condition will be satisfied for biradical concentrations >0.25 mM as in Fig. 3.2a. Thus, polarization build-up times will not depend on diffusion rates among bulk $^1$H nuclei and are mono-exponential (see Appendix 3A1, Fig.

3A2) for typical DNP formulations of 1 – 16 mM AMUPol at 100 K, 9.4 T, and 12.5 kHz MAS. However, because spin flips rely on dipole couplings, the effective rate of polarization transfer across the spin-diffusion barrier, as reflected by $k_{DNP}$, is expected to be sensitive to matrix $^1$H spin density. Larger $k_{DNP}$ values correspond to more effective polarization transfer across the barrier region and generally manifest shorter $T_{DNP}$ buildup times, as observed here.

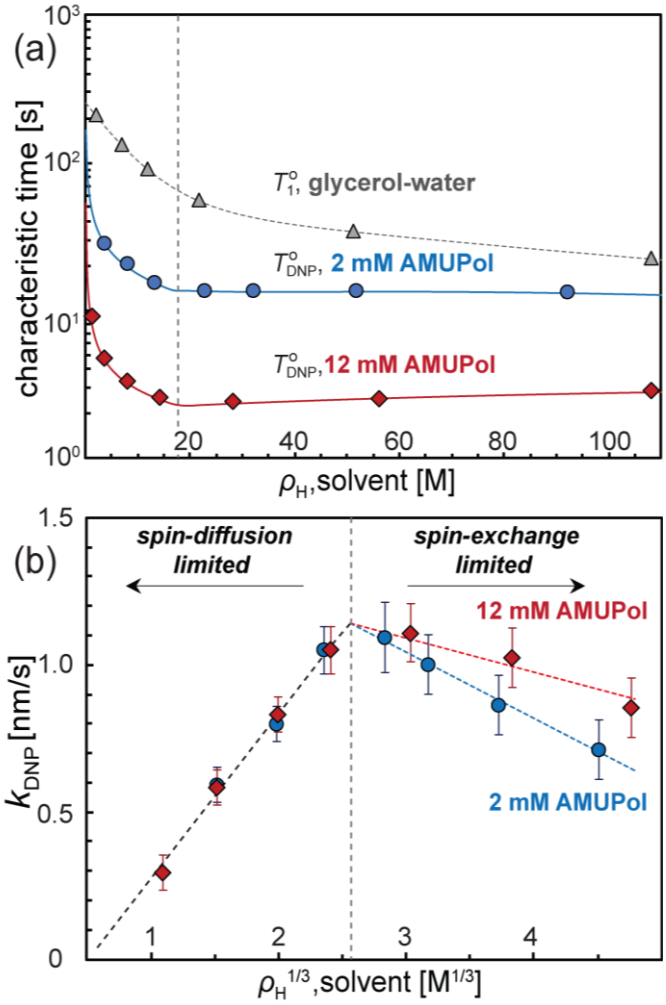


**FIGURE 3.3.** (a) Characteristic times $T_1^o$ or $T_{DNP}^o$ measured by $^1$H spin-echo saturation recovery at 12.5 kHz MAS, 9.4 T, and 100 K for frozen glycerol-water matrices with different $^1$H densities $\rho_H$ and different concentrations of paramagnetic centers: without biradical (▲), with 2 mM (●) or 12 mM (◆) AMUPol; (b) $k_{DNP}$ values as functions of $\rho_H^{1/3}$. Solid lines in (a) are from Eq. (4) using measured or fitted values for $T_1^o$ and $k_{DNP}$.

Interestingly, two regimes are observed in Fig. 3.3b with distinct linear dependences of $k_{DNP}$ on $\rho_H^{1/3}$ associated with different rate-limiting polarization-transfer processes. The positively sloped linear dependence of $k_{DNP}$ on $\rho_H^{1/3}$ matches the predicted scaling relationship of the "two-film theory (without relaxation)" in Eq. 3.3a which describes a slow-diffusion step over a thick barrier. For low $^1$H spin densities ($\rho_H$<17 M), $k_{DNP}$ values tend to be small as a consequence of weak $^1$H–$^1$H dipolar couplings, so that it is speculated that spin diffusion limits the rate at which hyperpolarization is delivered to the bulk. However, increasing $k_{DNP}$ values could also suggest that the rate of spin polarization generation is increasing due to a greater number of electron-nuclear spin pairs within the core. Generally, for higher $\rho_H$, $^1$H dipolar couplings become stronger, resulting in more effective polarization transfer, as manifested by larger values for $k_{DNP}$, though only up to a point. At high $\rho_H$ values, there are more $^1$H nuclei to polarize per biradical and shorter $^1$H $T_1$ relaxation times, which render the DNP matrix and barrier region a stronger polarization sink. A subtle inversion point between regimes is identified by determination of $k_{DNP,}$ which by Eq. 3.5a, is intrinsically related to known or measured values of $T_1^o$, $T_{DNP}^o$, and AMUPol concentration ($\rho_{pc}$), the latter by means of, $L$, the characteristic spin packet length. The maximum value of $k_{DNP}$ occurs for $\rho_H$ =17 M ($\rho_H^{1/3}$=2.55 $M^{1/3}$), above which $k_{DNP}$ values decrease with increasing $^1$H spin density. This spin-exchange-limited regime is representative of the complicated dissipative spin dynamics occurring near paramagnetic centers, which depend upon the relative rates of cross-effect DNP, $^1$H spin-lattice relaxation, $^1$H spin-spin relaxation, or cross-relaxation phenomena.[16,17] The decrease in $k_{DNP}$ values suggests that, at higher $^1$H spin density, either the rate of spin polarization generation by direct DNP transfer or propagation rates by spin-diffusion is insufficient to overcome paramagnetic relaxation within the barrier. This is consistent with similar kinetic

phenomena reported for solid-effect DNP where build-up times for polarization agents such as Gd-DOTA are highly sensitive to $^1$H spin density and plateau at ~20 M, compared to trityl radicals that are less sensitive to such effects.[26] Together, prior literature[15,18,20,24] and the present analyses suggest that the influence of the spin-diffusion barrier can greatly depend on the structure of the polarizing agent.

Here, these kinetic effects are phenomenologically encompassed within the polarization transfer coefficient, $k_{\mathrm{DNP}}$, the proportionality constant associated with the apparent rate of polarization transfer across the spin-diffusion barrier and can be used to predict polarization build-up times under different experimental conditions. By its definition in Eq. 3.2, the product, $\rho_{\mathrm{H}} C_{\mathrm{z}} k_{\mathrm{DNP}} (\bar{P}_{\mathrm{CE}} - \tilde{P}(\mathrm{t}))$ corresponds to the Zeeman energy flux entering the bulk calculated at $\lambda_{\mathrm{sdb}}$ = 1.8 nm, the designated barrier radius in the film approximation. Larger $k_{\mathrm{DNP}}$ values correspond to larger hyperpolarization transfer rates relative to the $^1$H spin density (an intensive property of the matrix) and more effective transfer between core and bulk nuclei. As demonstrated in Eq. 3.5a, in order to calculate a value for $k_{\mathrm{DNP}}$, it is necessary to measure the bulk solvent $T_1^{\mathrm{o}}$ relaxation time. Importantly, the data in Fig. 3.3a-b, correspond to, $T^{\mathrm{o}}_{\mathrm{DNP(on)}}$, the microwave on build-up times, however there are slight differences in, $T^{\mathrm{o}}_{\mathrm{DNP(off)}}$, microwave off build-up times, see data in Table 3A1 and Fig. 3A2 in Appendix 3A1. By plotting the normalized transient signal enhancement factor, $\varepsilon$(t),

$$\varepsilon(\mathrm{t}) = \frac{1 - \exp\left(-\frac{t}{\mathrm{T}_{\mathrm{DNP(on)}}}\right)}{1 - \exp\left(-\frac{t}{\mathrm{T}_{\mathrm{DNP(off)}}}\right)}\,, \tag{3.8}$$

a phenomenon known to occur in heterogeneous matrix-particle suspensions with dissimilar relaxation times[36,60,61] can be observed here and may also be used to identify kinetic regimes associated with different rate-limiting polarization transfer processes without

requiring knowledge of $T_1^o$ values. In Fig. 3.4a-b, $\varepsilon$(t) values are plot as a function of the recycle delay (see schematic pulse sequence in Appendix 3A1) and it is shown that initial profiles exhibit $\varepsilon$(t) < 1 for low $^1$H spin density and $\varepsilon$(t) > 1 for high $^1$H spin density. Interestingly, the crossover point occurs at roughly ~13 M for both 2 and 12 mM AMUPol, similar to the optimum value of the DNP transfer coefficient ca. 17 M in Fig. 3.3b. This phenomenon can be attributed to a "spin Hatta effect" as discussed above where polarization transfer rates are influenced by relaxation within the barrier.

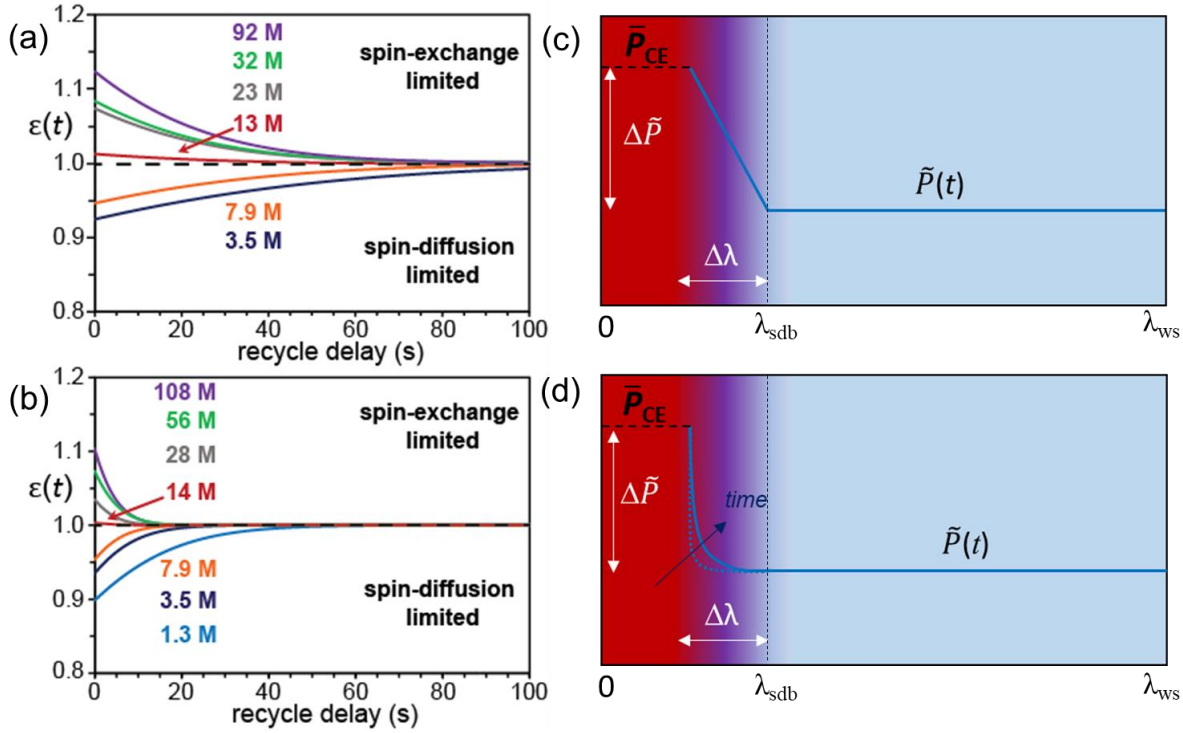


**FIGURE 3.4**. Normalized transient signal enhancement, $\varepsilon$(t), as a function of the recycle delay for (a) 2 mM AMUPol, and (b) 12 mM AMUPol in glycerol-water at different solvent $^1$H spin density. In both (a) & (b), a crossover point occurs roughly at $\rho_H \approx 13$ M similar to that observed in Fig. 3b. Schematic diagrams of mass transfer models including the "film theory" (c) without relaxation; and (d) with relaxation; applied to the description of hyperpolarization transfer between core and bulk nuclei, see text for discussion. It is hypothesized that (c) more closely resembles a diffusion-limited regime and (d) a spin-exchange limited regime; note that (c) is not expected to be linear when curvature and relaxation are non-negligible.

The behavior observed for $\varepsilon(t) < 1$ is consistent with the slow and steady flow of hyperpolarization to the bulk expected for the slow-diffusion process depicted in Fig. 3.4c. For these conditions, $T^{o}_{DNP(off)}$ will be slightly shorter than $T^{o}_{DNP(on)}$ due to classical spin thermodynamic considerations[24]; the initial state is closer to the final state in the absence of microwaves. The behavior observed for $\varepsilon(t) > 1$ is consistent with a diffusion barrier exhibiting higher relaxation rates (larger Hatta number) as depicted in Fig. 3.4d. Higher polarization levels over thermal equilibrium directly correspond to higher relaxation rates, such that $T^{o}_{DNP(on)}$ will be slightly shorter than $T^{o}_{DNP(off)}$ due to a "spin Hatta effect" consistent with the data in Fig. 3.4a&b. Although transfer across the barrier is accelerated for larger Hatta numbers, after a certain point no hyperpolarization will reach the bulk because it will be entirely consumed within the barrier. Together the data in Fig. 3.3b and Fig. 3.4a&b, suggest that net hyperpolarization transfer rates into the bulk are optimized near the point of crossover between the two regimes. For both limiting cases, mono-exponential build-up occurs among bulk nuclei $\tilde{P}(t)$ because polarization is rapidly and uniformly distributed over $\lambda_{sdb} < r < \lambda_{WS}$, under low Biot number conditions. Interestingly, the $\rho_H^{1/3}$-dependence of the transfer coefficient resembles a Sabatier diagram[62], which in heterogeneous catalysis, relates the adsorption enthalpy of a reactant to its apparent reaction rate; reaction rates are likewise highest for species with intermediate adsorption enthalpies. Here, polarization-transfer kinetics across an inhomogeneous field gradient are most effective at an intermediate value of $\rho_H$ for which $^1H$–$^1H$ dipole-dipole interactions are sufficient to relay polarization without contributing excessively to dissipative spin dynamics (*e.g*, spin-lattice relaxation). These insights are consistent with quantum mechanical treatments that have attributed solid-effect DNP in large systems to a "kinetically constrained diffusion" mechanism.[13]

## 3.5. Hyperpolarization levels generated by cross-effect DNP

Even if hyperpolarization transfer rates are slow, it is possible to accumulate large amounts of hyperpolarization, provided spin-lattice relaxation times are long. Understanding the extent of signal sensitivity enhancement achieved by DNP-NMR, however, can be challenging. As discussed above for absolute $^1$H polarization levels[52], the situation is simplified when the paramagnetic centers are dilute (*e.g.*, $\rho_{pc}$=2 mM), so that paramagnetic quenching is negligible[58,59]. Due to strong hyperfine interactions, $^1$H spins in closest proximity to paramagnetic centers ($r << \lambda_{sdb}$) are typically quenched or rendered otherwise NMR "invisible". Nevertheless, these hyperfine-coupled $^1$H spins are directly polarized by cross-effect transfer, and the resulting hyperpolarization is propagated by spin diffusion to more distant $^1$H spins in the diamagnetic bulk ($r > \lambda_{sdb}$). Importantly, $\bar{P}_{CE}$ is indicative of the efficacy of cross-effect transfer for a given set of experimental conditions and corresponds to the magnitude of the effective hyperpolarization that is transferrable directly to hyperfine-coupled $^1$H nuclei and indirectly to more distant $^1$H nuclei.

For cross-effect DNP, quantum conversion depends on the effective polarization difference between two coupled electron spins (*i.e.*, a nitroxide biradical) which satisfy a cross-effect frequency matching condition[12,20,27]. Partial saturation by microwave irradiation maintains an effective polarization difference between electron spins driving hyperpolarization transfer; however, in the absence of microwave irradiation, the cross-effect matching condition may still be satisfied under magic-angle-spinning, leading to depolarization effects[19,63]. Fitting the measured enhancements $\varepsilon_\infty^o$ and $\theta_{depo}^o$ in Fig. 3.5 using Eqs. 3.6 and 3.7 and $\rho_H$-dependent values for $T_1^o$ and $k_{DNP}$ (Fig. 3.3a,b) yields the blue and grey solid lines, which interestingly correspond to constant values for $\bar{P}_{CE(on)}$=148±14 and

$\bar{P}_{\mathrm{CE(off)}}$=0.42±0.09. The close agreements of the model fits with measured $\varepsilon_{\infty}^{\mathrm{o}}$ and $\theta_{\mathrm{depo}}^{\mathrm{o}}$ values establish that $\bar{P}_{\mathrm{CE(on)}}$ and $\bar{P}_{\mathrm{CE(off)}}$ are, under these conditions, independent of the $^1$H spin density in the frozen solvent (within experimental uncertainties) for 2 mM AMUPol. For constant $\bar{P}_{\mathrm{CE(on)}}$, the biradical maintains the capacity to polarize nearby $^1$H nuclei, however enhancement values decline at higher $^1$H spin density due to a decreasing rate of polarization transfer, $k_{\mathrm{DNP}}$, and shorter bulk $T_1$ values. It is unclear whether this observation would hold if the biradical molecule itself was deuterated because $^1$H species of the biradical may participate in spin-diffusion[15,18,64]. Currently, the dependence of $\bar{P}_{\mathrm{CE}}$ on AMUPol concentration is unknown, but it is anticipated that $\bar{P}_{\mathrm{CE}}$ will be strongly influenced by AMUPol concentrations by means of the inter-radical separation distance. Strong electron-electron dipole interactions[19,59], encountered at higher AMUPol concentrations or from radical clustering[27] may decrease $\bar{P}_{\mathrm{CE(on)}}$ values, due to enhanced electron spin-relaxation effects that diminish the efficacy of cross-effect DNP. For a similar $\bar{P}_{\mathrm{CE}}$ driving force, longer bulk $T_1^{\mathrm{o}}$ values result in greater accumulation of hyperpolarization (larger $\varepsilon_{\theta}^{\mathrm{o}}$, Fig. 3.5). From previous *ab initio* simulations[23], it is demonstrated that $\bar{P}_{\mathrm{CE}}$ values can be extracted from a $T_1$ vs. $\varepsilon_{\theta}^{\mathrm{o}}$ plot by taking the limit as the bulk $T_1$ value approaches infinity (see Appendix 3A6). The analytical expressions obtained from the lumped-element analysis thus relate the rate of Zeeman energy generated by an ensemble of biradicals ($\dot{Q}$) to the macroscopically observable accumulation of $^1$H spin hyperpolarization in a surrounding diamagnetic spin bath (*e.g.*, the frozen solvent matrix). DNP injection rates in units of Watts are calculated for 2 mM AMUPol in glycerol-water in Appendix 3A7.

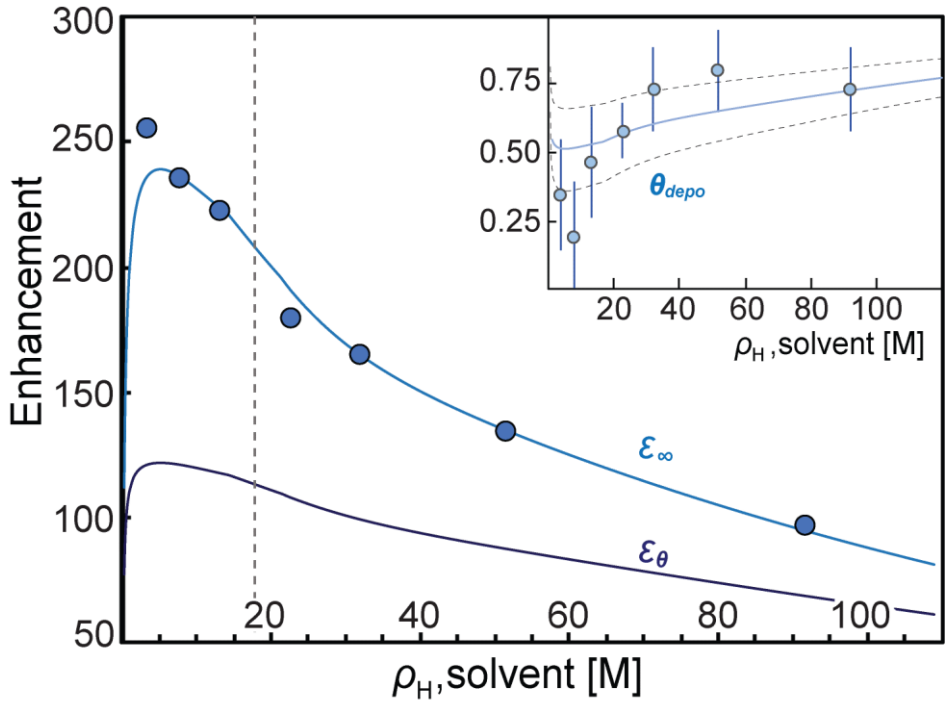


**FIGURE 3.5.** Steady-state NMR signal enhancements $\varepsilon_\infty^o$ (inset: depolarization factors $\theta_{depo}^o$) and $\varepsilon_\theta^o = \varepsilon_\infty^o \theta_{depo}^o$ versus $\rho_H$ for frozen 2 mM AMUPol glycerol-water measured by $^1$H spin-echo saturation recovery at 12.5 kHz MAS, 9.4 T, and 100 K. Solid lines are from Eqs. 6 and 7 using measured or fitted values for $T_1^o$, $k_{DNP}$, and $\bar{P}_{CE}$.

## 3.6. Hyperpolarization of solid-particle targets

An advantage of DNP-NMR is that hyperpolarization emanates from paramagnetic centers, enabling surface-enhanced NMR spectroscopy of porous or nonporous solids. As shown schematically in Fig. 3.1, hyperpolarization is transferred across the spin-diffusion barrier and is relayed by $^1$H spin diffusion into the solid-particle interior up to µm length scales. With $\rho_H$, $\rho_{pc}$, $T_1$, $k_{DNP}$, and $\bar{P}_{CE}$ known, polarization transfer kinetics can be predicted, including across interfaces in heterogeneous systems. For polarization transfer to a solid particle (*S*) in dipole-dipole contact with a DNP matrix (*M*), the process is analogous to energy conduction through a series of thermal resistances and can be treated similarly for each region *i*, such that:

$$\rho_{\mathrm{H},i} C_{\mathrm{z}} \frac{\partial \tilde{P}_i}{\partial t} - \nabla \cdot \left( \rho_{\mathrm{H},i} C_{\mathrm{z}} \mathcal{D}_{\mathrm{H},i} \nabla \tilde{P}_i \right) = \rho_{\mathrm{H},i} C_{\mathrm{z}} \frac{\left( \Pi_i - \tilde{P}_i \right)}{T^{\mathrm{o}}_{\mathrm{DNP},i}}, \tag{3.9}$$

where $\Pi_i$ is equal to either $\varepsilon^{\mathrm{o}}_{\theta,\mathrm{i}}$ or $\theta^{\mathrm{o}}_{\mathrm{depo},i}$ in the presence or absence of microwave irradiation as determined from Eqs. 3.6 and 3.7. Similarly, the characteristic time, $T^{\mathrm{o}}_{\mathrm{DNP},i}$, is determined from Eq. 3.5a by using known or measured values of $T^{\mathrm{o}}_{1,i}$, $k_{\mathrm{DNP},i}$, and $L_i$, as described above. For example, 2 mM AMUPol in glycerol-water ($\rho_{\mathrm{H,M}}$=12 M) yields values of $\varepsilon^{\mathrm{o}}_{\theta,M}$=120, $\theta^{\mathrm{o}}_{\mathrm{depo},M}$=0.53, and $T^{\mathrm{o}}_{\mathrm{DNP},M}$=16 s for the conditions in Figs. 3.3 and 3.5. In contrast, the interiors of solid polystyrene particles without paramagnetic centers ($L_S \rightarrow \infty$) are hyperpolarized solely by $^1$H spin diffusion, though recover polarization thermally, for which Eqs. 3.5, 3.6, 3.7 yield $\varepsilon^{\mathrm{o}}_{\theta,S}$=$\theta^{\mathrm{o}}_{\mathrm{depo},S}$=1 and $T^{\mathrm{o}}_{\mathrm{DNP},S}$=$T^{\mathrm{o}}_{1,S}$=1.3 s, the latter being the $^1$H spin-lattice relaxation time of polystyrene at 100 K, 9.4 T, and 12.5 kHz MAS. The interfacial boundary conditions[65] are analogous to those in heat conduction processes, such that the polarization and Zeeman energy flux are continuous across each interface, where $\tilde{P}_i = \tilde{P}_j$ and $q_{\mathrm{H}}|_i = q_{\mathrm{H}}|_j$, respectively. The relative propensity of each region to conduct spin polarization is scaled by the quantity $\rho_{\mathrm{H}} C_{\mathrm{z}} \mathcal{D}_{\mathrm{H}}$, which is the Zeeman conductivity. For polarization transfer between materials with different $^1$H spin densities, the effects associated with their different Zeeman heat capacities must be taken into account. Deuteration of the solvent increases $T_1$ relaxation times which allows for greater accumulation of hyperpolarization, however it also reduces the capacity of the solvent to relay Zeeman energy (by means of $\rho_{\mathrm{H}} C_{\mathrm{z}} \mathcal{D}_{\mathrm{H}}$). In general, partially deuterated frozen glycerol-water matrices propagate Zeeman energy less effectively than $^1$H-abundant polymeric solids, but, retain hyperpolarization to a greater extent.

In the presence of a solid-particle target, hyperpolarization generated in a DNP matrix must be distributed over relatively large distances (typically 1–100 nm) to reach the particle

surface. The extent to which the hyperpolarization is transferred to and propagates into the solid particle depends on the rates of spin diffusion and spin-lattice relaxation in the solid. Assuming hyperpolarization is transferred to the solid particle solely by matrix-mediated spin-diffusion, the polarizability of a spherical sink of radius $R$ is characterized by the Thiele modulus in the solid-particle, $\phi_S \equiv R/(\mathcal{D}_{\mathrm{H},S}T_{1,S}^{\mathrm{o}})^{0.5}$ and effectiveness factor $\eta=3\phi_S^{-2}(\phi_S\cdot\coth[\phi_S]-1)$, as derived in Appendix 3A4. Quantitatively, $\eta$ represents the ratio of the average rate of Zeeman energy dissipation in the particle interior, compared to the maximum rate that would occur if the particle interior were uniformly polarized to the level at the particle surface yielding an extent of hyperpolarization throughout the object. Larger $\phi_S$ values correspond to stronger polarization sinks, such that the effectiveness factor is $\eta\rightarrow 100$ % and $\eta\rightarrow 0$ % in the limits of $\phi_S\rightarrow 0$ and $\phi_S\rightarrow\infty$, respectively. Importantly, the surface polarization must be maintained by Zeeman energy generation and propagation within the DNP matrix. This requires that the rate of Zeeman energy dissipation within the solid-particle interior be equal to the rate of Zeeman energy flowing into the surface at steady-state satisfying the condition,

$$(q_H\cdot A)|_R=\iiint \rho_{\mathrm{H,S}}C_{\mathrm{z}}\frac{\left(\tilde{P}_S(r)-1\right)}{T_{1,S}^{\mathrm{o}}}\,\mathrm{d}V \quad , \tag{3.10}$$

$$\frac{\partial\tilde{P}}{\partial\tilde{r}}|_{\tilde{r}=1}=\tfrac{1}{3}\mathrm{Da_P}\eta\left(\tilde{P}|_{\tilde{r}=1}-1\right) \quad , \tag{3.11}$$

where Eq. 3.11 is obtained by nondimensionalizing Eq. 3.10 with respect to $\tilde{r}=r/R$ and $\tilde{t}=t/T_{1,S}^{\mathrm{o}}$, as detailed in the steady-state analytical solution to Eq. 3.9 in Appendix 3A5. Here,

a polarization analogue of the dimensionless Damköhler number ($\mathrm{Da_P}$) is expressed in terms of measurable or known quantities,

$$\mathrm{Da_P} = \frac{R^2 {T_{1,S}^{\mathrm{o}}}^{-1}}{\mathcal{D}_{\mathrm{H},M}} \cdot \frac{\rho_{\mathrm{H},S} C_{\mathrm{z}}}{\rho_{\mathrm{H},M} C_{\mathrm{z}}}, \tag{3.12}$$

for a given $^1$H spin density of the DNP matrix ($\rho_{\mathrm{H},M}$), the spin-diffusion coefficient of the DNP matrix ($\mathcal{D}_{\mathrm{H},M}$), the $^1$H spin density of the solid-particle interior ($\rho_{\mathrm{H},S}$), and the $^1$H spin-lattice relaxation time ($T_{1,S}^{\mathrm{o}}$) in the solid-particle interior. Here, $\mathrm{Da_P}$ may be regarded as a relative measure of the polarization inertia and relates the rate of energy dissipation in the interior versus the rate of DNP matrix-mediated spin-diffusion to the surface, weighted by the specific Zeeman heat capacity of each media. This is similar to the thermal inertia, however since temperature is not consumed by relaxation processes, a temperature analogue of the Damköhler number does not exist. In a composite heterogeneous spin system, high levels of hyperpolarization at particle surfaces can only be maintained if the polarization inertia of the DNP matrix is sufficient to overcome energy dissipation within the particle interior. Thus, in addition to the kinetic limitations presented by the spin-diffusion barrier, which are encompassed within the DNP source term, $\dot{Q}$, $^1$H spin thermodynamic properties associated with the DNP matrix (an energy 'source') and the solid-particle target (an energy 'sink') govern polarization transfer in composite systems.

Although previous numerical simulations[24] of matrix-particle suspensions yield similar insights as to those developed here, an advantage of dimensionless parameterization is that rate limiting polarization transfer phenomena can be assessed without computational methods. In Figure 3.6a-c., the normalized steady-state spatial polarization gain under microwave irradiation, $\varepsilon_{\theta,i}(\tilde{r})/\varepsilon_{\theta,M}^{\mathrm{o}}$, is plotted versus $\tilde{r}$ for different values of the Thiele

modulus ($\phi_S$) and Damköhler number ($Da_P$). Both Fig. 6a and 6b are generated using $Da_P$ = 0.2, however with $\phi_S$ values of 2.0 and 20, respectively. As a general rule, for small Damköhler numbers ($Da_P$<<1), the DNP solvent matrix will resist changes in its polarization level maintaining a high enhancement at particle surfaces. Meanwhile, the extent to which hyperpolarization is relayed into the particle interior depends on the Thiele modulus. Specifically, for $\phi_S$ = 2.0 and 20 the effectiveness factor ($\eta$) is calculated to be 81 % and 14 % which corresponds to the average dissipation rate of hyperpolarization in the interior relative to the surface. More usefully, the enhancement in the solid is related to the surface polarization by, $\varepsilon_{\theta,S} = \eta\left(\tilde{P}|_{\tilde{r}=1} - 1\right) + 1$, where $\tilde{P}|_{\tilde{r}=1}$ is denoted by the black dot in Fig. 3.6a-c. By comparison, in Fig. 3.6c, a similar profile is generated for values of $Da_P$ = 500 and $\phi_S$ = 2.0. Under large $Da_P$ conditions ($Da_P \rightarrow \infty$), the hyperpolarization reservoir within the DNP solvent matrix is partially exhausted near particle surfaces resulting in the formation of a depletion layer. Regardless, for $\phi_S$ = 2.0, the average dissipation rate of hyperpolarization within the interior relative to the, now diminished, surface polarization still corresponds to $\eta$ = 81 % as depicted in the schematic inset in Fig. 3.6c. For large $Da_P$ conditions, DNP matrix mediated spin-diffusion is an ineffective mechanism for polarizing solid-particle targets. Although the solution to Eq. 3.9 and the effectiveness factor will have a different functional form depending on geometry, both $Da_P$ and $\phi_S$ depend solely on the material properties of the system and can be used to parametrize the efficacy of polarization transfer between two or more media coupled by spin-diffusion.

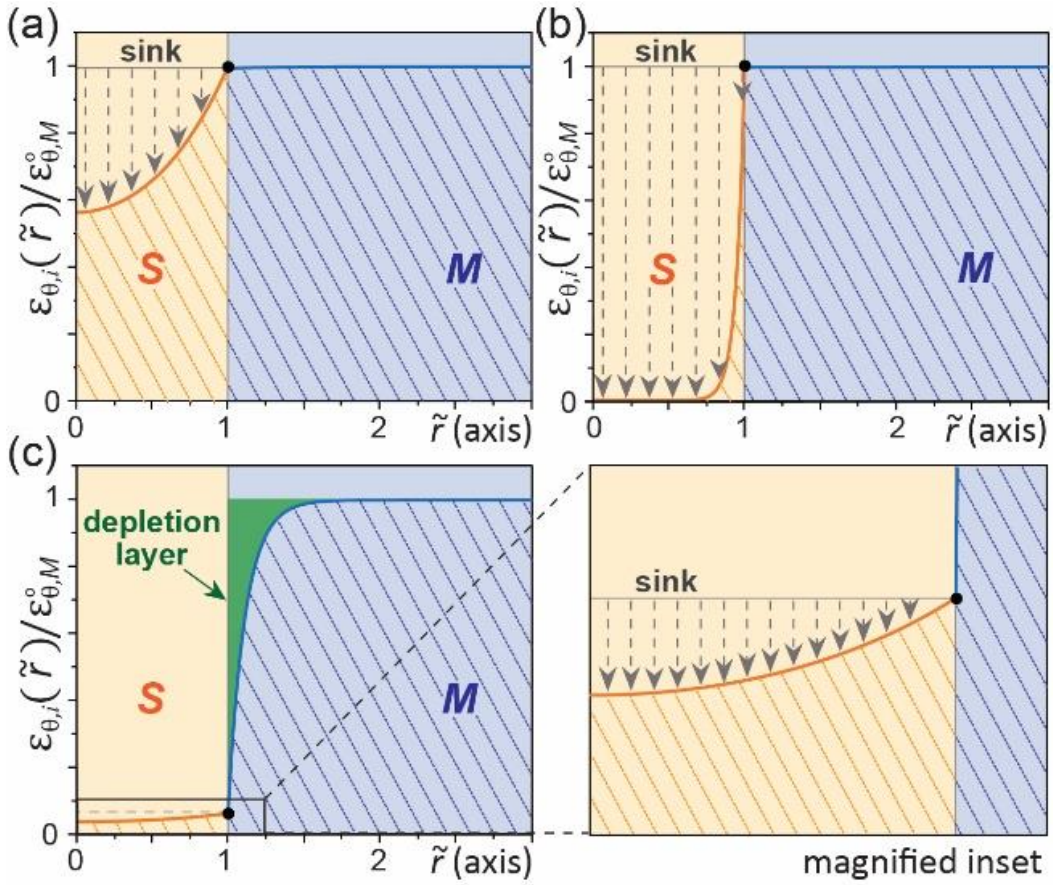


**FIGURE 3.6.** Normalized steady-state spatial polarization gain for conditions of (a) $Da_P$ = 0.02 and $\phi_S$ = 2.0; (b) $Da_P$ = 0.02 and $\phi_S$ = 20, and (c) $Da_P$ = 500 and $\phi_S$ = 2.0. Plots generated using analytical solution provided in methods section.

## 3.7. Direct versus spin-diffusion mediated polarization transfer at surfaces

Although thermal-like boundary conditions[65] are generally justified for homogenous diamagnetic systems, heterogeneous systems require accounting for the different rates of hyperpolarization propagation and dissipation within the dissimilar media, as well as transfer across their mutual interfaces. Importantly, higher local concentrations of biradicals at the solvent-solid interface can significantly influence local polarization transfer processes. In general, the effects of such interfacial phenomena have been challenging to elucidate for

composite spin systems, such as those exploited in hyperpolarized magnetic resonance[7,66] and for quantum interface control[11,67]. As schematically depicted in Fig. 3.1b, in DNP-NMR experiments, adsorbed or near-surface biradicals can directly polarize $^1$H nuclei within the solid-particle interior up to the range of the hyperfine interaction. It is assumed that the solid is free of paramagnetic impurities, which could otherwise diminish the efficacy of DNP cross-effect transfer[7]. Due to the different local environment experienced by near-surface paramagnetic centers, their associated DNP source term ($\dot{Q}$) differs from those in the bulk DNP matrix, according to the Zeeman conductivity and spin-relaxation properties of the surface with which they are in contact. This interfacial region, *I*, may be approximated as an additional film resistance separating the two bulk media over the annulus $R>r>(R-\lambda_{ws,I})$, as depicted in Fig. 3.7a. Specifically, it is assumed that the Zeeman energy flux (W/m$^2$) into Region *I* due to direct DNP is represented by, $\rho_{H,S}C_z k_{DNP}(\rho_{H,S})\,\Delta\tilde{P}$, such that the polarization build-up rate and signal gain over $R>r>(R-\lambda_{ws,I})$ can be calculated by the lumped-element approximation given previously in Eq. 3.5a, 3.6, and 3.7. The build-up rates and polarization gain are calculated to be $\varepsilon^{o}_{\theta,I}$=8.3, $\theta^{o}_{depo,I}$=0.97, and $T^{o}_{DNP,I}$=1.2 s for $k_{DNP}L^{-1}$ = 0.04 s$^{-1}$ corresponding to 2 mM AMUPol ($\lambda_{ws,I}$= 5.8 nm) and polystyrene ($\rho_H$= 70 M). Due to the relatively short $T^{o}_{1,S}$ = 1.3 s of amorphous polystyrene, these interfacial $^1$H nuclei retain polarization poorly compared to the DNP matrix. For this spin system, it can be determined from Eq. 3.9, that the near-surface radicals will exhibit a "spin Hatta effect" which yields an accelerated rate of polarization transfer relative to bulk radical species. Due to this accelerated rate of polarization transfer, at very early times ($t << T^{o}_{DNP,M}$) there will be an initial diffusive flux from Region '*I*' into Region '*M*' which will revert as the polarization gradient is established. Direct hyperpolarization of the solid-particle surface enhances fast relaxing $^1$H

spins near the interface, resulting in faster build-up times both in the DNP matrix and in the bulk solid particle due to $^1$H-$^1$H dipolar interactions. At steady-state, the measured DNP signal enhancement ($\varepsilon_{\infty,i}$) corresponds to the average polarization with, $\tilde{P}_i|_{\mathrm{on}}$, and without, $\tilde{P}_i|_{\mathrm{off}}$, microwave irradiation, $\varepsilon_{\infty,i} = 1/V_i \cdot \iiint (\tilde{P}_i|_{\mathrm{on}}/\tilde{P}_i|_{\mathrm{off}}) dV_i$, which can be independently measured for each region for which distinct NMR signals are resolved.

Assuming that the DNP matrix is uniformly distributed around each solid particle, Eq. 3.9, can be solved numerically to obtain spatial polarization profiles. For the conditions above, Fig. 3.7a shows a calculated plot of the steady-state $^1$H signal enhancement ($\varepsilon_{\infty,i}$) profile within a 100-nm polystyrene particle, across the interfacial region, and within a thin 12-nm DNP-matrix layer. For the thin DNP-matrix layer, $^1$H spin-lattice relaxation in the solid-particle sink significantly reduces polarization levels in the DNP matrix from the maximum value attainable for the homogeneous case, $\varepsilon^{\mathrm{o}}_{\infty,M}$=230, to that calculated for this heterogeneous suspension, $\varepsilon_{\infty,M}$=7. As discussed above, polarization dissipation rates in the interior are characterized by the Thiele modulus in the solid-particle, $\phi_S \equiv R/(\mathcal{D}_{\mathrm{H},S} T^{\mathrm{o}}_{1,S})^{0.5}$, where larger $\phi_S$ values correspond to stronger polarization sinks and diminished enhancements. In Fig. 3.7b, measured $\varepsilon^{\mathrm{o}}_{\infty,M}$, $\varepsilon_{\infty,M}$, and $\varepsilon_{\infty,S}$ values are plotted versus matrix $\rho_{\mathrm{H},M}{}^{1/3}$ for polystyrene-DNP-matrix suspensions, which elucidate both the contribution of direct DNP transfer to solid-particle surfaces and the utility of $\phi_S$ for predicting the extent to which a solid may be hyperpolarized. For longer $^1$H spin-lattice relaxation times, $\phi_S \rightarrow 0$, and the DNP signal enhancement in the solid particle $\varepsilon_{\infty,S}$ approaches the maximum value attainable, namely that of the homogeneous DNP matrix $\varepsilon^{\mathrm{o}}_{\infty,M}$ (Fig. 3.7b, ●). For the 100-nm polystyrene particles and conditions used here, $\phi_S$=2.0, which establishes that the internal rate of dissipation of $^1$H polarization by spin-lattice relaxation is twice the rate of $^1$H spin diffusion, leading to

significantly lower enhancements of both the polystyrene $\varepsilon_{\infty,S}$ (◆) and the DNP matrix $\varepsilon_{\infty,M}$ (×). For low $\rho_{H,M}$, the Zeeman conductivity ($\rho_H C_z \mathcal{D}_H$) of the DNP matrix is too low to efficiently polarize the solid-particle surface by matrix-mediated $^1$H spin diffusion alone. This corresponds to a large Damköhler number conditions and is analogous to thermal energy conduction between a low heat-capacity fluid and a high heat-capacity solid, the latter of which exhibits smaller changes in temperature. Deviation among $\varepsilon_{\infty,S}$ values from the analytical plot for $\phi_S$=2.0 in Fig. 3.7b provides strong evidence that hyperfine-mediated polarization transfer to the solid-particle surface contributes significantly to hyperpolarization of composite spin systems. As reflected in the analytical plots for $\phi_S$ >0.1, the magnitude and rate of hyperpolarization transfer by DNP matrix-mediated spin-diffusion is often not sufficient to overcome thermally driven spin-lattice relaxation in the solid particle target. Instead, polarization transfer at low $\rho_{H,M}$ may be dominated by direct DNP transfer from near-surface radical species[36]. Despite the complex nature of the interface, satisfactory agreement is obtained between experiment and numerical solutions (solid-yellow line) that incorporate radical-surface interactions, without adjustable parameters, under the conditions discussed above. Further evidence for such direct polarization transfer is provided by the nearly constant signal enhancement $\varepsilon_{\infty,M}$ (×) of the DNP matrix as a function of $\rho_{H,M}^{1/3}$ over the range of conditions examined. While energy transfer from the DNP matrix to the solid target is relatively poor when matrix $^1$H densities $\rho_{H,M}$ are low, the ensemble of spins in the DNP matrix is nevertheless rapidly polarized to $\varepsilon_{\infty,M} \approx \varepsilon^o_{\theta,I}$ by dipolar contact with the solid target surface which often has a larger Zeeman spin conductivity (due to partial deuteration of the DNP matrix, $\rho_{H,S}\mathcal{D}_{H,S}C_Z >> \rho_{H,M}\mathcal{D}_{H,M}C_Z$). Consequently, the steady-state hyperpolarization levels that are established in the dipole-dipole-coupled spin ensembles of the DNP matrix and solid

particles mutually depend on the relative rates of polarization generation, propagation, and dissipation in the respective media, in accordance with classical spin thermodynamics and the underlying quantum processes. The constitutive model thus yields quantitative understanding of the physical processes that account for the hyperpolarization levels that are measured experimentally, including the roles of interfacial interactions and non-equilibrium effects that are important in mesoscopic spin transport processes generally.

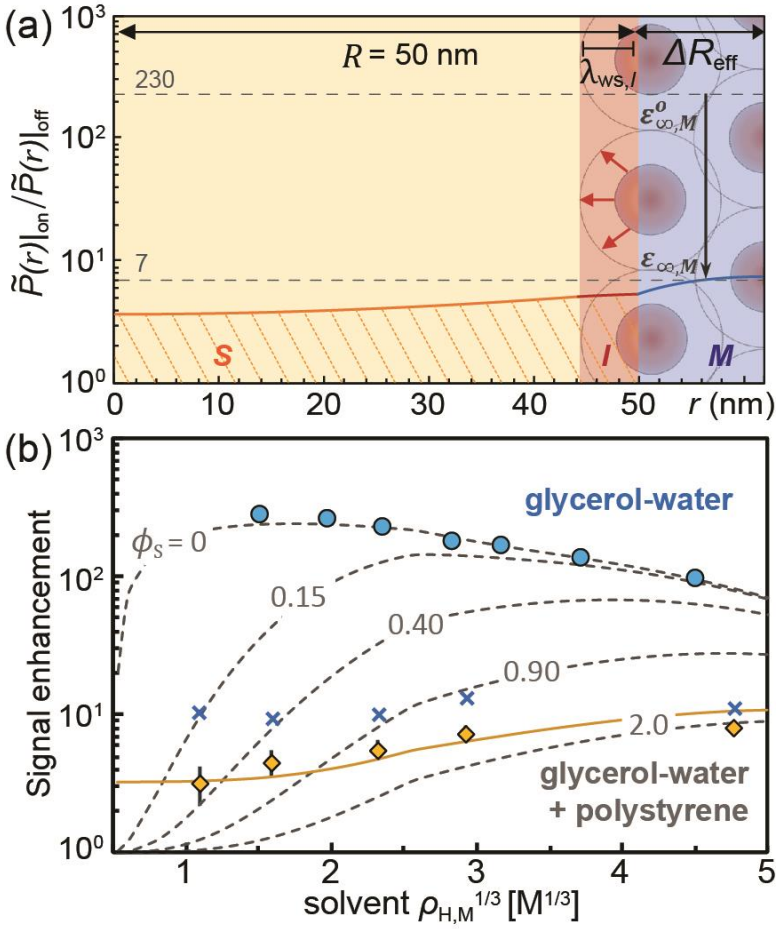


**FIGURE 3.7.** (a) Calculated steady-state $^1$H polarization profile as a function of position $r$ from the center of a 100-nm polystyrene sphere, surrounded by a 12-nm ($\Delta R_{\text{eff}}$, solvent-solid ratio 1.3 µL/mg) frozen glycerol-water matrix ($\rho_{\text{H},M}$=12 M) containing 2 mM AMUPol. (b) Measured enhancements $\varepsilon_{\infty,S}$ (◆) and $\varepsilon_{\infty,M}$ (×) for the polystyrene particle suspension, compared to the DNP matrix $\varepsilon^{\text{o}}_{\infty,M}$ (●, Fig. 3.4). Dashed grey lines correspond to analytical solutions for $\varepsilon_{\infty,S}(\phi_S)$ for $0<\phi_S<2$ (neglecting biradical-surface interactions); solid yellow line accounts for biradical-surface interactions with $\phi_S$=2.

## 3.8. Conclusions

The dimensional scaling analyses presented here generalize aspects of spin polarization transfer phenomena across multiple length scales and across strong local magnetic field gradients. In particular, the utility of such scaling analyses are shown to quantitatively describe hyperpolarization transfer to surrounding nuclear spin ensembles, mediated by slow exchange across a quantum interface, specifically the spin-diffusion barrier. The resulting bulk constitutive model is directly analogous to the heat equation and provides a continuum description of hyperpolarization transfer in non-conducting solids containing dilute paramagnetic centers. The rate of excess Zeeman energy transfer (*i.e.*, DNP injection rate) from paramagnetic centers is proportional to the product $\rho_{\mathrm{H}} C_{\mathrm{Z}} k_{\mathrm{DNP}}$, which is analogous to a heat transfer coefficient. Measurement of the DNP polarization transfer coefficient, $k_{\mathrm{DNP}}$, enables distinct kinetic regimes associated with different rate-limiting polarization transfer processes to be distinguished. Quantitative experimental evidence supports the existence of an energy barrier that impedes polarization transfer near paramagnetic centers and which is crucially influenced by the local $^{1}$H spin density. Although higher $^{1}$H spin densities are desirable to maximize the flux of Zeeman energy into the bulk matrix, a kinetic limit is encountered at intermediate values of the $^{1}$H spin density, after which the apparent rate of hyperpolarization transfer into the bulk matrix declines. This kinetically-limited regime is attributed to dissipative and transport limitations that occur among hyperfine-coupled $^{1}$H nuclei, but may also be associated with an intrinsic limitation of the cross-effect mechanism itself. The film-transfer model in the “thermally thin” limit yields simple quantitative criteria (see Eq. 3.5a, 3.6, and 3.7) for optimizing cross-effect DNP conditions or other hyperpolarization transfer protocols. A more general conclusion is that the utility of

hyperpolarization techniques could be significantly improved if kinetic limitations, such as the spin-diffusion barrier, were diminished. This motivates further development of new paramagnetic sources or electron/nuclear spin excitation methodologies to mitigate these kinetic factors, guided both by the dimensional property relationships presented here and by first-principles quantum mechanical calculations.

Far from paramagnetic centers, hyperpolarization transfer is shown to adhere to spin thermodynamic formalisms similar to thermal energy conduction processes. However, near the paramagnetic centers ($r < \lambda_{sdb}$) or in related phenomena involving polarization transfer between frequency-shifted nuclei (*e.g.*, nuclear spin waves[68,69]), such thermal-like conduction may not strictly apply and require modification, as presented here for the propagation of net nuclear magnetization, to obtain meaningful quantitative results. Lastly, interfacial phenomena, including adsorption of biradical polarizing agents, are shown to significantly influence polarization transfer kinetics between bulk reservoirs of nuclear spins. Despite these complexities, it is demonstrated that continuum analyses can provide important insights near quantum interfaces (*e.g.*, spin-diffusion barrier), as the Nernst-Planck equation does for dilute electrolyte systems. The DNP polarization transfer coefficient, as demonstrated here, is a useful concept to measure and compare polarization transfer rates in heterogeneous spin systems. Film coefficients are widely applied in heat and mass transfer, and, for the spin-diffusion barrier, further analogies may be extended to concepts in electrochemistry such as the Debeye length or the charge-transfer coefficient in the Butler-Volmer model[70]. In a broader context, these results provide a system-level description of complex composite spin systems. Such approaches may be used to guide the selection of material properties to optimize polarization transfer between dissimilar spin reservoirs which remains crucial to

hyperpolarized magnetic resonance and quantum information applications. Similar scaling analyses are expected to yield system-level insights into spin-transfer phenomena in other condensed matter systems where transitions from quantum mechanical to classical properties feature prominently.

## 3.9. Materials, Methods, and Derivations

### Sample preparation

DNP-NMR measurements were performed on a frozen biradical solution and on frozen polystyrene microparticle suspensions. Stock solutions containing 2 mM or 12 mM stable nitroxide biradical AMUPol (Cortecnet) were prepared by using glycerol/$H_2O$ (60/40 vol%) and $d_8$-glycerol/$D_2O$ (60/40 vol%). The partially deuterated solvents used in the MAS-DNP experiments were prepared by sequential dilution of the AMUPol glycerol/$H_2O$ (60/40 vol%) solutions with aliquots of AMUPol $d_8$-glycerol/$D_2O$ (60/40 vol%) solutions. Low-dispersity 0.1 ±0.01 μm polystyrene microbeads were acquired from Sigma-Aldrich, suspended in 99.99 atom% $D_2O$, and freeze-dried prior to use. For frozen biradical solutions, approximately 20 μL of each solution were injected into a 3.2 mm sapphire rotor, packed with a polytetrafluorethylene (PTFE) insert and capped with a zirconia MAS drive cap, and inserted into the pre-cooled spectrometer. For solid containing samples, approximately 13 mg of dry polystyrene particles were combined with 10 μL of DNP solution under incipient wetness conditions and were mixed by hand with a glass stir rod.

**DNP-NMR measurements**

Solid-state MAS-DNP measurements were conducted on a wide-bore 400 MHz ($B_0$ = 9.4 T) Bruker Avance IIIHD spectrometer equipped with 263 GHz gyrotron, a low-temperature cooling cabinet, and a triple-resonance (H-X-Y) 3.2 mm low-temperature MAS probe. The protocols for measuring $T_1$, $T_{\mathrm{DNP}}$, $\varepsilon_\infty$, $\varepsilon_\theta$, and $\theta_{\mathrm{depo}}$ values were similar to those described previously[27,53]. The $^1$H spin-echo saturation recovery experiments were conducted at 12.5 kHz MAS and 100 K with a fixed echo delay of $\tau_r$ =80 μs, proton 90° and 180° pulses calibrated to a pulse power of 83.3 kHz, and with a saturation train of twenty 90°-pulses separated by a 20 ms delay. Each data point in Fig. 3.3a and Fig. 3.5 corresponds to a saturation recovery plot containing 10 to 20 time increments measured with microwave irradiation and with the signal intensity, $S_{\mathrm{on},i}(t)$, normalized with respect to the steady-state microwave off signal intensity,

$$S_{\mathrm{on},i}(t) = \varepsilon_{\infty,i} \cdot \left[1 - \exp\left(-t/T_{\mathrm{DNP},i}\right)\right]. \tag{3.13}$$

corresponding to mono-exponential polarization build up kinetics. The characteristic time $T_{\mathrm{DNP},i}$ is similar both with, $T_{\mathrm{DNP(on)},i}$, and without, $T_{\mathrm{DNP(off)},i}$, microwave irradiation (see experimental values in Table 3A1 in Appendix 3A1). To determine depolarization factors ($\theta_{\mathrm{depo}}$) for frozen 2 mM AMUPol solutions shown in Fig. 3.5, quantitative single-pulse $^1$H MAS NMR experiments were conducted at 12.5 kHz MAS and 100 K with background subtraction. The depolarization factor in the limit of dilute paramagnetic centers is given by,

$$\theta^{\mathrm{o}}_{\mathrm{depo},i} = \frac{S_{\mathrm{off},i}(\text{with AMUPol})}{S_{\mathrm{off},i}(\text{without AMUPol})}\ , \tag{3.14}$$

where $S_{\mathrm{off},i}$, the signal intensity in the absence of microwave irradiation, is compared with external frozen glycerol-water standards that do not contain biradical species.

Meanwhile, at high concentrations of paramagnetic centers, it is necessary to perform static experiments to assess the influence of depolarization effects from paramagnetic quenching effects.

By a similar procedure, solid suspensions were measured by using $^{13}$C-detected 1D $^{13}$C{$^{1}$H} CP-MAS saturation recovery experiments with a CP contact time of 2 ms at 9.4 T, 11.5 kHz MAS, and 100 K. The $^{13}$C-detected experiment is used to independently determine $\varepsilon_{\infty,M}$ and $\varepsilon_{\infty,S}$ values for glycerol and polystyrene, respectively, for the analyses in Fig. 7b. For dry polystyrene particles, a value of $T_{1,S}^{o}$ = 1.3 ±0.1 s was measured by 1D $^{13}$C{$^{1}$H} CP-MAS saturation recovery experiments in the absence of a DNP matrix. Similarly, characteristic $^{1}$H DNP build-up times for polystyrene, $T_{\mathrm{DNP},S}$, and glycerol, $T_{\mathrm{DNP},M}$, are measured by $^{13}$C{$^{1}$H} CP-MAS saturation recovery (see experimental values in Table 3A2 in Appendix 3A1).

**Analytical solutions**

The analytical solutions to Eq. 3.7 used to generate the dashed lines in Fig. 3.5b assume that the lumped-element approximation for the DNP source term, $\dot{Q}$, is valid and that direct hyperpolarization of the solid-particle by hyperfine interactions does not occur. Within the solid-target particle over $0 < r < R$, the spatial polarization profile is:

$$\tilde{P}_S(\tilde{r}) = 1 + \frac{(\tilde{P}_S|_{\tilde{r}=1} - 1)}{\tilde{r}} \frac{\sinh[\emptyset_S \tilde{r}]}{\sinh[\emptyset_S]} \tag{3.13}$$

and within the DNP matrix over $R < r < R+\Delta R_{\mathrm{eff}}$ is:

$$\tilde{P}_M(\tilde{r}) = \Xi_M - \Gamma_I \frac{\frac{1}{3}\mathrm{Da_P}\,\eta\left(\tilde{P}_S|_{\tilde{r}=1} - 1\right)}{\sinh[\emptyset_M^*] - \Gamma_{II}\cosh[\emptyset_M^*]} \cdot \left(\frac{\sinh[\emptyset_M^* \tilde{r}]}{\tilde{r}} - \Gamma_{II}\frac{\cosh[\emptyset_M^* \tilde{r}]}{\tilde{r}}\right) \tag{3.14}$$

where $\tilde{r} = r/R$, $\emptyset_S$ is the Thiele modulus of the solid particle, and $\Xi_M$ is $\varepsilon^{\circ}_{\infty,M}$ or $\theta^{\circ}_{\mathrm{depo},M}$ in the presence or absence of microwave irradiation determined from Eq. 3.5 or Eq. 3.6, respectively. Here, $\tilde{P}_S|_{\tilde{r}=1}$ corresponds to the surface polarization at the interface between the DNP matrix and solid-particle target,

$$\tilde{P}_S|_{\tilde{r}=1} = \frac{\Xi_M + \frac{\mathrm{Da_P}\eta}{3\Gamma_I}}{1 + \frac{\mathrm{Da_P}\eta}{3\Gamma_I}} \quad , \tag{3.15}$$

which demonstrates the utility of the Damköhler number, $\mathrm{Da_P}$, and effectiveness factor, $\eta$, in evaluating the efficacy of DNP matrix-mediated hyperpolarization transfer to an arbitrary solid-target. For evaluation of Eqs. 3.13, 3.14, and 3.15, the effective Thiele modulus for the DNP matrix ($\emptyset^*_M$) is:

$$\emptyset^*_M = \emptyset_S \sqrt{\frac{\mathcal{D}_{\mathrm{H},S} T^{\circ}_{1,S}}{\mathcal{D}_{\mathrm{H},M} T^{\circ}_{\mathrm{DNP},M}}} \tag{3.16}$$

and geometry specific integration constants $\Gamma_I$ and $\Gamma_{II}$ corresponding to spherical 1D radial symmetry and thermal-like boundary conditions are:

$$\Gamma_I = -\frac{\tanh[\emptyset^*_M] - \Gamma_{II}}{\emptyset^*_M + \Gamma_{II} - \tanh[\emptyset^*_M]\,(1 + \emptyset^*_M \Gamma_{II})} \quad , \tag{3.17}$$

$$\Gamma_{II} = \frac{(1 + \frac{\Delta R_{\mathrm{eff}}}{R})\emptyset^*_M - \tanh\left[(1 + \frac{\Delta R_{\mathrm{eff}}}{R})\emptyset^*_M\right]}{(1 + \frac{\Delta R_{\mathrm{eff}}}{R})\emptyset^*_M \tanh\left[(1 + \frac{\Delta R_{\mathrm{eff}}}{R})\emptyset^*_M\right] - 1} \quad , \tag{3.18}$$

where, in Eq. 3.16, $T^{\circ}_{1,S}$ and $T^{\circ}_{\mathrm{DNP},M}$ correspond to the spin-lattice relaxation time of the solid and characteristic build-up time of the DNP matrix respectively; these '°' properties correspond to the individual components, not those of a matrix-particle suspension. The volumetric mean of the spatial polarization levels within the solid-particle target is,

$$< \tilde{P}_S >= \eta\left(\tilde{P}_S|_{\tilde{r}=1} - 1\right) + 1 \quad , \tag{3.19}$$

which corresponds to the solid-enhancement, $\varepsilon_{\theta,S} \equiv < \tilde{P}_{S(\mathrm{on})} >$, or depolarization factor, $\theta_{\mathrm{depo},S} \equiv < \tilde{P}_{S(\mathrm{off})} >$, in the presence or absence of microwave irradiation respectively. Importantly, the commonly reported signal enhancement is given, $\varepsilon_{\infty,S} \approx \varepsilon_{\theta,S}/\theta_{\mathrm{depo},S}$, for dilute $\rho_{\mathrm{pc}}$ where paramagnetic quenching is negligible. The dashed-lines in Fig. 3.5b correspond to these $\varepsilon_{\infty,S}$ values evaluated as a function of solvent and for $\emptyset_S$ values ranging from 0 to 2 to illustrate the influence of an increasingly strong solid-particle polarization sink. These expressions are useful in conceptualizing hyperpolarization transfer in composite systems but have limited utility considering the importance of radical-surface interactions in most systems. Similar analytical solutions to Eq. 3.7 accounting for radical-surface interactions may be developed, however numerical solutions are preferable. Importantly, without invoking the polarization-transfer coefficient, $k_{\mathrm{DNP}}$, and effective polarization-level generated by cross-effect DNP, $\bar{P}_{\mathrm{CE}}$, description of polarization transfer processes in composite systems would likely be analytically intractable.

**Numerical simulations**

Numerical solutions to Eq. 3.7 corresponding to the solid-line plotted in Fig. 3.5b in the main text were obtained using the Matlab™ *pdepe* solver function assuming 1D spherical symmetry for the specified conditions similar to that described previously[24]. All hyperpolarization generation, propagation, and relaxation rates were estimated analytically by the lumped-element approximation. Assuming negligible agglomeration and that the frozen homogeneous DNP solvent is uniformly distributed among the 100-nm particles, a solvent-solid ratio of ~1.3

mg/μL corresponds to an effective solvent shell thickness of $\Delta R_{\text{eff}}$ ~12 nm for spherically smooth polystyrene particles.

## Appendix 3A1. Experimental data and calibration

Schematic pulse sequences and representative spectra used for the determination of characteristic times ($T_1/T_{\text{DNP}}$), the NMR signal enhancement ($\varepsilon_\infty$), and the depolarization factor ($\theta_{\text{depo}}$) are given in Figure 3A1. Characteristic times are measured by incrementing $\tau_1$ delays and measuring the recovery of NMR signal intensity following a train of saturation pulses. The NMR signal enhancement ($\varepsilon_\infty$) is the ratio of signal intensity between the microwave on and microwave off spectra. During the echo delay ($2\tau_2$ = 160 μs), broad $^1$H signal intensity from the probe background and strongly hyperfine-coupled nuclei are significantly broadened and partially dephased due to their relatively short $T_2$ relaxation times. Consequently $^1$H spin-echo experiments preferentially detect diamagnetic $^1$H species in the frozen solvent matrix. It is assumed for all calculations that $T_{\text{DNP}} \equiv T_{\text{DNP(on)}} \approx T_{\text{DNP(off)}}$, since these values are generally within 10% of each other as reported in Table 3A1; noting that $T_{\text{DNP(on)}}$ values are used for all analyses presented in the main text. Only at 2 mM AMUPol concentrations and high glycerol-water $^1$H spin densities, $\rho_{\text{H}} > 50$ M, are the $T_{\text{DNP(off)}}$ values appreciably longer. This may be attributed to microwave heating, a greater weighting of faster-relaxing hyperpolarized $^1$H species near paramagnetic centers, or due to a slightly differences in the apparent rate constant, $k_{\text{DNP}}$, in the presence or absence of microwave irradiation. Regardless, these quantities are of the same order of magnitude suggesting that polarization transfer across the spin-diffusion barrier is similarly impeded both in the presence and absence of microwave irradiation.

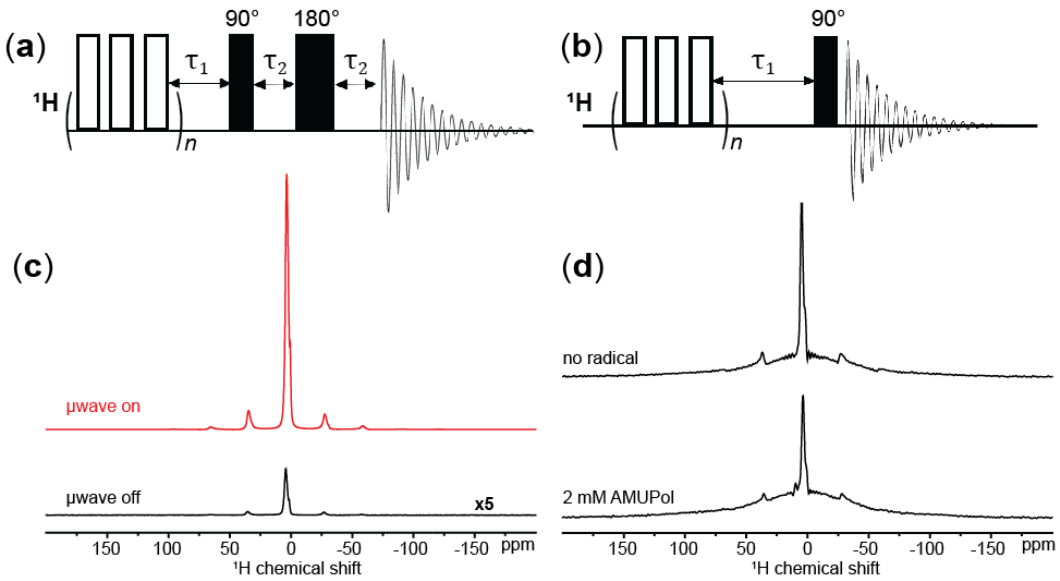


**FIGURE 3A1.** (a) Pulse sequence for spin-echo $^1$H saturation recovery experiment with $n$ = 20 saturation pulses, a fixed echo delay of $2\tau_2$ = 160 μs and a variable $\tau_1$ delay. (b) Pulse sequence for quantitative $^1$H single-pulse measurements with $n$ = 16 and a variable $\tau_1$ delay. (c) Spin-echo $^1$H spectra comparing μwave-on versus μwave-off signal intensity for 2 mM AMUPol in glycerol-water ($\rho_H$ = 3.5 M) at 9.4 T, 100 K, 12.5 kHz MAS. (d) Quantitative $^1$H signal intensity with and without 2 mM AMUPol in glycerol-water ($\rho_H$ = 3.5 M) at 9.4 T, 100 K, 12.5 kHz MAS.

**Table 3A1.** Experimental characteristic build-up times of frozen 2 mM and 12 mM AMUPol glycerol-water matrices as a function of $^1$H spin density with and without microwave irradiation.

| **2 mM AMUPol** | | | **12 mM AMUPol** | | |
|---|---|---|---|---|---|
| $\rho_H$ [M] | $T_{DNP,on}$ [s] | $T_{DNP,off}$ [s] | $\rho_H$ [M] | $T_{DNP,on}$[s] | $T_{DNP,off}$ [s] |
| 3.5 | 28.1 | 26.0 | 1.3 | 9.1 | 8.2 |
| 7.8 | 20.6 | 19.5 | 3.5 | 4.7 | 4.4 |
| 13 | 15.4 | 15.6 | 7.9 | 3.3 | 3.1 |
| 23 | 13.5 | 14.5 | 14 | 2.6 | 2.6 |
| 32 | 13.5 | 14.6 | 28 | 2.4 | 2.5 |
| 52 | 13.7 | 15.0 | 56 | 2.5 | 2.8 |
| 92 | 13.1 | 15.0 | 108 | 2.9 | 3.1 |

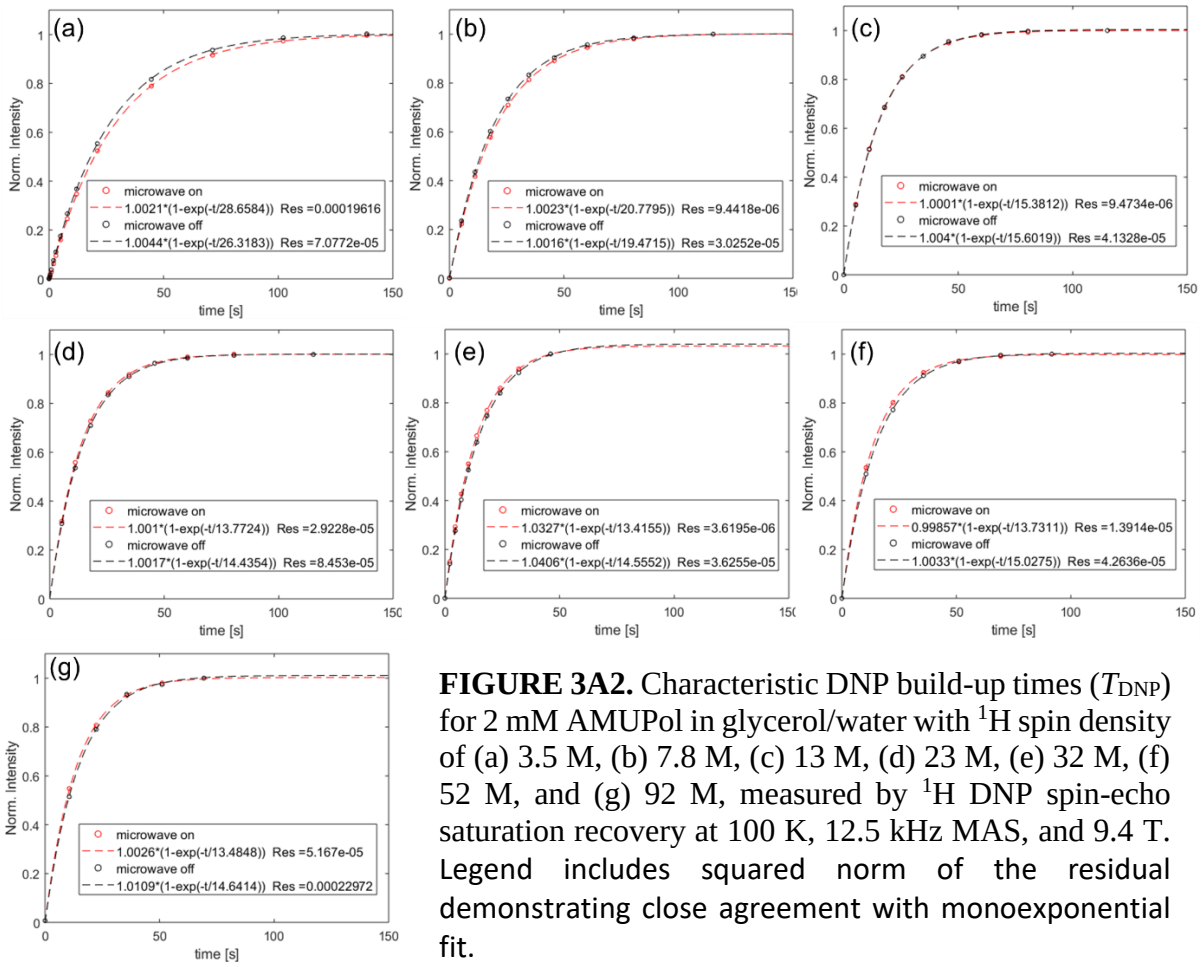


**FIGURE 3A2.** Characteristic DNP build-up times ($T_{DNP}$) for 2 mM AMUPol in glycerol/water with $^{1}$H spin density of (a) 3.5 M, (b) 7.8 M, (c) 13 M, (d) 23 M, (e) 32 M, (f) 52 M, and (g) 92 M, measured by $^{1}$H DNP spin-echo saturation recovery at 100 K, 12.5 kHz MAS, and 9.4 T. Legend includes squared norm of the residual demonstrating close agreement with monoexponential fit.

In the presence of paramagnetic centers, $^{1}$H signal intensity is partially "bleached" by paramagnetic quenching or MAS-induced depolarization, where the DNP contribution factor ($\theta_{DNP}$) is represented by the total fraction of remaining signal intensity, $\theta_{DNP} = \theta_{depo}\theta_{q}$, as determined from the experimental depolarization factor ($\theta_{depo}$) and quenching factor ($\theta_{q}$)[53]. For dilute biradical concentrations (*e.g.*, 2 mM AMUPol) it may be assumed that paramagnetic quenching is negligible, $\theta_{q} = 1$, as quenching arises due to strong paramagnetic interactions near paramagnetic centers[31]. In contrast, depolarization effects are relayed through the diamagnetic bulk by spin diffusion similarly to a DNP enhancement. In Figure 3A3, depolarization factors are measured as a function of $^{1}$H spin density by single-pulse $^{1}$H NMR

experiments. Although a linear calibration curve would be expected, the experimental curves are non-linear, Figure 3A3a, possibly due to dephasing by strong dipole interactions, r.f. inefficiencies, or a non-linear amplifier response. In Figure 3A3b, the depolarization factor as a function of $\rho_H$ is determined from Eq. 3.12 in Section 3.9 using the data in Figure 3A3a. The

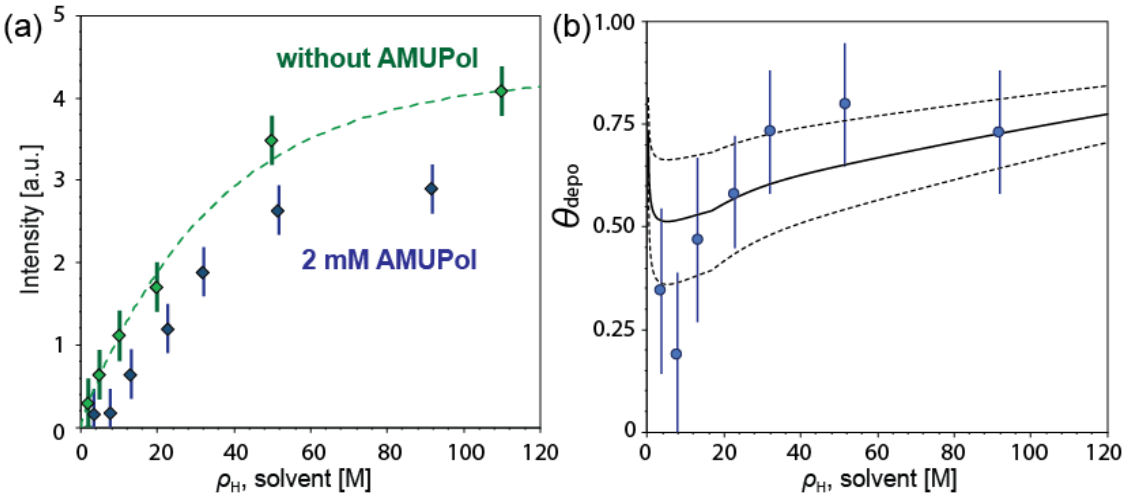


**FIGURE 3A3**. Quantitative single-pulse $^1$H MAS NMR measurements of glycerol-water solutions at 9.4 T, 100 K, 12.5 kHz MAS, including (a) $^1$H signal intensity with and without 2 mM AMUPol, and (b) DNP contribution factors ($\theta^0_{depo}$). larger error bars include different

observed $\rho_H$ dependence of the depolarization factor is consistent with quantum chemical simulations which have shown that nuclear depolarization decreases as solvent $T_1$ values decrease [23].

For polystyrene in AMUPol glycerol-water suspensions, overlapping $^1$H intensity prohibits the use of $^1$H spin-echo saturation recovery measurements to measure signal enhancements and build-up times. Instead, $^{13}$C-detected 1D $^{13}$C{$^1$H} CP-MAS saturation recovery experiments are used to measure enhancements $\varepsilon_{\infty,M}$ and $\varepsilon_{\infty,S}$ values, shown in Fig. 3.5b in Section 3.5. Similar to the enhancement values, characteristic build-up times are influenced by spin thermodynamic exchange between the dissimilar reservoirs. In Table 3A2,

experimental polarization build-up times for polystyrene, $T_{DNP,S}$, and the DNP matrix, $T_{DNP,M}$, are compared with the, typically, much longer $T^{o}_{DNP,M}$ values corresponding to the homogeneous DNP matrix. Thus, at lower matrix $\rho_{H,M}$, polarization build-up times within the polystyrene particle interior are only weakly influenced by solvent-mediated $^{1}$H spin diffusion. For such conditions, measured $T_{DNP,S}$ values are less than the $^{1}$H spin-lattice relaxation time, $T^{o}_{1,S}$ = 1.3 s, indicating that particle surfaces are directly polarized by hyperfine transfer from adsorbed biradicals as discussed in the main text. Meanwhile at higher matrix $\rho_{H,M}$, measured $T_{DNP,S}$ values increase as the Zeeman spin conductivity of the matrix, $\rho_{H,M}\mathcal{D}_{H,M}C_z$, increases. In general, DNP matrices with higher Zeeman spin conductivities (larger $\rho_{H,M}$) can more effectively relay hyperpolarization to a solid-particle sink. However, because DNP generation rates are limited by the spin-diffusion barrier, higher $\rho_{H,M}\mathcal{D}_{H,M}C_z$ may lead to diminished polarization levels as discussed for the homogeneous DNP matrix in the main text.

**Table 3A2:** Experimental characteristic build-up times $T_{DNP,M}$ and $T_{DNP,S}$ for a suspension of polystyrene in 2 mM AMUPol glycerol-water with different $^{1}$H densities.

| $\rho_{H,M}$ | 1.3 M | 4.0 M | 12.5 M | 25 M | 108 M |
|---|---|---|---|---|---|
| $^{\dagger}T^{o}_{DNP,M}$ [s] | 45.2 | 27.0 | 15.9 | 13.5 | 12.9 |
| $T_{DNP,M}$ [s] | 6.0 | 5.6 | 5.9 | 5.0 | 5.3 |
| $T_{DNP,S}$ [s] | 1.1 | 1.1 | 1.2 | 1.7 | 2.2 |

$^{\dagger}$ values extracted from the solid-line in Fig. 3.5 in Section 3.5

## Appendix 3A2. Applying the lumped-element approximation

For Eqs. 3.5, 3.6, and 3.7 in Section 3.3 it is assumed that a lumped-element approximation developed is valid. When spatial polarization gradients are negligible ($\nabla^2\tilde{P} = 0$), the bulk solvent matrix builds up uniformly to a single-polarization value for the hollow-sphere spanning from $\lambda_{sdb}<r<\lambda_{ws}$. Similar to lumped-parameter analyses in heat transfer processes,

the following equation satisfies the First Law of Thermodynamics under a lumped-parameter assumption:

$$\rho_{\mathrm{H}} C_{\mathrm{z}} \frac{\partial \tilde{P}}{\partial t} = \dot{Q} + \rho_{\mathrm{H}} C_{\mathrm{z}} \frac{(1-\tilde{P})}{T_1} \tag{3A1}$$

where the DNP source term per unit volume ($\dot{Q}$) is calculated by performing a surface integral of the polarization flux at the spin-diffusion barrier interface divided by the volume of bulk solvent:

$$\dot{Q} = \frac{1}{V} \cdot \iint (q_{\mathrm{H}} \cdot n) dS \quad , \tag{3A2}$$

where *n* is the unit normal vector, and the surface integral is performed at $r = \lambda_{\mathrm{sdb}}$, which leads to:

$$\dot{Q} = \rho_{\mathrm{H}} C_{\mathrm{z}} k_{\mathrm{DNP}} L^{-1} \Delta \tilde{P} \quad . \tag{3A3}$$

By substitution of Eq. 3A3 into Eq. 3A1, the following expressions are obtained describing polarization build-up with and without microwave irradiation:

$$\frac{\partial \tilde{P}}{\partial t} = \frac{\left(\frac{1 + k_{\mathrm{DNP}} L^{-1} \bar{P}_{\mathrm{CE(on)}} T_1}{1 + k_{\mathrm{DNP}} L^{-1} T_1} - \tilde{P}\right)}{T_1 / (1 + k_{\mathrm{DNP}} L^{-1} T_1)} \equiv \frac{(< \tilde{P}_{\mathrm{s.s.,on}} > - \tilde{P})}{T_{\mathrm{DNP,on}}} \tag{3A4}$$

$$\frac{\partial \tilde{P}}{\partial t} = \frac{\left(\frac{1 + k_{\mathrm{DNP}} L^{-1} \bar{P}_{\mathrm{CE(off)}} T_1}{1 + k_{\mathrm{DNP}} L^{-1} T_1} - \tilde{P}\right)}{T_1 / (1 + k_{\mathrm{DNP}} L^{-1} T_1)} \equiv \frac{\left(< \tilde{P}_{\mathrm{s.s.,off}} > - \tilde{P}\right)}{T_{\mathrm{DNP,off}}} \quad , \tag{3A5}$$

where $< \tilde{P}_{\mathrm{s.s.,on}} >$ and $< \tilde{P}_{\mathrm{s.s.,off}} >$ are the volume averaged steady-state polarization levels with and without microwave irradiation respectively in the bulk matrix ($\lambda_{\mathrm{sdb}} < r < \lambda_{\mathrm{ws}}$). These quantities, hereafter the absolute enhancement ($\varepsilon_{\theta}$) and depolarization factor ($\theta_{\mathrm{depo}}$), are directly proportional to the net magnetization and, in principle, the NMR signal intensity.

## Appendix 3A3. Error analysis for the lumped-element approximation

For high Biot number conditions, nuclear spin diffusion resistances in the bulk frozen glycerol-water matrix are expected to influence spatial polarization gradients, steady-state enhancements, and characteristic DNP build-up times. The lumped-parameter solution is no longer applicable as polarization-levels are diminished at distances progressively farther from the paramagnetic centers ($\nabla^2\tilde{P} \neq 0$). The steady-state spatial polarization-level, $\tilde{P}_{\text{s.s.}}(r)$, as a function of position, *r*, from the paramagnetic center may be solved for analytically. For an annular sphere spanning from $\lambda_{\text{sdb}}<r<\lambda_{\text{ws}}$, the steady-state general solution to Eq. 3.1 in Section 3.3 is given,

$$\tilde{P}_{\text{s.s.}}(r) = 1 + \frac{C_I}{r}\cdot\cosh[\alpha^{-1}\cdot r] + \frac{C_{II}}{r}\cdot\sinh[\alpha^{-1}\cdot r] \tag{3A6}$$

where $\alpha = \sqrt{\mathcal{D}_{\text{H}}T_1}$ and the boundary conditions are:

Boundary Condition #1: $\tilde{P}_{\text{s.s.}}|_{\lambda_{\text{sdb}}}$ at $r = \lambda_{\text{sdb}}$

Boundary Condition #2: $\frac{\partial\tilde{P}}{\partial r}|_{\lambda_{\text{ws}}} = 0$

assuming a homogeneous distribution of paramagnetic centers with a mean separation distance represented by twice the Wigner-Seitz radius, $2\lambda_{\text{ws}}$. Here α represents the characteristic diffusion length which is >100 nm for frozen glycerol-water solutions at 9.4 T, 100 K, and 12.5 kHz MAS. The integration constants $C_{\text{I}}$ and $C_{\text{II}}$ may be solved by application of the B.C.s to obtain:

$$C_I = \frac{\lambda_{\text{sdb}}(\tilde{P}_{\text{s.s.}}|_{\lambda_{\text{sdb}}} - 1)}{\cosh(\alpha^{-1}\lambda_{\text{sdb}}) - B_I\sinh(\alpha^{-1}\lambda_{\text{sdb}})} \tag{3A8}$$

$$C_{II} = -C_I B_I \tag{3A9}$$

$$B_I = \frac{\lambda_{ws}\alpha^{-1} \cdot \sinh(\lambda_{ws}\alpha^{-1}) - \cosh(\lambda_{ws}\alpha^{-1})}{\lambda_{ws}\alpha^{-1} \cdot \cosh(\lambda_{ws}\alpha^{-1}) - \sinh(\lambda_{ws}\alpha^{-1})} \tag{3A10}$$

where $\tilde{P}_{s.s.}|_{\lambda_{sdb}}$ is the steady-state nuclear polarization-level at the effective interface between hyperfine coupled $^1$H nuclei and the bulk. This quantity may be determined by recognizing that for conservation of energy the energy flux flowing into the frozen solvent matrix at $r = \lambda_{sdb}$, must equal the amount of energy being dissipated by spin-lattice relaxation over $\lambda_{sdb} < r < \lambda_{ws}$,

$$(q_H \cdot A)|_{\lambda_{sdb}} = \iiint \rho_H C_z \frac{\left(\tilde{P}_{s.s.}(r) - 1\right)}{T_1} \mathrm{dV} \tag{3A11}$$

with respect to the Zeeman energy flux ($q_H$) and interfacial area (A) which yields,

$$\tilde{P}_{s.s.}|_{\lambda_{sdb}} = \frac{\bar{P}_{CE} + \beta B_{II}/B_{III}}{1 + \beta B_{II}/B_{III}} \tag{3A12}$$

$$\begin{aligned} B_{II} = &-(\alpha^{-1}\lambda_{sdb} + B_I)\sinh(\alpha^{-1}\lambda_{sdb}) + (\alpha^{-1}\lambda_{sdb}B_I + 1)\cosh(\alpha^{-1}\lambda_{sdb}) \\ &+ (\lambda_{ws}\alpha^{-1} \\ &+ B_I)\sinh(\lambda_{ws}\alpha^{-1}) - (\lambda_{ws}\alpha^{-1}B_I + 1)\cosh(\lambda_{ws}\alpha^{-1}) \end{aligned} \tag{3A13}$$

$$B_{III} = \cosh(\alpha^{-1}\lambda_{sdb}) - B_I \sinh(\alpha^{-1}\lambda_{sdb}) \tag{3A14}$$

where $B_I$, $B_{II}$, and $B_{III}$ are geometry specific numerical constants. Importantly, $\beta$ naturally arises as the dimensionless scaling parameter,

$$\beta = \frac{\alpha^2 {T_1}^{-1}}{k_{\mathrm{DNP}} \lambda_{\mathrm{sdb}}} \tag{3A15}$$

that characterizes the ratio between the rate of energy dissipation in the bulk and the rate of energy transfer across a strong local magnetic field gradient (*e.g.*, the spin-diffusion barrier). This is analogous to the second Damköhler number ($Da_{II}$), which is commonly used in interphase mass transfer to describe the dissolution of particles. Here, it compares the rate of polarization transfer to the bulk relative to the rate of polarization dissipation in the bulk. By comparing the low and high Biot number solutions, it is demonstrated that the condition of Bi<0.65 is sufficient to justify the use of a lumped-element approximation for 1D spherically symmetric geometry; the same condition used in heat transfer analyses. Future work will address fast-relaxing reservoirs which can also influence the validity of lumped-element approximations. The error in the lumped-element calculation is determined as follows:

$$\%\mathrm{error} = \frac{|\tilde{P}_{\infty,\mathrm{analytical}}(\lambda_{\mathrm{sdb}}) - \tilde{P}_{\infty,\mathrm{lumped}}(\lambda_{\mathrm{sdb}})|}{\tilde{P}_{\infty,\mathrm{analytical}}(\lambda_{\mathrm{sdb}})} \times 100\% \tag{3A16}$$

where $\tilde{P}_{\infty,\mathrm{lumped}}(\lambda_{\mathrm{sdb}})$ is the solution developed in Appendix 3A2 above and $\tilde{P}_{\infty,\mathrm{analytical}}(\lambda_{\mathrm{sdb}})$ is the solution developed by Eqs. 3A6 – 3A15, the calculated error is presented in Figure 3A4 for a 2 mM AMUPol in glycerol-water matrix.

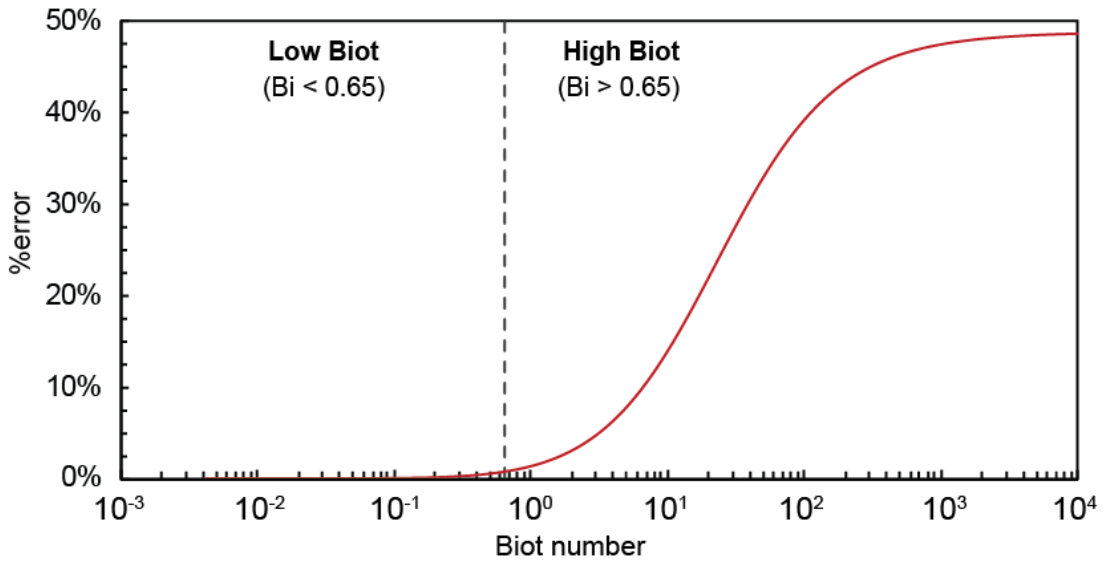


**Figure 3A4.** Calculated %error of the lumped-element approximation for a 2 mM AMUPol in glycerol-water matrix under the conditions described in the main text.

## Appendix 3A4. Derivation of the effectiveness factor ($\eta$)

For hyperpolarization transfer to a solid particle sink of radius *R* facilitated solely by DNP matrix mediated spin-diffusion, from Eq. 3.7 in Section 3.6, the internal dissipation of hyperpolarization over $0 < r < R$ is given,

$$\frac{\partial \tilde{P}_S}{\partial \tilde{t}} = \emptyset_S{}^{-2} \cdot \tilde{\nabla}^2 \tilde{P}_S - (\tilde{P}_S - 1) \tag{3A17}$$

Boundary Condition #1: $\lim_{\tilde{r}\to 0} \frac{\partial \tilde{P}_S}{\partial \tilde{r}} = 0$

Boundary Condition #2: $\tilde{P}_S|_{\tilde{r}=1}\ at\ \tilde{r} = 1$

where the Thiele modulus of the solid-particle, $\emptyset_S = R/\sqrt{\mathcal{D}_{\mathrm{H},S} T^{\mathrm{o}}_{1,S}}$ , is obtained using $\tilde{r} = r/R$ and $\tilde{t} = t/T^{\mathrm{o}}_{1,S}$ respectively. By application of the boundary conditions, the following

steady-state solution is obtained for $\tilde{P}_S(r)$, the spatial polarization profile within the particle interior,

$$\tilde{P}_S(\tilde{r}) = 1 + \frac{(\tilde{P}_S|_{\tilde{r}=1} - 1)}{\tilde{r}} \cdot \frac{\sinh[\emptyset_S \cdot \tilde{r}]}{\sinh[\emptyset_S]} \tag{3A18}$$

where the polarization at the particle surface, $\tilde{P}_S|_{\tilde{r}=1}$, is maintained by the rates of hyperpolarization generation and propagation in the DNP matrix. The effectiveness factor ($\eta$) is defined as the ratio between the energy dissipation rate throughout the solid-particle ($\bar{Q}_{\text{actual}}$) and the theoretical maximum energy dissipation rate ($\bar{Q}_{\text{max}}$) which would occur if the entire particle was polarized uniformly to the polarization-level at the particle surface,

$$\eta = \bar{Q}_{\text{actual}} \Big/ \bar{Q}_{\text{max}} \tag{3A19}$$

with Zeeman energy dissipation rates of,

$$\bar{Q}_{\text{max}} = \frac{4\pi R^3 \rho_{\text{H},S} C_{\text{z}}}{3T_{1,S}^{\text{o}}} \cdot (1 - \tilde{P}_S|_{\tilde{r}=1}) \tag{3A20}$$

$$\bar{Q}_{\text{actual}} = \frac{4\pi R^3 \rho_{\text{H},S} \text{C}_{\text{z}}}{3T_{1,S}^{\text{o}}} \cdot (1 - < \tilde{P}_S >) \tag{3A21}$$

with $< \tilde{P}_{S,\infty} >$ corresponding to the average steady-state polarization of the solid-particle interior. This is obtained by integration of the steady-state solution as follows,

$$< \tilde{P}_S >= 3 \int_0^1 \tilde{P}_S(\tilde{r}) \cdot \tilde{r}^2 \, d\tilde{r} \tag{3A22}$$

Evaluating this integral, and computing the effectiveness factor to obtain,

$$\eta = 3\emptyset_S{}^{-2} \cdot (\emptyset_S \cdot \coth[\emptyset_S] - 1) \tag{3A23}$$

Importantly $\eta$ provides a simple index to relate the polarization-level at the surface with the average polarization accrued through the particle interior. For DNP-NMR experiments, the

absolute polarization enhancement, $\varepsilon_{\theta,S}$, and depolarization factor, $\theta_{\mathrm{depo},S}$, are related to the surface polarization by,

$$\varepsilon_{\theta,S} = \eta(\tilde{P}_{S(\mathrm{on})}|_{\tilde{r}=1} - 1) + 1 \tag{3A24}$$

$$\theta_{\mathrm{depo},S} = \eta(\tilde{P}_{S(\mathrm{off})}|_{\tilde{r}=1} - 1) + 1 \tag{3A25}$$

in the presence and absence of microwave irradiation respectively. To explicitly determine $\tilde{P}_{S(\mathrm{on})}|_{\tilde{r}=1}$ and $\tilde{P}_{S(\mathrm{off})}|_{\tilde{r}=1}$ additional information is needed regarding the efficacy of hyperpolarization transfer to the particle surface.

## Appendix 3A5. Efficacy of hyperpolarization transfer to a particle surface and the Damköhler number

For hyperpolarization transfer to a spherical particle sink (*S*) of radius *R* coated with a DNP matrix (*M*) of thickness $\Delta R_{\mathrm{eff}}$, Eq. 3.9 in Section 3.7 corresponds to:

$$\rho_{\mathrm{H},M} C_{\mathrm{z}} \frac{\partial \tilde{P}_M}{\partial t} = \nabla\left(\rho_{\mathrm{H},M} C_{\mathrm{z}} \mathcal{D}_{\mathrm{H},M} \nabla \tilde{P}_M\right) - \rho_{\mathrm{H},M} C_{\mathrm{z}} \frac{(\tilde{P}_M - \Xi_M)}{T^o_{DNP,M}} \tag{3A26}$$

$$\rho_{\mathrm{H},S} C_{\mathrm{z}} \frac{\partial \tilde{P}_S}{\partial t} = \nabla\left(\rho_{\mathrm{H},S} C_{\mathrm{z}} \mathcal{D}_{\mathrm{H},S} \nabla \tilde{P}_S\right) - \rho_{\mathrm{H},S} C_{\mathrm{z}} \frac{(\tilde{P}_S - 1)}{T^o_{1,S}} \tag{3A27}$$

I.C.

$$\tilde{P}_M(r,0) = \tilde{P}_S(r,0) = 0$$

$$\Xi_M = \begin{bmatrix} \varepsilon^o_{\theta,M} \text{ ; microwave on} \\ \theta^o_{\mathrm{depo},M} \text{; microwave off} \end{bmatrix}$$

B.C. #1

$$\tilde{P}_M(R,t) = \tilde{P}_S(R,t)$$

B.C. #2

$$\rho_{\mathrm{H},M} \mathcal{D}_{\mathrm{H},M} \frac{\partial \tilde{P}_M}{\partial r}|_R = \rho_{\mathrm{H},S} \mathcal{D}_{\mathrm{H},S} \frac{\partial \tilde{P}_S}{\partial r}|_R$$

B.C. #3

$$\lim_{r\to 0}\frac{\partial \tilde{P}_S}{\partial r}=0$$

B.C. #4

$$\lim_{r\to(R+\Delta R_{\text{eff}})}\frac{\partial \tilde{P}_M}{\partial r}=0$$

assuming that hyperpolarization is solely delivered to the particle surface by DNP matrix-mediated spin diffusion. By nondimensionalizing of Eq. 3A26 using $\tilde{r}=r/R$ and $\tilde{t}=t/T_{1,S}^{o}$, respectively,

$$\frac{T_{\text{DNP},M}^{\text{o}}}{T_{1,S}^{\text{o}}}\cdot\frac{\partial \tilde{P}_M}{\partial \tilde{t}}=\emptyset_M^{*\,-2}\tilde{\nabla}^2\tilde{P}_M-\left(\tilde{P}_M-\Xi_M\right) \tag{3A28}$$

where a composite Thiele modulus for the DNP matrix ($\emptyset_M^*$) in a heterogeneous solvent-solid suspension may be represented as,

$$\emptyset_M^*=\emptyset_S\sqrt{\frac{\mathcal{D}_{\text{H},S}T_{1,S}^{\text{o}}}{\mathcal{D}_{\text{H},M}T_{\text{DNP},M}^{\text{o}}}} \tag{3A29}$$

which yields the following steady-state solution,

$$\tilde{P}_{M,\infty}(\tilde{r})=\Xi_M+\frac{C_{III}}{\tilde{r}}\cdot\cosh[\emptyset_M^*\cdot\tilde{r}]+\frac{C_{IV}}{\tilde{r}}\cdot\sinh[\emptyset_M^*\cdot\tilde{r}] \tag{3A30}$$

where the integration constants $C_{\text{III}}$ and $C_{\text{IV}}$ are most conveniently obtained by application of B.C.s #1 and #4. However, as was the case for Eq. 3A18, this yields the steady-state spatial polarization profile within the DNP matrix $\tilde{P}_{M,\infty}(\tilde{r})$ in terms of, $\tilde{P}_S|_{\tilde{r}=1}$, the unknown surface polarization. For conservation of energy, the rate of energy dissipation within the solid-

particle interior must be equal to the rate of energy flowing into the particle surface at steady-state imposing the condition,

$$4\pi R^2 \rho_{\mathrm{H},M} C_{\mathrm{z}} \mathcal{D}_{\mathrm{H},M} \frac{\partial \tilde{P}_M}{\partial r} = \bar{Q}_{\mathrm{actual}} \tag{3A31}$$

$$\bar{Q}_{\mathrm{actual}} \equiv \eta \bar{Q}_{\mathrm{max}} = -\frac{4\pi R^3 \rho_{\mathrm{H},S} C_{\mathrm{z}}}{3 T_{1,S}^{\mathrm{o}}} \cdot \eta (1 - \tilde{P}_S|_{\tilde{r}=1}) \tag{3A32}$$

where $\eta$ is the solid-particle effectiveness factor. By nondimensionalization Eq. 3A31 is then,

$$\frac{\partial \tilde{P}_M}{\partial \tilde{r}}|_{\tilde{r}\,=\,1} = \tfrac{1}{3}\mathrm{Da_P} \cdot \eta (\tilde{P}_S|_{\tilde{r}=1} - 1) \tag{3A33}$$

where the polarization analogue of the Damköhler number ($\mathrm{Da_P}$) for the frozen DNP solvent matrix is given,

$$\mathrm{Da_P} = \frac{R^2 {T_{1,S}^{\mathrm{o}}}^{-1}}{\mathcal{D}_{\mathrm{H},M}} \cdot \frac{\rho_{\mathrm{H},S}}{\rho_{\mathrm{H},M}} \tag{3A34}$$

which is the ratio between the rate of energy dissipation at the surface versus the rate of energy transfer to the surface by DNP matrix mediated spin-diffusion weighted with respect to the specific Zeeman heat capacity of each medium. From which it may be demonstrated that,

$$\tilde{P}_M(\tilde{r}) = \Xi_M - \Gamma_I \frac{\frac{1}{3}\mathrm{Da}\,\eta\left(\tilde{P}_S|_{\tilde{r}=1} - 1\right)}{\sinh[\emptyset_M^*] - \Gamma_{II}\cosh[\emptyset_M^*]} \cdot \left(\frac{\sinh[\emptyset_M^* \cdot \tilde{r}]}{\tilde{r}} - \Gamma_{II}\frac{\cosh[\emptyset_M^* \cdot \tilde{r}]}{\tilde{r}}\right) \tag{3A35}$$

$$\tilde{P}_S|_{\tilde{r}=1} = \frac{\Xi_M + \frac{\mathrm{Da_P}\eta}{3\Gamma_I}}{1 + \frac{\mathrm{Da_P}\eta}{3\Gamma_I}} \tag{3A36}$$

where $\Gamma_I$ and $\Gamma_{II}$ are geometry specific numerical constants,

$$\Gamma_I = -\frac{\tanh[\emptyset_M^*] - \Gamma_{II}}{\emptyset_M^* + \Gamma_{II} - \tanh[\emptyset_M^*] \cdot (1 + \emptyset_M^* \Gamma_{II})} \tag{3A37}$$

$$\Gamma_{II} = \frac{\zeta\emptyset_M^* - \tanh[\zeta\emptyset_M^*]}{\zeta\emptyset_M^* \cdot \tanh[\zeta\emptyset_M^*] - 1} \tag{3A38}$$

where $\zeta = 1+\Delta R_{\mathrm{eff}}/R$ corresponds to the $\tilde{r}$ boundary position of the DNP solvent matrix. From Eq. 3A36, the steady-state solid enhancement, $\varepsilon_{\theta,S} \equiv < \tilde{P}_{S(\mathrm{on})} >$, or depolarization factor, $\theta_{\mathrm{depo},S} \equiv < \tilde{P}_{S(\mathrm{off})} >$, is calculated,

$$< \tilde{P}_S >= 3 \int_0^1 \tilde{P}_S(\tilde{r}) \cdot \tilde{r}^2 d\tilde{r} \tag{3A39}$$

$$< \tilde{P}_S >= \eta \left( \frac{\Xi_M + \frac{\mathrm{Da_P}\,\eta}{3\Gamma_I}}{1 + \frac{\mathrm{Da_P}\,\eta}{3\Gamma_I}} - 1 \right) + 1 \tag{3A40}$$

importantly the measured NMR signal enhancement, $\varepsilon_{\infty,S} \equiv < \tilde{P}_{S(\mathrm{on})} > / < \tilde{P}_{S(\mathrm{off})} >$, may be obtained directly from Eq. 3A40. This analytical solution is used to generate the dotted lines in Fig. 3.7b in Section 3.7.

## Appendix 3A6. Comparison of lumped-element solution with previous *ab initio* predictions

As discussed in the main text, by invoking a DNP transfer coefficient the polarization build-up rates and gain may be quantitatively predicted from reported values of $k_{DNP}$ and $\bar{P}_{CE}$ as a function of sample composition or relaxation properties. In particular, previous quantum mechanical simulations have calculated the dependences of $T_1$ vs. $T_{DNP}$ and $T_1$ vs. $\varepsilon_\theta^o$ which may be directly compared to the predictions of Equation 3.5a and 3.6 in Section 3.3. The crosses correspond to simulated values extracted from reference[23] corresponding to a simulation of a "TOTAPol-like" isolated biradical. Although the description of the system does not specify a biradical concentration, the extracted $k_{DNP}L^{-1}$ value of 0.137 $s^{-1}$ is bounded between those measured in the present study, see Figure 3A5a. From the data in the main text $k_{DNP}L^{-1}$ values range from 0.03 – 0.06 $s^{-1}$ and 0.10 – 0.40 $s^{-1}$ measured for 2 mM or 12 mM AMUPol glycerol-water solutions at varying deuteration levels, respectively. This indicates that the simulation predicts polarization build-up rates that agree with values expected for commonly used DNP matrix formulations. Also from the simulation, by fixing $k_{DNP}L^{-1}$ constant, the effective polarization-level of core nuclei under microwave irradiation, $\bar{P}_{CE(on)}$, may be obtained as demonstrated in Figure 3A5b. Again, the simulated value is in agreement with the value of $\bar{P}_{CE(on)}$ = 148 ±14 measured for 2 mM AMUPol solutions. Although the depolarization factor was not measured for 12 mM AMUPol solutions in this work, using the data provided in Fig. 2b of reference[54] and the enhancement factors reported in Table 3A3 below, a value of $\bar{P}_{CE(on)}$ = 75 ±5 is estimated for 12 mM AMUPol. Therefore it may be concluded that the $\bar{P}_{CE(on)}$ value associated with the simulated data is a realistic estimate

bounded by the conditions used in the present study. The *ab initio* simulation accurately describes cross-effect events, which might be expected to generate a nuclear polarization as high as 658. Within the context of the film-transfer model, this is not the maximum predicted enhancement that can be physically delivered to bulk nuclei. It appears that the simulation predicts a similar limit to the maximum polarization level which can be delivered to the bulk. Specifically, $\bar{P}_{\mathrm{CE(on)}}$ corresponds to the limit of the curve in Figure 3A5b. as the bulk $T_1$ value approaches infinity. From the present work it is unclear why this value is less than 658, however this may be explained by electron relaxation effects as discussed in the main text.

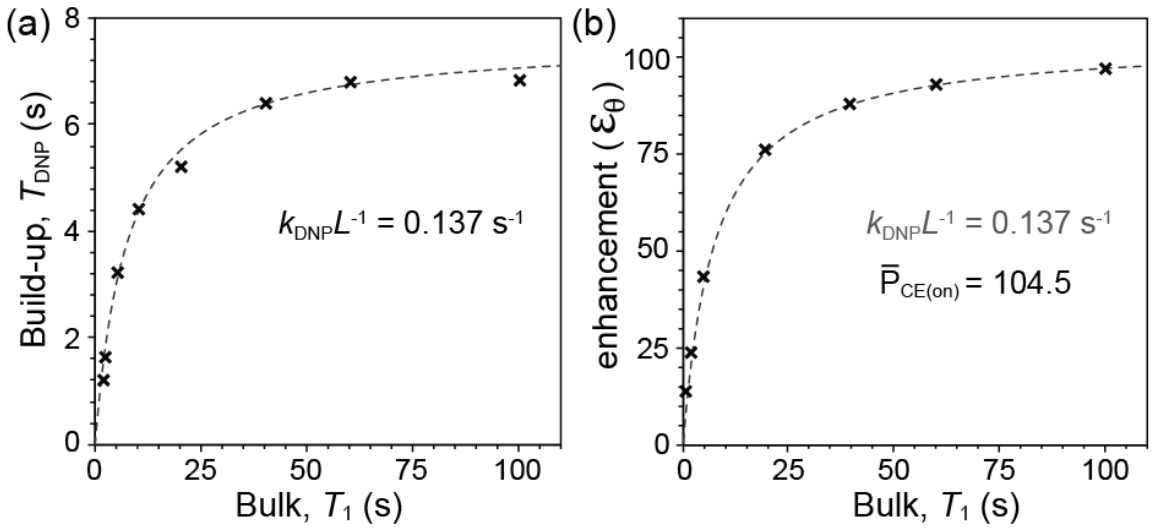


**FIGURE 3A5**. Comparison of lumped-element solution with previous *ab initio* predictions with data for (a) $T_1$ vs. $T_{DNP}$ and (b) $T_1$ vs. $\varepsilon_\theta^0$ extracted from Fig. 9 in reference[23].

| **Table 3A3:** Experimental $\varepsilon_\infty$ values and calculated $\bar{P}_{\mathrm{CE(on)}}$ values of frozen 12 mM AMUPol glycerol-water matrices as a function of $^1$H spin density | | | | | | | |
|---|---|---|---|---|---|---|---|
| $\rho_{\mathrm{H},M}$ | 1.3 M | 3.5 M | 7.9 M | 14 M | 28 M | 56 M | 108 M |
| $\varepsilon_\infty$ | 247 | 265 | 254 | 243 | 213 | 184 | 176 |
| $^{\dagger}\bar{P}_{\mathrm{CE(on)}}$ | 80 | 81 | 78 | 76 | 71 | 67 | 75 |

*Value of $\bar{P}_{\mathrm{CE(off)}} = 0.28$ is calculated using $\theta^{o}_{\mathrm{depo}}$= 0.305 (10 kHz MAS) from Fig. 2b in reference[54] and from Eq. 3.7 in Section 3.3 with $T_1^o$ = 79 s and $k_{\mathrm{DNP}}L^{-1}$ = 0.38 $s^{-1}$ corresponding to 12 mM AMUPol in glycerol-water ($\rho_{\mathrm{H}}$ = 14 M).
†Values of $\bar{P}_{\mathrm{CE(on)}}$=75 ±5 calculated from Eq. 3.7 in Section 3.3 and averaged for values in Table 3A3.

## Appendix 3A7. Calculation of DNP injections rates in units of Watts

For 2 mM AMUPol in glycerol/water the DNP injection rate in units of W/biradical may be straightforwardly calculated from the reported $k_{\mathrm{DNP}}$ and $\bar{P}_{\mathrm{CE}}$ values. At steady-state, the energy being dissipated by $T_1$ relaxation processes must exactly match that being delivered into the bulk across the spin-diffusion barrier. The rate of energy dissipation by $T_1$ relaxation processes is,

$$Q_{\mathrm{con}} = -\int_{\lambda_{\mathrm{sdb}}}^{\lambda_{\mathrm{ws}}} \rho_{\mathrm{H}} C_{\mathrm{z}} \cdot \frac{\tilde{P}(r) - 1}{T_1} 4\pi r^2 dr \tag{3A41}$$

which for low Biot conditions is simply,

$$Q_{\mathrm{con}} = -\frac{4\pi}{3}({\lambda_{\mathrm{ws}}}^3 - {\lambda_{\mathrm{sdb}}}^3)\rho_{\mathrm{H}} C_{\mathrm{z}} \cdot \frac{\varepsilon_\theta - 1}{T_1} \tag{3A42}$$

under conditions of microwave irradiation. By comparison the rate of hyperpolarization transfer to bulk nuclei is represented by,

$$Q_{\mathrm{gen}} = 4\pi {\lambda_{\mathrm{sdb}}}^2 \cdot \rho_{\mathrm{H}} C_{\mathrm{z}} k_{\mathrm{DNP}} (\bar{P}_{\mathrm{CE(on)}} - \varepsilon_\theta) \tag{3A43}$$

and these expressions may be evaluated using reported $\bar{P}_{\mathrm{CE(on)}}$, $k_{\mathrm{DNP}}$, and $T_1$ values Section 3.4 and 3.5. Equation 3A42 and 3A43 are evaluated and compiled for 2 mM AMUPol in glycerol/water in Table 3A4 below. The measured hyperpolarization rates are only tabulated for $^1$H nuclei in the bulk spanning $\lambda_{sdb} < r < \lambda_{ws}$. The present analyses do not allow for the accounting of energy dissipation occurring among core $^1$H nuclei, spectator nuclei (e.g., $^2$H, $^{13}$C), or energy which is transferred to reservoirs other than that of the Zeeman Hamiltonian. The DNP injection rate (W) in plotted in Figure 3A6a,b normalized with respect to the number of biradical molecules and the number of bulk $^1$H nuclei respectively.

**Table 3A4.** Calculation of DNP injection and dissipation rates by Equation S42 and S43 for 2 mM AMUPol in glycerol-water at 100 K, 12.5 kHz MAS, and 9.4 T.

| $\rho_H$ [M] | $T_1$ [s] | $k_{DNP}$ [nm/s] | $\varepsilon_\theta$ | $Q_{con}$ [W/biradical | $Q_{gen}$ [W/biradical] |
|---|---|---|---|---|---|
| 3.5 | 180 | 0.59 | 125 | $-4.93\cdot10^{-23}$ | $+4.93\cdot10^{-23}$ |
| 7.8 | 123 | 0.80 | 123 | $-1.59\cdot10^{-22}$ | $+1.59\cdot10^{-22}$ |
| 13 | 83 | 1.05 | 121 | $-3.86\cdot10^{-22}$ | $+3.86\cdot10^{-22}$ |
| 23 | 53 | 1.09 | 111 | $-9.60\cdot10^{-22}$ | $+9.60\cdot10^{-22}$ |
| 32 | 42 | 1.00 | 101 | $-1.50\cdot10^{-21}$ | $+1.50\cdot10^{-21}$ |
| 52 | 34 | 0.86 | 89 | $-2.74\cdot10^{-21}$ | $+2.74\cdot10^{-21}$ |
| 92 | 25 | 0.71 | 70 | $-5.25\cdot10^{-21}$ | $+5.25\cdot10^{-21}$ |

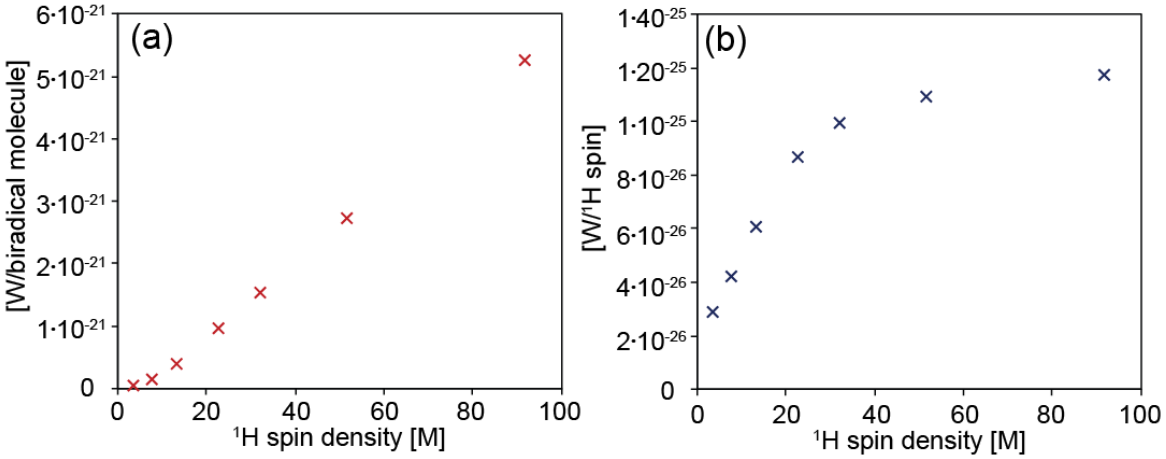


**Figure 3A6.** DNP injection rates (W) normalized with respect to (a) the number of biradical molecules, or (b) the number of bulk $^{1}$H nuclei, respectively. Measured for 2 mM AMUPol in glycerol-water at 9.4 T, 100 K, and 12.5 kHz MAS by $^{1}$H spin-echo DNP saturation recovery and calculated from data in Table 3A3.

## References


1 W. G. Whitman and J. L. Keats, *Ind. Eng. Chem.*, 1922, **14**, 186–191.
2 E. M. Purcell, *Am. J. Phys.*, 1977, **45**, 3–11.
3 S. J. Nelson, J. Kurhanewicz, D. B. Vigneron, P. E. Z. Larson, A. L. Harzstark, M. Ferrone, M. van Criekinge, J. W. Chang, R. Bok, I. Park, G. Reed, L. Carvajal, E. J. Small, P. Munster, V. K. Weinberg, J. H. Ardenkjaer-Larsen, A. P. Chen, R. E. Hurd, L.-I. Odegardstuen, F. J. Robb, J. Tropp and J. A. Murray, *Sci. Transl. Med.*, 2013, **5**, 198ra108.
4 Y. Lee, G. S. Heo, H. Zeng, K. L. Wooley and C. Hilty, *J. Am. Chem. Soc.*, 2013, **135**, 4636–4639.
5 T. Theis, G. X. Ortiz, A. W. J. Logan, K. E. Claytor, Y. Feng, W. P. Huhn, V. Blum, S. J. Malcolmson, E. Y. Chekmenev, Q. Wang and W. S. Warren, *Sci. Adv.*, 2016, **2**, 1–8.
6 M. Cavaillès, A. Bornet, X. Jaurand, B. Vuichoud, D. Baudouin, M. Baudin, L. Veyre, G. Bodenhausen, J. N. Dumez, S. Jannin, C. Copéret and C. Thieuleux, *Angew. Chemie - Int. Ed.*, 2018, **57**, 7453–7457.
7 P. R. Zangara, J. Henshaw, D. Pagliero, A. Ajoy, J. A. Reimer, A. Pines and C. A. Meriles, *Nano Lett.*, 2019, **19**, 2389–2396.
8 Y. Shiomi, J. Lustikova, S. Watanabe, D. Hirobe, S. Takahashi and E. Saitoh, *Nat. Phys.*, 2019, **15**, 22–26.
9 G. Kurizki, P. Bertet, Y. Kubo, K. Mølmer, D. Petrosyan, P. Rabl and J. Schmiedmayer, *Proc. Natl. Acad. Sci. U. S. A.*, 2015, **112**, 3866–3873.
10 V. Ranjan, G. de Lange, R. Schutjens, T. Debelhoir, J. P. Groen, D. Szombati, D. J. Thoen, T. M. Klapwijk, R. Hanson and L. Dicarlo, *Phys. Rev. Lett.*, 2013, **110**, 067004.
11 D. A. Gangloff, G. Éthier-Majcher, C. Lang, E. V. Denning, J. H. Bodey, D. M. Jackson, E. Clarke, M. Hugues, C. Le Gall and M. Atatüre, *Science (80-. ).*, 2019, **364**, 62–66.
12 A. S. Lilly Thankamony, J. J. Wittmann, M. Kaushik and B. Corzilius, *Prog. Nucl. Magn. Reson. Spectrosc.*, 2017, **102**–**103**, 120–195.
13 A. Karabanov, D. Wiśniewski, I. Lesanovsky and W. Köckenberger, *Phys. Rev. Lett.*, 2015, **115**, 1–5.
14 G. Sharma, T. Gaebel, E. Rej, D. J. Reilly, S. E. Economou and E. Barnes, *Phys. Rev. B*, 2019, **205423**, 1–12.
15 K. O. Tan, M. Mardini, C. Yang, J. H. Ardenkjær-Larsen and R. G. Griffin, *Sci. Adv.*, 2019, **5**, eaax2743.
16 C. Ramanathan, *Appl. Magn. Reson.*, 2008, **34**, 409–421.
17 J. J. Wittmann, M. Eckardt, W. Harneit and B. Corzilius, *Phys. Chem. Chem. Phys.*, 2018, **20**, 11418–11429.
18 F. A. Perras, M. Raju, S. L. Carnahan, A. C. T. Van Duin, A. J. Rossini and M. Pruski, *J. Phys. Chem. Lett.*, 2020, **11**, 5655–5660.
19 K. R. Thurber and R. Tycko, *J. Chem. Phys.*, 2012, **137**, 084508.
20 F. Mentink-Vigier, *Phys. Chem. Chem. Phys.*, 2020, **22**, 3643–3652.

21 K. L. Ivanov, A. N. Pravdivtsev, A. V. Yurkovskaya, H. M. Vieth and R. Kaptein, *Prog. Nucl. Magn. Reson. Spectrosc.*, 2014, **81**, 1–36.
22 F. A. Perras and M. Pruski, *J. Chem. Phys.*, , DOI:10.1063/1.5042651.
23 F. Mentink-Vigier, S. Vega and G. De Paëpe, *Phys. Chem. Chem. Phys.*, 2017, **19**, 3506–3522.
24 A. Pinon, J. Schlagnitweit, P. Berruyer, A. Rossini, M. Lelli, E. Socie, M. Tang, T. Pham, A. Lesage and L. Emsley, *J. Phys. Chem. C*, 2017, **121**, 15993–16005.
25 A. A. Smith, B. Corzilius, A. B. Barnes, T. Maly and R. G. Griffin, *J. Chem. Phys.*, 2012, **136**, 015101.
26 B. Corzilius, A. A. Smith and R. G. Griffin, *J. Chem. Phys.*, 2012, **137**, 0–12.
27 A. Leavesley, S. K. Jain, I. Kaminker, H. Zhang, S. Rajca, A. Rajca and S. Han, *Phys. Chem. Chem. Phys.*, 2018, **20**, 27646.
28 A. Z. Genack and A. G. Redfield, *Phys. Rev. Lett.*, 1973, **31**, 1204–1207.
29 N. Bloembergen, *Physica*, 1949, **15**, 386–426.
30 A. Abragam, *The Principles of Nuclear Magnetism*, Oxford University Press, 1961.
31 P. G. de Gennes, *J. Phys. Chem. Solids*, 1958, **7**, 345–350.
32 A. E. Dementyev, D. G. Cory and C. Ramanathan, *Phys. Rev. B - Condens. Matter Mater. Phys.*, 2008, **77**, 1–5.
33 Khutsishvilli, *Usp. Fiz. Nauk*, 1965, **87**, 211–254.
34 Q. Chen and K. Schmidt-Rohr, *Solid State Nucl. Magn. Reson.*, 2006, **29**, 142–152.
35 B. J. Walder, N. A. Prisco, F. M. Paruzzo, J. R. Yarava, B. F. Chmelka and L. Emsley, *J. Phys. Chem. Lett.*, 2019, **10**, 5064–5069.
36 A. C. Pinon, Lausanne, EPFL, 2018.
37 M. E. Halse, A. Zagdoun, J. N. Dumez and L. Emsley, *J. Magn. Reson.*, 2015, **254**, 48–55.
38 A. C. Pinon, École polytechnique fédérale de Lausanne, 2018.
39 A. A. Lee, C. S. Perez-Martinez, A. M. Smith and S. Perkin, *Phys. Rev. Lett.*, 2017, **119**, 1–5.
40 G. R. Khutsishvilli, *Sov. Phys. JETP-USSR*, 1957, **4**, 382–384.
41 M. Goldman, *Phys. Rev.*, 1965, **138**, 1675–1681.
42 C. Sauvée, M. Rosay, G. Casano, F. Aussenac, R. T. Weber, O. Ouari and P. Tordo, *Angew. Chemie - Int. Ed.*, 2013, **52**, 10858–10861.
43 D. J. Kubicki, G. Casano, M. Schwarzwälder, S. Abel, C. Sauvée, K. Ganesan, M. Yulikov, A. J. Rossini, G. Jeschke, C. Copéret, A. Lesage, P. Tordo, O. Ouari and L. Emsley, *Chem. Sci.*, 2016, **7**, 550–558.
44 D. Mance, P. Gast, M. Huber, M. Baldus and K. L. Ivanov, *J. Chem. Phys.*, 2015, **142**, 234201.
45 D. J. Kubicki, A. J. Rossini, A. Purea, A. Zagdoun, O. Ouari, P. Tordo, F. Engelke, A. Lesage and L. Emsley, *J. Am. Chem. Soc.*, 2014, **136**, 15711–15718.
46 W. G. Whitman, *Int. J. Heat Mass Transf.*, 1962, **5**, 429–433.
47 W. Nernst, *Zeit. Phys. Chem.*, 1904, **47**, 52–55.
48 P. V. Danckwerts, *Chem. Eng. Sci.*, 1953, **2**, 1–13.
49 D. Peaceman, 1951.
50 H. S. Carslaw and J. C. Jaeger, *Conduction of Heat in Solids*, Oxford Science Publications, 2nd edn., 1959.

51 D. W. van Krevelen and P. J. Hoftijzer, *Recl. des Trav. Chim. des Pays-Bas*, 1948, **67**, 563–586.
52 T. Sugishita, Y. Matsuki and T. Fujiwara, *Solid State Nucl. Magn. Reson.*, 2019, **99**, 20–26.
53 A. J. Rossini, A. Zagdoun, M. Lelli, D. Gajan, F. Rascón, M. Rosay, W. E. Maas, C. Copéret, A. Lesage and L. Emsley, *Chem. Sci.*, 2012, **3**, 108–115.
54 F. Mentink-Vigier, S. Paul, D. Lee, A. Feintuch, S. Hediger, S. Vega and G. De Paepe, *Phys. Chem. Chem. Phys.*, 2015.
55 K. R. Thurber and R. Tycko, *J. Chem. Phys.*, , DOI:10.1063/1.4874341.
56 K. K. Frederick, V. K. Michaelis, M. A. Caporini, L. B. Andreas, G. T. Debelouchina, R. G. Griffin and S. Lindquist, *Proc. Natl. Acad. Sci. U. S. A.*, 2017, **114**, 3642–3647.
57 A. Zagdoun, G. Casano, O. Ouari, M. Schwarzwälder, A. J. Rossini, F. Aussenac, M. Yulikov, G. Jeschke, C. Copéret, A. Lesage, P. Tordo and L. Emsley, *J. Am. Chem. Soc.*, 2013, **135**, 12790–12797.
58 B. Corzilius, L. B. Andreas, A. A. Smith, Q. Z. Ni and R. G. Griffin, *J. Magn. Reson.*, 2014, **240**, 113–123.
59 S. Lange, A. H. Linden, Ü. Akbey, W. Trent Franks, N. M. Loening, B. J. Van Rossum and H. Oschkinat, *J. Magn. Reson.*, 2012, **216**, 209–212.
60 A. J. Rossini, A. Zagdoun, F. Hegner, M. Schwarzwälder, D. Gajan, C. Copéret, A. Lesage and L. Emsley, *J. Am. Chem. Soc.*, 2012, **134**, 16899–16908.
61 J. Schlagnitweit, M. Tang, M. Baias, S. Richardson, S. Schantz and L. Emsley, *J. Am. Chem. Soc.*, 2015, **137**, 12482–12485.
62 J. K. Nørskov, T. Bligaard, B. Hvolbæk, F. Abild-Pedersen, I. Chorkendorff and C. H. Christensen, *Chem. Soc. Rev.*, 2008, **37**, 2163–2171.
63 F. Mentink-Vigier, Ü. Akbey, H. Oschkinat, S. Vega and A. Feintuch, *J. Magn. Reson.*, 2015, **258**, 102–120.
64 F. A. Perras, R. R. Reinig, I. I. Slowing, A. D. Sadow and M. Pruski, *Phys. Chem. Chem. Phys.*, 2016, **18**, 65–69.
65 J. Clauss, K. Schmidt-Rohr and H. W. Spiess, *Acta Polym.*, 1993, **44**, 1–17.
66 F. A. Perras, L. L. Wang, J. S. Manzano, U. Chaudhary, N. N. Opembe, D. D. Johnson, I. I. Slowing and M. Pruski, *Curr. Opin. Colloid Interface Sci.*, 2018, **33**, 9–18.
67 J. O. Tenorio-Pearl, E. D. Herbschleb, S. Fleming, C. Creatore, S. Oda, W. I. Milne and A. W. Chin, *Nat. Mater.*, 2017, **16**, 208–213.
68 P. G. de Gennes and P. A. Pincus, *Phys. Rev.*, , DOI:10.1103/PhysRev.135.A1616.
69 C. K. A. Mewes, *Nat. Phys.*, 2019, **15**, 8–9.
70 C. Lin, E. Laborda, C. Batchelor-Mcauley and R. G. Compton, *Phys. Chem. Chem. Phys.*, 2016, **18**, 9829–9837.

**Chapter IV.**

# Measurement of Proton Spin Diffusivity in Hydrated Cementitious Solids

B.J. Walder; N.A. Prisco; F.M. Paruzzo; J.R. Yarava; B.F. Chmelka; L. Emsley; To be submitted to *J. Phys. Chem. Lett*, **2019**, 10 (17), pp 5064 - 5069.

Adapted with permission from Walder, et al., J. Phys. Chem. Lett., **2019**, 10(17), pp 5064.

## 4.1. Abstract

The study of hydration and crystallization processes involving inorganic oxides is often complicated by poor long-range order and the formation of heterogeneous domains or surface layers. In solid-state NMR, $^{1}$H-$^{1}$H spin diffusion analyses can provide information on spatial composition distributions, domain sizes, or miscibility in both ordered and disordered solids. Such analyses have been implemented in organic solids, but crucially rely on separate measurements of the $^{1}$H spin diffusion coefficients in closely related systems. In this Chapter, an experimental NMR method is presented, in which "holes" of well-defined dimensions are created in proton magnetization. Model solutions can be applied to determine spin diffusion coefficients in cementitious solids hydrated with $^{17}$O enriched water. We determine proton spin diffusion coefficients of 240 ± 40 nm$^2$/s for hydrated tricalcium aluminate and 140 ± 20 nm$^2$/s for hydrated tricalcium silicate under quasi-static conditions.

## 4.2. Introduction

Solid-state NMR can often resolve different components of a mixture and is a method of choice for characterizing complex domains on the nanoscale.[1-2] Conventional examples include characterization of domain sizes in heterogeneous and semi-crystalline polymers and spatial composition distributions in lipid membranes.[3-5] Recent advances involving the relay of nuclear hyperpolarization through interfaces,[6-7] as generated by dynamic nuclear polarization[8-10] are proving particularly effective in this regard. In such experiments, proton hyperpolarization in one phase sets up large magnetization gradients at interfaces with a second phase of interest. As hyperpolarization builds up outside the second phase, efficient proton spin diffusion spontaneously and simultaneously transports magnetization into it. Magnetization gradients large enough to permit domain size analysis can also be established by domain selective enhancement of relaxation by doping with paramagnetic species[11] or by selective saturation.[3, 12-14]

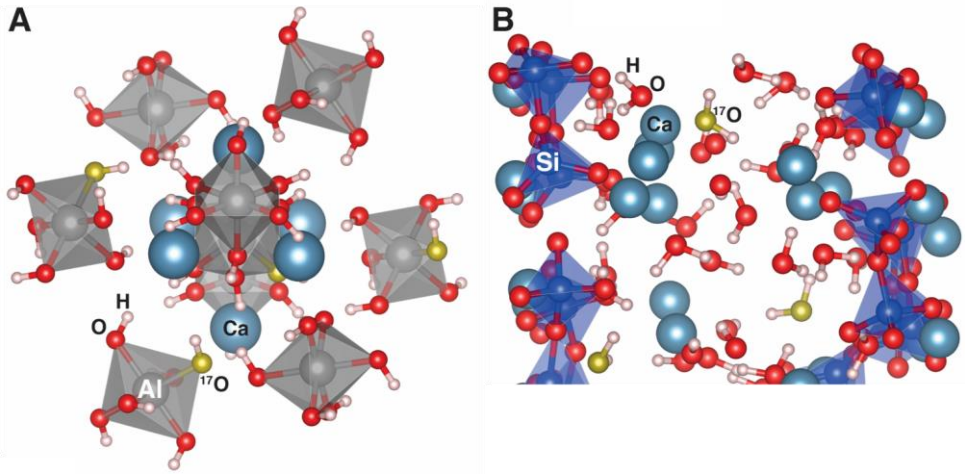


**FIGURE 4.1)** Schematic structures of hydrated tricalcium aluminate (A) and hydrated tricalcium silicate (B). By using water isotopically enriched in $^{17}O$ (golden atoms), spin labels are introduced that permit controllable burning of holes in the $^{1}H$ magnetization density.

Such domain size analyses rely on knowledge of proton spin diffusion coefficients, $D_H$, which are usually estimated based upon proton density or chemical similarity in the rigid limit. In more complex systems (*e.g.*, calcium silicate or aluminate hydrates), structural disorder, chemical heterogeneity, or molecular mobility of intralayer water may influence $D_H$ values. An experimental determination of proton spin diffusion coefficients usually depends on prior knowledge of the length scale of initial magnetization gradients, $L$, as the NMR observables are functions not of $D_H$ alone, but rather the characteristic diffusion time $L^2/D_H$. In many cases, $L$ is governed by the sizes of the domains being studied and is thereby connected to the unknown parameters of prior interest. In most systems, domain sizes cannot be reliably controlled, which prevents direct measurement of spin diffusion coefficients.

Here we show this paradox can be overcome for silicates with an NMR experiment that burns "holes" of well-defined size in proton magnetization,[15, 19] thus establishing $L$ regardless of any particular chemical character of the hydrated phase. The experiment we develop here is based upon the method introduced by Chen and Schmidt-Rohr,[15] which utilizes spin-pair dephasing in order to burn approximately spherical holes in the proton magnetization. The holes can exceed 1 nm in diameter, and subsequent hole filling by spin diffusion could be monitored through the same nucleus (in their case, $^{13}C$) used to burn the hole, provided a proton was bonded to it. In adapting their approach to cementitious solids, specifically tricalcium aluminate ($Ca_3Al_2O_6$) and tricalcium silicate ($Ca_3SiO_5$) after hydration, we chose to use $^{17}O$ nuclei (as shown in Figure 4.1) for hole burning, due to ease of incorporation using $^{17}O$-enriched water and because hydrogen bonds to oxygen. These structural characteristics are illustrated in Figure 4.1.

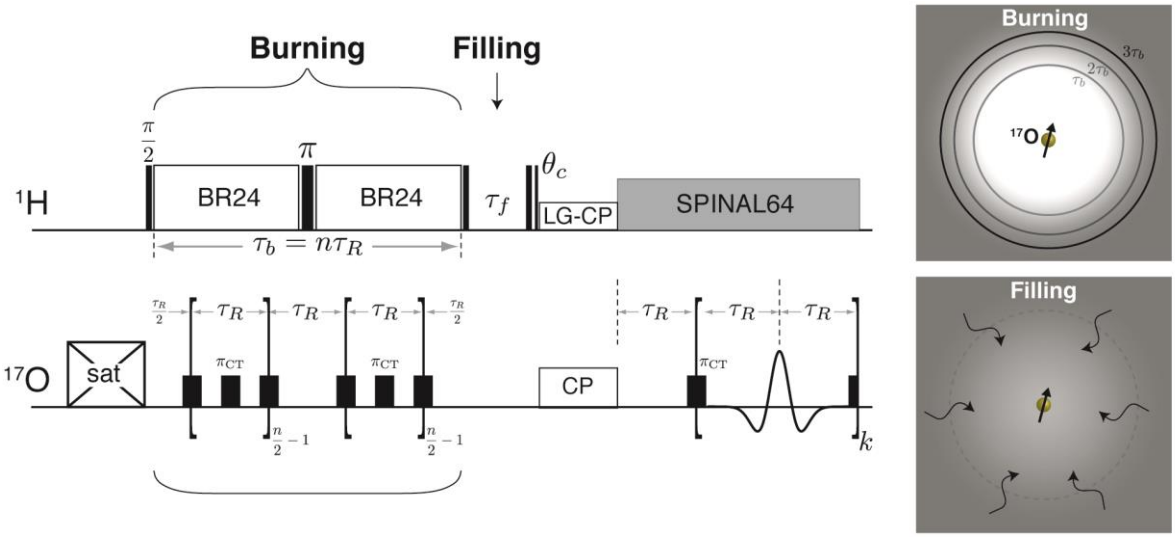


**FIGURE 4.2)** Hole-burning pulse sequence used for measuring proton spin diffusion coefficients in cementitious solids, based on the pulse sequence introduced by Chen and Schmidt-Rohr.[15] During the hole-burning interval, REDOR[16] pulses that are selective for the $^{17}$O central transition ($\pi$CT) are used to dephase the polarization of nearby protons ($^1$H). This is represented by a "hole", the radius of which grows in proportion to $\tau_b^{1/3}$. This is depicted in the tile labeled "Burning", where the proton magnetization is depicted as a gray continuum. During this step, homonuclear $^1$H decoupling is applied to suppress proton spin diffusion to validate the use of spin-pair dephasing principles for calculating the spatial profile of the hole. During the hole-filling interval, magnetization returns to the $^{17}$O nucleus by spontaneous proton spin diffusion, as illustrated in the tile labeled "Filling". Following this, the $^1$H magnetization near the center of the hole is monitored by magnetization transfer to $^{17}$O using a short (10 μs) CP contact pulse with LG irradiation[17] of $^1$H rf to again suppress proton spin diffusion during the transfer. Multiple-echo acquisition with CPMG[18] is used to enhance sensitivity. The signal intensity is analyzed as a function of $\tau_f$ for different $\tau_b$ to determine the proton spin diffusion coefficient $D_H$ using an analytic diffusion model. In all our experiments the sample rotation period for magic-angle spinning, $\tau_R$, was 0.33 ms. Additional experimental details are given in the supplementary information.

Our implementation of the hole-burning pulse sequence under slow magic-angle spinning (MAS) is shown in Figure 4.2. Following saturation of $^{17}$O magnetization, the magnetic dipoles of $^{17}$O nuclei are used to destroy nearby $^1$H magnetization. The application of a homonuclear proton decoupling method during dephasing, such as the BR-24 technique used here,[22] is essential in two ways. First, it arrests proton spin diffusion. Second, it allows the dephasing dynamics to be approximated by spin-pair processes. Under these two conditions,

a hole is burned in the proton magnetization. Chen and Schmidt-Rohr defined the radius of the hole to be the distance from the heteronucleus at which the $^1$H magnetization rises to half the value it reaches well outside of the hole,[15]

$$r_{0.5} = \sqrt[3]{\frac{5}{4} Q \tau_b}, \tag{4.1}$$

where $\tau_b$ is the hole-burning interval and $Q$ is a dephasing constant,

$$Q = \lambda_{cs} h \frac{\mu_0}{4\pi} \frac{|\gamma_I \gamma_S|}{4\pi^2}, \tag{4.2}$$

which depends on the scaling factor $\lambda_{cs}$ accounting for the attenuation of the $^1$H-$^{17}$O heteronuclear dipolar interaction by BR-24, the gyromagnetic ratios of the *I* and *S* spins, and the fundamental constants $\mu_0$ and $h$. The *S* spin here, $^{17}$O, is quadrupolar (*S* = 5/2), but because central transition selective π pulses were used (labeled $\pi_{CT}$ in Figure 4.2), Eq. (4.2) remains valid.[23] Taking $\lambda_{cs} = 0.38$ for BR-24,[24] we calculate $Q = 6.2$ Å$^3$/ms for our implementation of pairwise $^1$H-$^{17}$O dipolar dephasing.

Following the hole-burning interval, the proton magnetization refills the hole by spontaneous proton spin diffusion. Under the experimental conditions used, transport of proton magnetization is, to a good approximation, governed by the isotropic diffusion equation

$$\frac{\partial M}{\partial t} = D_H \nabla^2 M, \tag{4.3}$$

where *M* is a scalar field representing the longitudinal proton magnetization density and $D_H$ is the isotropic proton spin diffusion coefficient. If the $^{17}$O spin labeling is sparse, we can solve Eq. (4.3) assuming the holes are far enough apart to be treated as an ensemble of isolated, spherically symmetric wells, which yields $M(r, t)$ as a function of the radial coordinate and

time. The solution for the recovery of magnetization at the center of a spherical well, defined by the boundary conditions,

$$M(r,0) = \begin{cases} M_1 \text{ if } r < R, \\ M_2 \text{ if } r > R, \end{cases}$$

$$\left.\frac{\partial M}{\partial r}\right|_{r=0} = 0, \forall t,$$

$$\lim_{r\to\infty} M(r,t) = M_2, \forall t,$$

is given by

$$M(0,t) = M_2 + (M_1 - M_2)\left[\text{erf}\left(\frac{R}{\sqrt{4D_H t}}\right) - \frac{R}{\sqrt{\pi D_H t}}\exp\left(-\frac{R^2}{4D_H t}\right)\right]. \quad (4.4)$$

The spherical well profile is defined by an abrupt change of magnetization from $M_1$ within the burned hole to the bulk polarization value $M_2$ at the edge of the hole at $r = R$. While such an initial profile of magnetization is unrealistic, the solution can be adapted for an initial profile that features a smoother transition across the edge by introducing the advancement parameter, $\Delta t$, and making the substitution $t \to t + \Delta t$ in Eq. (4.4). In this way, the initial profile is modeled as the solution of diffusion into a spherical well at a nonzero time $t = \Delta t$, and Eq. (4.3) does not need to be solved for a more complicated set of boundary conditions.[15]

As discussed, Eq. (4.3) does not possess a term corresponding to a magnetization sink. In reality, our data is affected by longitudinal $^1$H spin relaxation, characterized by the time constant, $T_1$, which is on the order of milliseconds. The effects of relaxation, however, become significant only after most of the magnetization has returned to the hole by diffusion (*vide infra*), such that the behavior of magnetization exists approximately in two separate regimes, one diffusion dominated and one relaxation dominated. For the latter case, the magnetization

behaves like $M(t) = M_0 \exp(-t/T_1)$ for some initial value of magnetization $M_0$. Given this approximate separability, we take $M_0$ to be equal to Eq. (4.4), in spite of its time dependence.

Putting all of this together, we obtain the following analytic expression to model the magnetization recovery data,

$$M_c(\tau_f) = \left[M_2 + (M_1 - M_2)\left[\mathrm{erf}\left(\frac{R}{\sqrt{4D_H(\tau_f+\Delta t)}}\right) - \frac{R}{\sqrt{\pi D_H(\tau_f+\Delta t)}}\exp\left(-\frac{R^2}{4D_H(\tau_f+\Delta t)}\right)\right]\right]\exp\left(-\frac{\tau_f}{T_1}\right), \quad (4.5)$$

where the signal dependence on the parameter $\tau_f$ has now been made explicit. We see from this expression that hole filling data can be analyzed for $M_1$, $M_2$, $\Delta t$, $T_1$, and the characteristic diffusion time $R^2/D_H$. For our calculations, we take $R = r_{0.5}$ according to Eq. (4.1) to derive $D_H$. This expresses a $\tau_b^{1/3}$ dependence on the duration of hole burning, providing a straightforward means of controlling the size of the hole.

We note that this model of diffusion into a spherical well does not explicitly incorporate spin exchange or motional dynamics. Since these are modulated by settings such as the MAS rate and sample temperature, the set of model parameters we determine, including $D_H$, pertain to a specific set of experimental conditions. Our experiments have been carried out at a temperature around 95 K, where significant molecular motion is frozen, and a magic-angle spinning rate of 3030 Hz, much lower than the strongest $^1$H-$^1$H dipolar coupling frequencies. This prevents the suppression of spin diffusion by molecular motion and places us in a quasi-static regime where $^1$H spin diffusion is not significantly affected (and may even be slightly enhanced) by sample rotation.[20-21]

## 4.3. Measurement of the spin-diffusion coefficient

To selectively monitor the magnetization near the center of the hole and validate the use of Eq. (4.5), we used a very short (10 μs) cross-polarization (CP) contact time, with off-resonance $^{1}H$ irradiation in the manner of Lee and Goldburg[17] for additional suppression of proton spin diffusion during the CP transfer. Such a short contact time transfers polarization between only the most strongly dipole-coupled nuclei, which are those $^{1}H$ nuclei within a few bond lengths of the $^{17}O$ nucleus at the center of each spherical well.

The magnetization recovery data and the best fit to $M_c(\tau_f)$ given by Eq. (4.5) for $Ca_3Al_2O_6$ hydrated with 20% $^{17}O$-enriched water for 24 h are plotted in Figure 4.3A. The parameters $M_2$, $\Delta t$, $T$, and $D_H$ in Eq. (4.5) were determined as a part of the numerical fit. More details regarding the samples (including $^{17}O$ enrichment levels after hydration) and fitting procedure are given in the appendices. The appendices also show analogs of Figure 4.3A for the $Ca_3Al_2O_6$ sample hydrated with 3% $^{17}O$-enriched water for 24 h and a $Ca_3SiO_5$ sample hydrated with 5% $^{17}O$-enriched water for 50 d. Our analysis of $Ca_3SiO_5$ is complicated by the fact that it is known to form mixtures of poorly-ordered calcium silicate hydrate (C-S-H) as well as crystalline $Ca(OH)_2$ upon hydration. In the appendices, we show high-resolution $^{17}O$ spectra of our hydrated $Ca_3SiO_5$ sample (as well as the $Ca_3Al_2O_6$ samples) and carry out a quantitative analysis which reveals that less than 20% of the $^{17}O$ is present as $Ca(OH)_2$. Given the poor signal-to-noise ratios of our $Ca_3SiO_5$ datasets, our analysis should not be led into serious error by assuming our results pertain solely to the major hydration product, C-S-H.

We see that Eq. (4.5) leads to excellent fits of three datasets acquired for hole-burning intervals of 0.66 ms, 1.32 ms, and 2.64 ms, corresponding to $r_{0.5}$ values of 0.17 nm, 0.22 nm, and 0.27 nm from Eq. (4.1). Signal intensities near zero were recorded for filling intervals less

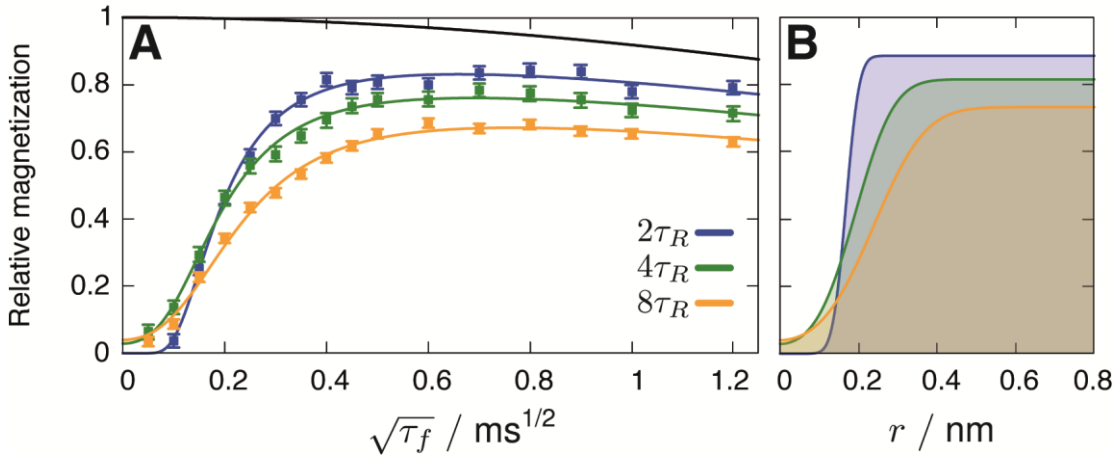


**FIGURE 4.3)** Profiles of $^{1}$H magnetization for the hole-burning experiments for 20% $^{17}$O-enriched tricalcium aluminate. A) Recovery of the $^{17}$O-detected $^{1}$H signal intensities plotted as functions of the square root of the hole-filling interval $\tau_f$ for three values of $\tau_b$: 0.66 ms ($2\tau_R$; 2 rotor periods at the 3030 Hz MAS rate), 1.32 ms ($4\tau_R$), and 2.64 ms ($8\tau_R$). The curves are best fits to the experimental data (points), according to the hole-filling model, Eq. (4.5). The intensities are relative to a reference experiment without $^{17}$O REDOR pulses, in which case homonuclear $^{1}$H decoupling is still applied but no hole is burned. The black line corresponds to the recovery limit based upon a component of spin relaxation with time constant $T_1 =$ 11.7 ms. B) Simulated radial magnetization profiles immediately after hole burning ($\tau_f = 0$), corresponding to $M(r, 0)$, using parameters from the best-fit analysis. The sample temperature was near 95 K.

than 10 μs, validating the constraint $M_1 = 0$. For $\tau_f > 10$ μs, there is onset of rapid recovery of the magnetization toward $M_2$, which represents the volume average proton polarization after hole burning. Measured with respect to a reference experiment in which the $^{17}$O dephasing pulses are deactivated and no holes are burned in the proton polarization, we should expect $M_2 < 1$, with the value of unity obtained only in the limit of infinite $^{17}$O dilution. This recovery limit is indicated by the black line in Figure 4.3A, and indeed we see that in the case

of hydrated $Ca_3Al_2O_6$ the intensities do not reach this limit. Rather, we find decreasing $M_2$ values of 0.88, 0.81, and 0.73 for increasing durations of hole burning. For otherwise identically hydrated $Ca_3Al_2O_6$ (3%), we find much lower respective $M_2$ values of 1.00, 0.94, and 0.91. This trend versus $\tau_b$ corresponds to (-7.5 ± 1.1) %/ms for $Ca_3Al_2O_6$ (20%) and (-4.5 ± 1.6) %/ms for $Ca_3Al_2O_6$ (3%). The ratio of these values (20% over 3%) is only 1.7, yet the ratio of $^{17}O$ concentrations is 6.7. This is consistent with incipient hole overlap for the $Ca_3Al_2O_6$ (20%) sample, even at the shortest hole-burning intervals used here. Further discussion pertaining to hole overlap leading to less than expected destruction of average proton polarization is given in the appendices. For the $Ca_3SiO_5$ sample, which has a lower $^{17}O$ concentration than $Ca_3Al_2O_6$, is it difficult to assess whether $M_2$ departs from unity because of low signal-to-noise ratios and so here we fit with the constraint $M_2 = 1$, as described in the appendices.

From the full solution of Eq. (4.3), we can also calculate initial magnetization profiles $M(r, 0)$ in the context of the analytic model for each value of $\tau_b$, which is shown in Figure 4.3B using parameters determined from the best fit analysis. The appearance of nonzero magnetization at $r = 0$ may appear in contradiction to the constraint $M_1 = 0$, but in fact this is a consequence of the advancement parameter increasing from 2 μs to 13 μs to 22 μs with increasing $\tau_b$. This accounts for the decreasing slope of the hole edge and reflects the fact that we are not truly sampling the $^1H$ magnetization at the single point $r = 0$, but rather over a small neighborhood near $r = 0$, over which the integrated signal intensity tends to a small but nonzero value for sufficiently large (but finite) holes, even for ideal dipolar dephasing. Residual spin diffusion during hole burning may also contribute.

The behaviors of the $M_2$ and $\Delta t$ parameters are consistent with expectations, increasing our confidence that $D_H$ should behave similarly. The proton spin diffusion coefficients we determine by our analysis for each of the samples are given in Table 4.1. The proton concentrations, $c$, of hydrated $Ca_3SiO_5$ and hydrated $Ca_3Al_2O_6$ are around 20 M and 90 M, respectively. Assuming that $D_H \propto c^{1/3}$,[25-26] we would expect $D_H$ for hydrated $Ca_3SiO_5$ to be about 60% of that for hydrated $Ca_3Al_2O_6$, which is consistent with the values shown in Table 1.

**Table 4.1)** Proton spin diffusion coefficients, $D_H$ / $\mathrm{nm^2 s^{-1}}$, for hydrated $Ca_3Al_2O_6$ and hydrated $Ca_3SiO_5$ with different extents of $^{17}O$ enrichments, determined for different hole burning intervals.

| Sample | Hole burning interval | | | |
|---|---|---|---|---|
| | $2\tau_R$ | $4\tau_R$ | $8\tau_R$ | $\infty$ |
| $Ca_3Al_2O_6$ (20%) | 156 ± 11 | 204 ± 15 | 222 ± 12 | **245 ± 4** |
| $Ca_3Al_2O_6$ (3%) | 165 ± 11 | 200 ± 13 | 214 ± 11 | **232 ± 2** |
| $Ca_3SiO_5$ (5%) | 71 ± 7 | 105 ± 12 | 120 ± 12 | **137 ± 2** |

Rather than exhibiting behaviors that are independent of $\tau_b$, we observe in Table 4.1 that the spin diffusion coefficients $D_H$ increase with the duration of hole burning $\tau_b$. This effect is consistent across the different samples. This phenomenon was also observed by Chen and Schmidt-Rohr in their $^{13}C$ hole-burning experiments on polymer samples,[15] systems for which the results of the hole-burning method could be compared with techniques that were suitable over somewhat larger length scales (roughly 10 nm). They attributed such dependence on $\tau_b$ to anisotropic spin diffusion on nanometer length scales, and to a lesser extent on nondiffusive spin dynamics on microsecond time scales. The hole-burning method was found to underestimate $D_H$ compared to methods probing diffusion on larger length scales by a factor

of about two or three, depending on the size of the hole. Given the tendencies for hydrated calcium aluminates and silicate to form clustered and layered structures, similar anisotropic effects may also be factors here.

Ultimately, transport of a continuous proton magnetization by spin diffusion is a simple way to parameterize the very complicated spin exchange dynamics of protons in solids. By the parameterization of Eq. (4.3), the exchange dynamics during hole filling are such that diffusion genuinely appears to slow down as the sub-nanometer length scale is reached. Conversely, the difference between the diffusion coefficients we determine and the "macroscopic" proton spin diffusion coefficient, which we refer to as $D_H^\infty$, should diminish as the size of the hole increases. By plotting our $D_H$ values against $\tau_b^{-1}$, a linear relationship emerges for all of our samples, as shown in Figure 4.4. The intercept of the trendline corresponds to the bulk spin diffusivity $D_H^\infty$, which is given the rightmost column of Table 4.1 for the hydrated $Ca_3Al_2O_6$ and $Ca_3SiO_5$ materials with different $^{17}O$ enrichments.

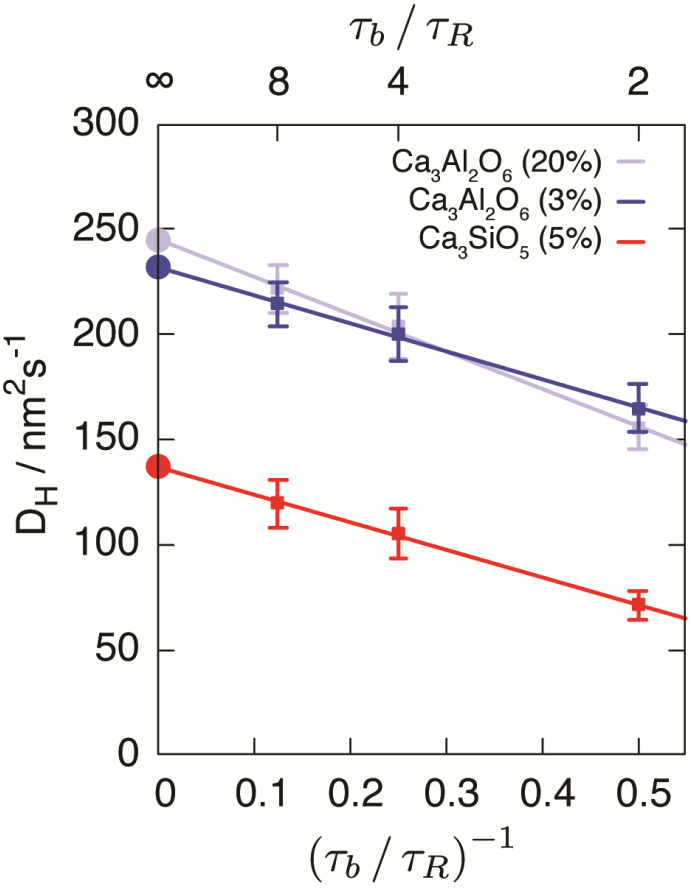


**FIGURE 4.4)** Plots of macroscopic proton spin diffusion coefficients $D_H$ versus hole-burning intervals $\tau_b$ for hydrated $Ca_3Al_2O_6$ and hydrated $Ca_3SiO_5$ with different extents of $^{17}O$ enrichments obtained by extrapolation from finite hole burning intervals.

We find that $D_H^{\infty}$ is about twice the value of $D_H$ analyzed at the shortest hole-burning interval of 0.66 ms ($2\tau_R$) for hydrated $Ca_3SiO_5$, and about 50% larger for the hydrated $Ca_3Al_2O_6$ materials. The values and trendlines for both the 3% and 20% $^{17}O$-enriched $Ca_3Al_2O_6$ samples cluster together; despite clear indications of hole merging at the 20% enrichment level (*vide supra*), they have not yet reached levels where the diffusion coefficients we analyze are significantly affected. It would seem that our model, Eq. (4.5), compensates for the effect of hole merging primarily through the $M_2$ and $\Delta t$ parameters.

Further research would indicate the concentration of hole-burning nuclei required to incur a significant error in apparent $D_H$.

The most significant source of uncertainty is a systematic one arising from the selection of $R$, which was defined by reasonable though somewhat arbitrary criteria. Instead of Eq. (4.1), the radius of natural dimensionality,

$$r_{\text{nat}} = \sqrt[3]{Q\tau_b}, \tag{4.6}$$

could have been used. If we take $R = r_{\text{nat}}$ instead of $r_{0.5}$, then the diffusion coefficients we determine will be $(r_{\text{nat}}/r_{0.5})^2$ = 86.2% of those reported in Table 4.1. On this basis, we are confident in our values of $D_H$ to a level of ±15%. A better procedure may be to select fixed values of $R$ and $\Delta t$ by regression to the theoretical dephasing profile. We anticipate that this uncertainty could be reduced by investigating the performance of the pulse sequence under different homonuclear decoupling schemes (to change the scaling factor $\lambda_{cs}$) and faster sample rotation (to modulate spin diffusion).[27-28]

## 4.4. Conclusions

In summary, under quasi-static conditions such as the 3030 Hz magic-angle spinning used here, we determine the macroscopic proton spin diffusion coefficient should fall within 240 ± 40 nm$^2$/s for hydrated tricalcium aluminate and 140 ± 20 nm$^2$/s for hydrated tricalcium silicate. Physically, this means that proton magnetization is transported across space faster in hydrated tricalcium aluminate than in hydrated tricalcium silicate. We determined these values by hydrating with $^{17}$O-enriched water, which introduces spin labels that can be used to burn holes in the $^1$H magnetization. The shape of the hole is well-described by dipolar dephasing

principles and establishes boundary conditions for the return of magnetization into the hole by $^{1}H$ spin diffusion. The isotropic radial diffusion equation yields an approximate analytical solution to these boundary conditions, the validity of which is verified by our experimental measurements. The solution to the radial equation leads to an analytic expression for the recovery of magnetization in the hole which fits excellently to the experimental data. The model parameters determined by our analyses can be physically rationalized, including the positive correlation of the diffusion coefficient with the duration of hole burning.

These are the first measurements of spin diffusivity in silicates. Independent measurement of spin diffusivities allows the size of nanoscale domains to be determined with phase selectivity by, for example, magnetization relayed NMR methods.[6, 11] For silicates, this would permit tracking the appearance, size, and depth of the various hydrated phases that gradually form, crystallize, or react across the induction, acceleration, and deceleration stages of tricalcium silicate hydration.[29] Our results thus provide crucial parameters and methodology for future work investigating such hydration processes which are discussed in Chapter five of this manuscript.

## 4.5. Materials, Methods, & Derivations

*Sample Information*

Anhydrous tricalcium aluminate ($Ca_3Al_2O_6$, Mineral Research Processing, France) was hydrated with either 20.9% $^{17}O$-enriched water or 3.14% $^{17}O$-enriched water for 24 h at 90 °C, with a water-to-solids ratio of 1.00 ± 0.05. Anhydrous monoclinic tricalcium silicate ($Ca_3SiO_5$, Mineral Research Processing, France) was hydrated with 5.23% $^{17}O$-enriched water for 50 d at 25 °C, with a water-to-solids ratio of 0.50 ± 0.05. The batches of 3.14% and 5.23%

$^{17}$O-enriched water were made by dilution of the 20.9% $^{17}$O-enriched water with ordinary distilled water in a polyethylene vial; actual $^{17}$O concentration was determined by mass measurements. Hydration was initiated by vortex mixing ~200 mg of the dry solid the vial containing partially $^{17}$O-enriched water for 2 min and sealing the mixture under ambient atmosphere. After hydration, the samples were submerged in liquid $N_2$ and lyophilized for 24 h at 0.10 Torr and -40 °C to quench the hydration process and remove unreacted bulk or weakly adsorbed water. This workup method is not expected to influence the structure of the hydrated solids in any significant way.[30] Upon hydration, $Ca_3SiO_5$, is known to form mixtures of poorly-ordered calcium silicate hydrates and $Ca(OH)_2$.[31] Hydration of $Ca_3Al_2O_6$ in the absence of sulfates results in the formation of crystalline katoite, $Ca_3Al_2(OH)_{12}$, which is comprised of Al(VI) species as indicated by its $^{27}$Al shift shown in Fig. 4.5. The density of $^{1}$H nuclei estimated from bulk densities and stoichiometry is generally between 15 M and 30 M for fully hydrated silicates and 88 M for katoite.[32]

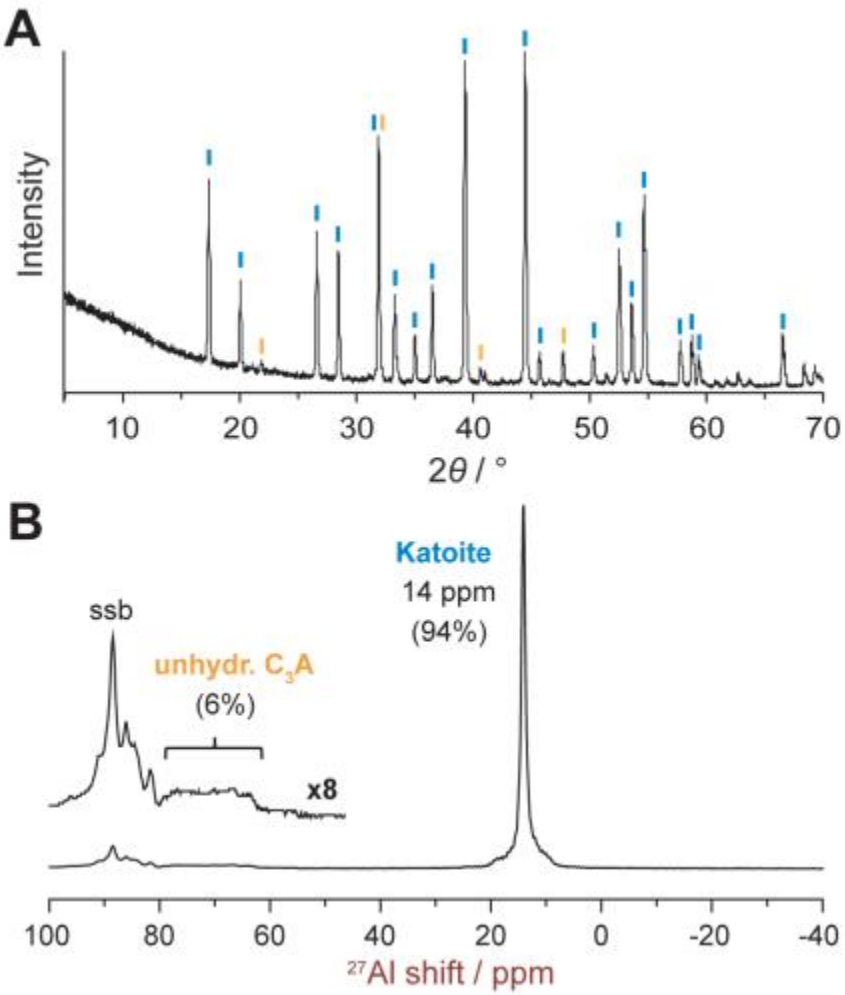


**FIGURE 4.5)** (A) Powder X-ray diffraction patterns with reflections indexed to $Ca_3Al_2O_6$ (orange) and $Ca_3Al_2(OH)_{12}$ respectively. (B) Quantitative $^{27}Al$ solid-state NMR (18.8 T, 16 kHz MAS, 25 °C) of hydrated tricalcium aluminate indicating ~94% conversion to $Ca_3Al_2(OH)_{12}$.

*NMR Parameters*

Hole burning experiments were performed on a Bruker 900 US2 wide-bore Avance Neo NMR spectrometer operating at 21.14 T, equipped with an HXY 3.2 mm DNP probe operating in $^{1}H/^{17}O$ double-resonance mode. Samples were restricted to the central third of a rotor with inner diameter of 2.2 mm in order to maximize rf homogeneity.

To measure spin diffusion coefficients the sequence shown in Figure 4.2 was used. All experiments were run at a rotational frequency of 3030 Hz. BR24 was coded into a decoupling program (CPD) to ensure synchronization with the REDOR block, such that the cycle time of

the decoupling was calculated to fit an integer number of full cycles inside the window permitted by the REDOR cycles. During BR24, the $^{1}$H rf amplitude was 156.25 kHz (90° pulse length of 1.6 μs, transmitter power near 300 W) and the length of the decoupling cycle ($\tau_c$) was near 82 μs. The spin diffusion coefficients were measured using REDOR dephasing periods of 2, 4, 8 and 16 $\tau_R$ (corresponding to 0.66, 1.32, 2.64 and 5.28 ms), and hole filling interval $\tau_f$ up to 1.44 ms. For each REDOR dephasing time, sixteen reference spectra with $\tau_f$ of 1.44 ms (repeated to increase certainty of the recovery limit intensity) and without REDOR dephasing were acquired and used to normalize the intensities to a scale of relative magnetization. The transfer of the magnetization from $^{1}$H to $^{17}$O was done using LG-CP with a contact time of 10 μs in order to minimize spin diffusion and ensure the transfer is local, permitting the approximation that the signal observed corresponds to the center of the hole. Immediately prior to this, the $^{1}$H magnetization was placed along the effective field with a 35° pulse (skinny black bar labelled $\tau_c$ in Figure 4.2). The sensitivity of the $^{17}$O acquisition was improved by echo train acquisition using CPMG implementing central transition selective refocusing pulses. Twenty echoes, truncated to maximize sensitivity at the expense of resolution[33] were acquired with an echo shift of one rotor period. For experiments at hole burning periods of 2, 4, 8 and 16 $\tau_R$, the following respective number of scans were collected:

**20%-enriched hydrated $Ca_3Al_2O_6$** = 4, 8, 16, 40 scans

**3%-enriched hydrated $Ca_3Al_2O_6$** = 16, 32, 64, 512 scans

**5%-enriched hydrated $Ca_3SiO_5$** = 256, 512, 768, 1536 scans

Reconstruction of CPMG data involved a matching procedure which exploited the sampling synchronicity of the windowed acquisition. The echo train was cut and appended as a function of echo count k. The amplitude of each data point comprising the kth echo by the filter function,

$$L(\tau_k) = \exp\left(-(\tau_k/\mathrm{T})^{\beta}\right), \qquad (4.7)$$

where $\tau_k$ is the time after excitation for the kth echo top and the parameters T = 5 ms and β = 0.77 match the decay of the CPMG envelope. The $L(\tau_k)$ apodized echo dimension is summed out leaving the signal of an echo with a significant sensitivity enhancement. Processing of the reconstructed signal continued with partial integration of the $^{17}$O line shape over the most

intense points. No zero filling was used in this process. The resulting intensities were left as a function of normalized to noise. All spectral processing was carried out using the macOS application RMN, versions 1.8.4 or 1.8.6.5.[34]

*Analysis of high-resolution $^{17}O$ spectra*

The high-resolution $^{17}O$ spectra of the hydrated tricalcium aluminate samples are shown in Figure 4.6. These spectra are typical of the MAS NMR powder pattern of a single $^{17}O$ site broadened by the second-order quadrupolar interaction. The spectra exhibit well-defined shoulders and sharp singularities, confirming the hydrated tricalcium aluminate phase corresponds to crystalline katoite, $Ca_3Al_2(OH)_{12}$.

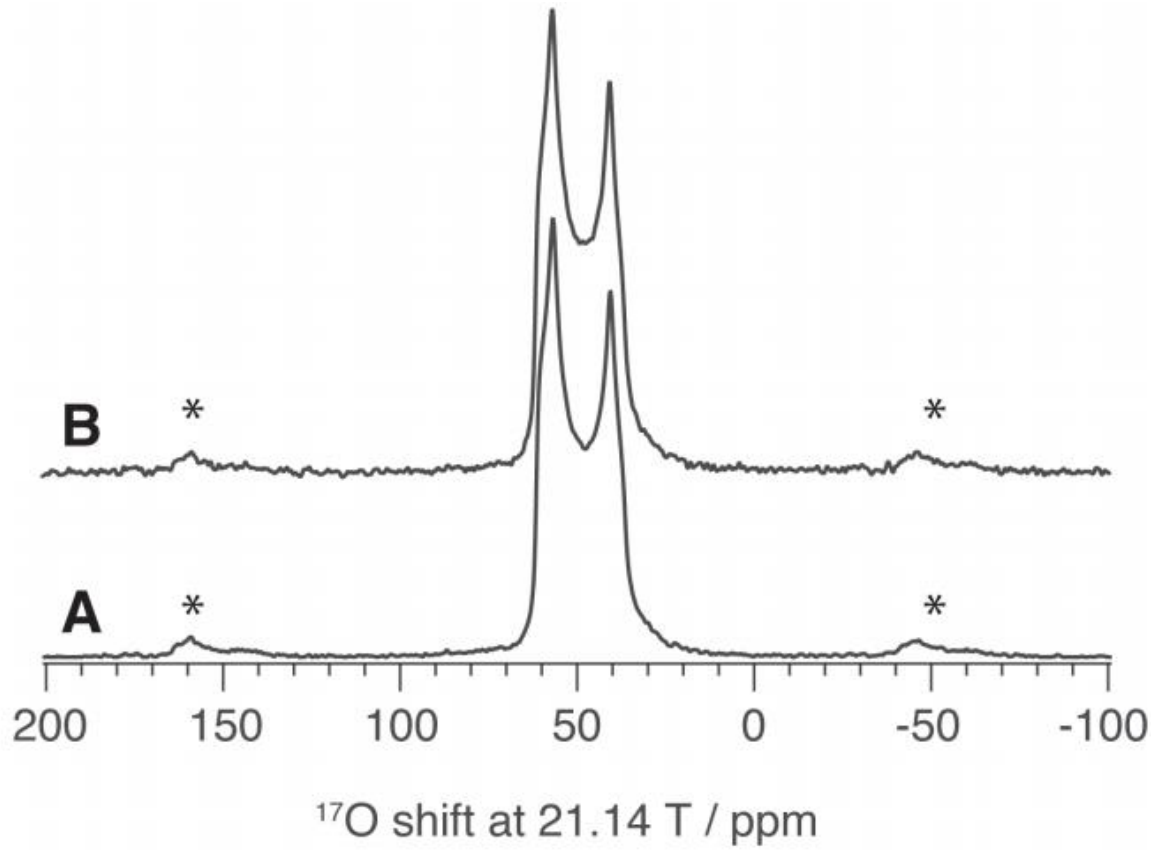


**FIGURE 4.6)** Direct excitation $^{17}O$ spectra at 21.14 T, 95 K, and 12.5 kHz MAS of (A) $Ca_3Al_2O_6$ (20%) with 128 scans, 5 s recycle delay, (B) $Ca_3Al_2O_6$ (3%) with 1024 scans, 2 s recycle delay. Proton decoupling with SPINAL64 and an rf amplitude of 125 kHz was applied during acquisition. Approximate frequency referencing is given with respect to the $^1H$ spectrum of the $Ca_3Al_2O_6$ (20%) sample assuming its maximum is at 4 ppm (split between water and hydroxyl type signals). Asterisks indicate spinning sidebands.

The hydration of tricalcium silicate is more complicated than tricalcium aluminate since calcium hydroxide is formed as a coexisting phase using our method of hydration. The high-resolution $^{17}O$ spectra of the hydrated tricalcium silicate sample is shown in Figure 4.7. This spectrum is dominated by broad features which were assigned to different C-S-H oxygen environments by Cong and Kirkpatrick,[35] between 100 and 130 ppm (silicate nonbridging oxygens), 30 ppm and 80 ppm (Ca-OH moieties and silicate bridging oxygens), and a low intensity tail going down to about -40 ppm (silanols and bound water). In addition to these broad features, the appearance of modest singularities at 44 ppm and 62 ppm correspond to $^{17}O$ in the secondary phase, crystalline $Ca(OH)_2$. We quantify the fraction of $^{17}O$ in each phase by modeling the shift distribution of the environments of $^{17}O$ in C-S-H as three separate normal distributions, roughly corresponding to the regions described above. Fitting to a normal distribution is expected to be an adequate approximation for the C-S-H environments because the high magnetic field at which the measurements were performed reduces the skewedness of the line shape induced by the second- order quadrupolar interaction while at the same time amplifies the Gaussian broadening due to chemical shift disorder. The shift distribution of $^{17}O$ in $Ca(OH)_2$ is modeled as MAS NMR powder pattern of a single $^{17}O$ site broadened by the second-order quadrupolar interaction. This powder pattern was calculated using $C_q$ = 7.0 MHz, $\eta_q$ = 0, and an isotropic chemical shift of $\delta_{iso}$= 74 ppm, in line with previously reported values.[35] This fixes the shape and frequency distribution of the $Ca(OH)_2$ signal, with only the amplitude allowed to vary. The shift, width, and amplitude of the normal distributions were allowed to vary freely. The result of the fit is shown as the decomposition shown in Figure 4.7. We see that $Ca(OH)_2$ is a minor constituent, with 18% of the total $^{17}O$

present in this phase, leaving 82% present in the C-S-H. The residuals shown in Figure 4.7 appear as noise, improving the confidence in our parameterization.

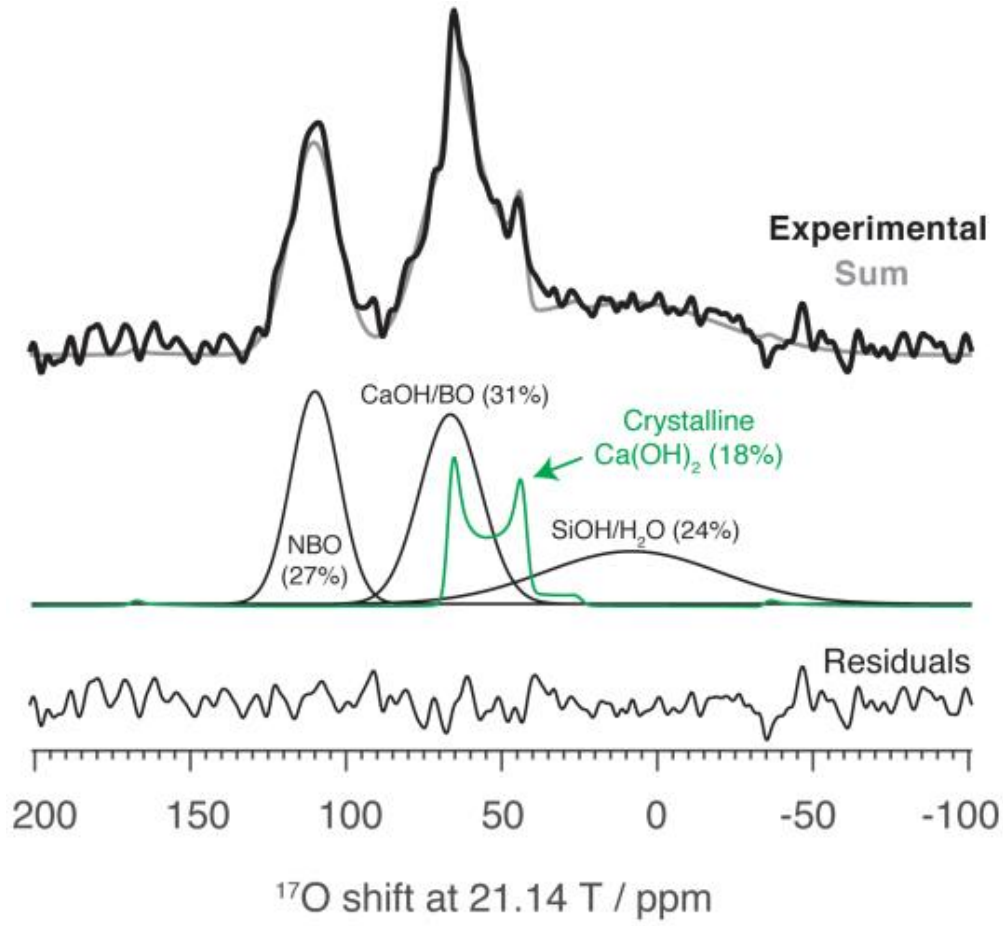


**FIGURE 4.7)** Quantitative decomposition of the high-resolution $^{17}O$ direct excitation MAS NMR spectrum of $Ca_3SiO_5$ (5%) (top, black) into three Gaussian components (center, black) and a second-order quadrupole powder pattern (center, green). The former represents the $^{17}O$ environments in the poorly ordered calcium silicate hydrate phase whereas the latter corresponds to the spectrum of a coexisting crystalline $Ca(OH)_2$ phase. The residuals (bottom) are the difference between the experimental spectrum and the sum of the calculated components (top, gray). The contribution of each component to the total area of the calculated spectrum is given in percent next to the corresponding oxygen species (NBO – silicate non-bridging oxygen; BO – silicate bridging oxygen). Spectrum was acquired with 512 scans, 10 s recycle delay at 21.14 T, 95 K, and 12.5 kHz MAS. Proton decoupling with SPINAL64 and an rf amplitude of 125 kHz was applied during acquisition. Approximate frequency referencing is given with respect to the $^1H$ spectrum of the $Ca_3Al_2O_6$ (20%) sample by assuming its maximum is at 5 ppm.

*Data Reproducibility*

Owing to the high rf duty cycle of the hole burning pulse sequence (see Figure 4.2), we occasionally observed bizarre behavior from circuit detuning in which the signal response of a repeating hole burning experiment would become erratic and/or diminish when the hole burning period exceeded $8\tau_R$. This is illustrated in Figure 4.8 for repeated experiments at the shortest BR24 cycle time we could achieve that was commensurate with the 330 μs rotor period: $\tau_c \approx 66$ μs (giving $\tau_c/\tau_R \approx 5$).

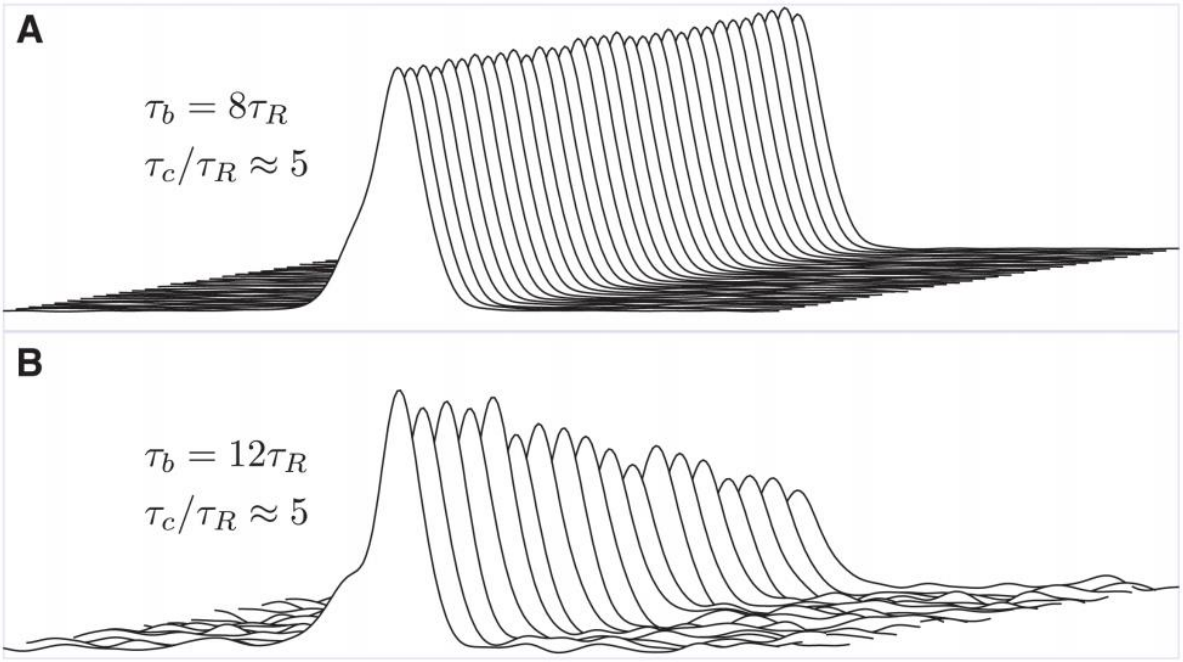


**Figure 4.8)** Reconstruction of (truncated) $^{17}O$ CPMG intensities for repeated hole burning experiments to test reproducibility. Horizontal axis is frequency and the span of each spectrum is constant. The first iteration of the experiment begins with the spectrum on the left. Sequentially to the right, each spectrum is the result of an identical hole burning experiment executed immediately following the preceding iteration. (A) Intensity profile of hole burning experiments at $\tau_b = 8\tau_R$ (2.64 ms) and $\tau_c \approx 66$ μs. The intensities of subsequent iterations are constant to within noise and the experiment is reproducible. (B) Intensity profile of hole burning experiments at a slightly longer $\tau_b = 12\tau_R$ (3.96 ms) and the same $\tau_c \approx 66$ μs. The intensities of subsequent iterations diminish and reproducibility is lost.

For $\tau_b > 8\tau_R$ and $\tau_c \approx 66$ μs it would often take minutes for the circuit to recover. Reproducibility was greatly improved by using a longer BR24 cycle time $\tau_c \approx 82$ μs ($\tau_c/\tau_R \approx 4$) in which the decoupling pulse lengths and powers were unchanged but longer delays were incorporated into each decoupling period, thus reducing the duty cycle. The experiment we analyze for diffusion coefficients use the longer $\tau_c \approx 82$ μ s. No drop in decoupling efficiency relative to $\tau c \approx 66$ μs was apparent.

*Data Analysis*

Data fitting was carried out using scripts written for *gnuplot*. The fit to Eq. (4.5) in Section 4.3 was carried out in a multibranch fashion, fitting branches for each sample and at hole burning periods of 2, 4, 8 and 16 $\tau_R$ simultaneously. Specific constraints were as follows:

Constraints across entire fit:

$T_1$ = 11.713127 ms (determined from Eq. (4.5) fit to the $Ca_3Al_2O_6$ (20%) branch)

$M_1 = 0$

$M_2 = 1$ (for 5% $Ca_3SiO_5$ only, due to poorer SNR resulting from greater $^{17}O$ dilution)

$R$ ($2\tau_R$) = 0.1722 nm (constant used to return $D_H$ from the characteristic diffusion time)

$R$ ($4\tau_R$) = 0.2170 nm

$R$ ($8\tau_R$) = 0.2734 nm

$R$ ($16\tau_R$) = 0.3444 nm

Fit but constrained to be equal across sample branches:

Advancement parameters $\Delta t$ (property of hole burning; should be sample independent)

Free parameters for each sample and $\tau$b:

$M_2$ (except for $Ca_3SiO_5$ (5%) as noted above)

$D_H$

The results are given in the following table. We suggest that the fit errors reported in the table, insofar as they reflect upon uncertainty in the extrapolated "macroscopic" values of $D_H$, are unimportant in comparison to the uncertainty in the selection of $R$.

Fitted data:

**Table 4.2)** Complete table of parameters determined by fitting the hole burning data to Eq. (4.5) of the main text, subject to the constraints described in this section. Error ranges corresponds to asymptotic standard errors reported by the goodness of fit routine.

| Parameter | Sample | Hole burning interval | | | |
|---|---|---|---|---|---|
| | | $2\tau_R$ | $4\tau_R$ | $8\tau_R$ | $16\tau_R$ |
| $D_H$ / $nm^2s^{-1}$ | $Ca_3Al_2O_6$ (20%) | 156 ± 11 | 204 ± 15 | 222 ± 12 | 268 ± 24 |
| | $Ca_3Al_2O_6$ (3%) | 165 ± 11 | 200 ± 13 | 214 ± 11 | 264 ± 23 |
| | $Ca_3SiO_5$ (5%) | 71 ± 7 | 105 ± 12 | 120 ± 12 | 187 ± 30 |
| $M_2$ / % | $Ca_3Al_2O_6$ (20%) | 88.4 ± 1.1 | 81.5 ± 1.3 | 73.2 ± 0.9 | 65.4 ± 1.5 |
| | $Ca_3Al_2O_6$ (3%) | 100.4 ± 1.1 | 94.5 ± 1.1 | 90.9 ± 1.0 | 76.1 ± 1.6 |
| $\Delta t$ / μs | | 2.2 ± 1.6 | 13.5 ± 1.9 | 22.1 ± 2.1 | 24.0 ± 4.4 |

Plots in the manner of the main text Figure 4.3 for all samples, and which includes the data for the hole burning interval $\tau_b$ = 5.28 ms ($16\tau_R$), are plotted below as Figure 4.9.

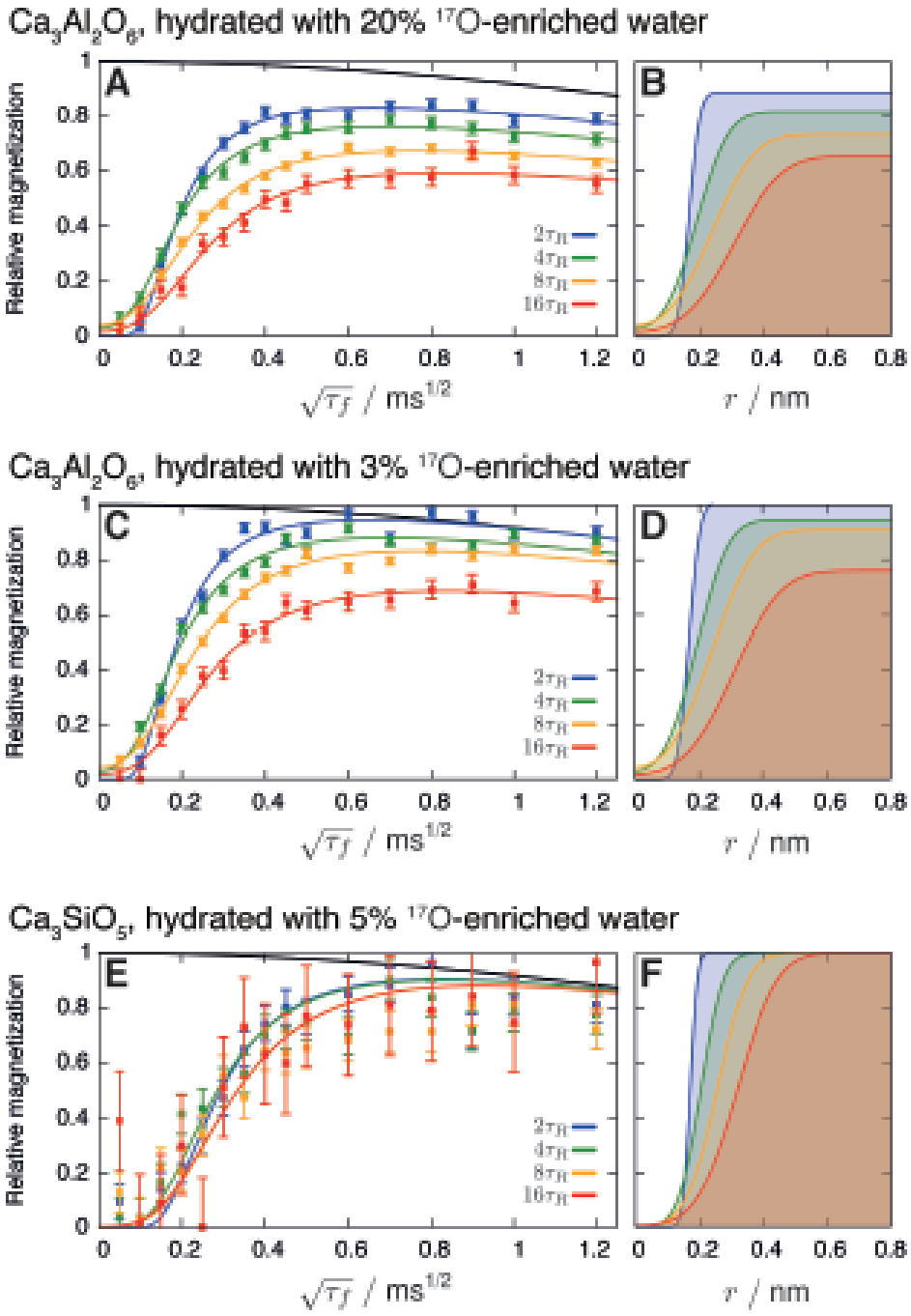


**FIGURE 4.9)** Temporal profiles of experiment hole filling recovery intensities, normalized to an experiment without REDOR pulses, for (A) $Ca_3Al_2O_6$ (20%), (B) $Ca_3Al_2O_6$ (3%), (C) $Ca_3SiO_5$ (5%). Initial radial magnetization profiles in the model context are given in panels B, D, and F, respectively for each sample.

For reasons discussed above, we excluded the $16\tau_R$ data from our primary discussion. This data (at the lower duty cycle $\tau_c/\tau_R \approx 4$) does not seem internally inconsistent, however, and should perhaps be included. We find that our results are not significantly affected if we include the $16\tau_R$ data in the extrapolation to infinite hole burning period, as shown in Figure 4.10 and Table 4.3. The consistently and anomalously high $D_H$ we analyze in the $16\tau_R$ data, if legitimate, could indicate a transition to a regime where diffusion adopts a different character, perhaps due to the diminishing importance of nondiffusive spin dynamics or diffusion anisotropy at the larger hole sizes.

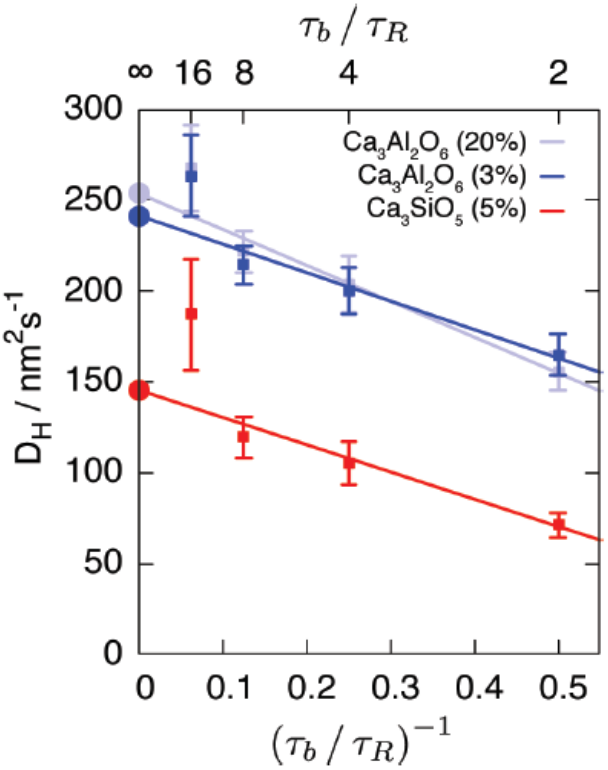


**FIGURE 4.10)** Determination of the macroscopic proton spin diffusion coefficients $D_H^\infty$ by extrapolation from finite hole burning intervals, including the parameters determined by analysis of the $16\tau_R$ data. The data points and error bars correspond to the parameters given in Table 4.2.

**Table 4.3)** Comparison of the macroscopic proton spin diffusion coefficients, $D_H^{\infty}$ between analyses which include and exclude the $16\tau_R$ data.

| Sample | $D_H^{\infty}$ / $nm^2s^{-1}$ Excluding $16\tau_R$ | $D_H^{\infty}$ / $nm^2s^{-1}$ Including $16\tau_R$ |
|---|---|---|
| $Ca_3Al_2O_6$ (20%) | $245 \pm 4$ | $254 \pm 12$ |
| $Ca_3Al_2O_6$ (3%) | $232 \pm 2$ | $242 \pm 14$ |
| $Ca_3SiO_5$ (5%) | $137 \pm 2$ | $145 \pm 16$ |

*Hole Overlap*

In our model the $M_2$ coefficient can be physically interpreted in terms of hole overlap and the concentration of $^{17}O$ nuclei in the samples, according to

$$M_2 = (1 - C_S V_{hole}) + M_\Delta, \quad (4.8)$$

Here, $C_S$ is the number concentration of $^{17}O$ spins in the sample, $V_{hole}$ is the effective volume of a polarization hole due to dephasing, and $M_\Delta$ is defined as the excess fraction of unburned polarization. The quantity $(1 - C_S V_{hole})$ is the residual magnetization assuming all holes burn to the maximum extent of their capability, which is the case when holes do not overlap. We therefore expect $M_\Delta > 0$ as shared hole volume permits an excess of unburned magnetization. In the limit of infinite $^{17}O$ dilution, and as hole volume shrinks, we expect $M_\Delta \to 0$.

The parameter $C_S$ can be calculated assuming the bulk density of katoite, 2.76 g/cm3, the hydrated stoichiometry $Ca_3Al_2O_6(H_2O)_6$, and completeness of oxygen exchange between water and tricalcium aluminate. These assumptions lead to an estimated $^{17}O$ enrichment of 14.9% and 2.2% along with $C_S$ values of 7.87 nuclei/$nm^3$ and 1.18 nuclei/$nm^3$ for the

nominally $Ca_3Al_2O_6$ (20%) and $Ca_3Al_2O_6$ (3%) samples, respectively. $V_{hole}$ is calculated assuming the effective radius of the spherical hole is determined by $r_{0.5}$.

In Fig 4.11, experimentally derived values of the $M_2$ coefficient are plotted against $r_{0.5}$. The difference between the solid lines and the experimental data points is $M_\Delta$. For the $Ca_3Al_2O_6$ (3%) sample, we see that $M_2$ coefficients cluster around the solid line, suggesting that hole overlap is not significant at this $^{17}O$ concentration. For the $Ca_3Al_2O_6$ (20%) sample, however, we observe substantially nonzero values of $M_\Delta$, especially at $\tau_b = 8\tau_R$, when the hole volume is 0.086 $nm^3$. This is consistent with our expectation that higher $^{17}O$ concentrations and larger hole volumes lead to more significant hole overlap.

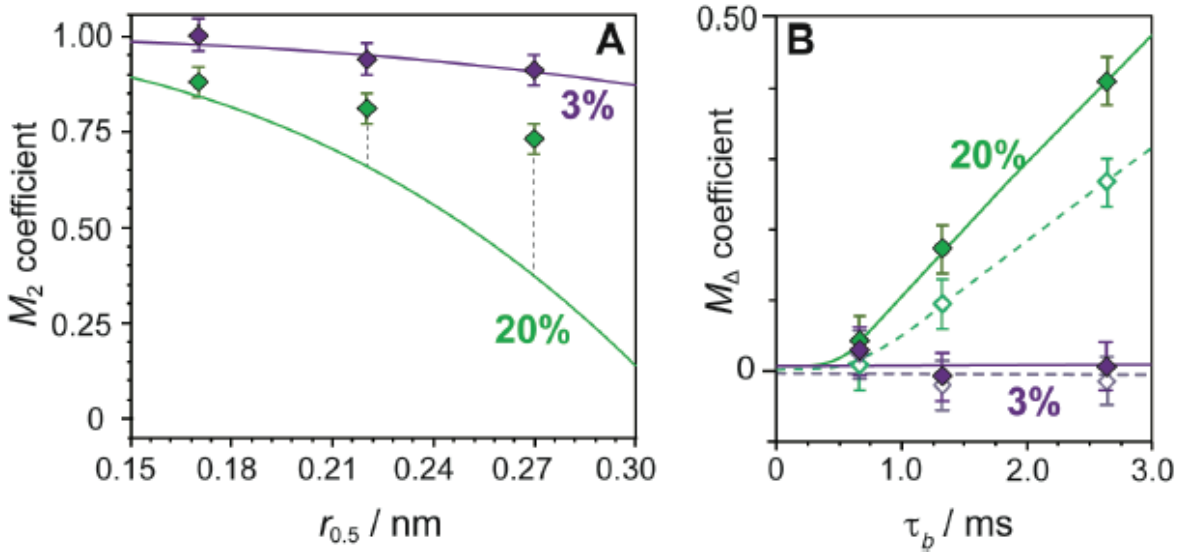


**FIGURE 4.11)** (A) Values of the $M_2$ coefficient versus hole size ($r_{0.5}$) for the 3%-enriched (purple) and 20%-enriched (green) hydrated $Ca_3Al_2O_6$. The solid lines are graphs of $(1 - C_S V_{hole})$, presenting a lower bound on $M_2$. Dashed vertical lines correspond to $M_\Delta$. (B) Excess fraction of unburned polarization, $M_\Delta$, for the two samples, plotted against the duration of hole burning. Filled and unfilled diamonds correspond to using $r_{0.5}$ and $r_{nat}$, respectively, to approximate the size of the hole. The solid ($r_{0.5}$) and dashed ($r_{nat}$) lines serve only to guide the eye.

The excess fraction of unburned polarization we calculate also depends on the accuracy of the effective hole volume, $V_{\text{hole}}$. In Fig. 4.11B, we plot $M_\Delta$ for two sets of estimates for $V_{\text{hole}}$, one based upon $r_{0.5}$ and the other $r_{\text{nat}}$. The smaller hole size, $r_{\text{nat}}$, leads to smaller predicted values of $M_\Delta$. These results are summarized in Table 4.4 below.

**Table 4.4)** Numerical values of $M_\Delta$ for the hydrated tricalcium aluminate samples, calculated for two sets of effective hole radii and three different hole burning intervals. Estimated $2\sigma$ uncertainties for the $M_\Delta$ are ±3%.

| Sample | Actual $^{17}O$ concentration | $R = r_{0.5}$ | | $R = r_{\text{nat}}$ | |
|---|---|---|---|---|---|
| | | $V_{\text{hole}}$ / nm$^3$ | $M_\Delta$ / % | $V_{\text{hole}}$ / nm$^3$ | $M_\Delta$ / % |
| $Ca_3Al_2O_6$ (20%) | 14.9% | 0.0214 | 5.2 | 0.0171 | 1.9 |
| | | 0.0428 | 15.2 | 0.0342 | 8.4 |
| | | 0.0856 | 40.6 | 0.0685 | 27.1 |
| $Ca_3Al_2O_6$ (3%) | 2.24% | 0.0214 | 2.9 | 0.0171 | 2.4 |
| | | 0.0428 | -0.4 | 0.0342 | -1.5 |
| | | 0.0856 | 1.0 | 0.0685 | -1.0 |

*General solution of the radial diffusion equation for the spherical well*

We are solving the three-dimensional isotropic diffusion equation, Eq. (4.3) in Section 4.2,

$$\frac{\partial M}{\partial t} = D\nabla^2 M,$$

with $M \equiv M(r, \theta, \phi, t)$, and the diffusion coefficient $D$, for the initial value problem,

$$M(r,0) = \begin{cases} M_1 \text{ if } r < R, \\ M_2 \text{ if } r > R, \end{cases}$$
$$\left.\frac{\partial M}{\partial r}\right|_{r=0} = 0, \forall t,$$
$$\lim_{r\to\infty} M(r,t) = M_2, \forall t,$$

and $M$ is independent of $\theta$ and $\phi$. Eq. (4.3) can be transformed into the homogenous Helmholtz equation,

$$(\nabla^2 + k^2)g = 0$$

where $g \equiv g(r, \theta, \phi)$, is stripped of its time-dependence by its relation to the "normal modes"

$$M_k(r, \theta, \phi, t) = g_k(r, \theta, \phi) e^{-Dk^2 t}$$

indexed by the eigenvalue $k$, which has units of inverse length. The solutions to the homogeneous Helmholtz equation for cases of spherical symmetry are given by the spherical wave solutions $g_k(r) = e^{-ikr}/r$. From this we have the general solution,

$$M(r, t) = \int_{-\infty}^{+\infty} A(k) \frac{e^{-ikr}}{r} e^{-Dk^2 t}\, dk.$$

The combination of modes which solves the initial value problem is given by the function $A(k)$. There is no need to solve for $A(k)$ in terms of $k$, as the above equation can be transformed into,

$$M(r, t) = M_2 + \frac{M_1 - M_2}{\sqrt{4\pi D t}} \frac{1}{r} \int_{-R}^{+R} r'\, e^{-\frac{(r-r')^2}{4Dt}}\, dr'$$

by use of the convolution theorem of Fourier transforms and application of the boundary conditions. The integral in this expression can be evaluated to yield the analytic solution,

$$M(r, t) = M_2 + \frac{M_1 - M_2}{2} \left[ \left( \operatorname{erf}\left( \frac{r + R}{\sqrt{4Dt}} \right) - \operatorname{erf}\left( \frac{r - R}{\sqrt{4Dt}} \right) \right) + \sqrt{\frac{4Dt}{\pi}} \frac{1}{r} \left( e^{-\frac{(r+R)^2}{4Dt}} - e^{-\frac{(r-R)^2}{4Dt}} \right) \right]$$

from which, upon taking the limit as $r \to 0$, we obtain Eq. (4.4) in Section 4.2.

## References


1. Plassais, A.; Pomiès, M. P.; Lequeux, N.; Korb, J. P.; Petit, D.; Barberon, F.; Bresson, B. Microstructure Evolution of Hydrated Cement Pastes. *Phys. Rev. E* **2005,** *72* (4), 041401.
2. Schmidt-Rohr, K.; Spiess, H. W. *Multidimensional Solid-State NMR and Polymers*. Academic Press: 1994.

3. Clauss, J.; Schmidt-Rohr, K.; Spiess, H. Determination of Domain Sizes in Heterogeneous Polymers by Solid-State NMR. *Acta Polym.* **1993,** *44* (1), 1-17.
4. Hedesiu, C.; Demco, D. E.; Kleppinger, R.; Buda, A. A.; Blümich, B.; Remerie, K.; Litvinov, V. M. The Effect of Temperature and Annealing on the Phase Composition, Molecular Mobility and the Thickness of Domains in High-Density Polyethylene. *Polymer* **2007,** *48* (3), 763-777.
5. Huster, D.; Yao, X.; Hong, M. Membrane Protein Topology Probed by $^{1}$H Spin Diffusion from Lipids Using Solid-State NMR Spectroscopy. *J. Am. Chem. Soc.* **2002,** *124* (5), 874-883.
6. Pinon, A. C.; Schlagnitweit, J.; Berruyer, P.; Rossini, A. J.; Lelli, M.; Socie, E.; Tang, M.; Pham, T.; Lesage, A.; Schantz, S.; Emsley, L. Measuring Nano- to Microstructures from Relayed Dynamic Nuclear Polarization NMR. *J. Phys. Chem. C* **2017,** *121* (29), 15993-16005.
7. Pinon, A. C.; Skantze, U.; Viger-Gravel, J.; Schantz, S.; Emsley, L. Core-Shell Structure of Organic Crystalline Nanoparticles Determined by Relayed Dynamic Nuclear Polarization NMR. *J. Phys. Chem. A* **2018,** *122* (44), 8802-8807.
8. Hall, D. A.; Maus, D. C.; Gerfen, G. J.; Inati, S. J.; Becerra, L. R.; Dahlquist, F. W.; Griffin, R. G. Polarization-Enhanced NMR Spectroscopy of Biomolecules in Frozen Solution. *Science* **1997,** *276* (5314), 930-932.
9. Lesage, A.; Lelli, M.; Gajan, D.; Caporini, M. A.; Vitzthum, V.; Miéville, P.; Alauzun, J.; Roussey, A.; Thieuleux, C.; Mehdi, A.; Bodenhausen, G.; Coperet, C.; Emsley, L. Surface Enhanced NMR Spectroscopy by Dynamic Nuclear Polarization. *J. Am. Chem. Soc.* **2010,** *132* (44), 15459-15461.
10. Rossini, A. J.; Zagdoun, A.; Hegner, F.; Schwarzwälder, M.; Gajan, D.; Copéret, C.; Lesage, A.; Emsley, L. Dynamic Nuclear Polarization NMR Spectroscopy of Microcrystalline Solids. *J. Am. Chem. Soc.* **2012,** *134* (40), 16899-16908.
11. Schlagnitweit, J.; Tang, M.; Baias, M.; Richardson, S.; Schantz, S.; Emsley, L. Nanostructure of Materials Determined by Relayed Paramagnetic Relaxation Enhancement. *J. Am. Chem. Soc.* **2015,** *137* (39), 12482-12485.
12. Buda, A.; Demco, D. E.; Bertmer, M.; Blümich, B.; Reining, B.; Keul, H.; Höcker, H. Domain Sizes in Heterogeneous Polymers by Spin Diffusion using Single-Quantum and Double-Quantum Dipolar Filters. *Solid State Nucl. Magn. Reson.* **2003,** *24* (1), 39-67.
13. Demco, D. E.; Johansson, A.; Tegenfeldt, J. Proton Spin Diffusion for Spatial Heterogeneity and Morphology Investigations of Polymers. *Solid State Nucl. Magn. Reson.* **1995,** *4* (1), 13-38.
14. Schlagnitweit, J.; Tang, M.; Baias, M.; Richardson, S.; Schantz, S.; Emsley, L. A Solid-state NMR Method to Determine Domain Sizes in Multi-Component Polymer Formulations. *J. Magn. Reson.* **2015,** *261*, 43-48.
15. Chen, Q.; Schmidt-Rohr, K. Measurement of the Local $^{1}$H Spin-Diffusion Coefficient in Polymers. *Solid State Nucl. Magn. Reson.* **2006,** *29* (1-3), 142-152.
16. Gullion, T.; Schaefer, J. Rotational-Echo Double-Resonance NMR. *J. Magn. Reson.* **1989,** *81* (1), 196-200.
17. Lee, M.; Goldburg, W. I. Nuclear-Magnetic-Resonance Line Narrowing by a Rotating rf Field. *Phys. Rev.* **1965,** *140* (4A), A1261-A1271.

18. Meiboom, S.; Gill, D. Modified Spin-Echo Method for Measuring Nuclear Relaxation Times. *Rev. Sci. Instrum.* **1958,** *29* (8), 688-691.
19. Roos, M.; Micke, P.; Hempel, G. Monitoring Nuclear Spin-Flip Processes and Measuring Spin-Diffusion Constants via Hole Burning into the Magnetization. *Chem. Phys. Lett.* **2012,** *536*, 147-154.
20. Björgvinsdóttir, S.; Walder, B. J.; Pinon, A. C.; Emsley, L. Bulk Nuclear Hyperpolarization of Inorganic Solids by Relay from the Surface. *J. Am. Chem. Soc.* **2018,** *140* (25), 7946-7951.
21. Roos, M.; Micke, P.; Saalwächter, K.; Hempel, G. Moderate MAS Enhances Local $^{1}$H Spin Exchange and Spin Diffusion. *J. Magn. Reson.* **2015,** *260*, 28-37.
22. Burum, D. P.; Rhim, W. K. Analysis of Multiple Pulse NMR in Solids. III. *J. Chem. Phys.* **1979,** *71* (2), 944-956.
23. Fyfe, C. A.; Mueller, K. T.; Grondey, H.; Wong-Moon, K. C. Dipolar Dephasing Between Quadrupolar and Spin-1/2 Nuclei. REDOR and TEDOR NMR Experiments on VPI-5. *Chem. Phys. Lett.* **1992,** *199* (1), 198-204.
24. Burum, D. P.; Linder, M.; Ernst, R. R. Low-Power Multipulse Line Narrowing in Solid-State NMR. *J. Magn. Reson.* **1981,** *44* (1), 173-188.
25. Khutsishvili, G. R. Spin Diffusion. *Sov. Phys. Uspekhi* **1966,** *8* (5), 743-769.
26. Wenckebach, W. T. *Essentials of Dynamic Nuclear Polarization*. Spindrift Publications: 2016.
27. Clough, S.; Gray, K. W. Spin Diffusion and Nuclear Magnetic Resonance in Rotating Solids. *P. Phys. Soc.* **1962,** *80* (6), 1382.
28. Halse, M. E.; Zagdoun, A.; Dumez, J.-N.; Emsley, L. Macroscopic Nuclear Spin Diffusion Constants of Rotating Polycrystalline Solids from First-Principles Simulation. *J. Magn. Reson.* **2015,** *254*, 48-55.
29. Bullard, J. W.; Jennings, H. M.; Livingston, R. A.; Nonat, A.; Scherer, G. W.; Schweitzer, J. S.; Scrivener, K. L.; Thomas, J. J. Mechanisms of Cement Hydration. *Cement Concrete Res.* **2011,** *41* (12), 1208-1223.
30. Rawal, A.; Smith, B. J.; Athens, G. L.; Edwards, C. L.; Roberts, L.; Gupta, V.; Chmelka, B. F. Molecular Silicate and Aluminate Species in Anhydrous and Hydrated Cements. *J. Am. Chem. Soc.* **2010,** *132* (21), 7321-7337.
31. Pustovgar, E.; Sangodkar, R. P.; Andreev, A. S.; Palacios, M.; Chmelka, B. F.; Flatt, R.J.; Lacaillerie, J.-B. d. E. d. Understanding Silicate Hydration from Quantitative Analyses of Hydrating Tricalcium Silicates. *Nat. Commun.* **2016,** *7*, 10952.
32. Geng, G.; Myers, R. J.; Qomi, M. J. A.; Monteiro, P. J. M. Densification of the Interlayer Spacing Governs the Nanomechanical Properties of Calcium-Silicate-Hydrate. *Sci. Rep.* **2017,** *7* (1), 10986.
33. Dey, K. K.; Ash, J. T.; Trease, N. M.; Grandinetti, P. J. Trading Sensitivity for Information: Carr-Purcell-Meiboom-Gill Acquisition in Solid-State NMR. *J. Chem. Phys.* **2010,** *133* (5), 054501.
34. PhySy Ltd, RMN, Version 1.8 (www.physyapps.com, PhySy Ltd., Grandview Heights, OH 43212).
35. Cong, X.; Kirkpatrick, R. J. 17O MAS NMR Investigation of the Structure of Calcium Silicate Hydrate Gel. *J. Am. Chem. Soc.* **1996,** *79* (6), 1585-1592.

## Chapter V.

# Compositions and thicknesses of surface hydration layers on tricalcium silicate particles

N. Prisco; R. Sangodkar; T. Farmer; B. Walder; L. Emsley; M. Doherty; T. Ley; G. Scherer; B. Chmelka. To be submitted to *Langmuir*.

## 5.1. Abstract

The dimensions of particles, domains, and surface layers strongly influence overall material properties, for example, during the hydration and solidification of cementitious silicate-water mixtures, which enable their widespread applications. Hydration of cementitious silicate particles is initiated at surfaces in contact with water and proceeds over different timescales which are commonly described as distinct kinetic stages (*e.g.*, induction, acceleration, deceleration). Despite several decades of detailed investigation, the transformations occurring at the liquid-solid interface during early times (*ca.* hours) have remained elusive. Characterization of these hydrated near-surface silicates is challenging due to the poor long-range order of cement hydrates and the exceedingly dilute quantities of hydration products formed at early times. Here, dynamic nuclear polarization (DNP) surface-enhanced NMR analyses enable the simultaneous measurement of the molecular-level compositions and meso-scale dimensions of hydrated surface domains and offer new insights into the origins of the induction period. Such transformations occurring at the silicate particle surface are important to understand as they are thought to influence silicate dissolution,

hydration, and subsequent strength development. The results demonstrate the use of non-equilibrium NMR spin polarization transfer to assess the compositions of complicated multicomponent materials over challenging *ca*. <1 nm to 100 nm length scales which may be inaccessible by other means. These analyses suggest that silicate particle surfaces initially form a thin layer of disordered hydrates (<10 nm) upon contact with water that continue to evolve over the course of the induction period until relatively ordered calcium silicate hydrates are observed.

## 5.2. Introduction

Dimensions of particles and surface layers are often central to the development of diverse physicochemical properties in a variety of systems, including solid catalysts, semiconductors, structural materials, and batteries. For example, large differences in the optical and electronic properties of semiconducting nanoparticles result for small differences in the shapes and sizes of individual nanoparticles, and also their assemblies into one-, two- or three-dimensional domains.[1] Similarly, the initial formation and subsequent growth of dendrite layers on the surfaces of electrodes in lithium ion batteries severely limits the performance and safety of such devices.[2] The particle sizes and formation of surface passivation layers (e.g., coke, oxides) on solid catalysts strongly influence the accessibility of chemical species to active sites, which consequently affects catalyst activities and selectivities.[3,4] The mechanical properties of alloys and composites are also directly correlated to the sizes of individual particles and intra-particle domains of the component species.[5] Similar influences of particle size and thickness of surface layers are important in cement hydration, which is initiated at particle surfaces in contact with water.[6] However, the thicknesses of layers in these systems,

especially hydrating cementitious materials, are exceedingly challenging to establish due to the difficulties associated with measuring length scales of *ca*. 10's nm in heterogeneous particulate systems.

Upon contact with water, tricalcium silicate ($Ca_3SiO_5$), the primary constituent of Portland cement ~50 – 70 wt%, undergoes rapid dissolution over the first <5-10 minutes releasing Ca and Si into solution at concentrations up to ~20 mmol/L and ~20 to 100 µmol/L respectively.[7–9] This is typically followed by a latent period of 2 – 4 hours where little further hydration, dissolution, or precipitation is observed.[6,10–12] The origins of this induction period remain of high technological and fundamental interest since it represents the initial period over which cement can be transported and poured. Importantly, the increased use of supplementary cementitious materials (SCM's) and additives (*i.e.*, superplasticizers) are desirable to mitigate the environmental impact of concrete and improve its mechanical properties, however their presence in hydrating cementitious mixtures can have a complex influence on silicate hydration chemistry and kinetics.[13] The two main theories which have been proposed to explain the induction period are the passivation layer hypothesis[14,15] and dissolution control[16,17]. Both models can phenomenologically reproduce early hydration kinetics, however, have important mechanistic distinctions that may influence admixture design criteria[12]. Dissolution control models suggest that at high undersaturation (*i.e.*, in deionized water) rapid dissolution of $Ca_3SiO_5$ forms etch pits which, after reaching a point of low undersaturation, gradually release ions into solution to form calcium silicate hydrate nucleation seeds[17]. However, a key distinction between the dissolution of $Ca_3SiO_5$ and other minerals (*i.e.*, dolomite) which appear to conform to similar models[18], is the high chemical reactivity of anhydrous $Ca_3SiO_5$ with water as quantitatively discussed by Gartner[15]. Thus,

application of dissolution control theories for cementitious systems typically require that the solubility of $Ca_3SiO_5$ in water is modified by surface hydroxylation[13,19,20] or adsorption of ionic species[12]. Consensus has been reached that initial Si concentrations drop off rapidly after the initial dissolution, consistent with either the formation of calcium silicate hydrate seeds or the precipitation of an intermediate calcium silicate hydrate surface layer.[12] Previous solid-state nuclear magnetic resonance (NMR)[21,22] and X-ray photoelectric spectroscopy (XPS)[23] analyses have indicated that these early hydrates have different compositions than the semi-crystalline calcium silicate hydrates that form post-induction period, but conventional NMR and XPS techniques are challenged by poor sensitivity or poor resolution, respectively. In hydrating cementitious mixtures, the presence of additive species including calcium silicate hydrate seeds[24], inorganic salts (*i.e.*, $CaCl_2$)[11], or organic molecules (*i.e.*, sucrose)[25] can have profound influences on the length of the induction period and on silicate hydration chemistry which remains challenging to elucidate.[26] Improved understanding of the molecular-level transformations occurring at hydrating $Ca_3SiO_5$ particle surfaces is needed to inform admixture design and to predict hydration rates in modern low $CO_2$ footprint cement formulations.

Although particle sizes or film thicknesses are conventionally measured by using scattering analyses or electron microscopy,[27,28] these methods are typically incapable of measuring length scales ca. <1 to 10's nm in heterogeneous particulate systems. These challenges are additionally exacerbated for cementitious solids due to their lack long-range order, low-particle surface areas, and poor contrast between hydrated and non-hydrated silicates. Recently, combined X-ray computed tomography and XRF elemental analysis has been used to monitor changes occurring among $Ca_3SiO_5$ particles upon hydration.[29] These

techniques can resolve physical features including changes in particle boundaries or density, but, with a pixel size exceeding 50 nm, they provide limited insights into atomic-level transformations occurring at surfaces in contact with water. By comparison, a reaction front comprised of hydration products with dimensions of *ca*. 10 nm has been observed by STEM imaging of $Ca_3SiO_5$ particles hydrated for 4 h, shortly after the end of the induction period.[30] However, any chemical transformations or morphological changes that may occur at $Ca_3SiO_5$ particle surfaces at the earliest hydration times ≤ 2.5 h remain challenging to elucidate. Compared to conventional methods for measuring film thicknesses, solid-state NMR spectroscopy allows chemically distinct species to be identified and distinguished based on relative differences in the respective local (<1 nm) environments and relaxation behaviors of constituent NMR-active nuclear spins (e.g., $^{1}H$, $^{13}C$, $^{29}Si$). Particle and domain sizes have previously been measured by using NMR experiments that rely on the transfer of polarization by the process of $^{1}H$-$^{1}H$ nuclear spin diffusion between $^{1}H$ moieties interacting via through-space dipole-dipole couplings.[31–33] Such measurements initially generate a non-equilibrium $^{1}H$ spin polarization and subsequently monitor the re-equilibration of the spin polarization, which can be modeled to estimate the dimensions of domains, for example, in complicated multicomponent polymer systems that lack long-range structural order.[34] However, preparation and detection of a $^{1}H$ spin polarization gradient within thin hydrated silicate surface layers formed on $Ca_3SiO_5$ particles is infeasible by conventional NMR techniques.

Recently developed dynamic nuclear polarization (DNP)-enhanced solid-state NMR techniques afford significantly enhanced signal sensitivity,[35,36] enabling the detection of dilute species at particle surfaces. Although conventional NMR is a bulk characterization technique that does not provide direct insights regarding the spatial distributions of components, DNP-

NMR experiments can be used to measure characteristic domain sizes ranging from <1 nm to μm's in ordered or disordered solids. In such measurements, solid particles are suspended in a frozen glassy solvent matrix (*i.e.*, glycerol/water) containing dilute amounts of a stable biradical polarizing agent as depicted in Figure 5.1. A high non-equilibrium $^{1}H$ spin polarization (hereafter referred to as hyperpolarization) is locally generated by microwave excitation of unpaired electrons contained within the biradical polarizing agent. DNP induced polarization transfer increases the net $^{1}H$ nuclear magnetization, the origin of NMR signal intensity, by a factor up to $\gamma_e/\gamma_H$ = 658 over thermal equilibrium. Once generated, $^{1}H$ hyperpolarization then propagates by $^{1}H$-$^{1}H$ spin diffusion into hydrated particle surfaces to distances ranging from <1 nm to 100's nm where it is attenuated over time by thermally driven spin-lattice relaxation. This generates a large NMR signal enhancement and transient response within the hydrated surface layer but not the anhydrous $Ca_3SiO_5$ core which is largely $^{1}H$ deficient and, thus, does not receive $^{1}H$ hyperpolarization. Specifically, the transfer, accumulation, and attenuation of $^{1}H$ hyperpolarization can be monitored by NMR experiment and subsequently modeled by classical spin thermodynamic analyses to measure a mean film thickness. This kinetic process is closely analogous to thermal energy transfer and may be regarded as a 'spin calorimetry' experiment where Zeeman energy (spin polarization) is generated with the frozen solvent matrix (the source) and is transferred to the hydrated surface layer (the sink). Such combined DNP NMR measurements and modeling analyses have been previously used to estimate sub-micron particle or domain sizes in peptide nanocrystals,[37] microcrystalline solids,[38] and pharmaceutical formulations.[39] Overall, the solid-state DNP NMR measurements can be used to generate an initial non-equilibrium $^{1}H$ polarization and

subsequently monitor the dynamics of polarization transfer and depletion in the sample, which provides insights on the dimensions of particles, layers, or domains.

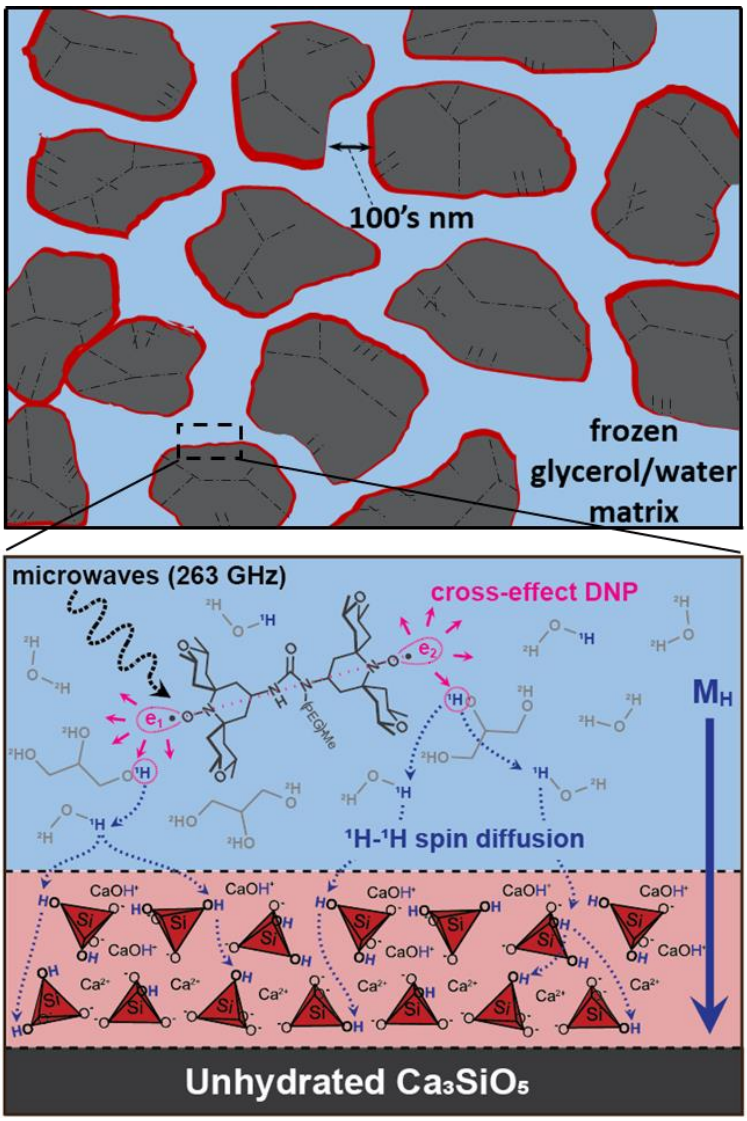


**FIGURE 5.1)** Schematic diagram of hydrated tricalcium silicate particles suspended in a partially deuterated frozen glycerol/water matrix at 100 K. Inset depicts microwave irradiation of the DNP polarizing agent, AMUPol, which has two unpaired electrons, $e_1$ and $e_2$. Cross-effect DNP transfers hyperpolarization to nearby $^1H$ nuclei (magenta), which is subsequently relayed into the hydration layer by $^1H$-$^1H$ spin diffusion (dashed blue arrow). The solid blue arrow depicts the direction of, $M_H$, the net nuclear magnetization vector.

Such analyses are especially important to establish the thicknesses and compositions of the hydrated layers at surfaces of tricalcium silicate particles, which have important effects on the progress of silicate dissolution and hydration. For tricalcium silicate, the principal component of commercial cements, anhydrous $Q^0$ silicate species at surfaces of particles with low ($\leq$1-2 $m^2/g$) mean surface areas react with water to form monomeric silanol $Q^0$(h) that subsequently yield partially cross-linked $Q^1$ and $Q^2$ species, the latter of which are associated with calcium silicate hydrates. ($Q^n$ refers to silicon atoms that are covalently connected via bridging oxygen atoms to $n \leq 4$ other silicon atoms.[40]) The calcium silicate hydrates have poor long-range structural order[41,42] that typically presents challenges for their characterization[43], but which are nevertheless crucial to understand as they are central to the development of mechanical strength in cements. In contrast to the anhydrous $Q^0$ species present in the core of the low-surface-area (<1 $m^2/g$) particles, the silanol $Q^0$(h) and hydrated ($Q^1$, $Q^2$) species are formed at silicate particle surfaces in contact with water. For early hydration times (i.e., before onset of the acceleration stage of cement hydration),[44] previous experimental and modeling studies of tricalcium silicate and related minerals have proposed the formation of a layer of hydration products at particle surfaces.[10,18,23,45] It has been suggested that this early hydration layer acts as a reactive substrate for the nucleation of calcium silicate hydrates during the acceleration period.[30] Alternatively, even for thin layers, the presence of surface hydroxylation or an intermediate hydration layer may stabilize interfacial energy and impede further tricalcium silicate dissolution after initial wetting.[13] The importance of interfacial interactions on early hydration rates is evidenced by the marked influence that additive species can have on the length of the induction period. For example, at exceedingly dilute concentrations sucrose acts as a hydration accelerator, but, at roughly monolayer coverage, it is a strong

hydration retardant.[46,47] The mechanism of action of other commonly used hydration accelerators, such as $CaCl_2$, remains largely unknown. It is hypothesized that changes in atomic-level surface compositions, dimensions, and morphology of such layers in response to additive species strongly influence subsequent dissolution and hydration processes, which consequently affect the temporal evolution of mechanical properties in cements.

Despite the importance of these hydration layers, it has been generally difficult to directly measure their mean thickness and molecular compositions, due to their poor long-range structural order, dilute quantities on low-surface-area particles, and associated dimensions that are challenging to characterize. Nevertheless, here, monoclinic tricalcium silicate hydrated under industrially relevant conditions and formulations is examined using DNP-NMR experiments and spin thermodynamic modeling analyses to monitor and evaluate the transfer of DNP-enhanced $^1$H spin polarization in the hydrated surface layers. The large DNP sensitivity improvements enable the detection of dilute silicate hydrates formed on the surface of industrially relevant $Ca_3SiO_5$ particles during the induction period. Although hydration rates are initially slow, the surface of the particles undergo hydration forming a disordered layer consisting of $Q^0$(h), $Q^1$, and $Q^2$ silicates with a characteristic domain size less than 10 nm determined by $^1$H-$^1$H spin diffusion analyses. The surface compositions of $Ca_3SiO_5$ particles hydrated without additive species are compared with those formed under similar conditions in the presence of dilute additive species (*i.e.*, $CaCl_2$, sucrose) or treatments (*i.e.*, thermal annealing) known to influence the duration of the induction period. These results provide new insights into the molecular compositions of surface hydrate layers which importantly influence hydration rates and mechanical strength development in the solidification of cementitious mixtures.

## 5.3. Materials and Methods

Anhydrous monoclinic tricalcium silicate ($Ca_3SiO_5$, Mineral Research Processing, France), 1,1,2,2,-tetrachloroethane ($C_2H_2Cl_4$, Sigma Aldrich), glycerol (Sigma Aldrich), 98 %D d8-glycerol (Sigma Aldrich), and 99.9 %D $D_2O$ (Sigma Aldrich) were used as received. Hydrated samples were prepared by mixing approximately 400 mg of the anhydrous monoclinic tricalcium silicate and Milli-Q water (water-to-solids ratio = 0.45) in polyethylene containers by using a vortex mixer operating at 3000 rpm for 2 min. The samples were subsequently maintained at 25 °C and 100 % relative humidity for times ranging from 30 min to 8 h, which correspond to hydration conditions and compositions that are similar to those in industrially relevant cement formulations. Following hydration, the pastes were solvent exchanged twice using 50 mL isopropyl alcohol (IPA) and were vacuum-dried at 0.1 bar and 40 ºC to remove the organic solvent. Solvent exchange by IPA has been previously shown to minimally influence cement microstructure and compositions.[48] The vacuum-dried hydrated samples were ground to a powder, sealed in polyethylene containers, and stored at 0.1 bar and ambient temperature in a desiccator prior to subsequent analyses.

Powder X-ray diffraction measurements were conducted on a Panalytical Empyrean powder X-ray diffractometer using Cu *K*α radiation with a wavelength of 1.54 Å. Samples of anhydrous and hydrated tricalcium silicate were scanned at 0.04°/min between 2$\theta$ angles of 5 - 70°. X-ray photoelectron spectroscopy (XPS) measurements were used to identify the elemental surface compositions of anhydrous and hydrated tricalcium silicate and were conducted on a Kratos Axis Ultra X-ray photoelectron spectroscopy system. High-resolution calcium (Ca *2p*) and silicon (Si *2p*) XPS spectra for anhydrous and hydrated tricalcium silicate were recorded between 377-358 and 92-113 eV, respectively, with a step size of 0.05 eV and

pass energy of 20 eV. BET surface area measurements (six point isotherm) were performed using a Micromeritics 3Flex Porosimeter nitrogen physisorption device with approximately 200 mg solids. Prior to collecting nitrogen adsorption isotherms, the partially hydrated $Ca_3SiO_5$ specimen were degassed under dry flowing $N_2$ at 80 °C for five hours. Solid-state $^{29}Si$ MAS NMR measurements were used to characterize the atomic structures and compositions of silicate species in tricalcium silicate. The experiments were conducted on an 11.7 T Bruker AVANCE-II spectrometer operating at frequencies of 499.84 and 99.31 MHz for $^{1}H$ and $^{29}Si$, respectively, and using a 4 mm H-X-Y triple resonance MAS probehead and zirconia rotors. One dimensional (1D) quantitative single-pulse $^{29}Si$ MAS spectra were recorded with a 4 μs $^{29}Si$ π/2 pulse, SPINAL-64 $^{1}H$ decoupling[49] (2.5 μs $^{1}H$ π/2 pulses), and a recycle delay of 500 s (~5 x $^{29}Si$ spin-lattice relaxation time).[47,50] The long recycle delays were crucial to ensure quantitativeness of the relative integrated $^{29}Si$ intensities observed in the $^{29}Si$ MAS spectrum and reflect the high degree of crystallinity of anhydrous tricalcium silicate. The $^{29}Si$ isotropic chemical shifts were referenced to tetramethylsilane, using tetrakis(trimethylsilyl)silane as a secondary standard.[51]

Solid-state dynamic-nuclear-polarization (DNP)-enhanced NMR measurements provide significantly enhanced signal sensitivity and enable the selective detection and analysis of hydrated species at silicate particle surfaces.[35,36] For quantitative measurement of hydration layer thicknesses by DNP-NMR $^{1}H$-$^{1}H$ spin-diffusion analyses, samples were prepared with an aqueous solution containing 2 mM AMUPol (stable biradical species) in partially deuterated glycerol-water (97%D, $^{1}H$ spin density of 3.5 M). For qualitative measurement of surface silicate compositions, samples were prepared using an organic solution containing 8 mM TEKPol (stable biradical species)[52] in 1,1,2,2-tetrachloroethane[53]. Each sample was

prepared using 40 mg of the dried powder with ca. 10 µl of the DNP matrix as described previously[47], and shuttled into the 100 K precooled DNP NMR probehead within 10 minutes after particle wetting. Solid-state DNP NMR measurements were conducted on a 9.4 T Bruker ASCEND NMR spectrometer operating at frequencies of 399.95 and 79.46 MHz for $^{1}$H and $^{29}$Si, respectively, using a Bruker 3.2 mm H-X-Y variable temperature MAS probehead, and under conditions of 8 kHz MAS and 100 K. The spectrometer was equipped with a cooling cabinet and 263 GHz gyrotron microwave source and waveguide system.[54] 1D $^{13}$C- or $^{29}$Si-detected $^{1}$H saturation recovery DNP NMR spectra were acquired without and with continuous microwave irradiation at 263 GHz, under otherwise identical conditions with SPINAL-64 $^{1}$H decoupling and delay times ($\tau_D$) in the range of 0.05-120 s, see pulse sequence in Figure 5.2.

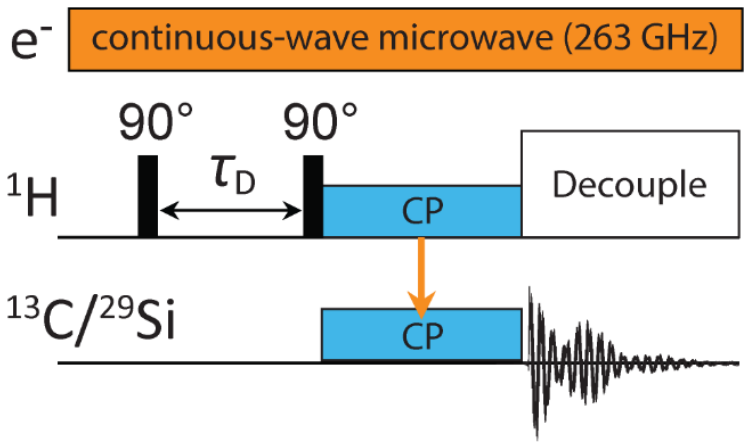


**FIGURE 5.2)** Schematic diagram of $^{13}$C- or $^{29}$Si-detected DNP CP-MAS saturation recovery experiment.

Compared to the spectra acquired with microwaves, the spectra acquired without microwave irradiation were typically recorded with greater signal averaging due to the associated lower NMR signal sensitivity in the absence of DNP. The $^{13}$C{$^{1}$H} or $^{29}$Si{$^{1}$H} DNP signal enhancements $\varepsilon(t)$ were estimated as the ratios of the $^{13}$C or $^{29}$Si signal intensity

in spectra acquired with microwaves to that without microwaves. The relaxation behaviors of the NMR-active $^{1}H$ nuclei were measured by incrementing the time delay ($\tau_D$) for seven values ranging from 10 μs to 50 s to ensure that the transient polarization build-up kinetics were adequately sampled and reached steady-state. The uncertainties associated with the steady-state $\varepsilon$ values were estimated by the propagation-of-error method by using the signal-to-noise ratios of the corresponding spectra acquired without and with continuous microwave irradiation. Steady-state analytical solutions to the spin thermodynamic models necessary for quantitative DNP NMR analyses are provided in the appendices. Alternatively, numerical finite-element analysis facilitated by Matlab pdepe solver was used to simulate the time-dependent transfer, attenuation, and accumulation of hyperpolarization in the hydrated surface layers.

## 5.4. Long-range and local structures of hydrating silicate particles

The reaction of tricalcium silicate with water at early hydration times results in the formation of dilute quantities of hydration products at particle surfaces. Monoclinic tricalcium silicate is the primary (50-70 wt%)[55] component of commercial cement mixtures and is therefore a representative example to measure and elucidate the compositions and mean thickness of layers of hydration products formed at particle surfaces. Complementary X-ray diffraction, X-ray photoelectron spectroscopy, BET nitrogen sorption, in-situ calorimetry, and solid-state NMR spectroscopy measurements were used to probe the bulk and surface of tricalcium silicate particles hydrated for short times (30 min to 8 h). For example, the hydration of $Ca_3SiO_5$ is exothermic and can be monitored by in-situ calorimetry as shown in Figure 5.3a. In the calorimetry curve, there is an initial heat release attributed to particle

wetting and rapid dissolution, followed by an induction period lasting approximately 2.5 h characterized by a period of low heat evolution. Additionally, the BET surface area of partially hydrated $Ca_3SiO_5$ particles shown in Figure 5.3b. remains relatively constant at ~1.2 $m^2/g$ over the course of the induction period.

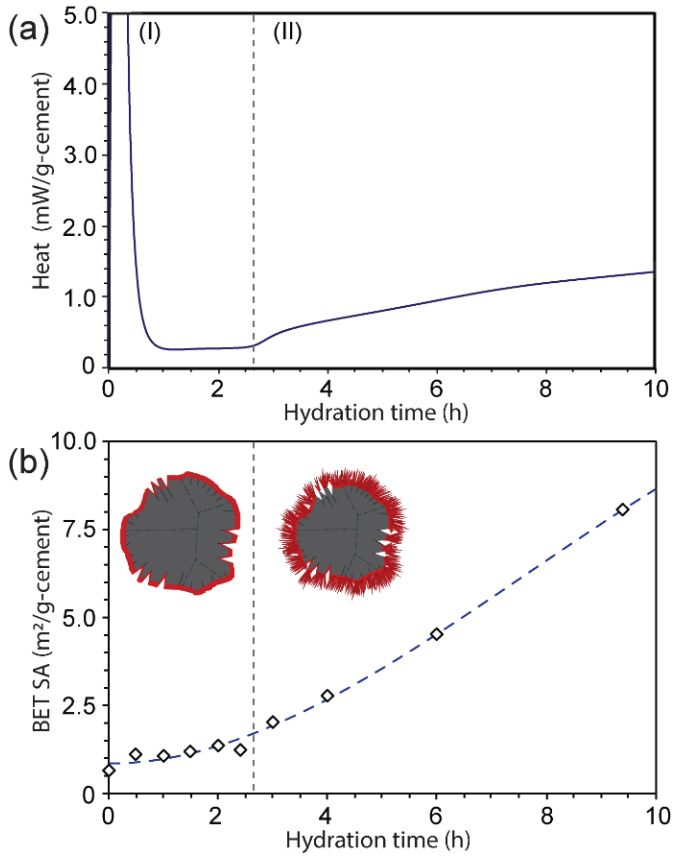


**FIGURE 5.3)** Bulk analysis of early hydration (<10 h) including (a) *in situ* calorimetry of monoclinic $Ca_3SiO_5$ at w/s = 0.40 and 25 °C, (b) BET surface area of vacuum-dried monoclinic $Ca_3SiO_5$ hydrated at w/s = 0.45 and 25 °C as described in the methods section. Calorimetry is used to identify the (I) induction and (II) acceleration period, respectively.

This is consistent with previous studies of the early hydration of $Ca_3SiO_5$ by electron microscopy which indicate that the surface remains relatively 'smooth' or morphologically unaltered during the induction period.[30] Regardless of the mechanistic origin of the induction period, the onset of the acceleration period corresponds to an increase in particle surface areas

leading to greater nucleation rates and renewed dissolution[12]. This is observed in Figure 5.3a-b., after 2.5 h, there is an increase both in heat evolution and the BET surface area that may be attributed to the roughening of particle surfaces and nucleation of calcium silicate hydrates as schematically depicted in the inset. Based on previous studies of early cement pastes, it is expected that the surface area will reach a maximum and decline as the calcium silicate hydrate gel network densifies. These later hydration processes are comparatively well understood and are discussed in more detail elsewhere.[6] However, as discussed above, insights into the origins of the induction period are lacking due to the inability of conventional characterization techniques to resolve dilute silicate hydrates formed on low-surface area $Ca_3SiO_5$ particles.

For example, the powder X-ray diffraction patterns of anhydrous and hydrated (4 h, 25 °C) tricalcium silicate shown in Figure 5.4a,d exhibit multiple strong reflections, which are indexable to the monoclinic polymorph of anhydrous tricalcium silicate, as shown by the red markers.[56] In addition, the patterns display no detectable reflections from calcium silicate hydrates and calcium hydroxide, which are the primary products of silicate hydration. This indicates that such hydrated species exhibit poor long-range structural order and/or are associated with crystalline domain (particle) sizes that are below the detection limits of the diffraction measurements. Specifically, the former is consistent with the typically broad and weak reflections from calcium silicate hydrates that have previously been observed in scattering measurements, even for high-energy synchrotron X-rays.[41,57] The diffraction analyses indicate that there are no detectable quantities of hydration products associated with long-range structural order.

In contrast to X-ray diffraction that is sensitive to repeating periodic order, X-ray photoelectron spectroscopy (XPS) measurements provide insights on the elemental compositions at particle surfaces. Specifically, such measurements can measure the binding energies of different atoms located up to a depth of 10 nm from the particle surface, including for hydrating tricalcium silicate. For example, the Calcium *2p* high-resolution XPS spectra are shown in Figure 5.4b,e for anhydrous and hydrated tricalcium silicate, respectively. Each of the spectra exhibit peaks corresponding to identical (within ±0.1 eV) binding energies at 347.0 and 350.6 eV from Calcium $2p_{3/2}$ and $2p_{1/2}$, respectively, which are assigned based on previous XPS analyses of similar hydrating silicates.[21] Similarly, the Silicon *2p* high-resolution XPS spectra for the same anhydrous and hydrated (4 h, 25 °C) tricalcium silicate samples are shown in Figure 5.4c,f, each of which exhibit a single resolved peak at 101.7 eV.

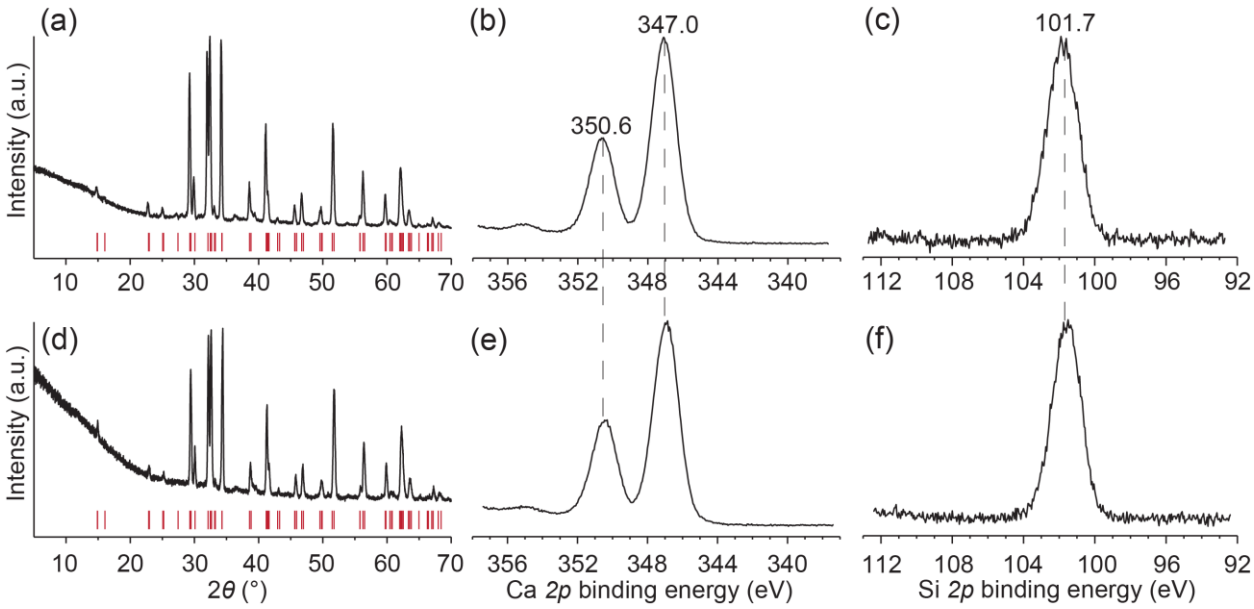


**FIGURE 5.4)** (a,d) Powder X-ray diffraction patterns, (b,e) Calcium (Ca) *2p* and (c,f) Silicon (Si) *2p* high-resolution XPS spectra of (a,b,c) anhydrous and (d,e,f) hydrated (4 h, 25 °C) tricalcium silicate. The reflections in (a,d) are indexable to the monoclinic polymorph of tricalcium silicate, as indicated by red markers.

In combination, the Calcium *2p* and Silicon *2p* XPS analyses indicate that there are no detectable differences between the surface calcium and silicon elemental compositions of the initial tricalcium silicate particles and those hydrated for 4 h at ambient temperature conditions.

Compared to X-ray diffraction and XPS analyses, the silicate structures and compositions of the hydrated tricalcium silicate can be interrogated at the atomic-level by using solid-state NMR spectroscopy, which is sensitive to the local bonding environments around the NMR-active $^{29}$Si isotope. Specifically, solid-state 1D single-pulse $^{29}$Si MAS NMR measurements allow the different types of anhydrous and hydrated $^{29}$Si silicate species to be identified and quantified based on their resolved $^{29}$Si signal intensities. For example, the quantitative single-pulse $^{29}$Si MAS spectrum of anhydrous tricalcium silicate shown in Figure 5.5a exhibits several broad overlapping $^{29}$Si signals in the range of -66 to -76 ppm that are associated with different anhydrous $Q^0$ species,[50,58] consistent with the eighteen chemically inequivalent crystallographic silicon sites in monoclinic tricalcium silicate.[59] The broad linewidths of the $^{29}$Si signals reflect a distribution of local $^{29}$Si environments that arise from the eighteen different $^{29}$Si sites and also result from the presence of impurity ions (e.g., $Mg^{2+}$, $Sr^{3+}$), which are often used during high-temperature (>980 °C) synthesis of monoclinic tricalcium silicate to ensure its stability at ambient temperature and pressure conditions.[55] Similar $^{29}$Si NMR measurements of hydrated tricalcium silicate are used to identify the types of $^{29}$Si species formed as a result of hydration and establish their respective relative populations. Specifically, Figure 5.5b shows the quantitative single-pulse $^{29}$Si MAS spectrum of hydrated (4 h, 25 °C) tricalcium silicate that exhibits strong $^{29}$Si signals from anhydrous $Q^0$ silicate species, similar to those observed for anhydrous tricalcium silicate (Figure 5.5a). By

comparison, the spectrum reveals weak $^{29}$Si signals centered at -79 and -84 ppm from hydrated $Q^1$ and $Q^2$ species, respectively, in calcium silicate hydrates, which are the primary products of silicate hydration.[60] The calcium silicate hydrates are composed of poorly ordered and partially cross-linked four-coordinate silicon moieties, as shown schematically in the inset of Figure 5.5a. Importantly, the relative populations of different $^{29}$Si species can be estimated by comparing the relative integrated intensities of their respective signals in the single-pulse $^{29}$Si MAS spectrum in Figure 5.5b.

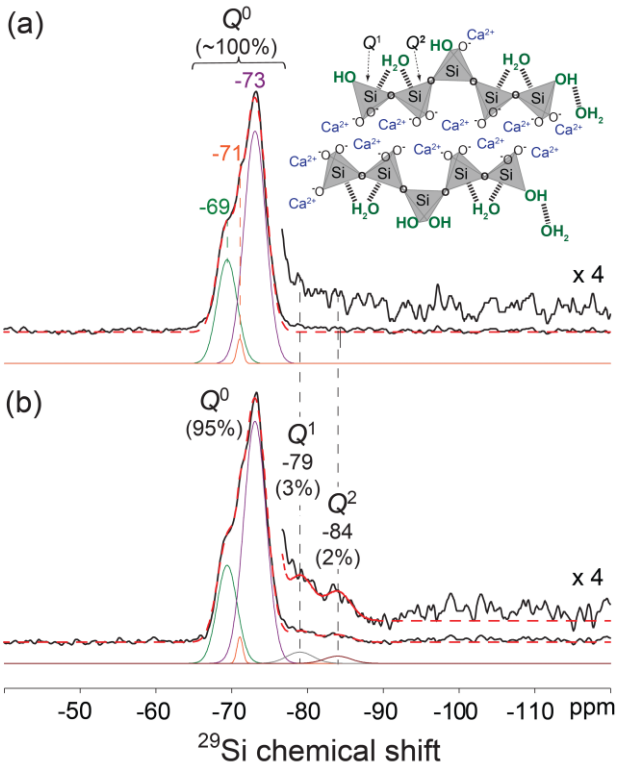


**FIGURE 5.5)** Solid-state quantitative 1D single-pulse $^{29}$Si MAS NMR spectra of (a) anhydrous and (b) hydrated (4 h, 25 °C) tricalcium silicate. The inset shows a schematic diagram of calcium-silicate-hydrates, along with the associated different partially cross-linked $Q^1$ and $Q^2$ four-coordinate $^{29}$Si moieties. The spectra were acquired at 11.7 T, 25 °C, 8 kHz MAS, and using a long (500 s) recycle delay between successive scans to ensure quantitativeness of the integrated signal intensities.

Such an analysis yields estimates of 95% (±2%), 3% (±2%), and 2% (±1%) for the anhydrous $Q^0$, hydrated $Q^1$, and hydrated $Q^2$ species, which indicates that 5% (±3%) of the initially anhydrous $Q^0$ species have transformed to form calcium silicate hydrates after hydration at 25 °C for 4 h. The quantitative $^{29}$Si NMR analyses enable the detection and quantification of dilute relative fractions of hydration products that are formed upon hydration of silicate particles, even after short times, which are otherwise undetectable in the X-ray diffraction measurements due to their poor long-range order.

## 5.5. Dimensions of hydrated layers on silicate particles

While the preceding $^{29}$Si NMR measurements provide insights on the atomic structures and bulk compositions of silicate particles at early hydration times, they require prohibitively long (~2 days) measurement times and provide limited insights regarding the compositions or spatial distributions of silicate species at particle surfaces. Nevertheless, solid-state dynamic-nuclear-polarization (DNP)-enhanced MAS NMR techniques provide significantly enhanced signal sensitivity that enables the selective detection of dilute species, including those present at low-surface-area (<1-2 $m^2/g$) silicate particles. For such experiments, powdered samples of hydrated tricalcium silicate were combined with minimal volumes of a solution of AMUPol (stable nitroxide biradical) in partially deuterated glycerol-water (the DNP-solvent matrix),[53] as discussed in the methods section. During the experiment, the dilute biradical polarizing agent is excited by high frequency (263 GHz) continuous microwave irradiation which generates large amounts of $^1$H spin hyperpolarization. This $^1$H hyperpolarization is then propagated by spontaneous $^1$H-$^1$H spin diffusion to other $^1$H nuclei in proximate solvent molecules (*i.e.*, $^1$H-containing glycerol or water), which serves as a reservoir for the

accumulation of DNP-enhanced $^{1}H$ spin polarization. Partial deuteration of the glycerol-water matrix is desirable to minimize the attenuation of $^{1}H$ hyperpolarization due to thermally driven spin-lattice relaxation processes. From this $^{1}H$-containing reservoir (the glycerol-water matrix), hyperpolarization is relayed to $^{1}H$ nuclei present at the surface of the hydrated layer, including structural water and hydroxyl groups, and subsequently transferred deeper into the surface hydration products via $^{1}H$-$^{1}H$ spin diffusion, as shown by the dashed blue arrows in Figure 5.1. Importantly, $^{1}H$-$^{1}H$ spin diffusion only relays hyperpolarization into the hydration product layer that is abundant in $^{1}H$ spins and not to the dense anhydrous interiors of the $Ca_3SiO_5$ particles, the latter of which is $^{1}H$ deficient. The build-up of $^{1}H$ hyperpolarization within the hydration layer is monitored by a $^{29}Si$-detected cross-polarization[61] experiment that results in the dipolar mediated transfer of DNP-enhanced $^{1}H$ polarization to nearby $^{29}Si$ nuclei. Overall, DNP NMR techniques provide significantly enhanced signal sensitivity that enables the selective detection of dilute silicate hydrates formed on particle surfaces. From which, the transient accumulation of $^{1}H$ hyperpolarization can be monitored and related, by quantitative $^{1}H$-$^{1}H$ spin diffusion analyses, to estimate the thickness of the hydrated surface layers.

Detailed information regarding the nanoscale thickness of the hydration layers can be extracted from DNP-NMR measurements using classical spin thermodynamic models that describe the generation, propagation, and dissipation of $^{1}H$ hyperpolarization. This approach can be regarded as a '$^{1}H$ spin calorimetry' experiment where the equilibration of $^{1}H$ hyperpolarization between the DNP solvent matrix and hydration layer depend on spin thermodynamic properties that can be experimentally modulated to optimize both signal and temporal contrast. For a given DNP matrix formulation, the amount of energy generated by microwave excitation is a function of the $^{1}H$ spin density and biradical concentration as

discussed in Chapter three. When the DNP matrix is in contact with a polarization sink (the hydration layer), the reservoir of $^{1}$H hyperpolarization in the source is depleted and this energy difference is taken up by the sink. Importantly, the effective penetration depth of $^{1}$H hyperpolarization into the hydration layer is represented by a characteristic diffusion length scale, $L = (\mathcal{D}_{H} T_1)^{1/2}$, with respect to the $^{1}$H-$^{1}$H spin diffusion coefficient ($\mathcal{D}_{H}$) and the spin-lattice relaxation time ($T_1$) of the hydrated layer. Recently, a value of $\mathcal{D}_{H} = 1.2 \cdot 10^{-16}$ m$^2$s$^{-1}$ has been directly measured for hydrated tricalcium silicate by means of a $^{17}$O hole-burning experiment.[62] Under the low-temperature (100 K) conditions of this experiment, the hydration layer has a spin-lattice relaxation time, $T_1 = 1.5$ s, as independently measured by $^{1}$H saturation recovery measurements of the hydrated tricalcium silicate particles at 9.4 T and 8 kHz MAS. Together, these quantities yield a characteristic diffusion length scale, $L = 13$ nm, which is the distance into the hydration layer over which $^{1}$H hyperpolarization is significantly attenuated, beyond which NMR signal enhancements ($\varepsilon$) are diminished. In addition to the measured signal enhancements, there is a kinetic response in the relaxation behavior of $^{1}$H spins in the hydrated layer due to $^{1}$H hyperpolarization conduction from the DNP matrix. For the experiment, temporal contrast is enhanced, at the expense of signal sensitivity, by using low 2 mM AMUPol concentrations such that the characteristic times of, $T_{DNP} = 27$ s, for the DNP matrix and, $T_1 = 1.5$ s, for the hydrated layer are substantially different. Importantly, the extent to which these media are influenced by coupled $^{1}$H-$^{1}$H spin diffusion processes depends on their mutual propensities to conduct and receive spin polarization.

For quantitative analyses of DNP-NMR experiments, classical spin thermodynamic models give a relationship between the Zeeman energy and polarization in a manner analogous to the relationship between thermal energy and temperature. The Zeeman energy

refers to the potential energy experienced by a spin ensemble in the presence of a static magnetic field, which maintains a Boltzmann distribution of spin states yielding net nuclear magnetization, the origin of NMR signal intensity. Microwave excitation of the biradical polarizing agent results in the transfer of Zeeman energy to nearby $^1$H nuclei generating large amounts of $^1$H hyperpolarization that propagates by $^1$H-$^1$H spin diffusion which is subsequently attenuated back to thermal equilibrium by $T_1$ relaxation processes. For hyperpolarization transfer between the DNP matrix (region '*M*') and the hydration layer (region '*S*'), the process is analogous to energy conduction through a series of thermal resistances and can be treated similarly such that:

$$\rho_{\mathrm{H},M} C_{\mathrm{z}} \frac{\partial \tilde{P}_M}{\partial t} = \nabla \cdot \left(\rho_{\mathrm{H},M} C_{\mathrm{z}} \mathcal{D}_{\mathrm{H},M} \nabla \tilde{P}_M\right) - \rho_{\mathrm{H},M} C_{\mathrm{z}} \frac{\left(\tilde{P}_M - \Pi_M\right)}{T^o_{DNP,M}} \qquad (5.1)$$

$$\rho_{\mathrm{H},S} C_{\mathrm{z}} \frac{\partial \tilde{P}_S}{\partial t} = \nabla \cdot \left(\rho_{\mathrm{H},S} C_{\mathrm{z}} \mathcal{D}_{\mathrm{H},S} \nabla \tilde{P}_S\right) - \rho_{\mathrm{H},S} C_{\mathrm{z}} \frac{(\tilde{P}_S - 1)}{T^o_{1,S}} \qquad (5.2)$$

Equation (5.1) and (5.2) are coupled differential equations representing spin polarization analogues to the heat equation. While these expressions contain spin thermodynamic and transport properties unfamiliar to most disciplines, such properties are either known explicitly or can be independently determined by NMR experiment[63]. For instance, the normalized spin polarization in the DNP matrix, $\tilde{P}_M(z,t)$, and hydrated surface alteration layer, $\tilde{P}_S(z,t)$, are the object functions and correspond to unity when the spin system is at thermal equilibrium. The $^1$H spin density of the DNP matrix, here $\rho_{\mathrm{H},M}$ = 3.5 M, is controlled by partial deuteration and is, $\rho_{\mathrm{H},S} \approx 16$ M, for calcium silicate hydrates prepared in $H_2O$ having a typical H/Si ratio of 1.3.[64] It is assumed for subsequent analyses that there is negligible H/D exchange during the brief DNP sample preparation period detailed in the methods section. The Zeeman heat

capacity is $C_z$ = 2.54x10$^{-2}$ J/mol per $^1$H polarization-level at a constant magnetic field strength of 9.4 T. Reference values for the $^1$H-$^1$H spin-diffusion coefficient (m$^2$s$^{-1}$) in rigid organic solids, $\mathcal{D}_{\mathrm{H},M}(\rho_{\mathrm{H},M})$ = 5·10$^{-16}$($\rho_{\mathrm{H},M}$/70 M)$^{1/3}$, and calcium silicate hydrates, $\mathcal{D}_{\mathrm{H},S}$ = 1.2·10$^{-16}$, have been measured previously and may be expected to scale with respect to the cube root of the $^1$H spin density.[63] The $^1$H spin-lattice relaxation time, $T_{1,S}^{o}$ = 1.5 s, of the hydrated tricalcium silicate samples gives the rate at which hyperpolarization is dissipated. Conversely, the characteristic DNP build-up time, $T_{DNP,M}^{o}$= 27 s, of the glycerol-water matrix gives the effective rate at which hyperpolarization is generated. For the DNP matrix formulation used here, as previously reported {cite PCCP}, the polarization-level generated in the matrix, $\Pi_M$, corresponds to either $\Pi_M$(on) = 125 or $\Pi_M$(off) = 0.51 in the presence or absence of microwave irradiation, respectively. Importantly, application of Equation (5.1) and (5.2) to obtain characteristic domain sizes (*i.e.*, the thickness of the hydration layer) requires a physically justified model geometry describing the material system.

For a suspension of hydrated tricalcium silicate particles in a glycerol-water matrix, it is anticipated that the particles will be distributed similarly to that of a saturated cement paste. As shown in the schematic diagram in Figure 5.1, the particles are depicted to be fully wetted with some extent of particle aggregation. Selecting solvent systems that minimize particle aggregation or capillary bridging is important, because the volume of DNP solvent around each particle serves as a $^1$H hyperpolarization reservoir. Thus, each particle is assumed to be uniformly coated by the aqueous DNP matrix with an effective solvent thickness, $\Delta L \approx V/A$, where $V$ is the total solvent volume and $A$ is the total particle surface area. For a solvent/solid ratio of 0.25 μL/mg, the effective solvent thickness, $\Delta L$, is expected to be ~200 nm for the measured BET surface areas (~1.1 m$^2$/g in Figure 5.3b). Due to the low-particle surface areas

and the limited amount of hydration products formed at early times (<2.5 h), the hydration layer is approximated by 1D slab geometry, see Figure 5.6a-b. The unknown hydration layer thickness, $\delta$, corresponds to the mean thickness of silanol $Q^0$(h) and hydrated $Q^1$ and $Q^2$ silicates formed on the particle surface. For solution of the coupled differential equations Equation (5.1) and (5.2), the boundary and initial conditions are given:

$$\tilde{P}_S(z,0) = \tilde{P}_M(z,0) = 0, \tag{5.3}$$

$$\tilde{P}_S(\delta,t) = \tilde{P}_M(\delta,t), \tag{5.4}$$

$$\rho_{\mathrm{H},S} C_{\mathrm{z}} \mathcal{D}_{\mathrm{H},S} \frac{\partial \tilde{P}_S(\delta,t)}{\partial z} = \rho_{\mathrm{H},M} C_{\mathrm{z}} \mathcal{D}_{\mathrm{H},M} \frac{\partial \tilde{P}_M(\delta,t)}{\partial z}, \tag{5.5}$$

$$\frac{\partial \tilde{P}_S(0,t)}{\partial z} = 0, \tag{5.6}$$

$$\frac{\partial \tilde{P}_M(\delta + \Delta L_{\mathrm{eff}},t)}{\partial z} = 0, \tag{5.7}$$

where the initial condition, Equation (5.3), corresponds to the pulse sequence in Figure 5.2. A representative steady-state solution to the spatial polarization profile, $\tilde{P}_S(z, t\rightarrow\infty)$, within the hydration layer and, $\tilde{P}_M(z, t\rightarrow\infty)$, within the DNP solvent matrix is shown in Figure 5.6b. The interfacial boundary conditions[31] are analogous to those in heat conduction processes, such that the polarization and energy flux are continuous across the solvent-solid interface, as in Equation (5.4) and (5.5), respectively. At the internal boundary of the hydration layer, $z$ = 0, there is a zero-flux condition, Equation (5.6), since the unhydrated $Ca_3SiO_5$ core does not conduct spin polarization. Between neighbouring particles in the DNP solvent matrix, $z$ = $\delta$+$\Delta L$, there is a local maximum, Equation (5.7), in the spatial polarization profile. Although the microstructure of hydrating cement pastes is complex, especially after the induction period

(>2.5 h), this model allows for quantitative interpretation of the DNP-NMR results which puts constraints on the mean thicknesses of surface hydration layers formed in contact with water.

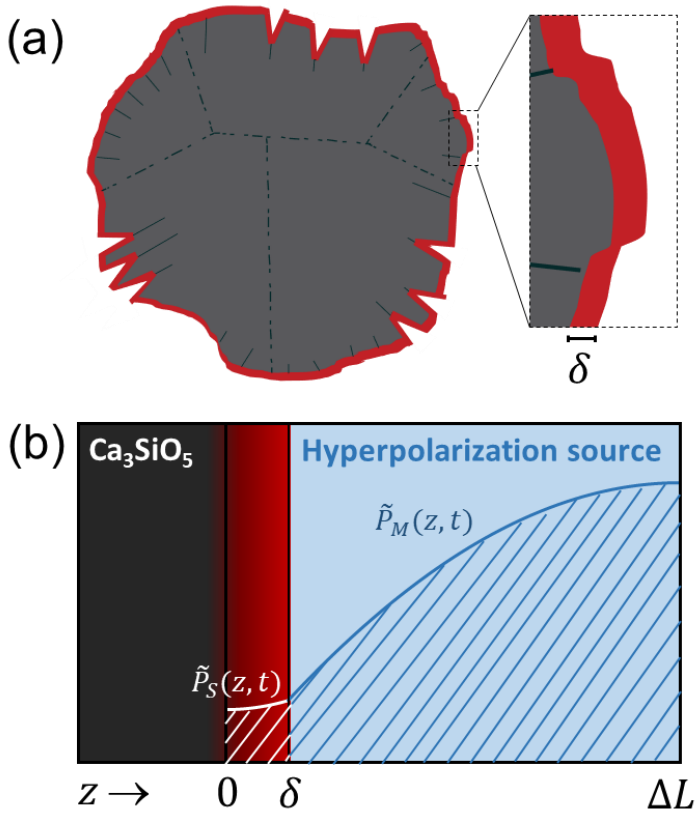


**FIGURE 5.6)** Schematic diagram of (a) the 1D slab approximation where the red film corresponds to a thin layer of silanol $Q^0$, hydrated $Q^1$, and hydrated $Q^2$ silicates on the surface of a tricalcium silicate grain; and (b) a representative spatial $^1$H polarization profile within, $\tilde{P}_M(z)$, the DNP solvent matrix and, $\tilde{P}_S(z)$, within the hydration layer.

By measuring and comparing $^{13}$C intensity arising from the DNP solvent matrix and $^{29}$Si intensity arising from the hydration layer in the presence and absence of microwave irradiation the transient accumulation of $^1$H hyperpolarization may be monitored in each region. It is not typically possible to measure spatial polarization profiles $\tilde{P}_S(z,t)$ or $\tilde{P}_M(z,t)$, instead the measured NMR signal enhancements $\varepsilon_S(t)$ and $\varepsilon_M(t)$ are related to the net nuclear magnetization ($M_H$) which is proportional to, $M_{H,i} \propto \rho_{H,i}\tilde{P}_i$, the product of the $^1$H spin density

and polarization level. Specifically, $\varepsilon_S(t)$ or $\varepsilon_M(t)$ values are measured by comparing the intensity of $^{29}Si\{^1H\}$ or $^{13}C\{^1H\}$ DNP CP-MAS spectra, respectively, acquired in the presence and absence of microwave irradiation. For the DNP solvent matrix, the $\varepsilon_M(t)$ enhancement is obtained by integrating $\tilde{P}_M(z,t)$ over $\delta < z < \delta + \Delta L$ by the relation,

$$\varepsilon_M(t) = \frac{\int_{\delta}^{\delta+\Delta L} \rho_{H,M} \tilde{P}_{M,\text{on}}(z,t) A dz}{\int_{\delta}^{\delta+\Delta L} \rho_{H,M} \tilde{P}_{M,\text{off}}(z,t) A dz}, \tag{5.8}$$

noting that the only difference between the microwave on and microwave off case determined by Equation (5.1) and (5.2) is the effective polarization levels generated in the DNP solvent matrix, $\Pi_M$(on) = 125 or $\Pi_M$(off) = 0.51 for each condition, respectively. In Equation (5.8), the integral for 1D slab geometry also includes, *A*, the particle surface area and, $\rho_{H,M}$, the $^1H$ spin density of the glycerol-water matrix. For the hydration layer, the $\varepsilon_S(t)$ enhancement is obtained by integrating $\tilde{P}_S(z,t)$ over $0 < z < \delta$ by the relation,

$$\varepsilon_S(t) = \frac{\rho_{H,0} V_0 + \int_0^{\delta} \rho_{H,S} \tilde{P}_{S,\text{on}}(z,t) A dz}{\rho_{H,0} V_0 + \int_0^{\delta} \rho_{H,S} \tilde{P}_{S,\text{off}}(z,t) A dz}, \tag{5.9}$$

which is calculated similarly to Equation (5.8). The additional term, $\rho_{H,0}V_0$, reflects that, although the unhydrated $Ca_3SiO_5$ core is largely $^1H$ deficient, there is some amount of $^1H$ moieties present that contribute to the measured signal intensity, but which do not receive $^1H$ hyperpolarization from the DNP matrix. Quantitative $^1H$ spin counting experiments of unhydrated tricalcium particles (see appendices) indicate that the particles have a $^1H$ spin density of $\rho_{H,0}$ = 0.14 ±0.07 M (roughly 1 H per 100 $Ca_3SiO_5$) that may be associated with hydrated lime, silanol impurities, or bound water within internal grain boundaries or defect sites; this $\rho_{H,0}$ value corresponds to ~40 ppm by mass which is similar to H contents of

nominally anhydrous minerals in the Earth's mantle. Considering that the internal particle volume is much larger than the volume of the hydration layer at early times, $V_0 >> A\delta$, these contributions to the NMR spectra must be accounted for as in Equation (5.9). The weight-averaged particle size of the unhydrated tricalcium calcium used here, determined by laser scattering, is $D_p$ = 8.6 μm which is used to estimate $V_0$ assuming that the particles are spherical. Nondimensionalized steady-state analytical solutions to Equation (5.8) and (5.9) are provided in appendices and can be directly fit to experimental NMR signal enhancements.

To determine values for the mean hydration layer thickness, 1D $^{13}C\{^1H\}$ and $^{29}Si\{^1H\}$ DNP CP-MAS saturation recovery experiments were acquired for tricalcium silicate particles hydrated from 30 min to 8 h. Comparison of the spectra acquired without and with microwave irradiation indicates that the latter exhibits significantly greater $^{13}C$ or $^{29}Si$ signal intensity, which reflects the sensitivity improved afforded by DNP NMR. Specifically, the enhanced sensitivity can be quantified by comparing the ratio of intensity between spectra acquired with and without microwave irradiation, which corresponds to $\varepsilon_{S,\infty}$ = 25 (±3) and $\varepsilon_{M,\infty}$ = 116 (±6) for Figure 5.7a (Top) and 5.7a (Bottom), respectively. In Figure 5.7b and 5.7c, the steady-state $\varepsilon_{S,\infty}$ and $\varepsilon_{M,\infty}$ enhancements were fit to the corresponding analytical solutions (see appendices) by varying the fitting parameters, $\delta$, the hydration layer thickness and, $\Delta L$, the effective solvent layer thickness. The effective solvent layer thickness, $\Delta L$, is varied to account for increases in particle surface area and minor solvent losses that occur during preparation (here, typically ~10 to 20 w% solvent). The obtained values for the hydration layer thickness are within, $\delta$ = 3.5 ± 1.1 nm, for tricalcium silicate particles hydrated at 0.5 h, 1 h, 2 h, 3 h, and 4 h. Notably, for a 40 mg sample size, in order to overcome thermally driven relaxation and maintain an enhancement factor of, $\varepsilon_{S,\infty}$ = 20, approximately 1 - 2 μW of

Zeeman energy over time must be supplied to $^1$H spins within the hydration layer. This power requirement, $Q$, is equal to the dissipation term in Equation (5.2) integrated over $0 < z < \delta$ such that:

$$Q = \int_0^{\delta} \rho_{\mathrm{H},S} C_{\mathrm{z}} \frac{(\tilde{P}_S(z,\infty) - 1)}{T_{1,S}^o} A dz \,. \tag{5.10}$$

Although the absolute power consumption is minuscule, it is drawn from the surrounding DNP matrix resulting in the partial depletion of the $^1$H hyperpolarization reservoir as observed experimentally in Fig. 5.7c and depicted schematically in Fig. 5.6b. In the absence of a relaxation sink, the DNP solvent matrix has a measured enhancement, $\varepsilon_{\mathrm{M},\infty} \equiv \Pi_M(\mathrm{on})/\ \Pi_M(\mathrm{on}) = 250$, compared to $\varepsilon_{\mathrm{M},\infty} \approx 80$ to 120 observed in these particle suspensions. By Equation (5.10), if H/D exchange occurs (*i.e.*, lower $\rho_{\mathrm{H},S}$ values), this reduces the power requirement to maintain the hyperpolarization profile, $\tilde{P}_S(z,\infty)$, such that, in this circumstance, the extracted $\delta$ values above underestimate the hydration layer thickness. Nevertheless, the fitted $\delta$ and $\Delta L$ values were subsequently used to numerically simulate the transient $^1$H build-up kinetics associated with the hydration layer to improve confidence in the fitted values, see Figure 5.8. The measured intensity build-up profile is less sensitive to changes in $\delta$ over the range of 0.4 nm to 40 nm in comparison to the enhancement factor but exhibits satisfactory agreement with the estimated value of $\delta \sim 4$ nm. Some deviation from model predictions is expected since a slab approximation does not accurately represent the distribution of DNP solvent matrix around solid particles. These results provide strong evidence that there is a thin film of hydrated silicates formed on tricalcium silicate particles, even at the earliest hydration times (<2.5 h), which consume $^1$H hyperpolarization from the surrounding DNP solvent matrix. Physically, values of $\delta \approx 4$ nm suggest that, during early hydration times, the reaction

front at particle surfaces in contact with water does not advance appreciably within the sensitive detection limits of the measurement.

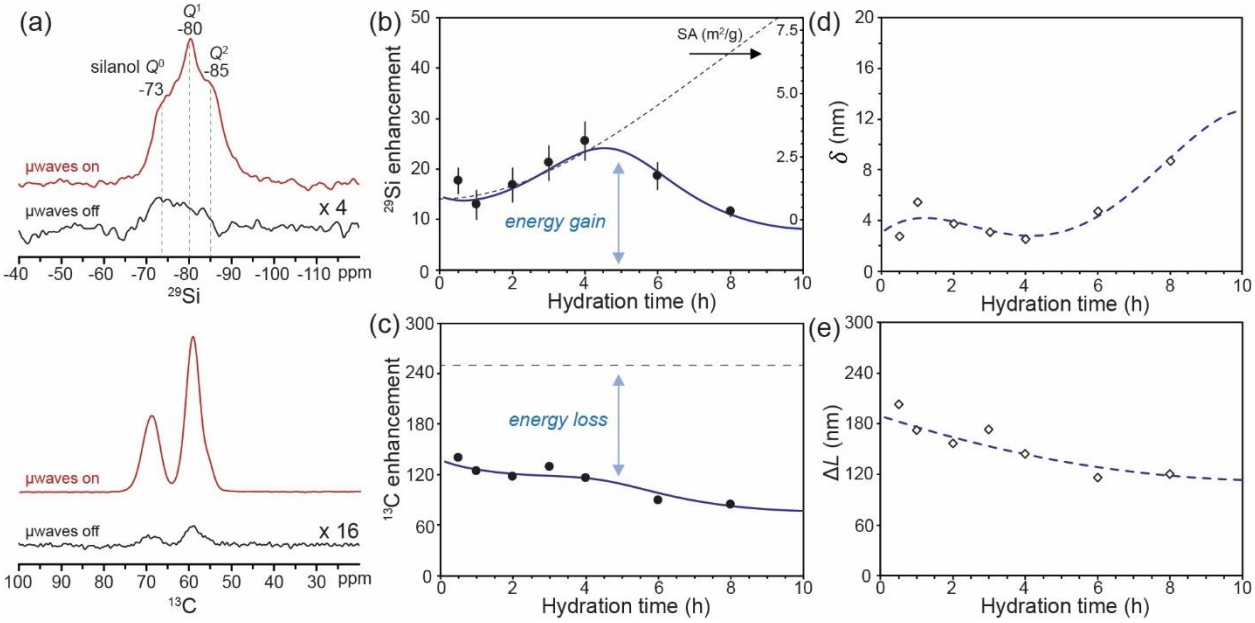


**FIGURE 5.7)** (a) Solid-state 1D $^{29}Si\{^{1}H\}$ DNP CP-MAS NMR of hydrated (4 h, 25 °C) $Ca_3SiO_5$ (Top), and 1D $^{13}C\{^{1}H\}$ DNP CP-MAS NMR of the glycerol/water matrix (Bottom). Model fit (solid blue line) to measured (b) DNP signal enhancement in hydrated $Ca_3SiO_5$, (c) DNP signal enhancement in frozen glycerol/water matrix. Extracted values for the (d) hydrated layer thickness, $\delta$, and (e) the matrix thickness, $\Delta L$, coating each particle. In (d,e) diamonds correspond to values calculated from the data in (b,c), while the dashed blue lines are used to generate the model fit in (b,c).

After approximately 2.5 h of hydration, coinciding with the end of the induction period, there is an increase in particle surface areas. The dependence of the $\varepsilon_{S,\infty}$ enhancement value on hydration time is strongly correlated to, $A$, the particle surface area as shown in Equation (5.9). Interestingly, although the surface area continues to increase, the measured $\varepsilon_{S,\infty}$ enhancement values decrease beyond 4 h suggesting that denser hydration products are formed beyond the solvent-particle interface. Specifically, decreasing $\varepsilon_{S,\infty}$ values establish that

the ratio between the amount of exposed hydration products formed on the external surface and those formed within the particle interior is also decreasing. Commonly, hydration products formed at later times are distinguished as 'outer' or 'inner' products whether they exist outside or within the original particle grain boundaries, respectively. At later hydration times (*i.e.*, 8 h), the slab approximation is a poorer representation of the particle surfaces, nevertheless the model results suggest that the mean hydration layer thickness increases to $\delta$ ~10 nm. Monitoring the compositions of the advancing hydration beyond >8 h hydration by the present technique is challenging because the DNP-enhanced $^{29}$Si spectra is overwhelmingly dominated by signal contributions from products on the external surface. Moreover, the notion of a hydration layer, as it applies to the compositions and thicknesses of a film of hydration products formed at the surface, is likely less pertinent during the period of accelerated hydration. Recently, other techniques and methods of analysis have been developed to characterize the evolving cement microstructure during this time which has been aptly described as a fractal colloidal gel.[65] The advantage of DNP-NMR is that it affords improved sensitivity and high chemical resolution capable of monitoring atomic-level transformations occurring at or near the solvent-particle interface at early (< 2.5 h) hydration times that challenge the sensitivity or resolution of other techniques.

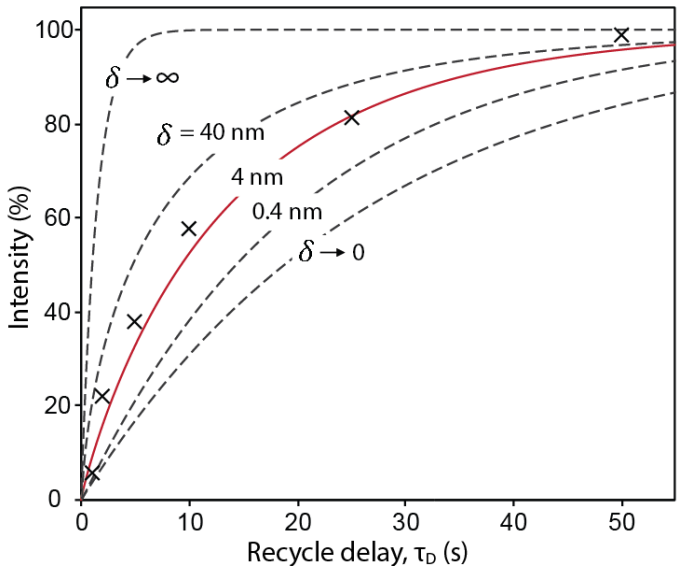


**FIGURE 5.8)** Solid-state 1D $^{29}$Si{$^{1}$H} DNP CP-MAS NMR saturation recovery experiment of hydrated (2 h, 25 °C) Ca3SiO5 overlaid with simulated intensity build-up profiles for $\Delta L$ = 160 nm and different values of, $\delta$, the hydration layer thickness. In the limit of $\delta \rightarrow \infty$ and $\delta \rightarrow 0$, characteristic build-up times approach values of $T_1$ = 1.5 s and $T_{DNP,M}$ = 27 s, respectively.

## 5.6. Compositions of hydrated layers on silicate particles

The For low-surface-area tricalcium silicate particles hydrated for short times (<2.5 h), the enhanced sensitivity of DNP NMR techniques enables the detection of dilute silanol $Q^0$(h) and hydrated $Q^1$ and $Q^2$ surface species, which are otherwise challenging to identify and resolve. Previous 1D $^{29}$Si single-pulse or $^{29}$Si{$^{1}$H} cross-polarization NMR analyses monitoring $Ca_3SiO_5$ hydration have relied on particle size reduction or costly $^{29}$Si isotopic enrichment.[19] These analyses have detected trace amounts of hydrated $Q^1$ or $Q^2$ silicates formed at early times, however, due to their low relative abundance, such signal contributions are typically obscured by $Q^0$ intensity arising from the unhydrated tricalcium silicate core. By comparison, Figure 5.9 shows a representative $^{29}$Si{$^{1}$H} DNP CP-MAS NMR spectrum of

monoclinic tricalcium silicate hydrated for 2 h at 25 °C which exhibits at least three broad and partially resolved $^{29}$Si signals centered at -73, -79, and -82 to -85 ppm from silanol $Q^0$, hydrated $Q^1$, and hydrated $Q^2$ species, respectively, which are associated with silicate hydration products.[47,60]. Although the thicknesses, $\delta$, may not appreciably increase during the induction period, the overlaid $^{29}$Si spectra in Figure 5.9 indicate that the silicate distributions on the particle surfaces continue to evolve even for early (<2.5 h) hydration times. The $^{29}$Si spectra are normalized with respect to the mass of the sample and the number of acquisitions and provide a semi-quantitative comparison of the surface compositions at different hydration times. Initially, there is a greater relative abundance of silanol $Q^0$ which is partially transformed into more crosslinked hydrated $Q^1$ and $Q^2$ silicates over the course of the induction period. Notably, for hydration times <2.5 h, the $^{29}$Si spectra exhibit broad, overlapping contributions of $Q^1$ and $Q^2$ intensity. These relatively broad signals likely arise from a broad distribution of local atomic environments consistent with the formation of a disordered surface hydrate layer. Meanwhile, post-induction period (*ca*. 4 h), relatively narrow $Q^1$ intensity arises in the same spectral region, consistent with calcium silicate hydrates with improved local order. Previously, it has been suggested that the formation of calcium silicate hydrates is autocatalytic, such that the hydration of the particle surface is accelerated after the initial formation of ordered calcium silicate hydrate nucleation seeds. The proposed structural diagram in the schematic inset of Figure 5.9 depicts the formation of relatively ordered (phyllosilicate-like) calcium silicate hydrates coexisting with a disordered intermediate hydration layer in a manner consistent with the $^{29}$Si DNP NMR results. These results provide new insights into structural transformations occurring at particle surfaces during, and, shortly after the induction period.

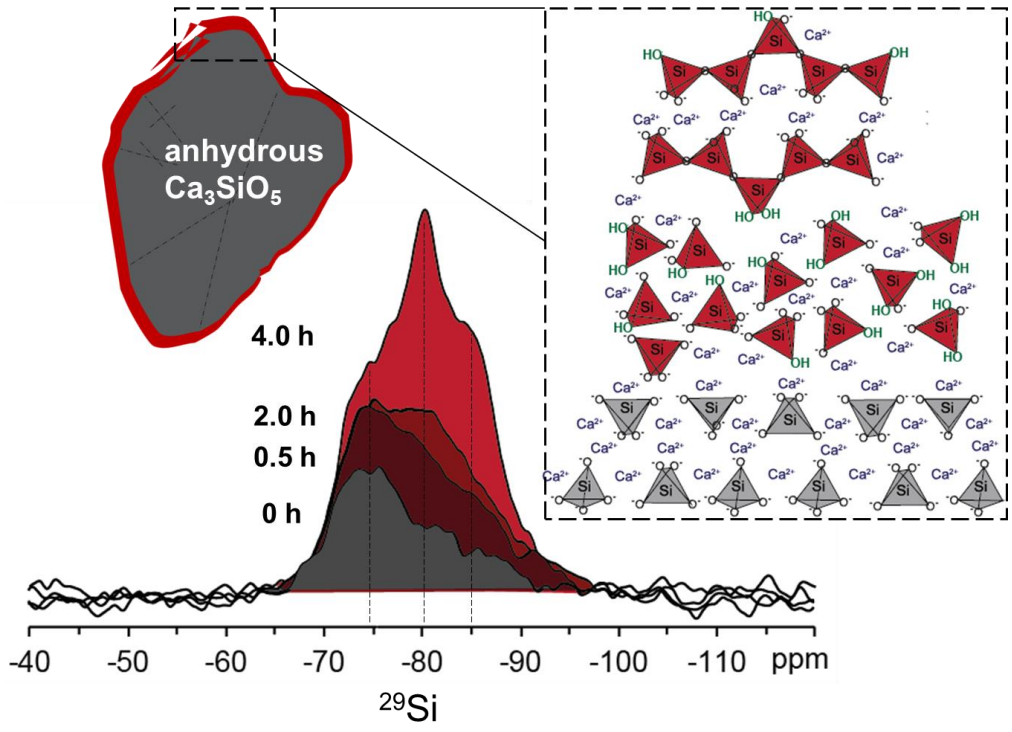


**FIGURE 5.9)** DNP surface-enhanced $^{29}Si\{^{1}H\}$ CP-MAS spectra of $Ca_3SiO_5$ hydrated for 0 h, 0.5 h, 2 h, and 4 h, vacuum-dried, and suspended in a glycerol/water matrix. Schematic inset depicts the formation of calcium silicate hydrate, a disordered surface hydrate alteration layer, and unhydrated $Ca_3SiO_5$ consistent with the measured signal intensity.

## 5.7. Influence of additive species on surface silicate compositions

While the preceding analyses have exclusively focused on the hydration of tricalcium silicate in unadulterated water, modern cementitious mixtures often incorporate dilute additive species to tune hydration kinetics or rheological properties. For example, in the presence of ~2 % by-weight-of-solids (bwos) $CaCl_2$ accelerator the induction period may be shortened to <30 min, while the induction period may last several weeks in the presence of ~0.5 %bwos sucrose retardant. In the case of sucrose, it has recently been demonstrated by advanced two-dimensional $^{13}C\{^{1}H\}$ and $^{29}Si\{^{1}H\}$ DNP heteronuclear correlation measurements that sucrose strongly adsorbs at hydrating particle surfaces, likely by a combination of H-bonding

interactions and Ca-binding, to competitively displace water.[66] However, in general, the influence of dilute additive species on surface silicate compositions remains poorly understood. In Fig 5.10, a series of 1D $^{29}Si\{^{1}H\}$ DNP CP-MAS spectra were obtained for tricalcium silicate specimen hydrated (blue) for 2.5 h in the presence of either (a) 2 %bwos $CaCl_2$, (b) unadulterated water, or (c) 0.5 %bwos sucrose and are overlaid with the $^{29}Si$ spectra of unhydrated tricalcium silicate (red) acquired under otherwise identical conditions. Here, for these semi-quantitative analyses, a hydrophobic DNP solvent matrix consisting of 8 mM TEKPol in 1,1,2,2-tetrachloroethane is used to minimally influence hydration chemistry. Generally, for hydrated tricalcium silicate particulate systems, hydrophobic DNP solvent matrices lead to diminished enhancement values and short polarization build-up times that may be attributed to partial dewetting or capillary bridging phenomena (*i.e.*, the sand-castle effect[67]) that yield poorer suspensions. Nevertheless, this formulation enables the direct comparison of unhydrated and hydrated tricalcium silicate particles with spectral acquisition times shorter than 30 minutes (compared to 2 days in Fig. 5.5). Such analyses enable the sensitive and preferential detection of dilute silicate hydrates formed on low-surface area tricalcium silicate particles with unprecedently short acquisition times providing new insights into interfacial transformations that are believed to influence early hydration kinetics and mechanical strength development.

Initially, the $^{29}Si$ spectra of unhydrated tricalcium silicate (red, a-d) indicates the presence of some $Q^1$ and $Q^2$ silicate hydrates due to its hygroscopic nature and reaction with atmospheric water. When hydrated in unadulterated water, there is a greater relative abundance of pairing $Q^2$ (ca. -85 ppm) silicates consistent with the formation of more crosslinked hydration products as hydration proceeds. Similarly to the series in Fig 5.9., it is

hypothesized that the formation of a crosslinked and disordered calcium silicate hydrate layer may constitute a barrier to the further dissolution and reaction of the particle interior, the possible atomistic origin of the induction period. By comparison, in the presence of 2%bwos $CaCl_2$, significantly more hydrates are formed overall, albeit the $^{29}Si$ intensity predominantly arises from $Q^1$ (ca. -79 ppm) and bridging $Q^2$ (ca. -82 ppm) silicates that are associated with shorter silicate chain lengths. Thus, it is concluded that competitive adsorption of $Ca^{2+}$ at the interface may prevent condensation or reprecipitation of dissolved Si yielding a reactive precursor gel that may pose less of an obstacle to further reaction or dissolution of the surface. Consistent with the discussion above, in the presence of 0.5%bwos sucrose, there are few detectable changes in the quantities and compositions of silicate hydrates after 2.5 h of hydration, as shown in Fig. 5.10c. It is speculated that both $CaCl_2$ and sucrose act by adsorption at the hydrating particle interface, however that sucrose binds more strongly and desorbs less readily. This may explain the complex influence of sucrose on tricalcium silicate hydration kinetics, where sucrose acts as an accelerant below monolayer coverage, but is a strong retardant at concentrations near or above monolayer coverage. Similar phenomena are known to influence the apparent reaction rate over heterogeneous catalysts (*i.e.*, the Sabatier principle), where strong adsorption of a reactant species leads to diminished apparent reaction rates.

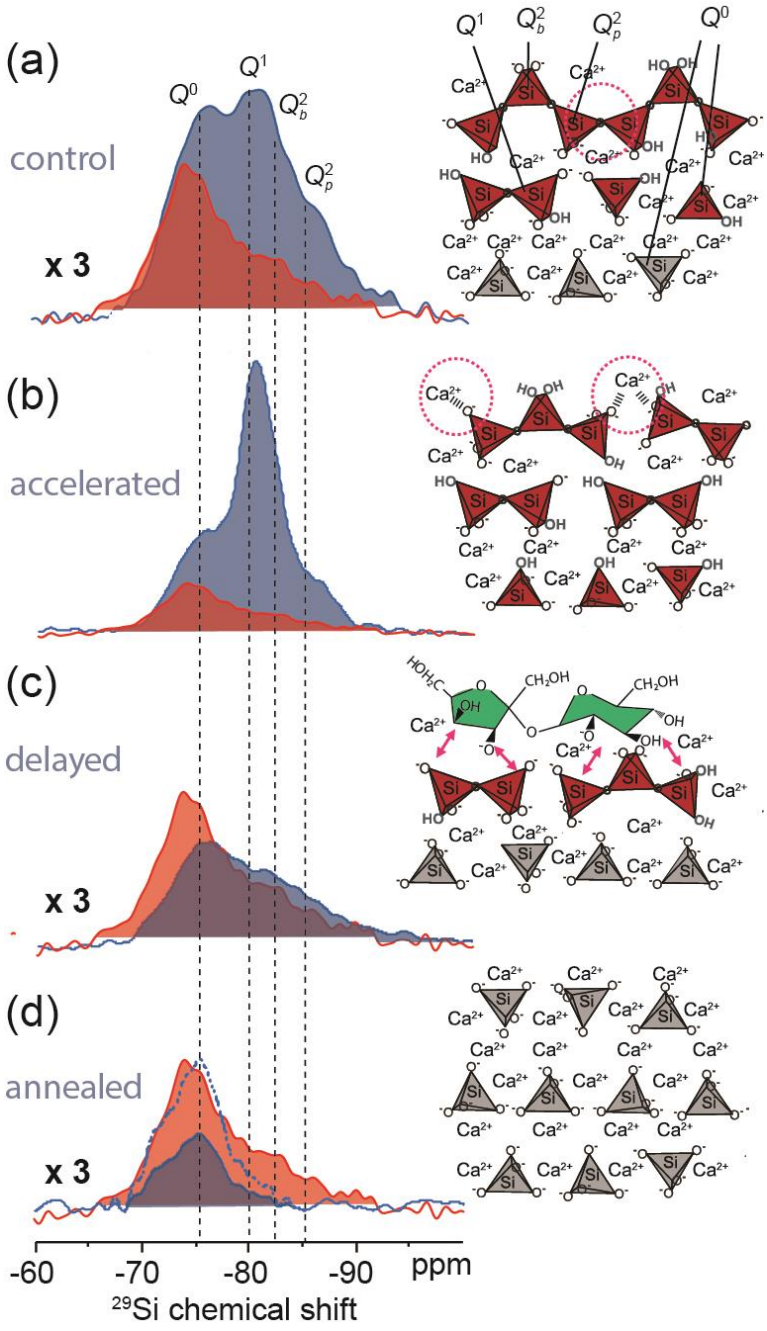


**FIGURE 5.10)** Surface silicate compositions of hydrated and unhydrated $Ca_3SiO_5$ measured by 1D $^{29}Si\{^1H\}$ DNP CP-MAS. Red spectrum is unhydrated $Ca_3SiO_5$ overlayed with blue spectra: (a) 2.5 h hydrated $Ca_3SiO_5$ without additives, (b) 2.5 h hydrated $Ca_3SiO_5$ with 2 bwos% $CaCl_2$, (c) 2.5 h hydrated $Ca_3SiO_5$ with 0.5 bwos% sucrose, and (d) unhydrated $Ca_3SiO_5$ annealed at 650 °C for 14 h. Spectra in (a, c-d) multiplied by a factor of three, in (d) the dotted-blue line is qualitatively scaled for comparison.

These results indicate that, perhaps more important than its physical dimensions, the compositions of the surface hydration layer influence the progression of hydration and dissolution processes responsible for the duration of the induction period. Furthermore, it is demonstrated in Figure 5.10 that thermal annealing (650 °C) of unhydrated tricalcium silicate particles reduces the abundance of silanol $Q^0$, hydrated $Q^1$, and hydrated $Q^2$ initially present on the surface. Similar treatments are known to lengthen the induction period and have been previously attributed to the removal of crystallographic defects that may render tricalcium silicate particles more reactive. Overall, the DNP NMR results highlight the role of interfacial chemistry in the early hydration of tricalcium silicate that, in addition to other factors (*i.e.*, defect density, particle size distribution), influence the apparent dissolution rates of industrially relevant cementitious mixtures.

## 5.8. Conclusions

The molecular compositions and mean thickness of hydrated layers at heterogeneous silicate particle surfaces are established by using DNP NMR methods and modelling analyses. Due to the challenging length scales associated with the thickness of such layers, these have typically been difficult and often infeasible to measure by conventional microscopy and diffraction analyses. These challenges are further exacerbated by the poor long-range structural order and dilute quantities of the component species in the hydrated layers, especially at early hydration times. Nevertheless, DNP-enhanced NMR measurements crucially provide the signal sensitivity that is necessary to detect such dilute quantities of hydrates and allow the transfer and/or distribution of DNP-enhanced spin polarization through the associated surface layers to be experimentally measured and monitored. The rate and

extents of such polarization transfer processes are directly related to the mean thickness of the surface layer, the latter of which is subsequently estimated by using diffusion-reaction equations to model the spatiotemporal evolution of the spin polarization measured in the DNP NMR experiments. The analyses establish that there are small quantities of silanol $Q^0$ and calcium silicate hydrate species present at surfaces at the early hydration times, which yield a layer with a mean approximate thickness of ca. 4 nm on the silicate particles. These dimensions are consistent with previous estimates by XPS analyses and synchrotron X-ray pair distribution analyses. The results suggest that hydration largely occurs within <10 nm of the surface and proceeds by an increase in particle surface areas that may be attributed to the nucleation of calcium silicate hydrates. Perhaps more important than the physical dimensions of this layer, is the compositions and extent of local order of the silicate hydrates formed at early times. It is shown that treatments and conditions known to influence the duration of the induction period have a marked influence on the types and quantities of silicate hydrates that are present. In summary, upon contact with water a disordered surface layer is formed at hydrating particle surfaces and continues to evolve over the course of the induction period forming crosslinked $Q^2$ silicates that may impede further dissolution. The $^{29}$Si DNP enhanced spectra suggest that $CaCl_2$, a hydration accelerator, may prevent this crosslinking yielding a greater relative abundance of dimeric $Q_1$ silicates. The analyses and results presented here are broadly relevant to measuring particle or domain sizes in a variety of multicomponent systems, including alloys, semiconductors, catalysts, where such attributes strongly influence overall material properties, but where the particle or domain dimensions are not amenable to conventional measurements.

## Appendix 5A1. Matlab script (steady-state analytical solution)

```
clear
T1S = 1.5; %T1 of calcium silicate hydrate [s] 1.5s 4 h dry C3S
Tdnp = 27; %DNP build-up time of matrix [s]
rhoM = 3.5*10^3; %1H spin density glycerol-water [mol m^-3]
rhoS = 16*10^3; %1H spin density calcium silicate hydrate [mol m^-3]
DHm = 5*10^-16*(rhoM/(70*10^3))^(1/3); %diffusion coefficient glycerol-
water [m^2s^1]
DHs = 1.2*10^-16*(rhoS/(16*10^3))^(1/3); %diffusion coefficient of CSH
[m^2s^-1]
MuON = 127; %absolute enhancement in matrix
MuOFF = 0.50; %depolarization factor in matrix


Lcap = 150*10^-9; %one-half capillary porosity [500 nm]
LcapM = [170,170,170,170,156,129,113].*10^-9;
LcapM = [182,176,164,153,144,128,118].*10^-9;
rhoO = 0.01*10^3; %1H spin density Ca3SiO5 interior [mol m^-3]
rhoO = 0.14*10^3;
Vtot =4/3*pi*(8.6/2*10^-6)^3; %volume of 10 micron particle [m^3]
t = [0.5, 1, 2, 3, 4, 6, 8];
enh = [17.6, 12.9, 16.8, 21.2, 25.5, 18.6, 11.58];
A = [1.11, 1.038, 1.34, 2.01, 2.75, 4.51, 6.61];
enhM = [155,124,117,129,116,89,84];
mass = Vtot*3.15*10^6; %grams per particle (density C3S = 3.15 g/cm^3)

global T1S_ rhoM_ rhoS_ DHm_ DHs_ Lcap_ Tdnp_ MuON_ MuOFF_ rhoO_ mass_;
T1S_=T1S; rhoM_=rhoM; rhoS_=rhoS; DHm_=DHm ; DHs_=DHs; Lcap_ = Lcap;
Tdnp_=Tdnp; MuON_ =MuON;MuOFF_=MuOFF;
rhoO_ =rhoO; mass_= mass;

%hydL = [0.01 0.1 1 10 100 1000];
%hydL = hydL.*10^-9;
%out = enhON(hydL,Leff)./enhOFF(hydL,Leff);


for i = 1:length(A)
Leff = LcapM(i);
myfun = @(x,k,j)
(rhoS.*k.*mass.*enhON(x,Leff).*x+rhoO.*Vtot)./((rhoS.*k.*mass.*enhOFF(x,Le
ff).*x+rhoO.*Vtot))-j;  % parameterized function
k = A(i);   %parameter
j = enh(i);
fun = @(x) myfun(x,k,j);    % function of x alone
guessL = 10*10^-9;
x(i) = fzero(fun,guessL);
SimON(i) = enhON(x(i),Leff);
SimOFF(i) = enhOFF(x(i),Leff);
SimSA(i) =
(rhoS.*k.*mass.*enhON(x(i),Leff).*x(i)+rhoO.*Vtot)./((rhoS.*k.*mass.*enhOF
F(x(i),Leff).*x(i)+rhoO.*Vtot));
end
```

```
hydL = x;
LayerThickness = x*10^9
SimENH = SimON./SimOFF
SimSA = SimSA
enh = enh;
fit = mean(LayerThickness);
function [conc] = enhON(y,Leff) %y is HydL
        conc = Eta(y).*(PsurfON(y,Leff)-1)+1;
end

function [conc] = enhOFF(y,Leff) %y is HydL
        conc = Eta(y).*(PsurfOFF(y,Leff)-1)+1;
end

function [conc] = PsurfON(y,Leff) %y is HydL
    global MuON_
        conc = (MuON_-Damkohler(y).*Eta(y)./Tau(y,Leff))./(1-
Damkohler(y).*Eta(y)./Tau(y,Leff));
end

function [conc] = PsurfOFF(y,Leff) %y is HydL
    global MuOFF_
        conc = (MuOFF_-Damkohler(y).*Eta(y)./Tau(y,Leff))./(1-
Damkohler(y).*Eta(y)./Tau(y,Leff));
end

function [conc] = Damkohler(y) %y is hydL
    global T1S_ rhoM_ rhoS_ DHm_
        conc = y.^2.*T1S_.^-1.*(rhoS_./rhoM_)./DHm_;
end

function [conc] = Thiele(y) %y is hydL
    global T1S_ DHs_
        conc = y./sqrt(DHs_.*T1S_);
end

function [eta] = Eta(y) %y is hydL
        global T1S_ DHs_
        eta = tanh(y./sqrt(DHs_.*T1S_))./(y./sqrt(DHs_.*T1S_));
end

function [conc] = Tau(y,Leff) %y is hydL
    global T1S_ DHs_ DHm_ Tdnp_
        phiM= (y./sqrt(DHs_.*T1S_)).*sqrt((DHs_.*T1S_)./(DHm_.*Tdnp_));
        NUM = sinh(phiM)-tanh(phiM.*(1+Leff./y)).*cosh(phiM);
        DENOM = cosh(phiM)-tanh(phiM.*(1+Leff./y)).*sinh(phiM);
        conc = phiM.*NUM./DENOM;
end
```

## Appendix 5A2. Matlab script (transient numerical solution)

```
m = 0; %0 = SLAB, 1 = CYLINDER, and 2 = SPHERE
%Dout = 400; %nm^2/s diffusivity {KHUTISVILI APPROXIMATION}
%Din = 90; %nm^2/s from relative dipole interactions (1.6 kHz @4.5A)

rSolv = 30; %nm of solvent
rPart = 150; %radius of particle bundle
filename = 'Polprof_delete.xlsx';
hydL = rPart+rSolv; %total system
Seff = 1.5; % effective T1 of dry C3S 2.3 s
depo = 1;
%Hsol = 13; %H atom/nm^3 in solution
%Htar = 26; %H atom/nm^3 in target
%Dout = 500*(Hsol/42)^(4/3);
%Din = 500*(Htar/42)^(4/3);
Hsol = 4; %M in solution
Htar = 16; % M in target
rhoAMU = 2; %mM biradical in starting solution
Din = 140;
Dout = 500*(Hsol/70)^(1/3);
%Dout = 160;


%For 2 mM AMUPol glycerol/water solution
T1 = 6.86+205.74*exp(-0.13*Hsol)+44.27*exp(-0.00981*Hsol); %solvent build-
up
if (Hsol <20.2)
   kdnp = -0.2254*Hsol^(1/3)+1.7199;
else
   kdnp = 0.4014*Hsol^(1/3)+0.0116;
end
%For variable AMUPol concentration
Udnp = (3*1.8^2/(5.83^3-1.8^3))*kdnp;
T1Mwon = T1/(1+Udnp*T1);
e0 = (1+Udnp*148*T1)/(1+Udnp*0.42*T1);

ta = [0.000003 2.107 4.463 7.133 10.217];
xa = [0 0.8504 0.9697 0.9921 1];
global rPart_ rSolv_ Dout_ Din_ Seff_ T1Mwon_ e0_ depo_ hydL_ Hsol_ Htar_;
rPart_ = rPart; rSolv_ = rSolv; Dout_ = Dout; Din_ = Din;
Seff_ = Seff; T1Mwon_ = T1Mwon; e0_ = e0; depo_ = depo; hydL_=hydL;
Hsol_ = Hsol; Htar_ = Htar;

%Initiliaze time-points for solution
low = linspace(0,0.1,4);
med = linspace(0.2,1.8,8);
high = linspace(2,15,16);
veryhigh = linspace(20,100,16);
t = [low med high veryhigh];

%Initiliaze spatial-points for solution
rstep=2000;% number of points in the length dimension in PDE solution.
```

```
r = linspace(0,hydL_,rstep);

%PDE for microwave on and off conditions
solution_on = pdepe(m,@pde_diffusionON,@pde_ic,@pde_bc_MW_on,r,t);
%microwave on
p_on = solution_on(:,:,1);%

solution_off= pdepe(m,@pde_diffusionOFF,@pde_ic,@pde_bc_MW_OFF,r,t);
%microwave off
p_off=solution_off(:,:,1);%

[epsilon,SignalPol,SignalRef]=CalcEpsilon(p_on,p_off,r,t,m);%this function
%calculates the expected observed enhancements given p_on, p_off, and

%Plot Everything Usefull
pSS = zeros(2,size(r,2));
for j=1:size(r,2)
pSS(1,j) = p_on(size(t,2),j);
pSS(2,j) = (hydL_/rstep)*j;
end
figure(1)
plot(pSS(2,:),pSS(1,:));
xL=[rPart,rPart];
yL=[0,1.1*e0_];
hold on
plot(xL,yL) %plot line where solid boundary is
hold off
%Approximate derivative of polarization at interface
frac = round(rstep*(rPart/hydL_));
mLHS = (pSS(1,frac-1)-pSS(1,frac-2))/(pSS(2,frac-1)-pSS(2,frac-2));
mRHS = (pSS(1,frac+2)-pSS(1,frac+1))/(pSS(2,frac+2)-pSS(2,frac+1));
A = [pSS(2,:) pSS(1,:)];
xlswrite(filename,A)
%Extract different domains buildup
intL = round(rstep*rPart/hydL_); %interface integer value
%Solid "Target" DATA
wTarMagON = zeros(size(t,2),intL); %Spatial Polarization in target
TarMagON = zeros(size(t,2),intL); %Spatial Polarization in target
TarSigON = zeros(size(t,2),1); %Signal in target
TarSigOFF = zeros(size(t,2),1); %Signal in target
wTarMagOFF = zeros(size(t,2),intL); %Spatial Polarization in target
TarMagOFF = zeros(size(t,2),intL); %Spatial Polarization in target
Pos = zeros(size(r,2),1);
%Solvent DATA
wSolMag = zeros(size(t,2),size(r,2)-intL); %Spatial Polarization in
solvent
TSolMag = zeros(size(t,2),size(r,2)-intL); %Spatial Polarization in
solvent
SolMag = zeros(size(t,2),size(r,2)-intL);
SolMagOFF = zeros(size(t,2),size(r,2)-intL);
wSolMagOFF = zeros(size(t,2),size(r,2)-intL);
SolSigON = zeros(size(t,2),1); %Signal in solvent
SolSigOFF = zeros(size(t,2),1); %Signal in solvent
%Weight functions for integrating spherical geometry (m=2)
```

```
weightSph = zeros(size(r,2),1);
weightCyl = zeros(size(r,2),1);
Dd = hydL_;
DdR = Dd/size(r,2);
for k = 1:size(r,2)
weightSph(k)=(4/3)*pi*((Dd-(k-1)*DdR)^3-(Dd-k*DdR)^3);
weightCyl(k)=pi*((Dd-(k-1)*DdR)^2-(Dd-k*DdR)^2);
Pos(k)=(hydL_/rstep)*k;
end
%Separate data for Target and Solvent domains
for o = 1:size(t,2)
    for k = 1:intL
        TarMagON(o,k) = p_on(o,k);
        TarMagOFF(o,k) = p_off(o,k);
    end
    if m == 1
        for k = 1:intL
        wTarMagON(o,k) = p_on(o,k)*weightCyl(k,1);
        wTarMagOFF(o,k) = p_off(o,k)*weightCyl(k,1);
        end
    end
    if m == 2
        for k = 1:intL
        wTarMagON(o,k) = p_on(o,k)*weightSph(k,1);
        wTarMagOFF(o,k) = p_off(o,k)*weightSph(k,1);
        end
    end
    for h = 1:(size(r,2)-intL)
        SolMag(o,h) = p_on(o,intL+h);
        SolMagOFF(o,h) = p_off(o,intL+h);
        if m==2
        wSolMag(o,h) = p_on(o,intL+h)*weightSph(intL+h,1);
        wSolMagOFF(o,h) = p_off(o,intL+h)*weightSph(intL+h,1);
        else
           wSolMag(o,h) = p_on(o,intL+h)*weightCyl(intL+h,1);
           wSolMagOFF(o,h) = p_off(o,intL+h)*weightCyl(intL+h,1);
        end
    end
    if m==0
    TarSigON(o)=sum(TarMagON(o,:));
    TarSigOFF(o)=sum(TarMagOFF(o,:));
    SolSigON(o)=sum(SolMag(o,:));
    SolSigOFF(o)=sum(SolMagOFF(o,:));
    end
    if m>0 %Use weighted functions for 1H profile
    TarSigON(o)=sum(wTarMagON(o,:));
    TarSigOFF(o)=sum(wTarMagOFF(o,:));
    SolSigON(o)=sum(wSolMag(o,:));
    SolSigOFF(o)=sum(wSolMagOFF(o,:));
    end
end
%Scale signals by repesctive 1H concentrations (ABSOLUTE signal intensity)
absTarSigON = TarSigON.*Htar_;
absTarSigOFF = TarSigOFF.*Htar_;
absSolSigON = SolSigON.*Hsol_;
```

```
absSolSigOFF = SolSigOFF.*Hsol_;
%Calculate enhancements (NORMALIZE)
enhancement = TarSigON(end)/TarSigOFF(end);
enhSOL = SolSigON(end)/SolSigOFF(end);
TarSigON = TarSigON./TarSigON(end);
SolSigON = SolSigON./SolSigON(end);
SolSigOFF = SolSigOFF./SolSigOFF(end);
%Steady-state polarization SAVE
%filename = 'SteadyStatePolC3S_200nm.xlsx';
%A = TarMagON(size(t,2),:);
%xlswrite(filename,A)
size(TarSigON')
%Find SIMULATED BUILD-UP TIMES
F = @(x,xdata) 1-exp(-x(1)*xdata); %exponential fit
Fstretch = @(x,xdata) 1-exp(-(x(1).*xdata).^x(2)); %exponential fit
Fbi = @(x,xdata) 1-(1-x(3)).*exp(-x(1).*xdata.^x(2))-x(3).*exp(-
x(4).*xdata)
%F = @(x,xdata) 1-exp(-x(1).*xdata.^x(2)); %biexponential fit
%FIT for TARGET MWON
x0 = [1/Seff]; %initial guess expon
x01 = [1/Seff 1]; %initial guess stretch
x02 = [1/Seff 1 0 1/T1Mwon]; %initial guess bi exponential fit
%[x,resnorm,~,exitflag,output] = lsqcurvefit(F,x0,t,TarSigON');
[x,resnorm,~,exitflag,output] = lsqcurvefit(Fstretch,x01,t,TarSigON');
%[x,resnorm,~,exitflag,output] = lsqcurvefit(Fbi,x02,t,TarSigON');
figure(2)
scatter(t,TarSigON');
hold on
plot(t,Fstretch(x,t))
scatter(ta,xa);
hold off
%Fit for stretched exponential
TtarFIT = x(1);
tarBeta = x(2);

%FIT for SOLVENT MWON
x0 = [1/T1Mwon]; %initial guess
[x,resnorm,~,exitflag,output] = lsqcurvefit(Fstretch,x01,t,SolSigON');
figure(3)
scatter(t,SolSigON');
hold on
plot(t,Fstretch(x,t))
hold off
TsolFIT = x(1);
solBeta = x(2)


SOLoutput = [enhSOL 1/TsolFIT solBeta]
TAROutput = [enhancement 1/TtarFIT tarBeta]
surfEnh = pSS(1,frac)
A = [t TarSigON' SolSigON'];
B = SOLoutput;
C = TAROutput;
xlswrite(filename,[A])
```

```
function [epsilon,SignalPol,SignalRef]=CalcEpsilon(p,pref,r,t,m)
global hydL_

        SignalPol=zeros([1,size(t,2)]);
        SignalRef=zeros([1,size(t,2)]);
        epsilon=zeros([1,size(t,2)]);
    %Slab Integration
    if m==0
        for i=2:size(t,2)
        SignalPol(i)=trapz(r,p(i,:));
        SignalRef(i)=trapz(r,pref(i,:));
        end
    end
     %Cylinder Integration
    if m == 1
    Dd = hydL_;
    DdR = Dd/size(r,2);
    wON = zeros([size(t,2),size(r,2)]);
    wOFF = zeros([size(t,2),size(r,2)]);
        for i = 1:size(r,2)
            weight = pi*((Dd-(i-1)*DdR)^2-(Dd-i*DdR)^2);
            wON(:,size(r,2)-i+1)= p(:,size(r,2)-i+1,1)*weight;
            wOFF(:,size(r,2)-i+1)= pref(:,size(r,2)-i+1,1)*weight;
        end
        for i=2:size(t,2)
           SignalPol(i) = sum(wON(i,:));
           SignalRef(i) = sum(wOFF(i,:));
        end
    end
    %Sphere Integration
    if m == 2
    Dd = hydL_;
    DdR = Dd/size(r,2);
    wON = zeros([size(t,2),size(r,2)]);
    wOFF = zeros([size(t,2),size(r,2)]);
        for i = 1:size(r,2)
            weight = (4/3)*pi*((Dd-(i-1)*DdR)^3-(Dd-i*DdR)^3);
            wON(:,size(r,2)-i+1)= p(:,size(r,2)-i+1,1)*weight;
            wOFF(:,size(r,2)-i+1)= pref(:,size(r,2)-i+1,1)*weight;
        end
        for i=2:size(t,2)
           SignalPol(i) = sum(wON(i,:));
           SignalRef(i) = sum(wOFF(i,:));
        end
    end

    %Calculate enhancements
    epsilon(1)=0;
    for i=2:size(t,2)
    epsilon(i)=SignalPol(i)./SignalRef(i); % ON & OFF BUILD UP TIMES
    %epsilon(i)=SignalPol(i); %only include for S(t) data
    end
```

```
    %epsilon = epsilon.*SignalPol(size(t,2))./SignalRef(size(t,2));%only
include for S(t) data
end

function [c,f,s] = pde_diffusionON(x,~,u,DuDx) %define components of the
PDE
c = 1*fconc(x);
f = (fD(x)*DuDx)*fconc(x);
s=-((u-fPeqON(x))/fS(x))*fconc(x);
end

function [c,f,s] = pde_diffusionOFF(x,~,u,DuDx) %define components of the
PDE
c = 1*fconc(x);
f = fD(x)*DuDx*fconc(x);
s=-((u-fPeqOFF(x))/fS(x))*fconc(x);
end

function u0 = pde_ic(~) %define initial condition
    u0=0;
end

function [pl,ql,pr,qr] = pde_bc_MW_on(~,~,~,~,~) %define two boundary
conditions; hard wall & no diffusion out of the slab
pl = 0;
ql = 1;
pr = 0;
qr = 1;
end

function [pl,ql,pr,qr] = pde_bc_MW_OFF(~,~,~,~,~)
pl = 0;
ql = 1;
pr = 0;
qr = 1;
end

function [D] = fD(y) %spatial diffusivity
    global rPart_ Dout_ Din_
         D = Din_+(Dout_-Din_)*heaviside(y-rPart_);
end

function [S] = fS(y) %relaxation parameter
    global Seff_ T1Mwon_ rPart_
         S = Seff_+(T1Mwon_-Seff_)*heaviside(y-rPart_);
end

function [Peq] = fPeqON(y) %steady-state polarization value (ON)
global e0_ rPart_
        Peq = 1+(e0_-1)*heaviside(y-rPart_);
end

function [Peq] = fPeqOFF(y) %steady-state polarization value (OFF)
```

```
global depo_ rPart_
        Peq = 1+(depo_-1)*heaviside(y-rPart_);
end

function [conc] = fconc(y) %1H concentration
    global Htar_ Hsol_ rPart_
         conc = Htar_+(Hsol_-Htar_)*heaviside(y-rPart_);
end
```

## References


1 A. P. Alivisatos, *Science.*, 1996, **271**, 933–937.
2 K. J. Harry, D. T. Hallinan, D. Y. Parkinson, A. A. MacDowell and N. P. Balsara, *Nat. Mater.*, 2013, **13**, 69–73.
3 P. G. Menon, *Chem. Rev.*, 1994, **94**, 1021–1046.
4 L. V Mattos, G. Jacobs, B. H. Davis and F. B. Noronha, *Chem. Rev.*, 2012, **112**, 4094–4123.
5 Y.-S. Yu, C. Kim, D. A. Shapiro, M. Farmand, D. Qian, T. Tyliszczak, A. L. D. Kilcoyne, R. Celestre, S. Marchesini, J. Joseph, P. Denes, T. Warwick, F. C. Strobridge, C. P. Grey, H. Padmore, Y. S. Meng, R. Kostecki and J. Cabana, *Nano Lett.*, 2015, **15**, 4282–4288.
6 J. W. Bullard, G. W. Scherer and J. J. Thomas, *Cem. Concr. Res.*, 2015, **74**, 26–34.
7 J. F. YOUNG, H. S. TONG and R. L. Berger, *J. Am. Ceram. Soc.*, 1977, **60**, 321–323.
8 F. Bellmann, T. Sowoidnich, H. M. Ludwig and D. Damidot, *Cem. Concr. Res.*, 2015, **72**, 108–116.
9 F. Bellmann and G. W. Scherer, *Cem. Concr. Res.*, 2018, **103**, 236–244.
10 S. Garrault and A. Nonat, *Langmuir*, 2001, **17**, 8131–8138.
11 L. Nicoleau, E. Schreiner and A. Nonat, *Cem. Concr. Res.*, 2014, **59**, 118–138.
12 J. W. Bullard and R. J. Flatt, *J. Am. Ceram. Soc.*, 2010, **93**, 1894–1903.
13 K. L. Scrivener and A. Nonat, *Cem. Concr. Res.*, 2011, **41**, 651–665.
14 E. M. GARTNER and H. M. JENNINGS, *J. Am. Ceram. Soc.*, 1987, **70**, 743–749.
15 E. Gartner, *Cem. Concr. Res.*, 2011, **41**, 560–562.
16 P. Juilland, E. Gallucci, R. Flatt and K. Scrivener, *Cem. Concr. Res.*, 2010, **40**, 831–844.
17 P. Juilland and E. Gallucci, *Cem. Concr. Res.*, 2015, **76**, 180–191.
18 A. C. Lasaga and A. Luttge, *Science (80-. ).*, 2001, **291**, 2400–2404.
19 E. Pustovgar, R. P. Sangodkar, A. S. Andreev, M. Palacios, B. F. Chmelka, R. J. Flatt and J. E. De Lacaillerie, *Nat. Commun.*, 2016, **7**, 10952.
20 L. Nicoleau, A. Nonat and D. Perrey, *Cem. Concr. Res.*, 2013, **47**, 14–30.
21 F. Bellmann, D. Damidot, B. Möser and J. Skibsted, *Cem. Concr. Res.*, 2010, **40**, 875–884.
22 S. A. Rodger, G. W. Groves, N. J. Clayden and C. M. Dobson, *J. Am. Ceram. Soc.*, 1988, **71**, 91–96.
23 F. Bellmann, T. Sowoidnich, H. Ludwig and D. Damidot, *Cem. Concr. Res.*, 2012, **42**, 1189–1198.

24 J. J. Thomas, H. M. Jennings and J. J. Chen, *J. Phys. Chem. C*, 2009, **113**, 4327–4334.
25 R. P. Sangodkar, B. J. Smith, D. Gajan, A. J. Rossini, L. R. Roberts, G. P. Funkhouser, A. Lesage, L. Emsley and B. F. Chmelka, *J. Am. Chem. Soc.*, 2015, **137**, 8096–8112.
26 A. Zingg, F. Winnefeld, L. Holzer, J. Pakusch, S. Becker and L. Gauckler, *J. Colloid Interface Sci.*, 2008, **323**, 301–312.
27 L. Alexander and H. P. Klug, *J. Appl. Phys.*
28 *Challenges in Characterizing Small Particles: Exploring Particles from the Nano- to Microscale: A Workshop Summary*, National Academies Press, Washington D. C., 2012.
29 Q. Hu, M. Aboustait, T. Kim, M. T. Ley, J. W. Bullard, G. Scherer, J. C. Hanan, V. Rose, R. Winarski and J. Gelb, *Cem. Concr. Res.*, 2016, **89**, 14–26.
30 E. Gallucci, P. Mathur and K. Scrivener, *Cem. Concr. Res.*, 2010, **40**, 4–13.
31 J. Clauss, K. Schmidt-Rohr and H. W. Spiess, *Acta Polym.*, 1993, **44**, 1–17.
32 K. Schmidt-Rohr and H. W. Spiess, *Multidimensional Solid-State NMR and Polymers*, Academic Press, 1994.
33 J. Schlagnitweit, M. Tang, M. Baias, S. Richardson, S. Schantz and L. Emsley, *J. Am. Chem. Soc.*, 2015, **137**, 12482–12485.
34 J. Clauss, K. Schmidt-Rohr and H. W. Spiess, *Acta Polym.*, 1993, **44**, 1–17.
35 A. Lesage, M. Lelli, D. Gajan, M. A. Caporini, V. Vitzthum, P. Miéville, J. Alauzun, A. Roussey, C. Thieuleux, A. Mehdi, G. Bodenhausen, C. Copéret and L. Emsley, *J. Am. Chem. Soc.*, 2010, **132**, 15459–15461.
36 A. J. Rossini, A. Zagdoun, M. Lelli, A. Lesage and C. Cop, *Acc. Chem. Res.*, 2013, **46**, 1942–1951.
37 P. C. A. van der Wel, K.-N. Hu, J. Lewandowski and R. G. Griffin, *J. Am. Chem. Soc.*, 2006, **128**, 10840–10846.
38 A. J. Rossini, A. Zagdoun, F. Hegner, M. Schwarzwälder, D. Gajan, C. Copéret, A. Lesage and L. Emsley, *J. Am. Chem. Soc.*, 2012, **134**, 16899–16908.
39 A. J. Rossini, C. M. Widdifield, A. Zagdoun, M. Lelli, M. Schwarzwälder, C. Copéret, A. Lesage and L. Emsley, *J. Am. Chem. Soc.*, 2014, **136**, 2324–2334.
40 G. Engelhardt and D. Michel, *High-Resolution Solid-State NMR of Silicates and Zeolites*, John Wiley & Sons: Chichester, 1987.
41 L. B. Skinner, S. R. Chae, C. J. Benmore, H. R. Wenk and P. J. M. Monteiro, *Phys. Rev. Lett.*, 2010, **104**, 195502.
42 R. J.-M. Pellenq, A. Kushima, R. Shahsavari, K. J. Van Vliet, M. J. Buehler, S. Yip and F.-J. Ulm, *Proc. Natl. Acad. Sci. U. S. A.*, 2009, **106**, 16102–16107.
43 A. Kumar, B. J. Walder, A. Kunhi Mohamed, A. Hofstetter, B. Srinivasan, A. J. Rossini, K. Scrivener, L. Emsley and P. Bowen, *J. Phys. Chem. C*, 2017, accepted.
44 J. W. Bullard, H. M. Jennings, R. A. Livingston, A. Nonat, G. W. Scherer, J. S. Schweitzer, K. L. Scrivener and J. J. Thomas, *Cem. Concr. Res.*, 2011, **41**, 1208–1223.
45 R. S. Arvidson, I. E. Ertan, J. E. Amonette and A. Luttge, *Geochim. Cosmochim. Acta*, 2003, **67**, 1623–1634.
46 V. K. Peterson and M. C. Garci Juenger, *Chem. Mater.*, 2006, **18**, 5798–5804.

47 R. P. Sangodkar, B. J. Smith, D. Gajan, A. J. Rossini, L. R. Roberts, G. P. Funkhouser, A. Lesage, L. Emsley and B. F. Chmelka, *J. Am. Chem. Soc.*, 2015, **137**, 8096–8112.
48 J. Zhang and G. W. Scherer, *Cem. Concr. Res.*, 2011, **41**, 1024–1036.
49 B. M. Fung, A. K. Khitrin and K. Ermolaev, *J. Magn. Reson.*, 2000, **142**, 97–101.
50 J. Skibsted, in *A Practical Guide to Microstructural Analysis of Cementitious Materials*, CRC Press, 2015, pp. 213–286.
51 S. Hayashi and K. Hayamizu, *Bull. Chem. Soc. Jpn.*, 1991, **64**, 685–687.
52 A. Zagdoun, G. Casano, O. Ouari, M. Schwarzwälder, A. J. Rossini, F. Aussenac, M. Yulikov, G. Jeschke, C. Copéret, A. Lesage, P. Tordo and L. Emsley, *J. Am. Chem. Soc.*, 2013, **135**, 12790–12797.
53 A. Zagdoun, A. J. Rossini, D. Gajan, A. Bourdolle, O. Ouari, M. Rosay, W. E. Maas, P. Tordo, M. Lelli, L. Emsley, A. Lesage and C. Copéret, *Chem. Commun.*, 2012, **48**, 654–656.
54 M. Rosay, L. Tometich, S. Pawsey, R. Bader, R. Schauwecker, M. Blank, P. M. Borchard, S. R. Cauffman, K. L. Felch, R. T. Weber, R. J. Temkin, R. G. Griffin and W. E. Maas, *Phys. Chem. Chem. Phys.*, 2010, **12**, 5850–5860.
55 H. F. W. Taylor, *Cement Chemistry*, Academic Press: London, 1990.
56 W. G. Mumme, *Neues Jahrb. Miner. Monatsh..*, 1995, 145–160.
57 A. J. Allen, J. J. Thomas and H. M. Jennings, *Nat. Mater.*, 2007, **6**, 311–316.
58 I. L. Moudrakovski, R. Alizadeh and J. J. Beaudoin, *Phys. Chem. Chem. Phys.*, 2010, **12**, 6961–6969.
59 F. Nishi, Y. Takeuchi and I. Maki, *Zeitschrift fur Krist.*, 1985, **172**, 297–314.
60 B. J. Smith, A. Rawal, G. P. Funkhouser, L. R. Roberts, V. Gupta, J. N. Israelachvili and B. F. Chmelka, *Proc. Natl. Acad. Sci. U.S.A.*, 2011, **108**, 8949–54.
61 A. Pines, M. G. Gibby and J. S. Waugh, *J. Chem. Phys.*, 1972, **56**, 1776–1777.
62 B. J. Walder, N. A. Prisco, F. M. Paruzzo, J. R. Yarava, B. F. Chmelka and L. Emsley, *J. Phys. Chem. Lett.*, 2019, **10**, 5064–5069.
63 A. Pinon, J. Schlagnitweit, P. Berruyer, A. Rossini, M. Lelli, E. Socie, M. Tang, T. Pham, A. Lesage and L. Emsley, *J. Phys. Chem. C*, 2017, **121**, 15993–16005.
64 G. Geng, R. J. Myers, M. J. A. Qomi and P. J. M. Monteiro, *Sci. Rep.*, 2017, **7**, 1–8.
65 K. Ioannidou, K. J. Krakowiak, M. Bauchy, C. G. Hoover, E. Masoero and S. Yip, *Proc. Natl. Acad. Sci.*, 2016, **113**, 2029–2034.
66 R. P. Sangodkar, B. J. Smith, D. Gajan, A. J. Rossini, L. R. Roberts, G. P. Funkhouser, A. Lesage, L. Emsley, B. F. Chmelka, H. Champs, I. De Sciences, A. Cnrs, E. N. S. Lyon, U. C. B. Lyon and U. De Lyon, *J. Am. Chem. Soc.*, 2015, **137**, 8096–8112.
67 D. J. Hornbaker, R. Albert, I. Albert, A. L. Barabasi and P. Schiffer, *Nature*, 1997, **387**, 765.

## Chapter VI.

# Atomic- and Meso-scale Compositions of Hydrated Volcanic Glasses in Roman-Inspired Structural Solids

N. Prisco; W. Pearl; S. Lewis; P. Corona; Z. Berkson; K. Weigandt; M. Helgeson; B. Chmelka. To be submitted to *J. Am. Chem. Soc.*

## 6.1. Abstract

Hydrothermal conversion of multicomponent aluminosilicate glasses into value-added products, including zeolites or cementitious materials, depends on complex hydration, dissolution, crystallization, and transport processes that are difficult to monitor by conventional characterization methods. Despite similarities in bulk compositions, local structural differences between vitreous precursors may result in significant variations in the quantities, distributions, and types of hydrothermal products that are formed. This has important consequences for Roman-inspired pozzolanic structural solids, which are of high current interest, due to their improved durability and reduced carbon footprint. Importantly, in such cementitious mixtures, similar volcanic glasses (*i.e.*, rhyolite) procured from different geographic formations may, nevertheless, exhibit dramatically different propensities for mechanical strength development. Advanced solid-state nuclear magnetic resonance (NMR) spectroscopy, small-angle neutron scattering (SANS), and macroscopic property analyses enable atomic-scale differences to be probed in volcanic glasses that lack long-range structural

order. In particular, two-dimensional (2D) solid-state $^{27}Al\{^{29}Si\}$ heteronuclear correlation NMR analyses reveal distinct distributions of Al-O-Si moieties in unhydrated volcanic glasses and the subsequent atomic-level changes that occur during hydration and conversion into cementitious binder phases. The NMR and SANS results show that the volcanic glasses are compositionally heterogeneous over nanoscale dimensions (1–25 nm) and comprised of locally ordered subunits that are similar to crystalline tectosilicate minerals, zeolites, or $SiO_2$ polymorphs. These analyses indicate that hydration activity is strongly correlated with the extent of Al incorporation into siliceous precursor domains, with Al-rich tectosilicate domains exhibiting high propensities for conversion into cementitious hydrates. Furthermore, the formation of binder phases, such as calcium aluminosilicate hydrate, a complicated layered mineral with varying extents of condensation, distributions of several distinct $Al^{IV}$ sites, and local structural order, are shown to be correlated with the development of mechanical strength. New composition-structure-property relationships are obtained that provide atomic-scale criteria for the design and optimization of cementious material compositions, reveal fundamental insights into the geological formation of vitreous pyroclastic minerals, and provide new understanding of structural mortars similar to those used in the construction of important cultural heritage sites.

## 6.2. Introduction

Depending on their physical origin, natural or synthetic aluminosilicate glasses can manifest vast differences in their physicochemical properties that may be attributed to variations in local compositions and structural ordering.[1,2] Hydrothermal reactions of

disordered precursors, which occur commonly in zeolite syntheses or during formation of pozzolanic concretes, often involve complicated and poorly-understood processes that result in heterogenous solid products, the properties of which are difficult to analyze, predict, or control. Ancient Greco-Roman societies first discovered that *pozzolana*, a class of vitreous pyroclastic minerals, reacts with hydrated lime, $CaOH_2$ (*aq*), to form a cementitious binder that is an important substituent in aggregate concretes.[3,4] In modern cement formulations, pozzolans are increasingly incorporated to improve mechanical strength, extend longevity, and to partially offset the 5-8% of global anthropomorphic $CO_2$ emissions associated with Portland cement.[5] Portland cement consists of complex blends of crystalline silicates and aluminates that react with water to form semi-crystalline calcium silicate hydrates.[6,7] These mixtures involve a delicate balance of coupled hydration, dissolution, and crystallization processes that enable short-term workability and long-term strength development, which are crucial to their applications.[8] By comparison, insights into the transformations undergone by vitreous pozzolans, their dependence on local compositions, and how they influence macroscopic hydration behaviors are even more challenging to establish, especially at the atomic-level. Under alkaline conditions, these heterogeneous non-equilibrium solid-oxide mixtures may partially react to form geopolymeric or other cementitious binder phases, which are of high current interest.[9] Although they often have similar bulk compositions, however, pozzolans can exhibit vastly different propensities for strength development in cementitious mixtures. Elucidating the composition-structure-property relationships associated with the hydration of vitreous aluminosilicate networks and their resulting solid products (e.g., mortars) is important for numerous technological, archaeological, and cultural heritage applications.

The use of finely ground volcanic ash in structural mortars dates back to at least 300 B.C., with Greek and Roman civilizations initially sourcing material from deposits near Santorini and Mt. Vesuvius, respectively[10]. Roman aggregate concretes are believed to be comprised of volcanic ash, aggregate rock, as little as 10 wt% quicklime (CaO), and have been intentionally hydrated using seawater or other chemical admixtures to improve mechanical performance. The latent heat of CaO hydration has been identified as an important contributor to early strength development in these systems.[11] Recent investigations of a Roman marine concrete by synchrotron X-ray diffraction analyses have found that the mechanical strength and superior durability of these 2,000 year-old materials can be attributed to the formation of Al-rich binder phases, including calcium aluminosilicate hydrates and zeolitic minerals.[4]

In cementitious mixtures, natural pozzolans may be partially consumed to form cementitious binder phases or otherwise function as an aggregate allowing for the nucleation of hydration products. Both calcium silicate hydrates formed from Portland cement and calcium aluminosilicate hydrates formed from Al-rich pozzolans are believed to be structural analogues of the rare mineral tobermorite. However, poorly crystalline cement hydrates can accommodate significant amounts of structural disorder, point defects, and non-stoichiometric and heterogeneous heteroatom contents, which may influence their mechanical properties.[7,12] Al-substitution into cementitious hydrates can occur in different components, sites, or local coordination environments, resulting in distributions of $Al^{IV}$, $Al^{V}$, and $Al^{VI}$ species.[6] Whereas $Al^{VI}$ is most abundant among hydration products formed from Portland cement, the hydration of Al-rich pozzolans can yield significant amounts of $Al^{IV}$ species that are attributed to substitution of Si tetrahedra in the phyllosilicate layers of calcium silicate hydrate. It has been proposed that incorporation of $Al^{IV}$ species induces crosslinks that increase the modulus of

nanoscale calcium aluminosilicate hydrates.[13,14] However, it remains unclear how Al substitution may influence -Si-O-Si- connectivity and whether these nanoscale structural variations may lead to either improved strength or durability. An alternate hypothesis for the mechanical resilience of Roman marine concrete is that Al-rich binder phases may promote a more favorable cement-aggregate interaction, as evidenced by observation of low-temperature zeolitization in ancient mortars.[4] This motivates further structural elucidation to identify unambiguously the compositions and distributions of Al heteroatoms within ordered or disordered cementitious binder phases.

Although the ancient Romans standardized sources of reactive volcanic ash for specific applications,[11] the performance of other natural or synthetic pozzolans is highly variable and challenging to predict. More commonly, modern pozzolans include vitreous or semi-crystalline industrial byproducts, such as fly-ash, blast furnace slag, or silica fume, which are nearing complete utilization.[5] For many industrial processes, including ferrosilicon production, byproduct siliceous pozzolans are a high-value product and contribute importantly to the overall economics. Importantly, pozzolans consume excess $Ca(OH)_2$, a byproduct of $Ca_3SiO_5$ hydration that can result in volume-expansion and subsequent stress-cracking (*e.g.*, via alkali silica reactions[15]), which contributes to material failure. Despite their desirable characteristics, natural pozzolans from different geographic sources exhibit vastly different hydration activities that may be attributed to their unique petrological origins. For rhyolitic volcanic glasses, similar bulk compositions might be expected regardless of geographic origin, as magma flowability[1] is strongly dependent on the ratios of Si, Al, and charge-modifying cations, such as $Na^+$ or $K^+$). However, depending on the quenching rate, viscosity, and composition of the aluminosilicate melt, significantly different distributions of local

structures may be preserved, influencing physicochemical properties, including chemical stability and hydrothermal reactivity. Elucidation of local structural features in quenched aluminosilicate melts remains of high fundamental interest to the Earth sciences and for many material science applications, including optical materials, ceramics, and cementitious solids.

Though the volcanic glasses lack long-range order, local structural ordering may nevertheless be prevalent in glass compositions over short length scales (0.2 to 2 nm).[16,17] For example, short-range solute-based clusters are believed to occur in window glass[16] and amorphous metals[18] and contribute to their novel material properties. This is especially pertinent to dissolution, hydration, and crystallization processes involved in cement hydration[12] or zeolite synthesis,[19,20] since the structure of vitreous precursors may influence dissolution and subsequent crystallization pathways or kinetics. For multicomponent Si-rich aluminosilicate melts, given the many stable $Na^+/K^+$- or $Na^+/Ca^{2+}$-type feldspar or feldspathoid phases and their associated low-temperature polymorphs, partial crystallization processes during quenching may result in the formation of locally ordered subunits without long-range periodicity.[21–23] Although feldspar minerals comprise 50% of the Earth's crust and are widely studied, even relatively well-ordered specimens may include variations in Al or Si distributions and zoning of different cation species, which are not well-described by reciprocal space methods.[23] Similarly, for highly siliceous glasses, it has been proposed that clusters of metal cations may coalesce into structures (*i.e.*, percolation clusters or channels) that can influence ion transport (*e.g.*, by the mixed alkali effect) and chemical stability. This appears to be similarly the case for $Na^+$,$K^+$-rich aluminosilicate systems with similar compositions to rhyolitic volcanic glasses, based on measurements of melt viscosity,[24] ionic conductivity,[25] local structure by NMR, Raman, and X-ray absorption spectroscopy,[24,26–28] synchrotron X-

ray scattering,[29] and molecular dynamics simulations.[25] Here, Roman-inspired mortars were prepared from different volcanic glasses (i.e., rhyolite) with similar bulk compositions, similar lack of long-range structural order, and similar particle sizes, distributions, and morphologies, but which exhibited dramatically different hydration properties and macroscopic mechanical behaviors. By using a combination of advanced 1D and 2D solid-state nuclear magnetic resonance (NMR) spectroscopy techniques and complementary small-angle neutron scattering (SANS) analyses, differences in the atomic-level and mesoscale compositions and structures of the glasses are established and correlated to their hydration properties. Importantly, certain types and distributions of volcanic glass structural features, specifically $Al^{IV}$ species dispersed in silica-rich networks, are determined to be particularly influential in hydrothermal reaction processes and account for the differences in the types and quantities of cementitious hydration products and their resulting mechanical properties.

## 6.3. Materials and Methods

Roman-inspired pozzolanic concrete mortars were prepared using volcanic glass sourced from the Rocky Mountain region, U.S.A. and other rhyolitic volcanic glasses procured from different geographic sources for comparison. Roman-inspired pozzolanic concretes were prepared using 3:1 volcanic glass:$Ca_3SiO_5$ mixtures hydrated for 8 days at 90 °C. In comparable ancient Roman formulations using quicklime (CaO), the enthalpies of hydration reactions in meter-tick mortars could maintain temperatures of ca. 90 °C for several months during prolonged solidification processes.[11] High purity triclinic tricalcium silicate ($Ca_3SiO_5$, Mineral Research Processing, France) was used in place of ordinary Portland cement. The $Ca_3SiO_5$ used here contained <0.1 %w Al impurities enabling $^{27}Al$ isotropic tracking of

transformations involving Al-containing volcanic glasses. Several ground rhyolitic volcanic glasses of different geographic origins were examined in order of decreasing compressive strength development: Rocky Mountain #1, East Asian #2, and Rocky Mountain #3 were supplied from the collection of Halliburton. In Table 6.1., the seven-day compressive strength of hydrated 3:1 volcanic glass:class A gray oilwell cement blends are compared.

**Table 6.1)** Compressive strength, surface area, and particle sizes of different volcanic glasses.

| | **BET [$m^2/g$]** | **Particle Size-D50 [µm]** | **Compressive Strength (psi)** |
|---|---|---|---|
| **#1** | 4.2 | 17 | 1024 |
| **#2** | 3.9 | 95 | 70 |
| **#3** | 3.6 | 16 | 324 |

Unless otherwise specified, all volcanic glass-cement mixtures were hydrated using a water-to-solids ratio of 0.58 mL/mg, consisting of a brine solution of 4% by-weight-of-solids (bwos) $Na_2SO_4$ and 4% NaCl. Generally, it has been observed that NaCl/$Na_2SO_4$ (*aq*.) have an acceleratory effect on the hydration of volcanic glass-cement blends at elevated temperatures, as shown in Figure 6.1, but this effect remains poorly understood. One possible explanation, is that alkali cations ($Na^+/K^+$) may depolymerize -Si-O-Si- bonds in calcium silicate hydrates, thereby promoting the formation of reactive sodium silicate precursors or gels.[30] The presence of NaCl is also known to accelerate the dissolution of amorphous silica, which may account for the improved hydration activity of volcanic glass blends.[31] Additionally, in the hydrothermal synthesis of tobermorite, excess $Na^+$ promotes the formation of non-tobermorite phases, including feldspathoids, zeolites, or poorly ordered sodium aluminosilicate hydrates

all of which may function as cementitious binders.[32–34] Similar types of products have been identified in the binder phase of ancient Roman seawater concrete as discussed above.

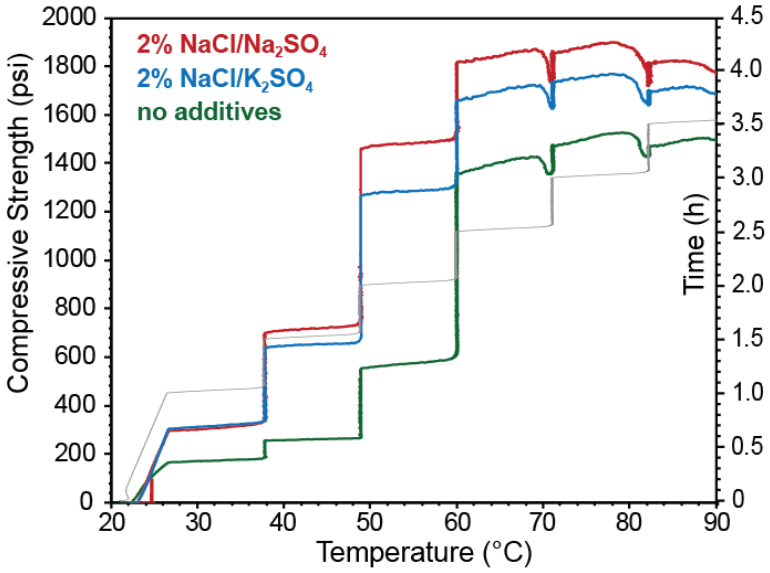


**FIGURE 6.1)** Early compressive strength versus temperature of 3:1 Rocky Mountain #1 volcanic glass:class A oilwell cement hydrated without additives (green), with 2% bwos $NaCl+K_2SO_4$ (blue,) or with 2% bwos $NaCl+Na_2SO_4$ (red) The gray trace corresponds to the time axis (hours). Compressive strength (psi) of hydrating pastes is estimated using an ultrasonic pulse velocity test.

Bulk elemental analysis was acquired using a Rigaku ZSX Primus IV Wavelength Dispersive X-Ray Fluorescence (XRF) analyzer. Prior to analysis, the samples were pelletized into 10 mm wafers. Table 6.2, shows XRF elemental analyses (wt% oxide basis) for the three rhyolitic volcanic glasses indicating that they have similar bulk compositions. As opposed to network charge-modifying cations ($Na^+$, $K^+$, $Ca^{2+}$) which may depolymerize Si-O-Si bonds in melts to form bridging or non-bridging oxide bonds, $Al^{III}$ species predominantly exist as $AlO_4^-$ tetrahedra and must be charge compensated. In tectosilicates, these $AlO_4^-$ tetrahedra are fully charge balanced and the network has a high degree of connectivity. Assuming that all $Na^+$, $K^+$, and $Ca^{2+}$ network modifiers are in tectosilicate environments corresponding to mixtures

of either the alkali feldspar series $Na_xK_{1-x}AlSi_3O_8$ or the plagioclase feldspar series $Na_xCa_{1-x}Al_{2-x}Si_{2+x}O_8$, then a range for the $SiO_2$ molar excess, $f_{silica}$, can be estimated to be bounded between,

$$\frac{n_{Si} - 3(n_{Na} + n_K) - 2n_{Ca}}{n_{Si}} < f_{silica} < \frac{n_{Si} - 3n_K - n_{Na}\left(2 + \frac{n_{Na}}{n_{Na} + n_{Ca}}\right)}{n_{Si}}, \quad (1)$$

where $n_{Si}$, $n_{Na}$, $n_K$, and $n_{Ca}$ are the total moles of Si, $Na^+$, $K^+$, and $Ca^{2+}$. Here, $f_{silica}$ corresponds to the molar fraction of Si in excess of a feldspar composition. All three volcanic glasses are $SiO_2$ oversaturated, suggesting that a significant fraction of -Si-O-Si- environments are siliceous and not charge compensated by metal cations, as indicated by $f_{silica}$ values in the range 0.39-0.49 shown in Table 6.2. Stoichiometrically, the entire volcanic glass series is metaluminous, $Al_2O_3<(Na_2O+K_2O+CaO)$ and $Al_2O_3 >(Na_2O+K_2O)$. Although such bulk analyses provide insights regarding expected network connectivity, the small variations in bulk compositions alone cannot account for the large differences in the hydration rates and products of the volcanic glasses.

Wide-angle X-ray scattering (WAXS) patterns were acquired on a Panalytical Empyrean powder diffractometer using Cu *K*α radiation with a wavelength of 1.54 Å. The volcanic glasses were scanned at 2°/min between 2θ angles of 15−65° and exhibited patterns that were dominated by broad scattering intensity from predominant glass-like components and were overlain with narrow reflections that were indexable to quartz (*Q*), plagioclase feldspar minerals (*P*), and possibly small amounts of magnetite (*M*) and cristobalite (*C*). Rietveld refinement was used to determine the amorphous fraction, which is >95% for the series, see Figure 6.1. Many of these XRD-detectable crystalline components can form by devitrification processes of unstable vitreous material near volcanic glass grain surfaces or within vesicles.[35]

Low-temperature components, such as quartz and feldspar, may crystallize directly from the primary magma phase under slow quenching conditions. Alternatively, dilute Fe can act as a nucleation agent, promoting the formation of Fe-containing crystallites including magnetite, pyroxenes, or nepheline during quenching.[28] While the presence of these minerals provides evidence regarding the petrology of the volcanic glasses, their small relative amounts and relatively high stabilities means that they are expected to contribute negligibly to overall hydration activity.

**Table 6.2)** Representative compositions (wt% on oxide basis) of volcanic glasses from X-ray Fluorescence (XRF) analyses.

| | **$SiO_2$** | **$Al_2O_3$** | **$K_2O$** | **$Na_2O$** | **CaO** | **$Fe_2O_3$** | **other** | **$f_{silica}$[a]** |
|---|---|---|---|---|---|---|---|---|
| **#1** | 75.3 | 12.8 | 6.2 | 2.6 | 1.1 | 1.3 | 0.7 | 0.46 – 0.49 |
| **#2** | 73.6 | 13.5 | 6.5 | 2.8 | 1.6 | 1.5 | 0.5 | 0.41 – 0.46 |
| **#3** | 74.3 | 13.9 | 6.3 | 3.4 | 0.9 | 0.8 | 0.5 | 0.39 – 0.42 |

[a] $f_{silica}$ is the estimated molar excess of $SiO_2$ based on feldspar stoichiometry considerations

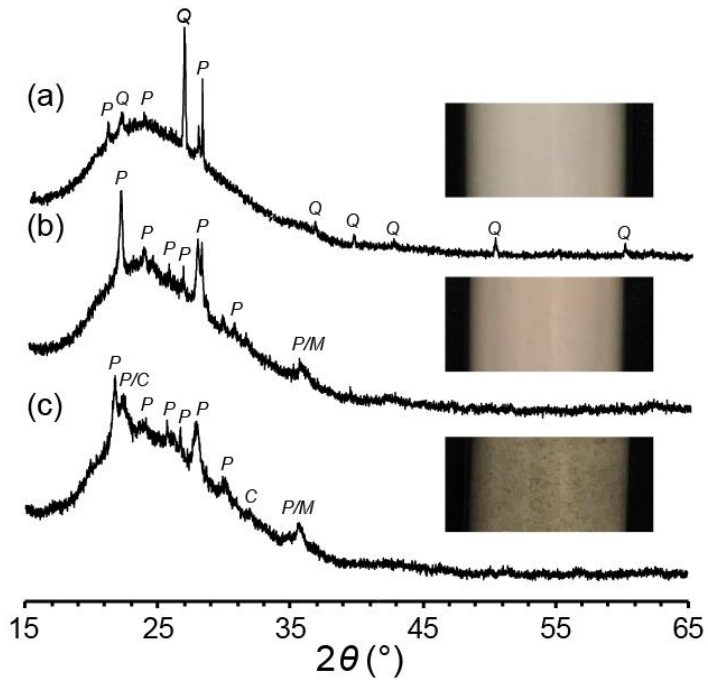


**FIGURE 6.2)** WAXS patterns and optical images of (a) Rocky Mountain volcanic glass #1 (white), (b) Rocky Mountain volcanic glass #3 (beige), and (c) Rocky Mountain volcanic glass #2 (light gray). Reflections indexable to quartz (*Q*), plagioclase minerals (*P*) magnetite (*M*), and cristobalite (*C*) are shown.

Solid-state NMR techniques are sensitive to ordered and disordered environments and have been used extensively to measure bulk compositions, local coordination environments, and network connectivity in aluminosilicate glasses, zeolites,[36] and cement hydrates.[14] Solid-state 1D single-pulse $^{29}$Si NMR and 1D spin-echo $^{29}$Si saturation recovery NMR were conducted at 295 K on a Bruker 500 MHz AVANCE-II NMR spectrometer operating at 99.31 MHz for $^{29}$Si with an 11.7 T widebore superconducting magnet, using an H-X magic-angle-spinning (MAS) probehead at 10 kHz MAS. Solid-state 1D single-pulse $^{27}$Al NMR and 2D $^{27}$Al 3Q-MAS NMR were conducted at 295 K on a Bruker 800 MHz AVANCE-III NMR spectrometer operating at 208.49 MHz for $^{27}$Al with an 18.8 T superconducting magnet and using an H-X MAS probehead at 22.5 kHz MAS. NMR lineshape analyses were conducted using the software DMFit, with Gaussian or Lorentzian line shapes fit according to signal

position, width, and amplitude. The $^{29}$Si NMR isotropic chemical shifts were externally referenced to tetramethylsilane, using tetrakis(trimethylsilyl)silane [$((CH_3)_3Si)_4Si$] as a secondary standard. The $^{27}$Al NMR shifts were externally referenced to 1M $Al(NO_3)_3$ solutions. Conventional 1D $^{29}$Si ($I$ = 1/2, 4.7% abundance) and $^{27}$Al ($I$ = 5/2, 100% abundance) NMR analyses typically only indicate the presence of broad overlapping distributions of local tetrahedral environments characteristic of a disordered solid; however the latter, supported by 2D $^{27}$Al 3Q-MAS measurements, can be used to estimate the amounts of "NMR visible" $Al^{IV}$, $Al^{V}$, and $Al^{VI}$ species. Such techniques provide important insights regarding bulk compositions but generally have insufficient resolution to identify local structural variations in complex solid-oxide mixtures.

Multi-dimensional 2D NMR techniques provide improved spectral resolution and may be used to measure local Si and Al environments in heterogeneous solids.[37,38] Low-temperature 2D $^{27}$Al{$^{29}$Si} dipolar-mediated HMQC NMR spectra were conducted at 95 K on a Bruker 400 MHz ASCEND DNP-NMR spectrometer operating at 400.13 MHz for $^{1}$H, 79.50 for $^{29}$Si, and 104.26 for $^{27}$Al with an 9.4 T widebore superconducting magnet and using a variable-temperature H-X MAS probehead at 8 kHz MAS. Each HMQC experiment was acquired with 10000 – 15000 scans, 10$t_1$ increments, a recycle delay of 0.5 s, a R42 dipolar recoupling block of 4.5 ms, and $^{27}$Al double-frequency sweep. Central-transition selective $^{27}$Al pulses in the HMQC experiment used a 90° pulse length of 10 μs and low r.f. powers. The HMQC experiments selectively detect through-space dipole-dipole-coupled $^{27}$Al–$^{29}$Si spin pairs and correlate their respective signals to yield improved spectral resolution. The time domain data were processed using a 2D Fourier transform to obtain a two-dimensional (2D) contour map of correlated signal intensity with the $^{27}$Al shift (ppm) and the $^{29}$Si chemical shift (ppm) on

the *x*-axis and *y*-axis referred to as the direct and indirect dimensions, respectively. Signal intensity in the 2D correlation map is dependent both on the abundance of the $^{27}Al$–$^{29}Si$ spin pairs and the strength of their mutual dipole-dipole interactions, which scale with distance as $\sim 1/r^3$ and atomic mobility. This provides a means to probe short-range structural order by direct measurement of Al-O-Si environments in the unhydrated volcanic glasses and enables tracking of $^{27}Al$ and $^{29}Si$ species in the volcanic glasses as they transform into cementitious binders upon hydration. In addition, the HMQC analyses are used to elucidate preferential $Al^{IV}$ siting and to semi-quantitatively estimate the degree of condensation of resulting calcium aluminosilicate hydrates, which vary among the different volcanic glasses.

SANS measurements were performed on unhydrated Rocky Mountain #1 volcanic glasses to identify mesoscale compositional and structural heterogeneities. Contrast-matching experiments were conducted on suspensions of Rocky Mountain #1 volcanic glasses in $D_2O/H_2O$ solvent using the NGB 10 m SANS instrument at the National Institute of Standards and Technology Center for Neutron Research (Gaithersburg, MD). Scattering from each sample was collected in the *q*-range from 0.004-0.9 $Å^{-1}$ with the wavelengths $\lambda$ = 5 and 12 Å and a wavelength spread of $\Delta\lambda/\lambda = 0.14$. The scattering vector *q* is defined as $q = 4\pi \sin(\theta/2)/\lambda$ where $\theta$ is the angle at which the neutron is scattered and $\lambda$ is the neutron wavelength. The scattering intensities were corrected for empty cell, plexiglass standard, and detector efficiency. Scattering patterns were reduced using standard NCNR protocols with Igor PRO software.

## 6.4. Measuring local Al-O-Si distribution of unhydrated volcanic glasses

As indicated by the WAXS analyses in Figure 6.2, the volcanic glasses are predominantly disordered and glass-like, comprised of a large majority fraction that lacks long-range structural order. Such disorder is also manifested at the atomic-level by quantitative solid-state 1D $^{29}$Si and $^{27}$Al MAS NMR spectra in Appendix 6A1, Fig. 6A1, which show broad overlapping signals that correspond principally to tetrahedrally coordinated Si and Al atoms, which are in distributions of local environments that are characteristic of multicomponent aluminosilicate glasses. The $^{29}$Si NMR signal intensity of Rocky Mountain #1 volcanic glass measured at a field strength of 11.7 T and 10 kHz MAS may be represented by Gaussian distributions centered at -95 ppm (I = 24%, fwhm = 16.7 ppm) and -105 ppm (I = 76%, fwhm = 15.9 ppm) consistent with a high degree of network connectivity. The $^{27}$Al NMR signal intensity of Rocky Mountain #1 volcanic glass measured at a field strength of 18.8 T and 22 kHz MAS may be represented by Gaussian distributions centered at 55 ppm (I = 97%, fwhm = 12.4 ppm) and 5 ppm (3%, fwhm = 12.2 ppm) associated with $Al^{IV}$ and $Al^{VI}$ species respectively with broad distributions of isotropic chemical shift and residual second-order quadrupolar interactions. As opposed to $Al^{IV}$, which most commonly participates as a 'network former', both $Al^{V}$ and $Al^{VI}$ typically act as charge-balancing 'network modifiers'. The presence of $Al^{V}$ or $Al^{VI}$ can significantly increase aluminosilicate melt viscosity and glass stability which may negatively impact hydration activity. However, in general, conventional scattering and spectroscopy techniques cannot resolve local structural differences or -Si-O-Al- spatial distributions within heterogeneous non-equilibrium solid-oxide mixtures.

In contrast to quantitative solid-state 1D $^{27}$Al or $^{29}$Si NMR which cannot resolve overlapping distributions of tetrahedral environments, dipolar-mediated 2D $^{27}$Al{$^{29}$Si} HMQC analyses

can measure and partially-resolve local Al-O-Si distributions arising from distinct composition domains. Of the two NMR-active nuclei, the $^{29}$Si chemical shift affords greater resolution with respect to changes in local bonding environments and network connectivity. By convention, tetrahedral $^{29}$Si species are described using the notation $Q^n(m\cdot\text{Al})$, where $n$ = 0, 1, 2, 3, or 4 refers to increasing extents of cross-linking corresponding to the number of covalent Si-O-Al or Si-O-Si bonds, and $m$ is the number of Al atoms ($m \leq n$) that are covalently bonded to Si atoms through bridging oxygen atoms. The $^{29}$Si chemical shift typically ranges from -65 ppm for $Q^0(0\cdot\text{Al})$ species to -115 ppm for $Q^4(0\cdot\text{Al})$ species. Additionally, each covalently bonded Al ($m$ = 1, 2, 3…) displaces the $^{29}$Si isotropic chemical shift by ~ 3 to 7 ppm to higher frequency. For materials with long-range order, tetrahedral bond angles generally exhibit a narrow discrete distribution that is commensurate with the crystal structure and accompanied also by relatively narrow $^{29}$Si NMR linewidths. In materials such as volcanic glasses or other glasses with poorly ordered aluminosilicate networks, bond lengths may be regarded as similar, though the bond angles are distorted from that associated with tetrahedral symmetry to accommodate distributions of local environments and charge-modifying cations. In principle, for $Al^{IV}$ in aluminosilicates, the $^{27}$Al isotropic chemical shift is approximately linearly related to the mean T-O-T bond angle (α) between tetrahedrally coordinated Si or Al atoms in the network and may be approximated by the relation, $\alpha = (137 - \delta_{27\text{Al,iso}})/0.532$, as discussed elsewhere.[39] However, spectral resolution is limited by the relatively narrow $^{27}$Al isotropic chemical shift range ~50 to 80 ppm for $Al^{IV}$, broadening due to second-order quadrupolar interactions, large distributions of T-O-T angles, and the effects of coordination to different modifying cations. Nevertheless, 2D $^{27}$Al{$^{29}$Si} HMQC spectra yield a correlated map of $^{27}$Al and $^{29}$Si frequencies between dipole-dipole-coupled nuclei, which allow distinct

Si-O-Al distributions or local other environments to be discerned in complex non-equilibrium solid oxide mixtures.

For a highly cross-linked aluminosilicate network, the extent of incorporation of four-coordinate Al heteroatoms within otherwise predominantly siliceous networks is associated with $Q^4(0{\cdot}\mathrm{Al})$ $^{29}$Si species. As indicated by the bulk elemental analyses in Table 6.2, rhyolitic volcanic glasses are oversaturated with $SiO_2$, such that significant amounts of $Q^4(0\mathrm{Al})$ species are expected. For a phase-separated system with highly siliceous and Al-rich tectosilicate regions, relatively large domains would be expected to have small fractions of $^{27}$Al- $Q^4(0{\cdot}\mathrm{Al})$ $^{29}$Si species, mostly at their mutual interfaces, and correspondingly manifest reduced correlated intensity in the $^{27}$Al dimension at ca. 55 ppm with signals in the $^{29}$Si dimension in the range -106 ppm to -115 ppm, as depicted schematically by the red arrows and dashed red boxes in Figure 6.3. For example in Figure 6.3a, the 2D $^{27}$Al{$^{29}$Si} HMQC spectrum of unhydrated volcanic glass #1 shows much weaker correlated signal intensity in the $^{27}$Al-$Q^4(0{\cdot}\mathrm{Al})$ $^{29}$Si region (small dashed red box), compared to the spectra for volcanic glass #3 (Fig. 6.3b) and volcanic glass #2 (Fig. 6.3c). Interestingly, in the 2D $^{27}$Al{$^{29}$Si} HMQC spectra in Figure 6.3, the volcanic glasses exhibit markedly different -Si-O-Al distributions suggesting both varying degrees of local order and extents of Al-$SiO_2$ intermixing. In Fig. 6.3b, $^{27}$Al-$Q^4(0{\cdot}\mathrm{Al})$ $^{29}$Si species yield correlated intensity in the high $^{29}$Si chemical shift region spanning from -104 to -115 ppm (dashed red box).

For these volcanic glasses, the mechanical strength of hydrated volcanic glass-cement blends is found to be inversely correlated to the amount of $^{27}$Al-$Q^4(0{\cdot}\mathrm{Al})$ $^{29}$Si intensity; in other words, Al-$SiO_2$ intermixing is detrimental to pozzolanic activity. It is known that the interaction of dilute Al heteroatoms with highly siliceous networks can impede dissolution, a

phenomenon that accounts for the long-term stability of ocean diatoms[31]. Alternatively, although volcanic glass granules are vesicular, they lack nanoporosity such that the formation of reactive Al-rich tectosilicate domains could enable preferential transformation of volcanic glasses granules within hydrating cementitious mixtures.

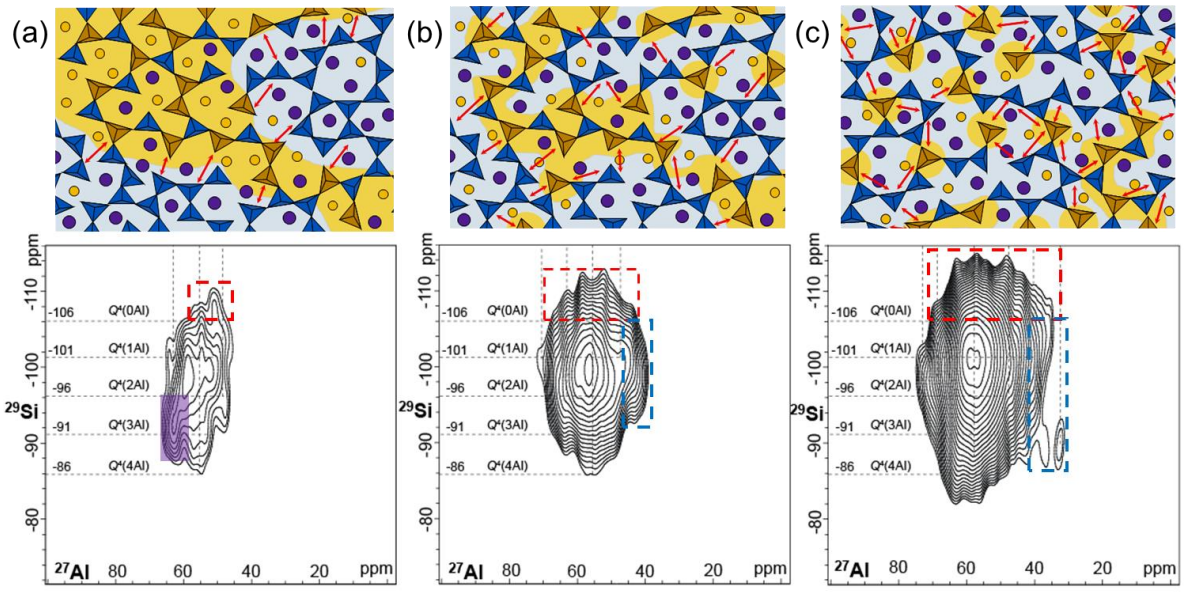


**FIGURE 6.3)** Correlated atomic-scale Al and Si environments in unhydrated (a) volcanic glass #1, (b) volcanic glass #3, and (c) volcanic glass #2 from left-to-right as determined by 2D $^{27}$Al{$^{29}$Si} dipolar-mediated HMQC NMR spectra acquired at 100 K, 9.4 T, and 8 kHz MAS. Schematic diagrams of Al-O-Si distributions in unhydrated volcanic glass with Si (blue tetrahedra), Al (orange tetrahedra), $K^+$ (purple spheres), and $Na^+$ (orange spheres). Red arrows correspond to dipolar-coupled $^{27}Al^{IV}$-O-$^{29}$Si $Q^4$(0Al) moieties, as established by correlated 2D intensity in the dashed red boxes of the 2D NMR spectra, and which manifest different extents of $Al^{IV}$ incorporation into densely cross-linked siliceous networks. Purple band in (a) corresponds to evidence of feldspathoid-type moieties.

The 2D $^{27}$Al{$^{29}$Si} dipolar-mediated HMQC spectra unambiguously demonstrates that, despite the broad distributions observed by conventional 1D $^{27}$Al or $^{29}$Si NMR, volcanic glass #1 is comprised of numerous overlapping distinct local environments with varying degrees of local order. For example, a relatively narrow ridge spanning 62 to 65 ppm in the $^{27}$Al dimension and spanning -86 to -96 ppm in the $^{29}$Si dimensions is consistent with the Al-rich

feldspathoid mineral series[40] or zeolitic environment which has a Si/Al ratio approaching unity. The relatively narrow linewidth in the $^{27}$Al dimension over this region suggests a relatively narrow distribution of tetrahedral bond angles consistent with increased short-range order. Importantly, crystallization of Al-rich phases represent a deleterious phenomenon in the vitrification of high-level nuclear wastes, but in concentrating $AlO_4^-$ from the surrounding matrix[22], may be desirable in promoting hydration activity in cementitious mixtures. Volcanic glass #1 also contains broad distributions spanning 50 to 60 ppm in the $^{27}$Al dimension and -85 to -104 ppm in the $^{29}$Si dimension consistent with a Si-rich feldspar glassy matrix[23] that dominates the 2D $^{27}$Al{$^{29}$Si} intensity map. There is a low intensity shoulder spanning 35 to 45 ppm in the $^{27}$Al dimension (blue dashed box) which may be attributed to either extra framework $Al^{IV}$ species as observed in zeolites and mullite-like minerals,[39] or otherwise attributed to a local environment approaching that of penta-coordinated $Al^{V}$. These extra framework Al species might be expected to act as strong 'network modifiers' similarly to metal cations rather than as 'network formers'. Similarly to Al-$Q^4$(0·Al) intensity, 2D $^{27}$Al{$^{29}$Si} intensity over 35 to 45 ppm in the $^{27}$Al dimensions is inversely correlated with mechanical strength development for the series volcanic glass #1 > volcanic glass #3 > volcanic glass #2. Comparatively, volcanic glass #2 exhibits similar types of Al-O-Si environments, but with significantly broader distributions of correlated intensity associated with either a more random network or smaller clusters of ordered domains. For a similar number of scans, greater overall 2D $^{27}$Al{$^{29}$Si} intensity is obtained for volcanic glass #2 consistent with an increased prevalence of Al-$SiO_2$ intermixing. Large amounts of $^{27}$Al-$Q^4$(0·Al) $^{29}$Si intensity for volcanic glass #2 suggest a high extent of Al-$SiO_2$ intermixing consistent with a more homogeneous glass composition expected for a rapidly quenched melt.

Weaker overall 2D $^{27}$Al{$^{29}$Si} intensity and specifically correlated intensity associated with $^{27}$Al-$Q^4$(0·Al) $^{29}$Si species for volcanic glass #1 suggest that Al-rich tectosilicate domains are large enough, at least several bond distances, that through-space correlations with surrounding silica rich regions are negligible. It is hypothesized that volcanic glass #1 was formed under conditions which allowed for a greater extent of devitrification or partial crystallization processes to occur (*i.e.*, reduced melt viscosity, slower quenching). This is represented in the schematic structures for volcanic glass #1, volcanic glass #3, and volcanic glass #2 proposed in Fig. 6.3., which correspond to Al-rich tectosilicate domains of varying dimensions. By Lowenstein's rule, it is generally expected that aluminosilicate glasses with highly intermixed Al-$SiO_2$ are more thermodynamically stable and will resist alkaline hydrolysis.[41] By this hypothesis, we anticipate that volcanic glasses with higher extents of Al/$SiO_2$ avoidance will exhibit higher propensities to form calcium aluminosilicate hydrates which is correlated with improved mechanical performance.

## 6.5. Compositions of Fe-containing phases in Rocky Mountain volcanic glass #1

Commonly, in magnetic resonance, dilute amounts of paramagnetic dopants are incorporated as a contrast agent to enhance relaxation rates and shorten overall experiment times. From the XRF analysis, volcanic glass #1 contains ~1.3 wt% of $Fe_2O_3$ (oxide basis), which results in relatively short $^{29}$Si $T_1$ relaxation times. Specifically, $^{29}$Si saturation recovery curves of volcanic glass #1 exhibit a stretched-exponential dependence consistent with an inhomogeneous distribution of paramagnetic centers.[42] As discussed previously, in many magma compositions, $Fe^{3+}$ is preferentially excluded from feldspar-like environments and

concentrated in Fe-containing mineral phases upon quenching. Recently, it has been demonstrated that dilute $Fe^{3+}$ concentrations in sodium aluminosilicate melts can promote the formation of nephelines which depletes Al from the surrounding glassy matrix[43]. Here, spin-echo $T_1$-filtered $^{29}Si$ NMR measurements allow for the preferential detection of the fastest relaxing $^{29}Si$ NMR visible species which are those closest to paramagnetic centers. In Figure 6.4, the $T_1$-filtered 1D $^{29}Si$ spin-echo spectra of volcanic glass #1 acquired at short filter delays ($\tau$ = 2 ms) indicates that the Fe-containing regions have improved local order in comparison to the bulk.

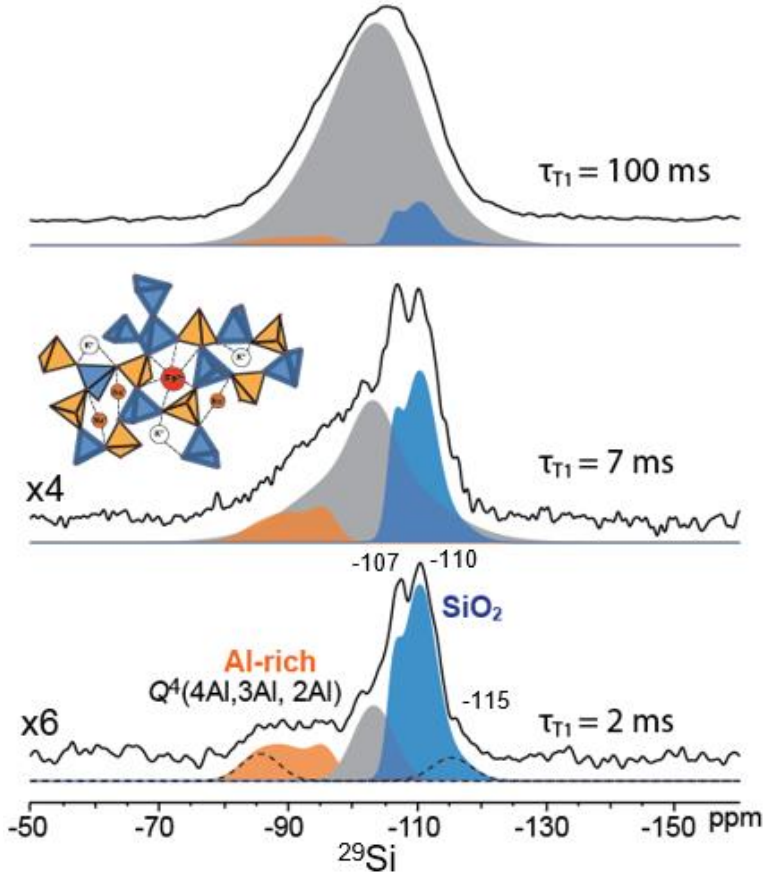


**FIGURE 6.4)** Solid-state 1D $^{29}Si$ spin-echo MAS NMR spectra of unhydrated Rocky Mountain volcanic glass #1 acquired at 295 K, 10 kHz MAS, 11.75 T, using an echo delay ($\tau_{echo}$) of 90 µs. The spectra were each acquired using 24,500 scans but with different nuclear spin-lattice relaxation-time filter delays of $\tau_{T1}$ = 2 ms, 7 ms, or 100 ms.

Notably, for τ = 2 ms, the contributions of feldspar-like $Q^4$(1Al) $^{29}$Si environments *ca*. -95 to -100 ppm are diminished in comparison to feldspathoid-like $Q^4$(4Al) and $Q^4$(3Al) $^{29}$Si environments *ca*. -80 to -95 ppm. Notably there are fast-relaxing distributions of $Q^4$(0Al) $^{29}$Si species with signals at ca. -107 to -109 ppm, which may be attributed to quartz-like environments, cristobalite-like environments, or amorphous silica. Additionally, there is a resolved intensity shoulder *ca*. -111 to -114 ppm which may be attributed to tridymite-like $SiO_2$. The $T_1$-filtered $^{29}$Si NMR measurements establish that paramagnetic impurities (*e.g.*, $Fe^{2+}$ or $Fe^{3+}$) are preferentially concentrated into Al-rich and highly siliceous environments but are excluded from feldspar-like environments *ca*. -95 to -104 ppm which otherwise make up a significant fraction of volcanic glass #1. Although, due to their short $^{29}$Si $T_1$ relaxation times, such Fe-containing phases may not appear in the 2D NMR correlation spectra in Fig. 6.3 which is obtained using a dipolar recoupling time of 4.5 ms. Nevertheless, in combination the 2D $^{27}$Al{$^{29}$Si} HMQC and the $T_1$-filtered spectra strongly indicate that volcanic glass #1 is comprised of heterogeneous distributions of local environments that are consistent with melt immiscibility or partial crystallization processes. The local $^{29}$Si or $^{27}$Al environments are similar to crystalline tectosilicate and siliceous minerals, though are not appreciably detected in WAXS, suggesting they are nanocrystalline or otherwise lack long-range structural order.

## 6.6. Characteristic scattering dimension of composition domains in unhydrated Rocky Mountain volcanic glass #1 by small-angle neutron scattering (SANS)

While NMR-based techniques can be used to probe local bonding environments near specific NMR-active (*e.g.*, $^{27}$Al, $^{29}$Si), complementary scattering techniques such as small-

angle neutron scattering (SANS) are sensitive to bulk nanostructural features of the material and can be used to estimate domain sizes. In SANS measurements, one probes the scattering of neutrons from a sample as a function of the wavevector, $q = \frac{4\pi \sin(\theta)}{\lambda}$ where θ is the angle the neutrons are scattered and λ is the neutron wavelength. The intensity of scattered neutrons is proportional to the Fourier transform of the scattering length density distribution in the material of interest, where $q$ is the transformed spatial coordinate. The scattering length density is dependent on the atomic composition of the sample, and isotopes of the same atom (*e.g.*, $H_2O$ and $D_2O$) can have drastically different scattering length densities. This phenomenon enables techniques known as contrast variation, whereby one can change the contrast between components in the sample. In contrast variation with water, the solvent composition is varied between $H_2O$ and $D_2O$. Since mixtures of $H_2O$ and $D_2O$ span nearly the entire range of scattering length densities, at some point in a mixing series the contrast of the solvent will reach a "match point" where the scattering length density of the solvent is equal to some feature in the system.

To probe nanostructural features within the volcanic glass grains, we employed a contrast variation series to reduce scattering contributions from the volcanic glass grains and the solvent. The solvent composition was varied from 100% $D_2O$ to 100% $H_2O$ and SANS patterns were measured. These experiments are conducted for the q-range from 0.01-0.05 $Å^{-1}$, which is sensitive to features on length scales ranging from ~10-50 nm. The results of the contrast variation study are included in Figure 6.5. In the contrast variation study, we find that the lowest measured scattering intensity is in the 60% $D_2O$/40% $H_2O$ sample, which indicates that this solvent composition is closest to the match point between the solvent and volcanic glass grains. For the samples other than the 60% $D_2O$/40% $H_2O$ sample, we find that the

scattering intensity smoothly decreases with increasing $q$ with a power law slope of approximately $q^{-3}$, which is indicative of a surface fractal structure. The measured scattering for these concentrations is indicative of scattering that is dominated by contrast between rough particles and solvent, as would be expected for the suspended volcanic glass samples far from the contrast match point. For the 60% $D_2O$/40% $H_2O$ sample we observe a significantly less smooth variation in scattering intensity. In particular, we observe shallow peaks at $q \approx 0.018$, 0.023 and 0.027 $Å^{-1}$. These shallow peaks are indicative of nanostructural features with length scales of approximately $\frac{2\pi}{q}$, i.e., approximately 25 nm. Since these peaks only appear when the contrast between solvent and grain is lowered, these features are attributable to the internal structure of the volcanic glass grains and not surface features on the grains.

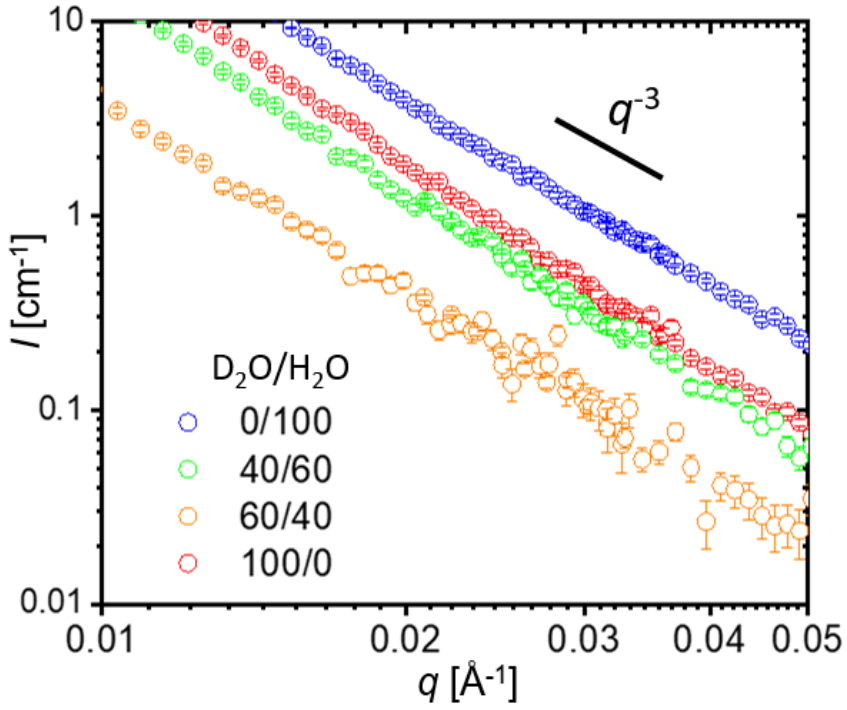


**FIGURE 6.5)** SANS contrast variation of unhydrated Rocky Mountain volcanic glass #1 dispersed in hydrating mixtures with different ratios of $D_2O$ to $H_2O$, colored symbols). The measured scattering intensity is included as a function of $q$. The error bars indicate the standard deviation of scattering intensity.

The physical origins of these scattering feature may arise from contrast between tectosilicate-rich and $SiO_2$-rich domains consistent with the proposed structure of volcanic glass #1 in Fig. 6.3a and with nanoscale phase separation. The SANS observations are consistent with 2D $^{27}Al\{^{29}Si\}$ HMQC and $T_1$-filtered 1D $^{29}Si$ spin-echo measurements which partially resolve overlapping contributions from several distinct local composition domains. Thus, the combined SANS and solid-state NMR analyses demonstrated here provide new insights regarding structure-property relationships in complex multicomponent aluminosilicate glasses with an emphasis on pozzolanic activity. However, although scattering features are resolved, the scattering intensity for the 60% $D_2O$/40% $H_2O$ sample decreases with increasing $q$ with a power law slope of less than $q^{-3}$, suggesting that scattering contributions from the solvent-grain correlations are still relevant and this solvent composition does not represent a perfect match point. Future work seeking to more precisely refine the internal structure of rhyolitic volcanic glass grains or synthetic aluminosilicate glasses against a candidate structure (*e.g.*, a fractal percolation network) by SANS would measure more solvent compositions near 60% $D_2O$/40% $H_2O$ to find a more precise contrast match point.

## 6.7. Transformations of volcanic glass Al-O-Si and structural elucidation of binder phases in hydrated volcanic glass cements

Upon hydration, the Al-O-Si distributions in hydrated volcanic glass-cement blends containing Rocky Mountain volcanic glass #1 are significantly altered indicating a high conversion of volcanic glass Al into calcium aluminosilicate hydrates (dashed blue box, Figure 6.3). Specifically, correlated signal intensity *ca*. -82 ppm in the $^{29}Si$ dimension arises

from $Q_P^2(1Al)$ species and provide unambiguous evidence that volcanic glass Al is incorporated into a cementitious binder with a layered clay-like structure similar to that of conventional calcium silicate hydrates. The subscript '$p$' denotes the pairing position of the phyllosilicate layer which represents tetrahedra strongly coordinated with the calcium oxide intralayer. This is consistent with molecular dynamics simulations[13] which indicate that Al preferentially substitutes at the bridging '$b$' positions which are typically coordinated with zeolitic $Ca^{2+}$ in calcium silicate hydrates at high Ca/Si ratios as schematically represented in Fig. 6.6. Of the three volcanic glass-cement blends, only Rocky Mountain volcanic glass #1 exhibits a significant amount of correlated $^{29}$Si signal intensity extending up to -85 ppm in the $^{29}$Si dimension which is associated with $Q_P^2(0\text{Al})$ species within a few bond distances of $^{27}$Al; this intensity has a similar linewidth to $Q_P^2(1\text{Al})$ $^{29}$Si intensity *ca*. -82 ppm consistent with disordered layered hydrates rather than a network aluminosilicate which has both narrower distributions of T-O-T bond angles and $^{27}$Al shifts. Importantly, the presence of $^{27}$Al-$Q_P^2(0\text{Al})$ $^{29}$Si intensity (solid blue box, Fig. 6.6a.) establishes that volcanic glass Al is incorporated into calcium silicate hydrate structures with longer chain lengths (pentamers, octamers, *etc*.), schematically depicted in Figure 6.6d, which are associated with improved mechanical strength.[12] Previous conventional solid-state 1D $^{29}$Si MAS NMR analyses have attributed signal intensity *ca*. -91 ppm and -96 ppm to interlayer $Q^3$(1Al) and $Q^3$(0Al) crosslinks respectively as present in the six-member ring channel of a normal 11 Å tobermorite structure.[44] It has been proposed that Al substitution strengthens cementitious binders by promoting $Q^3$(1Al) and $Q^3$(0Al) $^{29}$Si crosslinks which are not typically formed during the hydration of Portland cement. However, in hydrated volcanic glass-cement, most of the correlated 2D $^{27}$Al{$^{29}$Si} is broadly distributed *ca*. -82 ppm consistent with preferential $Al^{IV}$

incorporation into poorly ordered non-crosslinked layered silicates comparable to conventional cementitious hydrates. Importantly, on the basis of conventional 1D $^{29}$Si or $^{27}$Al NMR analyses alone, it is not possible to identify the influence of Al incorporation on local Si-O-Si or Si-O-Al connectivities in disordered cementitious hydrates. Specifically, the prevalence of $Q^2$(1Al) $^{29}$Si sites in calcium aluminosilicate hydrates has not been reliably established due to overlapping $^{29}$Si intensity with dimeric $Q^1$(0Al) species which are the most abundant early hydration product in conventional cementitious hydrates. The 2D $^{27}$Al{$^{29}$Si} HMQC analyses presented here, for Rocky Mountain volcanic glass #1-cement blends, indicate that volcanic glass Al has been substantially transformed into non-crosslinked calcium aluminosilicate hydrates after only 8 days at 90 ºC which encompasses the initial period of peak pozzolanic activity measured by calorimetry in similar systems.[45]

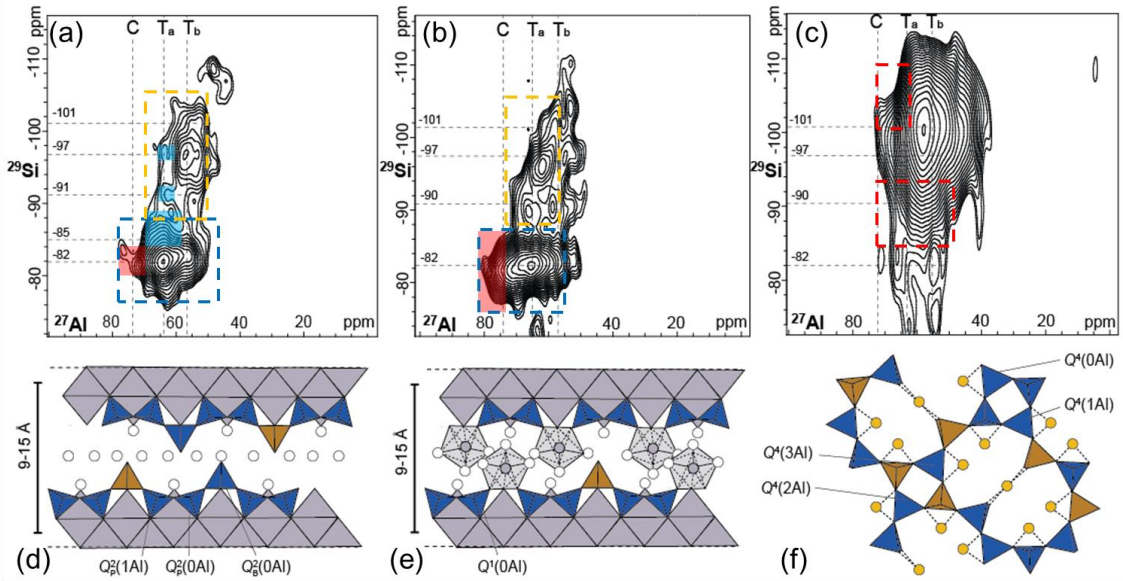


**FIGURE 6.6)** Solid-state 2D $^{27}$Al{$^{29}$Si} dipolar-mediated HMQC NMR spectra of 3:1 volcanic glass:$Ca_3SiO_5$ mixtures hydrated for 8 days at 90 °C with, water/solids = 0.58, 4% bwos NaCl, and 4% bwos $Na_2SO_4$ containing (a) volcanic glass #1, (b) volcanic glass #3, and (c) volcanic glass #2. The spectra were acquired at 100 K, 9.4 T, and 8 kHz MAS.

This provides important insights regarding the structural evolution of similarly formulated Roman mortars which continue to undergo low-temperature mineral conversion processes in marine environments strengthening over time.

Microstructural and spectroscopic analyses of Roman mortars and modern pozzolanic concretes have suggested the coexistence of calcium aluminosilicate hydrates with Al-containing geopolymeric binder phases (*e.g.*, zeolites). In ancient Roman marine concretes, zeolitic mineral growth has been observed both on calcium aluminosilicate hydrates and at the altered surface of dissolving feldspar granules.[4] These zeolitic minerals may act as a cementitious binder similar to hydrous sodium aluminosilicate gels which are the dominant hydration product in alkali-activated geopolymeric cements; however, alkali-activated concretes use high concentrations of NaOH (pH >14) at which layered calcium silicate hydrates do not appreciably form. Thus, Roman marine concretes and the volcanic glass-cement blends used here are more comparable to Portland cement formulations containing blast-furnace slag, for which improved mechanical properties have been linked to the interaction of two or more structurally dissimilar binder phases.[33,46] In these systems, the pore solution pH~10 to 12.5 is usually sufficiently low that calcium silicate hydrates and network aluminosilicates may coexist. The formation of network aluminosilicates in hydrated volcanic glass-cements, see Fig. 6.6a,b (dashed orange boxes), is supported by correlated 2D $^{27}$Al{$^{29}$Si} intensity at *ca*. -85 ppm, -91 ppm, -96 ppm, -101 ppm, and -108 ppm in the $^{29}$Si dimension with signals in the range of 50–65 ppm in the $^{27}$Al dimension, corresponding to distributions of $Q^4$(4Al), $Q^4$(3Al), $Q^4$(2Al), $Q^4$(1Al), and $Q^4$(0Al) $^{29}$Si species, respectively. Compared to the initial Al-O-Si distributions of unhydrated volcanic glass #1, correlated 2D $^{27}$Al{$^{29}$Si} intensity over this region in hydrated volcanic glass-cements exhibit relatively narrow

linewidths consistent with a higher degree of local structural order, albeit, still corresponding to overlapping signals that manifest a distribution of tetrahedrally-coordinated environments. The $^{27}$Al shift range of 50–65 ppm encompasses most framework zeolites, for which one $^{27}$Al resonance and multiple $^{29}$Si resonances are typically observed. In Fig. 6.6a,b there are multiple distinct $^{27}$Al shifts resolved for hydrated volcanic glass-cements which may arise from two or more environments in complex aluminosilicate hydrates or zeolitic minerals. Weaker 2D $^{27}$Al{$^{29}$Si} intensity shoulders in this region arise from interactions between different hydrate phases or unconsumed volcanic glass aggregate surfaces. The partially resolved correlated 2D $^{27}$Al{$^{29}$Si} signals in Fig. 6.6a (solid orange box) manifest relative $^{29}$Si intensity distributions of $Q^4$(2Al)> $Q^4$(1Al)> $Q^4$(3Al) >>> $Q^4$(4Al) ≈ $Q^4$(0Al). The most abundant corresponds to alkali aluminosilicate hydrate, which is consistent with the local environments present in the naturally occurring zeolitized mineral analcime.[47] In Fig. 6.7, complementary WAXS patterns of Rocky Mountain volcanic glass #1-cement blends produced with and without NaCl and $Na_2SO_4$ activators indicate that $Na^+$ may promote improved structural ordering among cement hydrates.

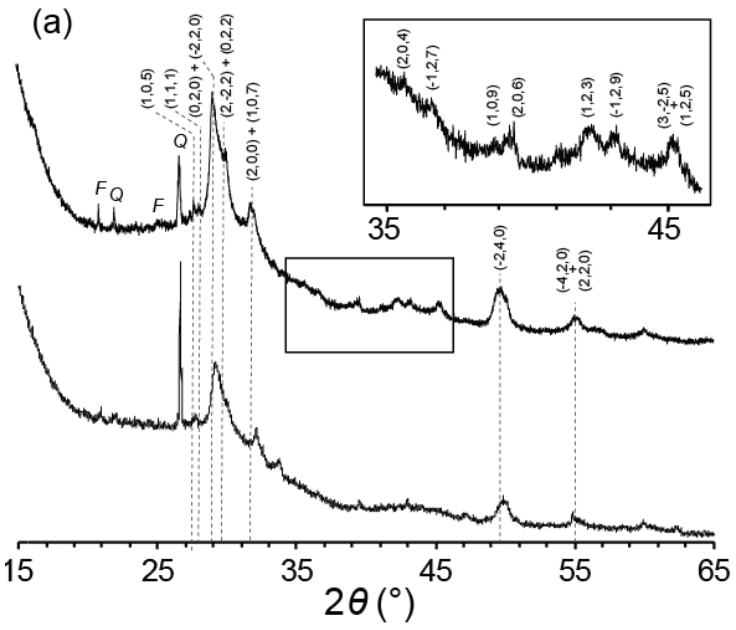


**FIGURE 6.7)** WAXS patterns of volcanic glass #1:$Ca_3SiO_5$ (3:1) mixtures hydrated for 8 days at water/solids = 0.58, 90 ºC (a) with 0.5 mM $Na_2SO_4$ and 1.2 mM NaCl and (b) without additives. Reflections are indexed to 11 Å tobermorite with a monoclinic polytype MD02 structure. Presence of $Na_2SO_4$ and NaCl results in narrower reflections associated with tobermorite.

Thus, the cementitious binders produced by hydration of volcanic glass-cements form a complex composite consisting both of non-crosslinked calcium aluminosilicate hydrates (dashed blue boxes) and network alkali aluminosilicate hydrates (dashed orange boxes). Under otherwise identical conditions, the different Al-O-Si distributions in the volcanic glasses yield cementitious binder phases with significantly different compositions and relative quantities, which account for the large differences in their rates of hydration and resultant mechanical properties.

Similar distributions of correlated 2D $^{27}Al\{^{29}Si\}$ intensity are observed for hydrated volcanic glass-cement blends containing both volcanic glass #1 and volcanic glass #3, however with notable structural differences. The most important of which is the lack of

correlated intensity associated with $^{27}$Al-O-$Q_P^2$(0Al) $^{29}$Si moieties at *ca*. -85 ppm in the $^{29}$Si dimension of volcanic glass #3 associated with Al incorporation into calcium silicate hydrates with longer silicate chain lengths (Fig. 6.6b). Additionally, the calcium aluminosilicate hydrates formed in volcanic glass #3 blends exhibit broad distributions of local $^{27}$Al environments without clearly resolved intensity maxima, consistent with relatively disordered hydrates. By comparison, for the volcanic glass #1 blend, there are resolved $^{27}$Al intensity maxima *ca*. 56 ppm, 64 ppm, and 75 ppm exhibiting narrower distributions of local $Al^{IV}$ environments, which manifest relatively ordered hydrates. Complementary 2D $^{27}$Al 3Q-MAS measurements on volcanic glass #1-cement conducted at 18.8 T confirm that these signals arise from at least three distinct $Al^{IV}$ sites, each with broad distributions of isotropic chemical shifts and second-order quadrupolar interactions (Appendix 6A1, Fig. 6A5). Based on $^{27}$Al chemical shift correlations, the signals at *ca*. 56 ppm, 64 ppm, and 75 ppm correspond to approximate mean T-O-T bond angles of 150°, 135°, and 120°, respectively. Two of these $^{27}$Al environments, *ca*. 56 ppm and 64 ppm, have previously been resolved in hydrothermally synthesized Al-tobermorite, with the relative fractions of each site depending on the compositions of the precursor material. For the $^{27}$Al species *ca*. 64 ppm, a mean T-O-T angle of 135 to 140° is consistent with Al substitution into the bridging position of the phyllosilicate layer. Meanwhile, the $^{27}$Al species *ca*. 56 ppm is consistent with a highly symmetric tetrahedral environment (similar to $Al^{IV}$ shifts in zeolites) and may also be expected to occur at the bridging position. Considering that both $Al^{IV}$ environments are present in synthetic Al-tobermorite, it is hypothesized that these $Al^{IV}$ sites correspond to differences in local coordination environments for bridging Al tetrahedra interacting with different charge modifiers (*e.g.*, $H^+$, $Na^+$, $K^+$, or $Ca^{2+}$). Specifically, due to the lack of $^{27}$Al-$Q_P^2$(0Al) $^{29}$Si

intensity associated with the $^{27}$Al species *ca*. 56 ppm, this environment is attributed to Al-rich calcium aluminosilicate hydrates where bridging sites have a higher Al occupancy rather than typical $Q_P^2(0\text{Al})$ silicates. In contrast, the $^{27}$Al species *ca*. 64 ppm, might be expected for Si-rich calcium aluminosilicate hydrates where Al bridging sites are relatively sparse and are within a few bond distances of $Q_P^2(0\text{Al})$ silicates giving rise to $^{27}$Al-$Q_P^2(0\text{Al})$ $^{29}$Si intensity in Fig. 6.6a. These assignments are consistent with molecular dynamics simulations which indicate that Al substitution: (*i*) is energetically favorable at the bridging position, (*ii*) is likely to occur when $Al^{3+}$ interacts with dimeric $Q^1(0\text{Al})$ silicates present in disordered calcium silicate hydrates, and (*iii*) requires additional charge compensation which influences local tetrahedral environments at high Al loadings. Nonetheless, Al substitution at pairing positions in the phyllosilicate layer is possible and may explain the $^{27}$Al species *ca*. -75, approximate ∠T-O-T = 120°, where mean bond angles are frustrated by strong coordination with the rigid calcium oxide sheet. Similar $^{27}$Al shifts are commonly observed in alkaline-activated slag cements[48], and based on the correlated 2D $^{27}$Al{$^{29}$Si} intensity measured here, likely correspond to highly aluminous hydrates with shorter mean chain lengths. Thus, it is demonstrated here that the quantities, compositions, and extent of order in calcium aluminosilicate hydrates is highly variable between different volcanic glasses. These differences may be attributed to complex competing solid-state and solution-phase processes in heterogeneous cementitious mixtures which lead to the formation, first, of calcium silicate hydrates by hydration of $Ca_3SiO_5$ and, subsequently, of calcium aluminosilicate hydrates by partial consumption of the volcanic glass granules.

Despite having a similar bulk composition, under otherwise identical hydration conditions, mixtures containing volcanic glass #2 form negligible amounts of calcium aluminosilicate

hydrate. As discussed above, for the three volcanic glasses, volcanic glass #2 has the highest fraction of $Q^4$(0Al) $^{29}$Si species, which may promote a higher glass stability but also diminished hydration reactivity in alkaline mixtures. To a large extent, the Al-O-Si distributions in volcanic glass #2 remain unaltered upon hydration, especially with respect to the $Q^4$(1Al) $^{29}$Si moieties, suggesting that these species act primarily as non-reactive aggregate domains with limited pozzolanic activity. Nevertheless, as indicated by the red boxes in Fig. 6.6c, certain 2D $^{27}$Al{$^{29}$Si} intensity correlations associated with Al-rich regions are partially diminished suggesting that these species are reactive and are either accessible to the pore solution or capable of solid-state $Ca^{2+}$ exchange. In contrast, for blends containing volcanic glass #1, the Al-containing fractions are substantially incorporated into cementitious binder phases which is correlated with macroscopic strength development. Nonetheless, to a large extent, highly siliceous regions within volcanic glass #1 remain unconsumed by pozzolanic reaction. As shown in Figure 6.8, 1D quantitative $^{29}$Si NMR analyses indicate that ~65% of all $^{29}$Si species in hydrated volcanic glass #1 cement occur broadly distributed in an amorphous $SiO_2$-rich component. For comparison, the spectra of unhydrated and hydrated volcanic glass #1 are overlayed with $^{29}$Si projections obtained from the indirect dimension of the 2D $^{27}$Al{$^{29}$Si} HMQC correlation maps in Fig. 6.3 and Fig. 6.6, respectively. Although not strictly quantitative, the HMQC projections correspond to intensity arising from tetrahedrally coordinated $^{29}$Si atoms that are dipole-dipole coupled to nearby $^{27}$Al species. As expected for unhydrated volcanic glass #1, the projected $^{29}$Si intensity in the HMQC spectrum largely corresponds to broad distributions of $Q^4$(1Al), $Q^4$(2Al), $Q^4$(3Al), and $Q^4$(4Al) aluminosilicate moieties, which exhibit progressively lower, by 5–8 ppm, isotropic $^{29}$Si chemical shift values with each Al next-nearest neighbor. In Fig. 6.8a, the scaled HMQC $^{29}$Si

projection (red) qualitatively compares the resolved distributions of Al-O-Si environments with the broader distributions of $^{29}$Si intensity arising from both Al-O-Si and Si-O-Si environments detected by quantitative 1D single-pulse $^{29}$Si MAS NMR. Upon hydration, the HMQC $^{29}$Si projection indicate that Al-O-Si environments are transformed into both layered silicates and $Q^4$(1Al), $Q^4$(2Al), $Q^4$(3Al)-containing aluminosilicate networks with narrower $^{29}$Si linewidths relative to the parent glass. However, despite the significant alteration of Al-O-Si environments, the 1D $^{29}$Si MAS NMR spectra indicates a large amount Al-depleted amorphous $SiO_2$ persists. After the initial pozzolanic reaction (ca. 8 days), this siliceous component may continue to consume $Ca(OH)_2$, thereby offering protection against undesirable volume expansion. These observations are consistent with characterization of ancient Roman marine concretes, which have reported that calcium aluminosilicate hydrates may be found deep within the grain boundaries of reactive aggregates. Thus, the propensity of volcanic glasses to form calcium aluminosilicate hydrates depends upon complicated incongruent dissolution or solid-state ion-exchange processes leading to preferential alteration of Al-rich silica domains.

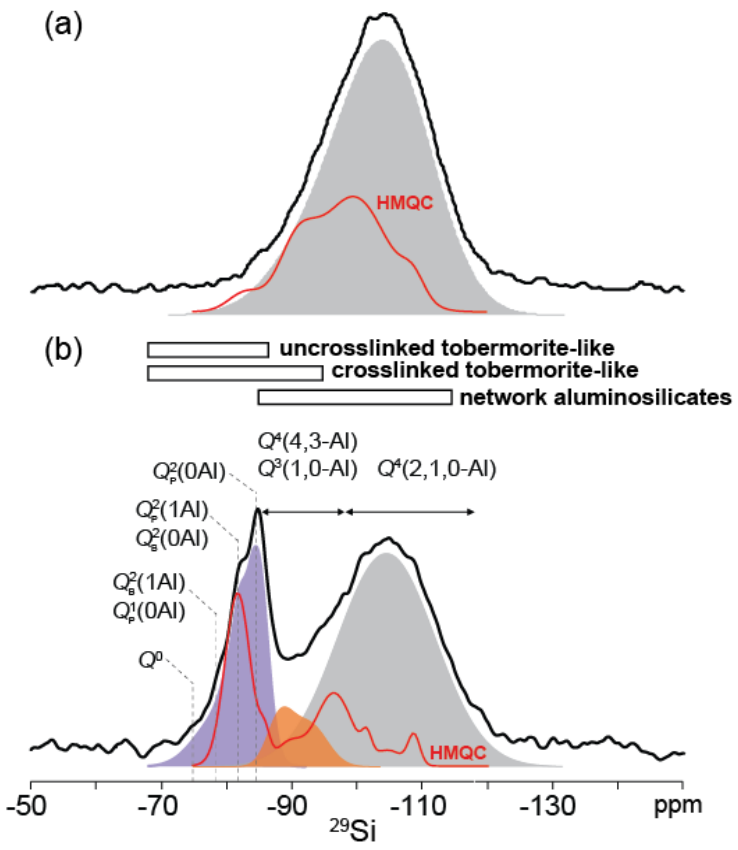


**FIGURE 6.8)** Quantitative 1D single-pulse $^{29}Si$ MAS NMR spectra of (a) volcanic glass #1:$Ca_3SiO_5$ (3:1) hydrated (water/solids = 0.58) at 90 ºC for 8 days with 0.5 mM $Na_2SO_4$ and 1.2 mM NaCl and (b) unhydrated volcanic glass #1. Deconvolution signals correspond to calcium silicate hydrates (purple), intermediate hydration species or aluminosilicates (orange), and a broad distribution of fully cross-linked siliceous species (grey). Red spectra correspond to projections 1D $^{29}Si$ intensity from the respective 2D $^{27}Al\{^{29}Si\}$ HMQC spectra and are scaled for comparison. Spectral regions typical for tobermorite and other fully aluminosilicates are shown above the spectrum in (b).

## 6.8. Conclusions

Hydrothermal transformations involving multicomponent aluminosilicate glasses (*e.g.*., rhyolites) are shown to be influenced by local compositional and structural differences arising from their unique formation conditions. Despite similarities in their bulk compositions, advanced solid-state NMR and complementary SANS measurements reveal volcanic glasses to be compositionally and structurally heterogeneous over sub-and nanometer length scales

from <1 nm to 25 nm. These results suggest that, during its geological formation, rhyolitic volcanic glasses are arrested at varying stages of crystallization, which influences the extent of local order and distributions of Al-O-Si moieties. The large differences in hydration activity observed between volcanic glasses sourced from different geographic regions is strongly correlated with the extent of $Al^{IV}$ incorporation into silica or silicate networks. Those volcanic glasses with higher fractions of $Q^4$(0Al) or $Q^4$(1Al)-containing aluminosilica networks are poor sources of reactive $Al_2O_3$, serve predominantly as non-reactive aggregates, and exhibit correspondingly lower mechanical strengths in pozzolanic concrete blends. More generally, it is demonstrated that 2D $^{27}Al\{^{29}Si\}$ HMQC analyses provide detailed insights on the types of Al-O-Si moieties and their atomic-scale distributions in multicomponent aluminosilicate volcanic glasses, which can account for differences in the hydration and mechanical properties of cementitious solids.

Several Roman-inspired pozzolanic concretes were prepared from mixtures of different volcanic glass and tricalcium silicate, $Ca_3SiO_5$, and hydrated for 8 days at 90 °C to evaluate initial pozzolanic reactions in the presence of NaCl and $Na_2SO_4$ activators. This allowed for monitoring of transformation involving volcanic glass-Al into cementitious binder phases, including calcium aluminosilicate hydrates and network aluminosilicates with improved relative order compared to the parent glass. The analyses provide unambiguous evidence that Al-containing silica moieties in reactive aggregates (*e.g.*, volcanic glass #1) are transformed into predominantly uncrosslinked calcium aluminosilicate hydrates with a phyllosilicate structure(s) similar to conventional calcium silicate hydrates. After the initial pozzolan reaction (*ca*. 8 days), there is limited evidence for crosslinked tobermorite-like $Q^3$(1Al) environments, which have been suggested to occur in these and similar cementitious systems.

Additionally, Al-rich aluminosilicate networks with appreciable fractions of $Q^4$(2Al) and $Q^4$(1Al) $^{29}$Si species, similar to zeolitic minerals such as analcime, are resolved after hydration. These species are believed to result from early zeolitization processes that occur during the initial pozzolanic reaction. The identified hydrate product distributions are similar to those observed in ancient Roman mortars, which show evidence of low-temperature zeolitization and which form complex mixtures of disordered and semi-crystalline calcium aluminosilicate hydrates. Comparison of HMQC $^{29}$Si projections and conventional 1D single-pulse $^{29}$Si MAS NMR spectra indicate that, for volcanic glass #1, Al-rich aluminosilica domains with larger relative fractions of $Q^4$(2Al), $Q^4$(3Al) and $Q^4$(4Al) $^{29}$Si moieties are preferentially consumed during hydration, leaving behind Al-depleted siliceous regions that may continue to react with $Ca(OH)_2$ over longer timescales. Interestingly, 2D $^{27}$Al{$^{29}$Si} HMQC and $^{27}$Al 3Q-MAS experiments confidently resolve at least three distinct types of $Al^{IV}$ sites associated with Al substitution into the phyllosilicate layers of calcium silicate hydrate. Comparison of several hydrated volcanic glass-cement blends indicate that the types and distributions of these calcium aluminosilicate hydrates vary widely and are correlated with the mechanical properties of the resulting mortars. These analyses provide new atomic-scale insights regarding the complex hydration, dissolution, and crystallization processes undergone by multicomponent aluminosilica glasses and the properties of their hydration products. The resulting composition-structure-property relationships provide new design criteria for the selection of materials and conditions that influence the mechanical strengths and stabilities of cementious materials. These are expected to contribute to the development of low-$CO_2$-footprint structural solids, improved syntheses of zeolite catalysts, as well as increased understanding of the remarkable properties of Roman cements.

## Appendix 6A1. Multi-nuclear $^{23}Na$, $^{27}Al$, and $^{29}Si$ characterization of raw materials and Rocky Mountain Volcanic Glass #1 cement blends

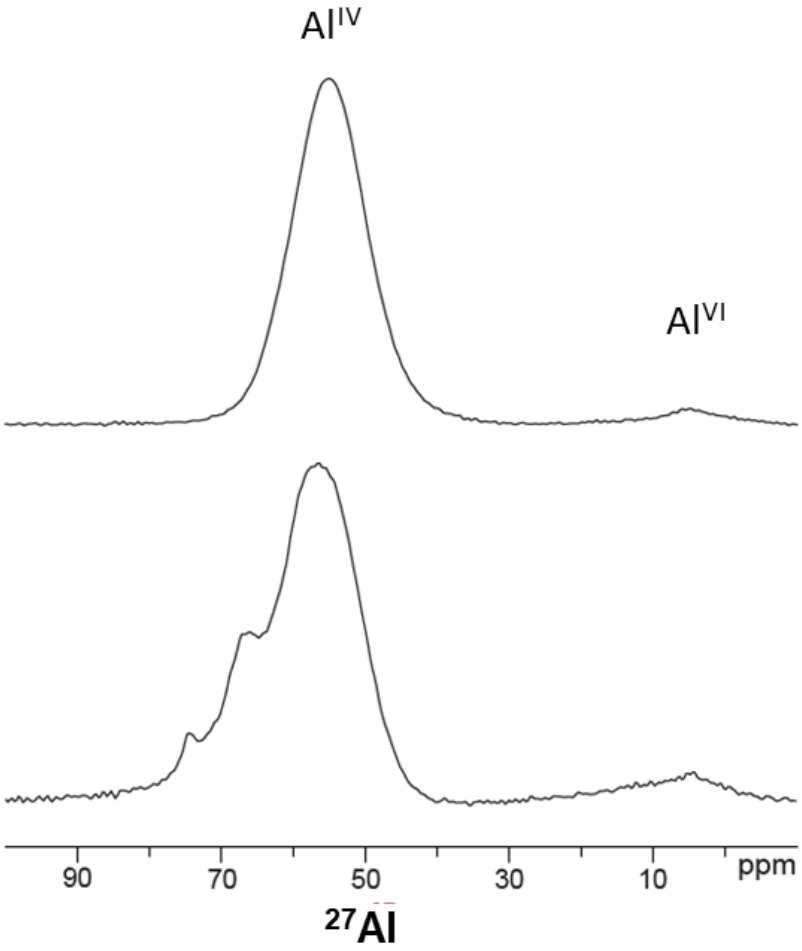


**FIGURE 6A1)** Solid-state $^{27}Al$ single-pulse NMR spectra of (top) unhydrated volcanic glass #1, and (bottom) hydrated (w/s = 0.58, 8 day, 90 °C) 3:1 volcanic glass #1:tricalcium silicate with 4%bwos NaCl/4%bwos $Na_2SO_4$ acquired at 18.8 T, 22 kHz MAS, and 298 K.

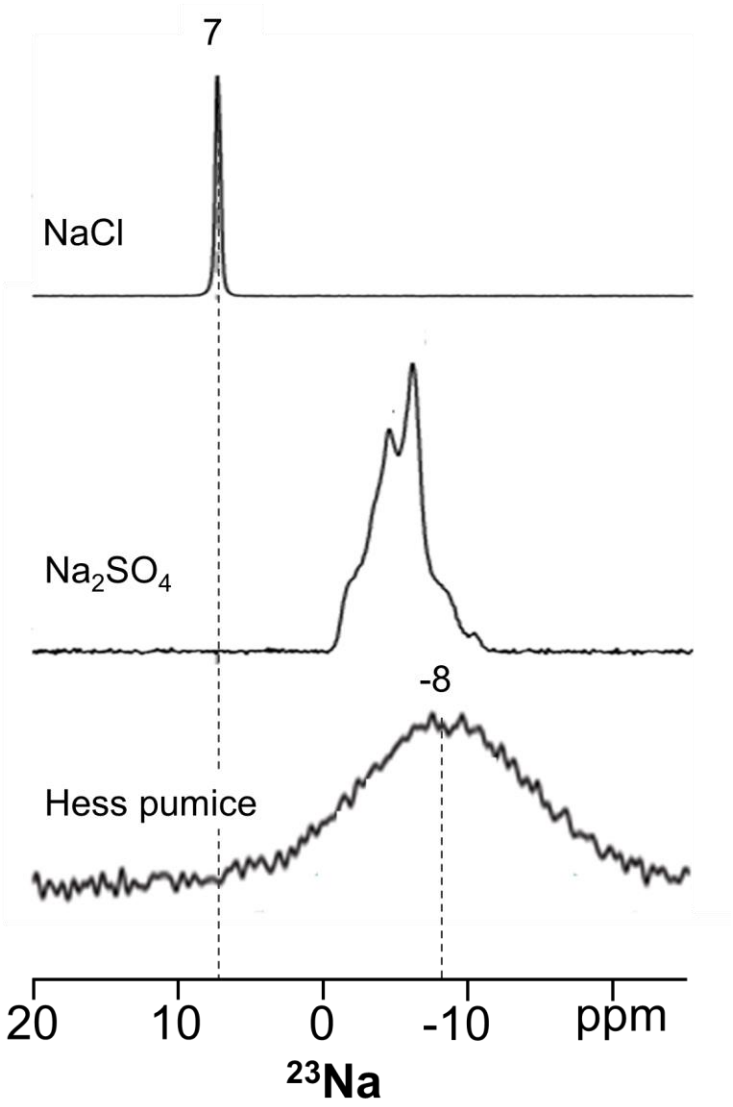


**FIGURE 6A2)** Solid-state $^{23}Na$ single-pulse NMR spectra of crystalline NaCl, crystalline $Na_2SO_4$, and unhydrated volcanic glass #1 acquired at 18.8 T, 22 kHz MAS, and 298 K.

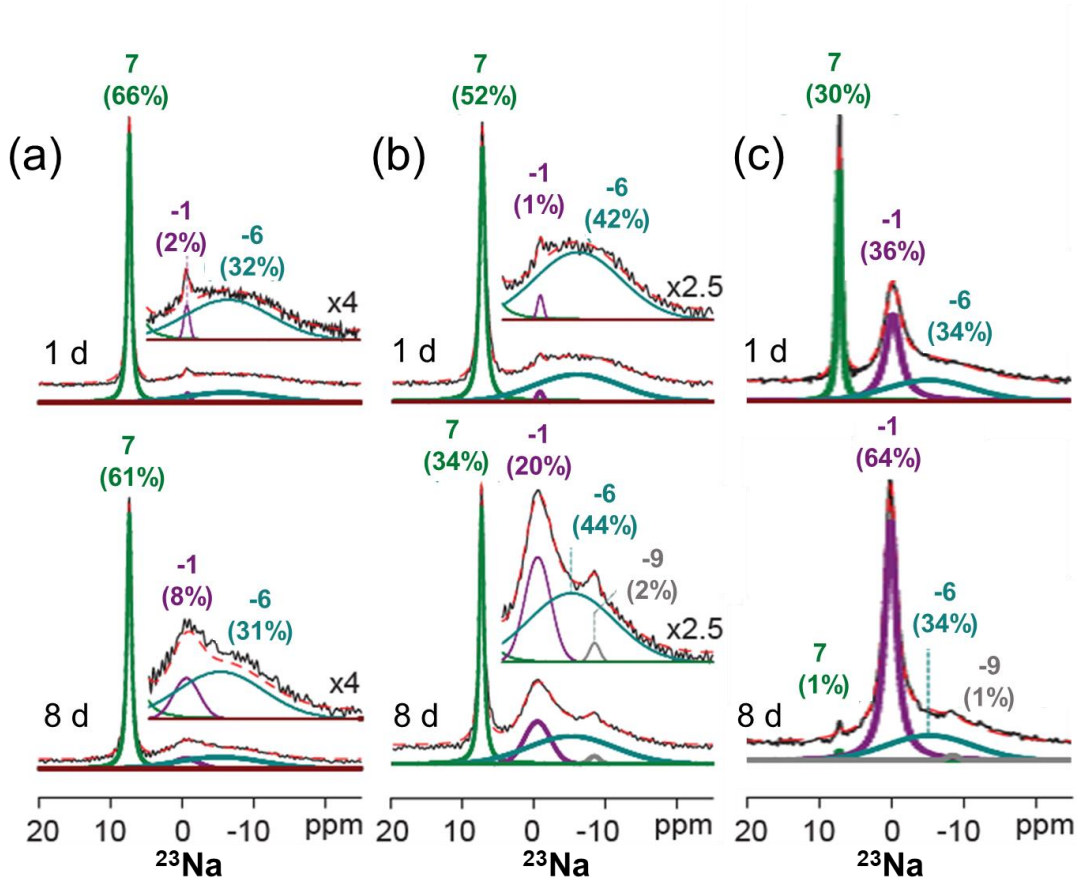


**FIGURE 6A3)** Solid-state $^{23}$Na single-pulse NMR spectra of hydrated (top =1 days, bottom = 8 days) volcanic glass-cement blends containing 4%bwos NaCl/4%bwos $Na_2SO_4$ activators including (a) 3:1 volcanic glass #1:Class A gray oilwell cement hydrated at 38 °C, (b) 3:1 volcanic glass #1:Class A gray oilwell cement hydrated at 90 °C, and (c) 3:1 volcanic glass #1:Tricalcium silicate hydrated at 90 °C acquired at 18.8 T, 22 kHz MAS, and 298 K. Spectra indicate that $Na_2SO_4$ is preferentially consumed in comparison to NaCl. Lower particle size of tricalcium silicate versus class A gray oilwell cement may explain increased NaCl conversion in (c). Water-to-solids ratio is 0.58 for all conditions.

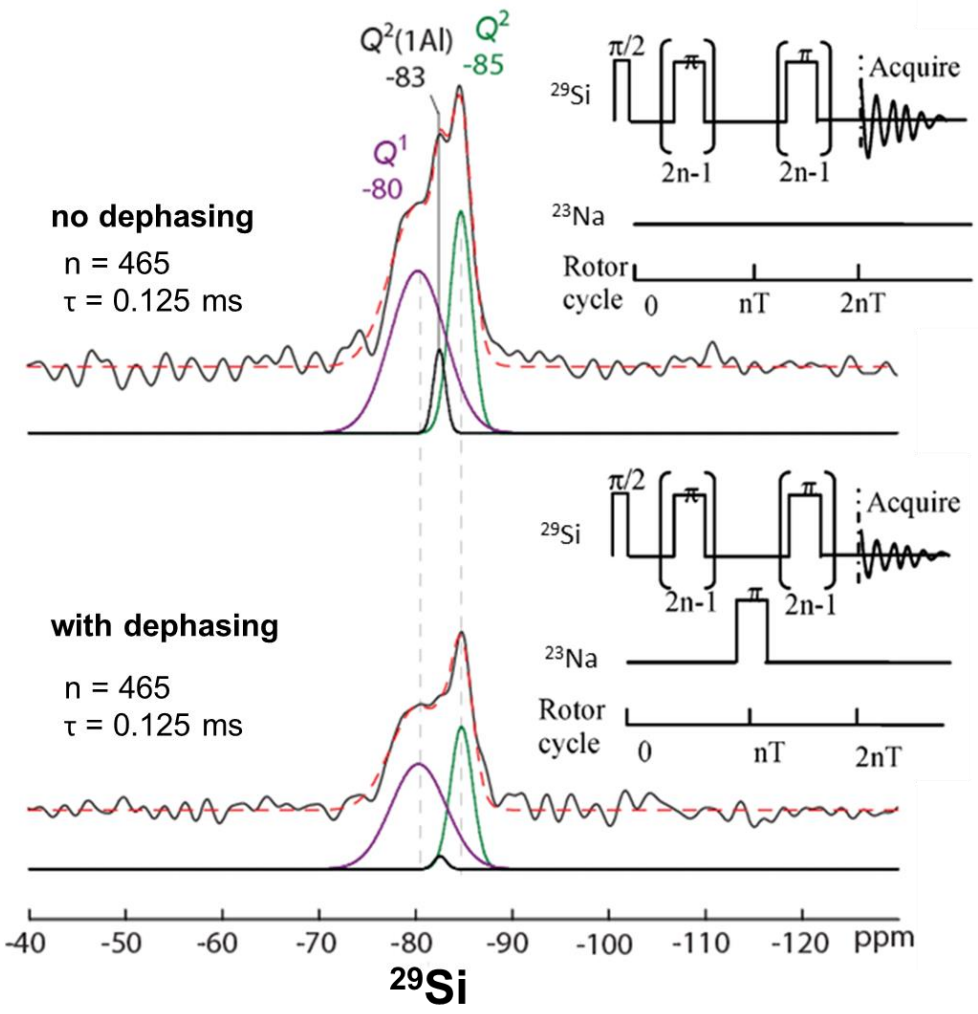


**FIGURE 6A4)** Spatial proximities of $^{29}Si$ and $^{23}Na$ species in hydrated (w/s = 0.58, 8d, 90°C) 3:1 volcanic glass #1:Tricalcium silicate containing 4%bwos NaCl/4%bwos $Na_2SO_4$ measured by 29Si{23Na} DNP CP-REDOR acquired at 9.4 T, 8 kHz MAS, and 95 K using a DNP solvent matrix comprised of 4 mM TEKPol in 1,1,2,2-tetrachloroethane. Partial dephasing of Q2(1Al) species indicates that Na+ is preferentially located near Al species in calcium aluminosilicate hydrates.

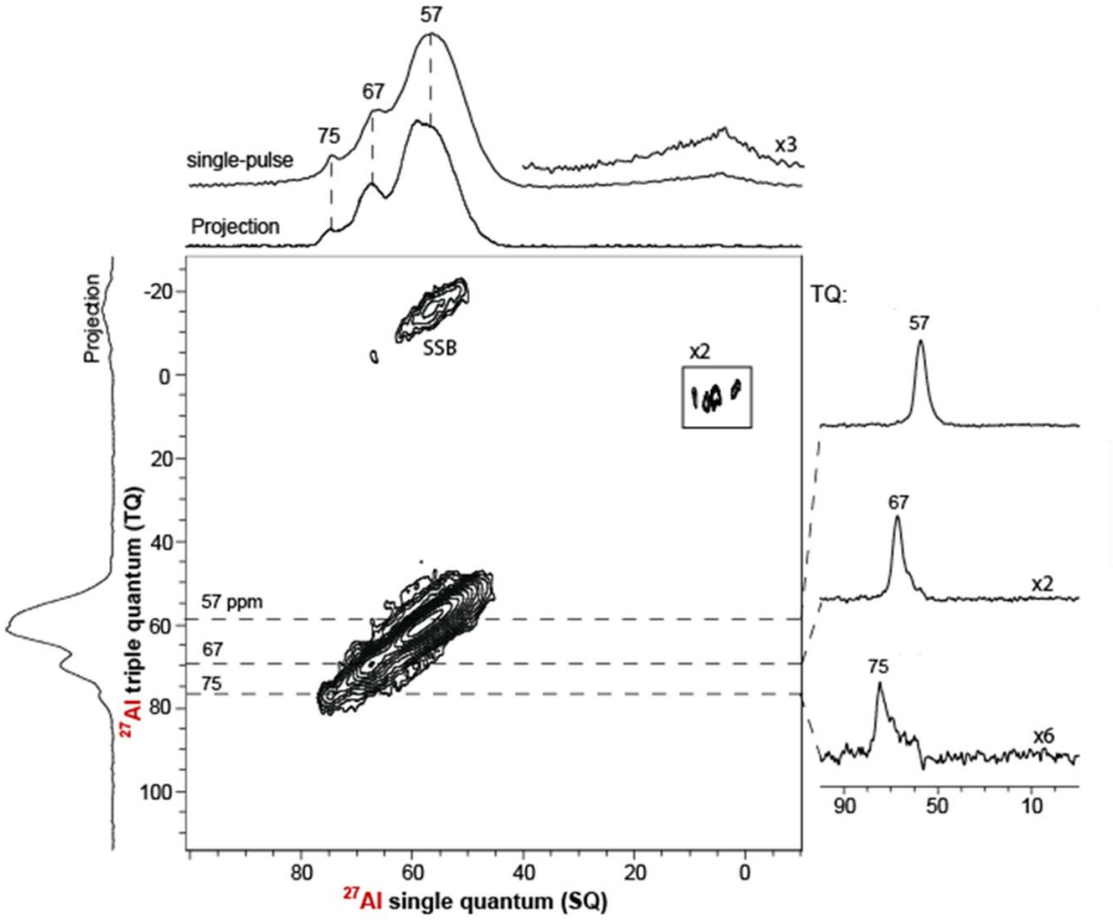


**FIGURE 6A5)** $^{27}$Al 3Q-MAS spectrum of hydrated (w/s = 0.58, 8d, 90 °C) 3:1 volcanic glass #1:Tricalcium silicate with 4%bwos NaCl/4%bwos $Na_2SO_4$ acquired at 18.8 T, 22 kHz MAS, at 298K. At least three distinct $^{27}$Al environments are resolved with broad distributions of isotropic chemical shifts and second-order quadrupolar interactions.

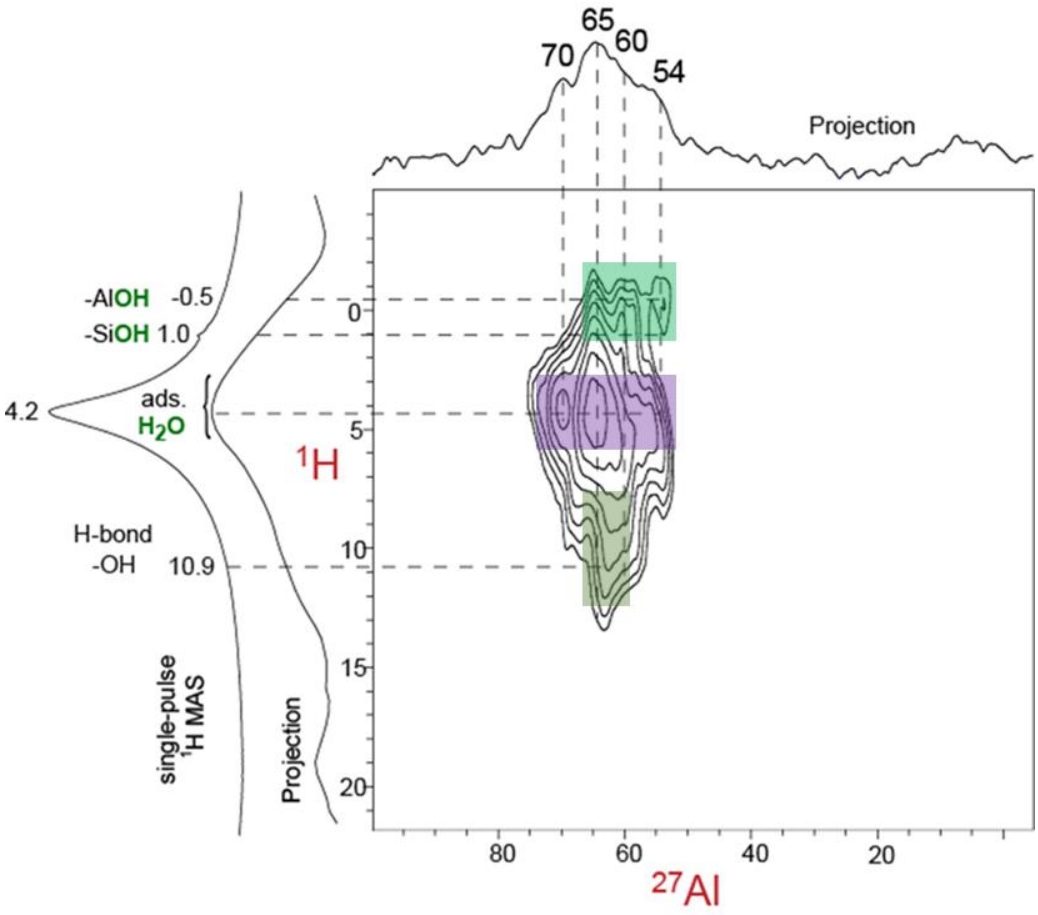


**FIGURE 6A6)** 2D $^{27}Al\{^{1}H\}$ DNP-HETCOR spectra of hydrated (w/s = 0.58, 8 d, 90 °C) 3:1 volcanic glass #1:Tricalcium silicate with 4 %bwos NaCl/4 %bwos $Na_2SO_4$ acquired at 9.4 T, 8 kHz MAS, and 95 K using a DNP solvent matrix comprised of 4 mM TEKPol in 1,1,2,2-tetrachloroethane. Surface-enhanced spectrum with $^{27}Al$ signal DNP enhancement factor of ~4, majority of correlated $^{27}Al\{^{1}H\}$ intensity likely arises from bulk.

## References


1 J. F. Stebbins and Z. Xu, *Nature*, 1997, **390**, 1996–1998.

2 C. Le Losq, D. R. Neuville, W. Chen, P. Florian, D. Massiot, Z. Zhou and G. N. Greaves, *Sci. Rep.*, 2017, **7**, 1–12.

3 M. D. Jackson, E. N. Landis, P. F. Brune, M. Vitti, H. Chen, Q. Li, M. Kunz, H.-R. Wenk, P. J. M. Monteiro and A. R. Ingraffea, *Proc. Natl. Acad. Sci.*, 2014, **111**, 18484–18489.

4 M. D. Jackson, *Am. Mineral.*, 2017, **102**, 1435–1450.

5 R. Snellings, *RILEM Tech. Lett.*, 2016, 50–55.

6 A. Rawal, B. J. Smith, G. L. Athens, C. L. Edwards, L. Roberts, V. Gupta and B. F. Chmelka, *J. Am. Chem. Soc.*, 2010, **132**, 7321–7337.

7 M. J. Abdolhosseini Qomi, K. J. Krakowiak, M. Bauchy, K. L. Stewart, R. Shahsavari, D. Jagannathan, D. B. Brommer, A. Baronnet, M. J. Buehler, S. Yip, F. J. Ulm, K. J. Van Vliet and R. J. M. Pellenq, *Nat. Commun.*, 2014, **5**, 1–10.

8 R. P. Sangodkar, B. J. Smith, D. Gajan, A. J. Rossini, L. R. Roberts, G. P. Funkhouser, A. Lesage, L. Emsley, B. F. Chmelka, H. Champs, I. De Sciences, A. Cnrs, E. N. S. Lyon, U. C. B. Lyon and U. De Lyon, *J. Am. Chem. Soc.*, 2015, **137**, 8096–8112.

9 P. Duxson, A. Fernández-Jiménez, J. L. Provis, G. C. Lukey, A. Palomo and J. S. J. Van Deventer, *J. Mater. Sci.*, 2007, **42**, 2917–2933.

10 J. Elsen, O. Cizer and R. Snellings, *Am. Mineral.*, 2013, **98**, 1917–1918.

11 M. D. Jackson, S. R. Chae, S. R. Mulcahy, C. Meral, R. Taylor, P. Li, A. H. Emwas, J. Moon, S. Yoon, G. Vola, H. R. Wenk and P. J. M. Monteiro, *Am. Mineral.*, 2012, **98**, 1669–1687.

12 E. Pustovgar, R. P. Sangodkar, A. S. Andreev, M. Palacios, B. F. Chmelka, R. J. Flatt J. E. De Lacaillerie, *Nat. Commun.*, 2016, **7**, 10952.

13 M. Javad, A. Qomi, F. Ulm and R. J. Pellenq, 2012, **1137**, 1128–1137.

14 G. Geng, R. J. Myers, J. Li, R. Maboudian, C. Carraro, D. A. Shapiro and P. J. M. Monteiro, *Sci. Rep.*, 2017, **7**, 1–10.

15 M. Thomas, *Cem. Concr. Res.*, 2011, **41**, 1224–1231.

16 G. N. Greaves and S. Sen, *Adv. Phys.*, 2007, **56**, 1–166.

17 Y. Hiraoka, T. Nakamura, A. Hirata, E. G. Escolar, K. Matsue and Y. Nishiura, *Proc. Natl. Acad. Sci. U. S. A.*, 2016, **113**, 7035–7040.

18 D. Z. Chen, C. Y. Shi, Q. An, Q. Zeng, W. L. Mao, W. A. Goddard III and J. R. Greer, *Science (80-. ).*, 2015, **349**, 1306–1311.

19 J. J. De Yoreo, P. U. P. A. Gilbert, N. A. J. M. Sommerdijk, R. L. Penn, S. Whitelam, D. Joester, H. Zhang, J. D. Rimer, A. Navrotsky, J. F. Banfield, A. F. Wallace, F. M. Michel, F. C. Meldrum, H. Cölfen and P. M. Dove, *Science (80-. ).*, , DOI:10.1126/science.aaa6760.

20 V. Valtchev and L. Tosheva, *Chem. Rev.*, 2013, **113**, 6734–6760.

21 J. F. Stebbins, J. B. Murdoch, I. S. E. Carmichael and A. Pines, *Phys. Chem. Miner.*, 1986, **13**, 371–381.

22 A. Deshkar, J. Marcial, S. A. Southern, L. Kobera, D. L. Bryce, J. S. McCloy and A. Goel, *J. Am. Ceram. Soc.*, 2017, **100**, 2859–2878.

23 L. Sánchez-Muñoz, J. Sanz, I. Sobrados and Z. Gan, *Am. Mineral.*, 2013, **98**, 2115–2131.
24 C. Le Losq and D. R. Neuville, *Chem. Geol.*, 2013, **346**, 57–71.
25 F. Lodesani, M. C. Menziani, H. Hijiya, Y. Takato, S. Urata and A. Pedone, *Sci. Rep.*, 2020, **10**, 1–18.
26 M. Moesgaard, R. Keding, J. Skibsted and Y. Yue, *Chem. Mater.*, 2010, **22**, 4471–4483.
27 S. J. G. G N Greaves, A Fontaine, P Lagarde, D Raoux, *Nature*, 1981, **293**, 611–616.
28 D. Di Genova, A. Caracciolo and S. Kolzenburg, *Lithos*, 2018, **318**–**319**, 209–218.
29 J. Marcial and J. McCloy, *J. Non. Cryst. Solids*, 2019, **505**, 131–143.
30 N. Garg, V. O. Özçelik, J. Skibsted and C. E. White, *J. Phys. Chem. C*, 2019, **123**, 24873–24883.
31 J. C. Lewin, *Geochim. Cosmochim. Acta*, 1961, **21**, 182–198.
32 M. W. Barnes and B. E. Scheetz, *MRS Proc.*, 1989, **179**, 243–272.
33 R. J. Myers, S. A. Bernal, R. San Nicolas and J. L. Provis, *Langmuir*, 2013, **29**, 5494.
34 C. Liu, H. Ma and Y. Gao, *Asia-Pacific J. Chem. Eng.*, 2019, **14**, 1–10.
35 C. J. Horwell, B. J. Williamson, E. W. Llewellin, D. E. Damby and J. S. Le Blond, *Bull. Volcanol.*, 2013, **75**, 1–19.
36 Z. J. Berkson, M. Hsieh, S. Smeets, D. Gajan, A. Lund, A. Lesage, D. Xie, S. I. Zones, L. B. McCusker, C. Baerlocher and B. F. Chmelka, *Angew. Chemie*, 2019, **131**, 6321–6325.
37 D. Jardón-Álvarez, K. J. Sanders, P. Phyo, J. H. Baltisberger and P. J. Grandinetti, *J. Chem. Phys.*, , DOI:10.1063/1.5020986.
38 G. Tricot, J. Trébosc, F. Pourpoint, R. Gauvin and L. Delevoye, *The D-HMQC MAS-NMR Technique: An Efficient Tool for the Editing of Through-Space Correlation Spectra Between Quadrupolar and Spin-1/2 (31P, 29Si, 1H, 13C) Nuclei*, Elsevier Ltd., 1st edn., 2014, vol. 81.
39 B. Walkley, G. J. Rees, R. San Nicolas, J. S. J. Van Deventer, J. V. Hanna and J. L. Provis, *J. Phys. Chem. C*, 2018, **122**, 5673–5685.
40 B. L. Phillips, R. J. Kirkpatrick and G. L. Hovis, *Phys. Chem. Miner.*, 1988, **16**, 262–275.
41 C. R. A. Catlow, A. R. George and C. M. Freeman, *Chem. Commun.*, 1996, 1311–1312.
42 V. I. Bakhmutov, *Chem. Rev.*, 2011, **111**, 530–562.
43 M. Ahmadzadeh, J. Marcial and J. McCloy, *J. Geophys. Res. Solid Earth*, 2017, 122, 2504–2524.
44 R. J. Myers, E. L. Hôpital, J. L. Provis and B. Lothenbach, *Cem. Concr. Res.*, 2015, **68**, 83–93.
45 G. Mertens, R. Snellings, K. Van Balen, B. Bicer-Simsir, P. Verlooy and J. Elsen, *Cem. Concr. Res.*, 2009, **39**, 233–240.
46 C. K. Yip, G. C. Lukey and J. S. J. Van Deventer, *Cem. Concr. Res.*, 2005, **35**, 1688–1697.
47 J. B. Murdoch, J. F. Stebbins, I. S. E. Carmichael and A. Pines, *Phys. Chem. Miner.*, 1988, **15**, 370–382.
48 P. J. Schilling, L. G. Butler, A. Roy and H. C. Eaton, *J. Am. Ceram. Soc.*, 1994, **77**,

2363–2368.